SHEAR-WAVE ANISOTROPY AND THE INTERPRETATION OF TEMPORAL CHANGE IN TIME DELAYS

by

YUN LIU

(B.Sc. Changchun Geological Institute, China)

Thesis submitted for the degree of Doctor of Philosophy
Department of Geology and Geophysics
University of Edinburgh

January 1995

DECLARATION

I hereby declare that this thesis was completed by myself and that the work described was entirely my own unless otherwise stated in the text.

ABSTRACT

Shear-wave splitting is observed in a three-years dataset recorded at the Parkfield borehole digital seismic network, on the Parkfield segment of the San Andreas fault, central California, and also at Cajon Pass with data recorded at a 2.5 km deep borehole, southern California. Shear-wave polarizations at five out of seven stations at Parkfield are aligned in the direction which is consistent with the direction of horizontal maximum compressive stress. In the San Andreas fault zone, shear-wave polarizations are aligned approximately parallel to the fault. Temporal variation of time delays between two split shear-waves is detected before and after a M_L=4 earthquake at Parkfield. The analysis of temporal variation based on the best quality data shows that the temporal change is significant at the 68% confidence level. The study of earthquake multiplets also shows similar variations. This means that there was probably a change in stresses, which modified the geometry of microcracks pervading the rockmass before and after this event, so that time delays between faster and slower shear-waves for the similar events travelling along nearly the same wave paths and occurring at different times display a distinct increase before the time of the M_L=4 earthquake, and a decrease afterwards. Normalised time delays in the fault zone are found to be about twice as large as those in the intact rocks. This suggests that fluid-filled cracks and fractures within the fault zone are more extensive than those in the surrounding rocks, and that the alignment of fault-parallel shear-wave polarizations in the fault zone is attributed to the fault internal structures.

Studying the causes of the temporal variation indicates that stress concentration before the M_L=4 earthquake had probably increased the number of cracks or the radius of the cracks; after the release of strain energy after the earthquake, stress reduced to a lower level, accompanied by healing and flattening of the cracks. The change of crack density and aspect ratio associated with the M_L=4 earthquake is interpreted as the cause of the observed temporal variation.

At Cajon Pass, modelling the observations of polarizations and time delays

using Genetic Algorithms suggests that the anisotropic structure near Cajon Pass is of orthorhombic symmetric structure, indicating the existence of stress-aligned parallel vertical cracks and aligned mineral grains and crystals in the seismogenic zone. The strike of the parallel vertical microcracks suggests that the maximum horizontal compressive stress direction is approximately N13°W, which is consistent with the results from earthquake source mechanisms, and is consistent with the motion of pure right-lateral strike-slip on the San Andreas Fault. It is further suggested from this dataset that the San Andreas Fault is likely to be driven by deeper tectonic stresses rather than the secondary structure, and the active secondary faulting and folding are probably driven by the relatively shallow stresses as measured in the deep borehole.

Shear-wave anisotropy is mainly concentrated in the upper 10-15 km in the crust at Parkfield. In the fault zone shear-wave anisotropy approximately extends up to 8 km. It suggests that fault gouge may terminate at such depth, which is coincident with other studies.

ACKNOWLEDGEMENTS

My greatest thanks go to my supervisor Professor Stuart Crampin for his enthusiastic support and constructive criticisms, and for finding funds, and for encouraging me to attend conferences. Stuart's desire to remain at the forefront of science and lead the way head has greatly impressed me. I am grateful to Dr Ian Main, my University supervisor, for his invaluable suggestions and helpful opinions on many aspects of my thesis. I thank both of them for their patience to read through this thesis.

Dr David Booth gave me great assistance and provided many useful comments during the course of this work, and guided me to use his anisotropic reflectivity program. Dr Russ Evans helped me to transfer the data and read the tapes, and also provided supports on many other occasions. Dr Robert Pearce kindly guided me to use his relative amplitude and polarity program for focal mechanism study, and commented on several major Chapters of this thesis. Stephen Horne, a fellow research student working on genetic algorithm inversion, allowed me to use his program to invert anisotropic structure in Chapter 6. John Lovell kindly read several major Chapters, which has improved the readability of this thesis. Dr Philip Wild and Charlie Fyfe helped me on computing problems. I must thank Dr Chris Browitt, former manager of the Global Seismology Research Groups (GSRG) of British Geological Survey (BGS) and now Assistant Director of BGS, for finding me part of the studentship. I thank both Chris and Terry Turbitt, now manager of GSRG, for allowing me to use all the necessary facilities.

I thank Dr Peter Leary (formerly at University of Southern California, USC, and now at University of Edinburgh) and Professor Peter Malin of Duke University in the United States for kindly providing me some of the Parkfield data. Many thanks go to Professor Tom McEvilly of University of California, Berkeley for providing information about data acquisition at Parkfield. Dr Peter Leary and Dr Rachel Abercrombie (USC) kindly provided the Cajon Pass data which made the work in Chapter 6 possible. I thank both Rachel and Peter for their suggestions and comments

on the results from this dataset.

The postgraduate students in BGS gave me constant advice, suggestions, criticism and support: Aphrodite Karnassopoulou, Helen Rowlands, Henchang Dai, Gordon Holmes, Brian Baptie, Stephen Horne, Colin Slater, and Xinwu Zeng.

My postgraduate studentship was sponsored by both Overseas Research Student Award (ORS) and the British Geological Survey. BGS also supported me to attend several national and international meetings. All the work in this thesis were carried out in BGS.

Last, but certainly not least, no words can be found to express my thanks to my mother, for her help to look after my child. This thesis would never have been completed without her help, encouragement, moral support, and above all her love. I thank my husband, Enru for his support and help on almost every aspects, and he also read most of this thesis. Finally, I apologize to my son, Steven and my family for many absent evenings during the course of my study.

CONTENTS

CHAPTER 1

INTRODUCTION

1.1 SEISMIC ANISOTROPY

Any homogeneous uniform elastic material whose physical properties vary with direction is anisotropic, and seismic anisotropy refers to the variation of seismic properties (usually velocities) with direction (say azimuth). Crampin (1986) pointed out that two types of anisotropy which have fundamental differences should be distinguished: vertical transverse isotropy or transverse isotropy with a vertical symmetry axis, in which elastic properties vary only with incidence angles in the vertical plane; and general anisotropy or transverse isotropy with a horizontal or subhorizontal symmetry axis, in which properties also vary with azimuth. The effective azimuthal seismic anisotropy, as shown by birefringence (splitting) of shear waves polarized in different directions, resulting from aligned cracks and pores, has been observed all over the world (Crampin, 1994) and recognised as a significant property of crustal rocks. Identifying shear-wave splitting in the crust requires two criteria to be met: digital three-component recordings at high sampling rates so that the phenomenon can be displayed; and sufficient understanding of the phenomenon to be able to interpret what is observed.

1.1.1 Observations of seismic anisotropy

The observation of seismic anisotropy first started in the upper mantle. Following the pioneering work of Hess (1964), a number of individual studies of crustal P_n-wave[1] velocity anisotropy have indicated P_n velocity anisotropy beneath

[1]Beyond a certain distance, generally in the range of 100 to 200 km, the first arrival from seismic sources in the crust corresponds to waves refracted from the top of the mantle, which are called P_n waves or crustal head waves.

the Rhinegraben (Bamford, 1977); velocity anisotropy of fundamental mode Rayleigh waves across the NAZCA plate (Forsyth, 1975); and anisotropic polarization anomalies in higher-mode surface waves across Eurasia (Crampin and King, 1977). Shear-wave splitting was first positively identified above small earthquakes by Crampin *et al.* (1980, 1985), and by Buchbinder (1985), and has been subsequently observed in many parts of the world in a wide variety of rocks in a wide variety of tectonic regimes (reviewed by Crampin, 1987; Crampin and Lovell, 1991). Shear-wave splitting has also been observed in controlled-source experiments: reflection surveys (Mueller, 1991; Li and Crampin, 1991); VSPs (Bush and Crampin 1991; Cliet *et al.*, 1991); crosshole surveys (CHSs) (Li and Crampin, 1991; Liu *et al.*, 1991) and reverse VSPs (RVSP) (Liu *et al.*, 1991). As a result anisotropy is now widely recognised in both earthquake and exploration seismology [refer to collection of papers in the proceedings of the sixth International Workshops on Seismic Anisotropy].

1.1.2 Causes of shear-wave splitting

Several possible sources of seismic anisotropy in the rockmass have been suggested. Following Crampin *et al.* (1984a), and Crampin and Lovell (1991), these causes are summarized below.

(a) Aligned crystals

Crystalline anisotropy occurs when the individual crystals in a crystalline solid have preferred orientations over a volume sufficiently large to affect the transmission of seismic waves. Such anisotropy caused by minerals, for instance olivine or orthopyroxene, has been widely used to explain the observations in the upper mantle (Hess, 1964; Francis, 1969; Avé Lallemant and Carter, 1970; Peselinick and Nicolas, 1978; Christensen and Salisbury, 1979; Fuchs, 1983; Silver and Chan, 1988).

(b) Direct stress-induced anisotropy

The elastic behaviour of an initially isotropic solid becomes anisotropic when

acted on by a sufficiently large stress (Dahlen, 1972; Nikitin and Chesnokov, 1984). However, the stresses required to cause anisotropic effects in seismic wave propagation are probably too great to cause observable seismic anisotropy in the Earth (Dahlen, 1972). It is suggested that direct stress-induced anisotropy is seldom likely to be the dominant source of anisotropy (Crampin *et al.*, 1984a).

(c) Lithologic anisotropy

A sedimentary rock has lithologic anisotropy when the individual grains, which may or may not be elastically anisotropic, are elongated or flattened where the shapes are aligned by gravity or fluid flow when the material is first deposited, or by plastic deformation thereafter. The well-know transverse isotropy of clays (Brodov *et al.*, 1984) and shales (Kaarsberg, 1968; Robertson and Corrigan, 1983) is an example of lithologic anisotropy resulting from aligned grains.

(d) Structural anisotropy

Periodic Thin-Layers (*PTLs*) or finely layered media display structural anisotropy. *PTL*-anisotropy is often found in sedimentary basins (Bush and Crampin, 1991); marine sediments; and calcareous sediments (Johnson *et al.*, 1977). In practice this type of anisotropy is often combined with anisotropy caused by aligned sediment grains in one or more periodic thin-layers (Puzyrev *et al.*, 1984). *PTL* is also referred to as transverse isotropy with a vertical symmetry axis (Levin, 1979; Helbig, 1984; Crampin, 1986).

(e) Stress-aligned crack-induced anisotropy

A rock containing a set of joints, cracks, microcracks or pores which have preferred orientations is effectively anisotropic. Fluids are a very common constituent of the crustal rock mass (Fyfe *et al.*, 1978). Meteoric water has been incorporated into most sedimentary rocks at deposition. Since water is one of the by-products of most prograde metamorphic processes, water will be released within most igneous and metamorphic rocks. Such water would be released by each grain within the rock

undergoing metamorphism, and the only mechanism for releasing water deep in an otherwise impermeable rock mass is by hydrofracture (Fyfe *et al.*, 1978). Deep wells (Kozlovsky, 1984) have found water-filled fractures deep in the crust, and even upper mantle xenoliths are pervaded by fluid-filled microcracks, where the fluid is largely CO_2 (Andersen *et al.*, 1984).

In the presence of differential stresses, cracks will tend to deform by a variety of stress-controlled mechanisms. Cracks with large aspect ratios will tend to elongate by spalling by the same processes that cause drill holes to become elliptical (Zoback, 1983) which will in time reduce the large aspect ratio to a distribution of small cracks. Small cracks will grow, or re-align, relative to the directions of stress, by subcritical crack growth caused mainly by stress corrosion, which is a physical-chemical reaction between rock and fluid occurring at crack tips causing subcritical growth of cracks or elastic "*bowing*" of crack walls (Atkinson, 1984; Atkinson and Meredith, 1987; Crampin and Atkinson, 1985). If the existing crack is not parallel to the direction of maximum compression, it closes, expelling its fluid content into the new cracks at its tips (Kranz, 1983). In the laboratory, initially randomly distributed (isotropic) pore spaces in sandstone take on the characteristics of distributions of aligned cracks when subjected to deviatoric stress (Fyfe *et al.*, 1978); and a Westerly granite in water shows pervasive microcracking aligned perpendicular to the applied tensile load throughout the sample (Main *et al.*, 1990a). All the above phenomena result in distributions of cracks which have preferred directions of orientation, parallel to the axis of maximum compression if $\sigma_1 >> \sigma_2 \geq \sigma_3$, or normal to the maximum tension if $\sigma_1 \geq \sigma_2 >> \sigma_3$. These pervasive stress-aligned fluid-filled cracks have been referred to as *Extensive-Dilatancy Anisotropy or EDA* (Crampin *et al.*, 1984b).

EDA may be caused by two phenomena. The predominant cause is the anelastic subcritical growth of existing cracks and microcracks by stress corrosion at the crack tip (Rutter and Mainprice, 1978; Atkinson, 1982) at the low strain rates and low stresses expected throughout earthquake preparation zones. This process requires the presence of some water to provide the chemical transport, but can occur over a wide range of water pressures. The second cause is the elastic bowing of existing

fluid-filled cracks and pores, which will be important at low shear stresses on those, possibly rare, occasions when the pore pressure is sufficiently high (Crampin *et al.*, 1984b). *EDA* cracks have been considered to be the most important source of crustal anisotropy, and are the cause of the shear-wave splitting observed world wide (Crampin and Lovell, 1991).

1.2 Basic theory and formulations for aligned cracks

There are several comprehensive books specifically devoted to seismic anisotropy, including the classic book by Love (1944), and the most recent one by Helbig (1993). As this thesis is concerned with analysis and interpretation of earthquake data in terms of the anisotropy concept, a detailed review of this theory is not necessary, and I shall only give the most basic equations which are relevant to this thesis. The elastodynamic equations of motion in a uniform purely-elastic anisotropic medium are:

$$\rho\ddot{u}_j = c_{jkmn}u_{m,nk} , \qquad \text{for j=1,2,3} \qquad (1.1)$$

where the elastic tensor has been rotated with elements c_{jkmn} by the usual tensor-transformation:

$$c'_{jkmn} = x'_{j,p}x'_{k,q}x'_{m,r}x'_{n,s}c_{pqrs} , \qquad \text{for j,k,m,n,p,q,r,s=1,2,3} \qquad (1.2)$$

the general expression for the harmonic displacement of a homogeneous plane-wave is:

$$u_j = a_j \exp[i\omega(t - q_k x_k)] \qquad (1.3)$$

where $\boldsymbol{a}$ is the amplitude vector specifying the polarization of the particle motion; and $\boldsymbol{q}$ is the slowness vector. Substituting the displacement (1.3) into the equation of motion (1.1) gives three simultaneous equations, which may be solved for c in any direction. However, the preferred procedure is to write the solution as a linear eigenvalue problem for ρc^2 (Crampin, 1981):

$$(\boldsymbol{T}-\rho c^2 \boldsymbol{I})\boldsymbol{a}=\boldsymbol{0} \tag{1.4}$$

where $\boldsymbol{T}$ is a 3x3 matrix with elements which are linear functions of elastic constants $\{c_{jlkl}\}$; $\boldsymbol{I}$ is an unit matrix; and, for convenience, the constant factor $\exp(i\omega t)$ has been omitted. The eigenvalue problem (1.4) has three real positive roots for ρc^2 with orthogonal eigenvectors $\boldsymbol{a}$. These roots refer to a quasi P-wave (qP) and two quasi shear waves ($qS1$and $qS2$)[2], where the term 'quasi' means that in an anisotropic medium P and S waves do not in general respectively polarize exactly parallel and perpendicular to the direction of propagation as in an isotropic medium.

The problem of wave propagation through an anisotropic medium is to use effective elastic constants for the cracked solid. Theoretical formulations for the elastic constants of a homogeneous and multilayered medium with random distributions of dry and liquid-filled inclusions have been studied by a number of investigators: Eshelby (1957), Hashin (1962), Walsh (1965), Wu (1966), Korringa (1973), O'Connell and Budiansky (1974, 1977), Kuster and Toksöz (1974). Crampin (1978) obtained effective elastic constants by modelling the variation of velocity through a cracked solid derived in a first-order approximation by Garbin and Knopoff (1973, 1975a, b). Hudson has developed a more general theoretical approach to calculating the elastic constants of cracked solids that includes first-order (Hudson, 1981) and second-order (Hudson, 1980) interactions between the scattering inclusions. All formulations assume

[2]Several different labels often appear in the literature. Sometimes, $qS1$ and $qS2$ are labelled qSH and qSV, which are, strictly speaking, only correct when waves propagate in the symmetry plane. Crampin (1989) and Winterstein (1990) have suggested a consistent notation.

that the material contains a uniform weak concentration of aligned cracks, and that the dimensions of cracks are small with respect to the seismic wavelength. Hudson (1981) developed techniques for modelling attenuation in a cracked solid. The most convenient formulation for anisotropic attenuation is to express the attenuation parameter $1/Q$ as the eigenvalue of a matrix of the imaginary parts of complex elastic constants (Crampin 1981) [note here $Q^{-1} \propto \omega^3$ is predicted by Hudson (ω is an angular frequency), whereas $Q^{-1} \propto \omega^{-1/2}$ is observed (Main, *et al.*, 1990b) because cracks are organised clustered, and scattering attenutation is more sensitive to the larger clusters of dilatant microcracks], where the real parts model the purely elastic behaviour. This then allows attenuative wave propagation to be calculated by the same range of anisotropy programs as the purely elastic behaviour. Hudson's expression for the elastic constants of a medium containing aligned cracks is:

$$c_{jkmn} = c^0_{jkmn} + \varepsilon c^1_{jkmn} + \varepsilon^2 c^2_{jkmn} \tag{1.5}$$

where crack density (CD or ε) is defined as the number of cracks in a unit volume, $\varepsilon = Na^3/V$, where N is the number of cracks of radius a in volume V (Budiansky and O'Connell, 1976). c^0_{jkmn} are elastic constants of the uncracked rock; and c^1_{jkmn} and c^2_{jkmn} are the first- and second-order perturbations due to cracks, respectively, which are explicitly given by Crampin (1984). The result may be formulated so that real parts model the velocity of body waves and imaginary parts model attenuation (Crampin, 1981). This allows wave propagation through a two-phase cracked solid to be modelled by wave propagation through a homogeneous anisotropic material with complex elastic constants.

Hudson's formulations are valid to crack density less than about 0.1 (Crampin, 1984), and aspect ratio, $AR = d/a$, less than about 0.1, where d is half-thickness of cracks (Douma, 1988). After an extensive comparison with Nishizawa's (1982) crack theory which is assumed to be valid for any crack density and any aspect ratio from thin fat up to circular pore, Douma (1988) indicated that the two techniques give

identical results up to an aspect ratio AR = 0. 1 and have similar angular patterns of velocity variations up to AR = 0. 3, although the absolute value of the velocities begins to differ for AR > 0. 1[3].

Hudson (1986, 1990) has extended his formulations to include distributions of cracks with more than one crack orientation. His latest formulations include the second-order interactions of the perturbations from cracks - the effective crack-to-crack interaction (Hudson, 1991).

1.3 SEISMIC BODY WAVES IN AN ANISOTROPIC MEDIUM

Crampin (1991a, 1991b, 1993) has studied the behaviour of seismic body waves in an anisotropic medium in detail. Figure 1.1 shows a schematic illustration of shear-wave splitting in the crust. A shear wave travelling along a ray path within about 35° of the vertical generally splits into two components. These two split shear-waves are usually nearly orthogonally polarized and propagate with different velocities. The polarization of the leading split shear-wave (faster wave) is usually parallel or subparallel to the direction of maximum horizontal stress, which is one of the most distinctive features of shear-waves in the crust. Shear waves are sensitive to changes in the geometry of thin inclusions, such as stress-aligned fluid-filled cracks, microcracks, and preferentially oriented pore-space. Time-delays between the two split shear-waves are more sensitive to the crack density. Figure 1.2 displays the theoretical behaviour of shear wave propagation through parallel fluid-filled microcracks. The variation of shear-wave velocities, polarizations and time-delays with fixed aspect ratio AR = 0.001 and increasing crack density; and fixed crack density CD = 0.025 with increasing aspect ratio are plotted respectively in Figure 1.2 (a) and (b). The isotropic rockmass has P-wave velocity V_p = 6.0 km/s, S-wave velocity V_s = 3.16 km/s, and density ρ = 2.65 g/cm^3, chosen from the parameters of the major layer

[3]Based on 46 separate results of shear-wave splitting, Crampin (1994) has recently suggested that there is a fracture criticality limit of crustal rocks $0.045 \leq \varepsilon \leq 0.1$, which separates intact rocks from heavily fractured rocks.

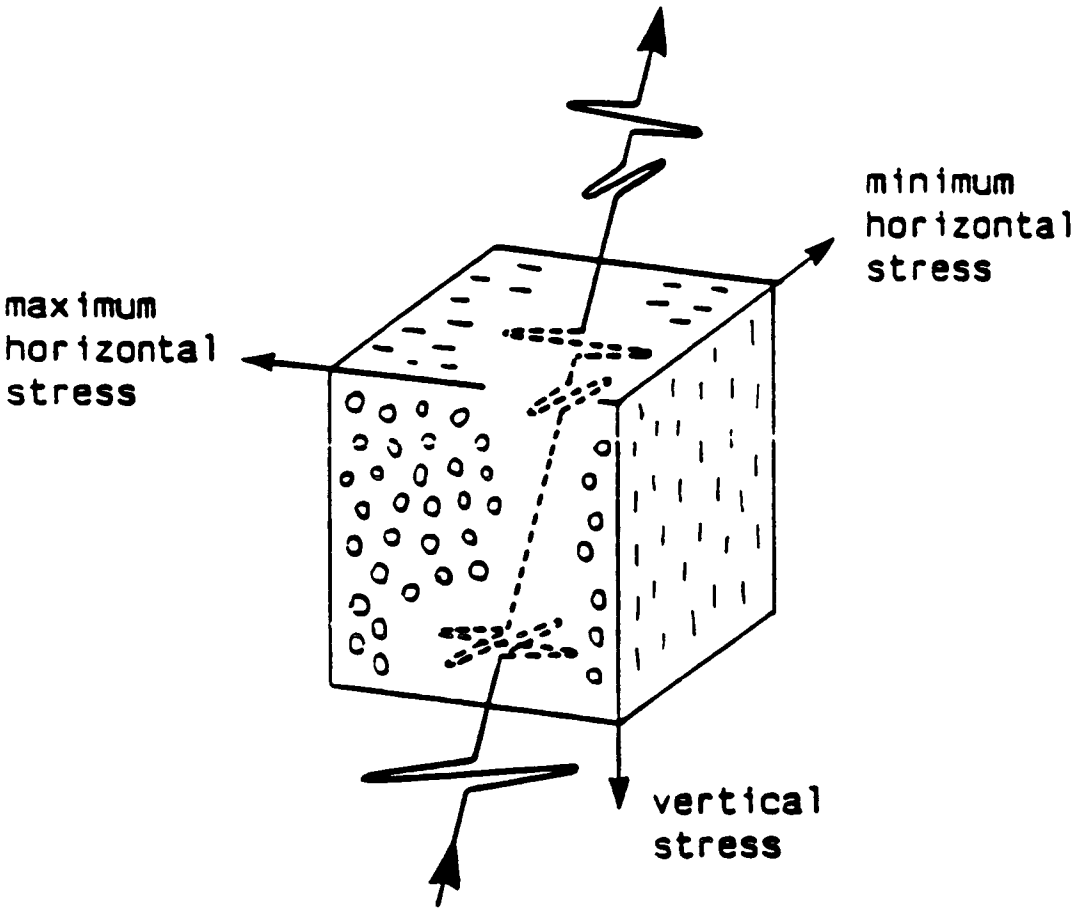

Figure 1.1. Schematic illustration of shear-wave splitting in the crust. A shear wave travelling along a ray path within about 35° of the vertical generally splits into two components with different arrival times and different, often nearly orthogonal, polarizations, where the polarization of the faster component is usually parallel, or sub-parallel, to the direction of maximum horizontal stress (after Crampin and Lovell, 1991).

Figure 1.2. Theoretical behaviour of shear wave propagation through parallel water-filled microcracks aligned perpendicular to the x-axis for a fixed aspect ratio AR=0.001 and a range of crack densities from CD=0.015 to CD=0.035 (modelling observations at Parkfield) in (a); and a fixed crack density CD=0.025 and a range of aspect ratio from AR=0.001 to AR=0.1 in (b). The theoretical formulations for the cracked rock are those of *Hudson* (1980, 1981). The left column of diagrams in (a) and (b) are the variations of shear wave velocities for directions in the quadrant between perpendicular (0°) and parallel (90°) to the faces of parallel microcracks. The solid line is the phase velocity and the dot-dashed line is the group velocity (barely separated because of weak anisotropy). The separation of the shear wave in directions between the intersection point of the two split shear waves and 90° to the crack normals is shaded in order to stress the changes with increasing crack density or aspect ratio; the central column is equal-area polar projections out to 90° of a hemisphere of directions corresponding with the change of parameter to the left of polarizations of leading split shear wave; and the right column, is time delays between split shear waves through the parallel cracks plotted in both contour equal-area polar projections and cross sections. Time delays are normalised in ms/km, except for the first projection and cross section in ms/10km in (a).

(a)

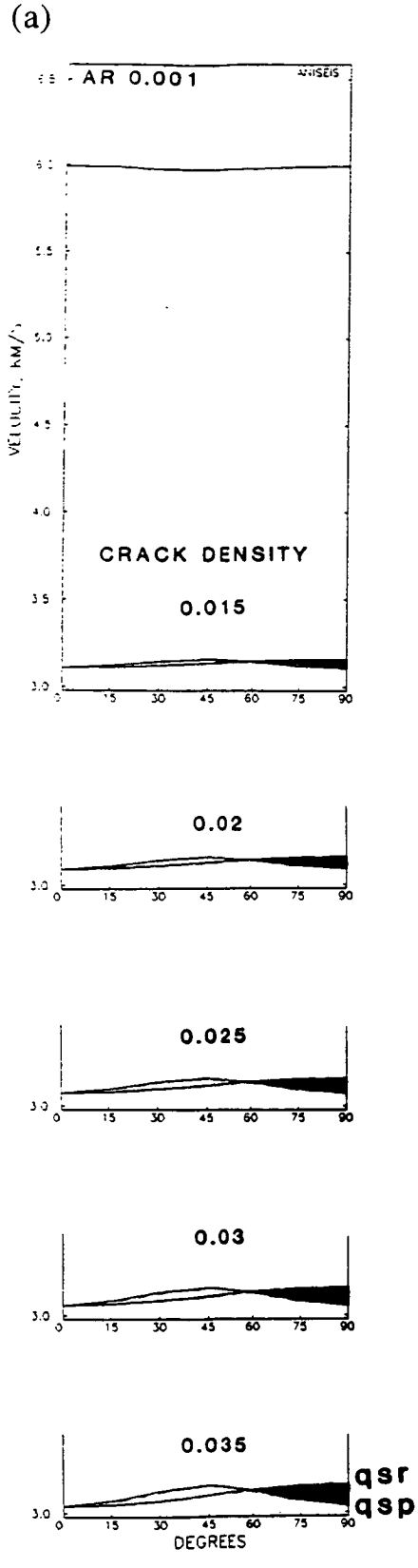
AR 0.001
ANISEIS
VELOCITY, KM/S
CRACK DENSITY
0.015
0.02
0.025
0.03
0.035
qsr
qsp
DEGREES

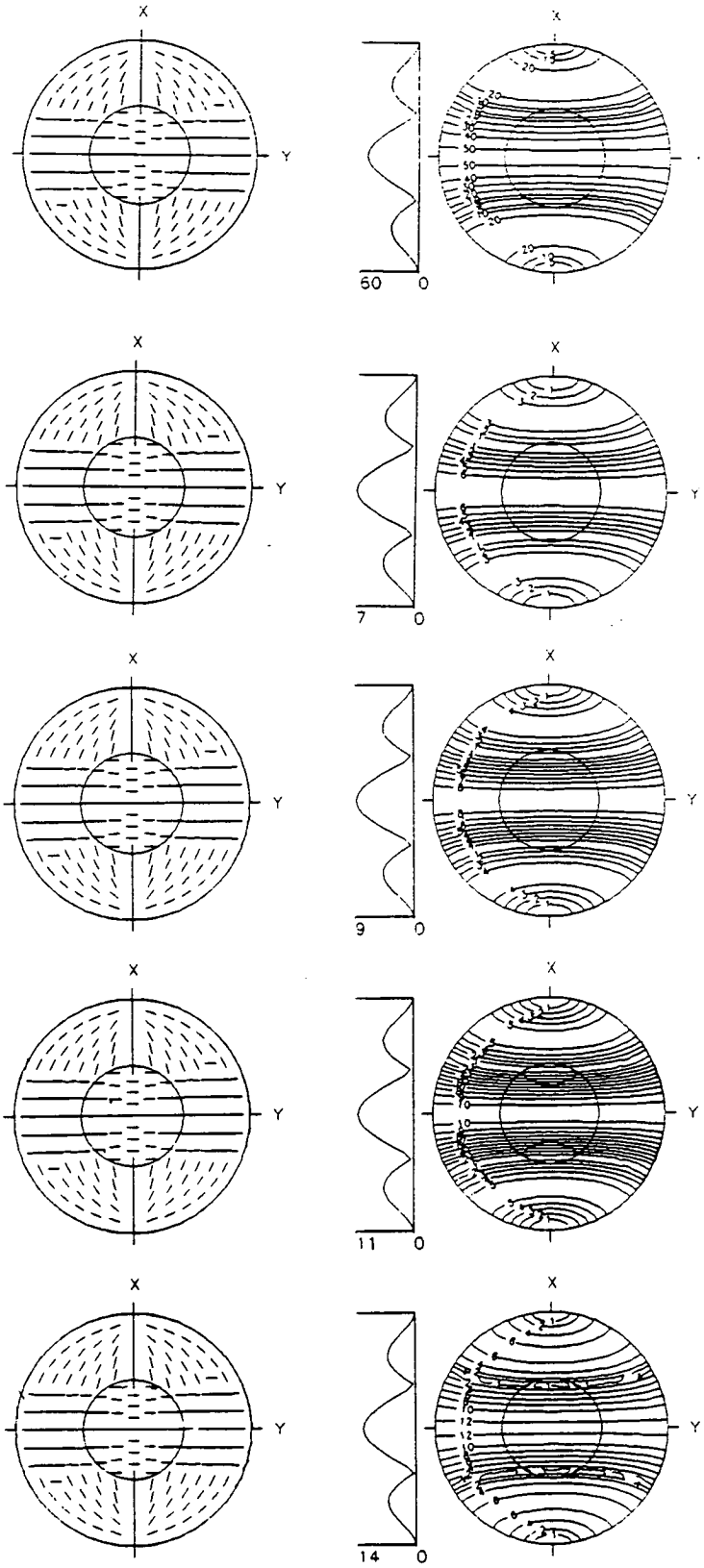
X
Y
60
0
7
9
11
14

(b)

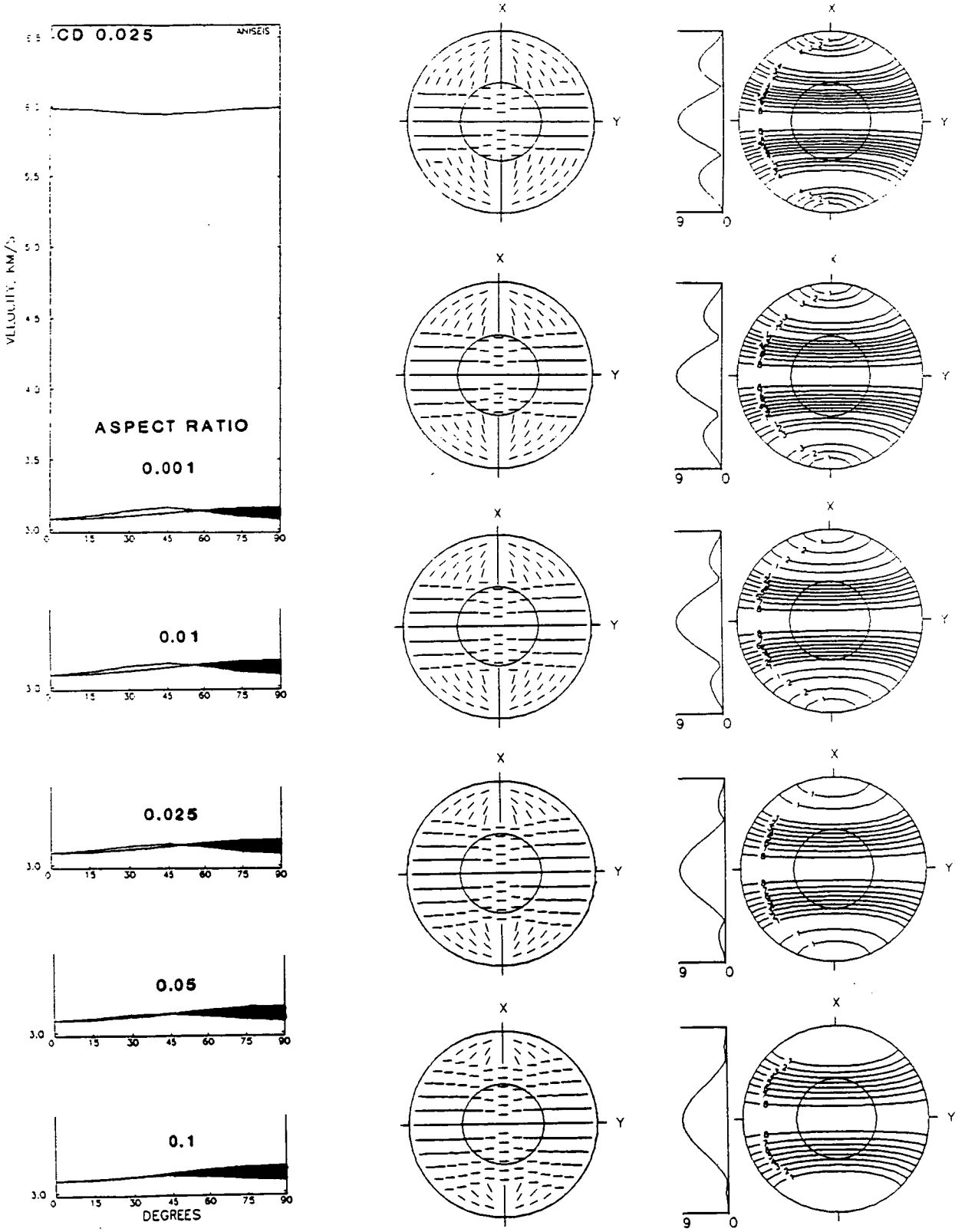

Figure 1.2 (continued)

for 1-D earthquake location at Parkfield. The pore-fluid is assumed to be water with a *P*-wave velocity of 1.5 km/s. The variation with directions (shaded area) of velocity difference between the two split shear waves can be clearly seen. It is also seen that an increase in crack density, caused either by an increase in the number of cracks or by an increase in the size (radius) of the cracks, will effectively increase the delays between the split shear wave along almost all raypaths within shear-wave window (shaded area and delay contour projections) shown in Figure 1.2 (a). An increase in aspect ratio of liquid-filled cracks at constant pore-fluid velocity, shown in Figure 1.2 (b), effectively moves the intersection point of the two split shear waves towards the left, or increases the width of the broad band of parallel polarizations in polar projections and the time delays in both contoured polar projections and cross sections of the contours of the projections.

1.4 THIS THESIS

Theoretical studies formulated above have shown that shear-wave splitting may be diagnostic of seismic anisotropy (Crampin, 1978). If so, then the study of shear-wave splitting may provide information about the structure of the anisotropic medium. The polarizations of the leading split shear waves are found usually parallel or subparallel to the horizontal maximum compressive stress (Crampin and Lovell, 1991), and it has been claimed that temporal variations of time delays between split shear-waves have been observed on several occasions (Peacock *et al.* 1988; Crampin *et al.* 1990; Booth *et al.*, 1990). Crampin *et al.* (1984b) postulated the *EDA* hypothesis as a common mechanism for a wide range of earthquake precursors as a result of regional stress and its variation. If this is the case, then monitoring the variation of time-delays may have potential application in earthquake prediction. As with all the theories behind earthquake 'prediction', there has been a serious debate on the utility and applicability of this hypothesis. The aim of this thesis is to re-address this problem by focusing on the following questions:

1. Is there clear evidence for the phenomenon of shear-wave splitting at Parkfield, central California, and Cajon Pass in southern California?

2. Is there any evidence that the observed shear-wave splitting is caused by stress-aligned fluid-filled cracks, or is another cause more likely?

3. How is the observed shear-wave splitting related to the geological structure in both areas?

4. Is there any evidence of temporal change in shear-wave splitting parameters derived from Parkfield dataset? And if so, how reliable and statistically significant is it?

5. Is there any correlation between the observed temporal changes and earthquake source size, such as seismic moment, or earthquake magnitude? If so, what is the most likely cause?

6. What constraints can be placed on the depth extent of any observed anisotropy?

To answer all of the above questions simultaneously is not easy as each of these questions will probably require a more comprehensive data analysis than is possible with the two datasets available. Nevertheless, the dataset I shall use in this thesis is unique in that it was continuously recorded over a three year period at one of the most important earthquake prediction investigation sites in the world. This thesis is organised as follows. In the first four chapters, I shall concentrate the Parkfield dataset. In Chapter 2, I will first describe the background knowledge about the Parkfield area including geological features and the regional stress field and readdress *EDA* hypothesis as a mechanism of earthquake precursor. Chapter 3 contains the preliminary study of the data prior to the analysis of shear-wave splitting. In Chapter 4, I shall present the results of my observations of seismic anisotropy at

Parkfield. Chapter 5 is devoted to interpretation of the observed seismic anisotropy, including shear-wave polarizations and observed temporal variations of time delays. Chapter 6 is an additional study of seismic anisotropy at Cajon Pass, southern California. Discussion, conclusions of the whole thesis and speculation about future work will be presented in Chapter 7. I will conclude that seismic anisotropy is prevalent in the upper crust, and that shear-wave polarizations are very useful in determining the maximum horizontal stress in the seismogenic zone. Temporal variation of time delays can be positively identified when good quality borehole data are available.

CHAPTER 2

PARKFIELD: THE BACKGROUND KNOWLEDGE

2.1 INTRODUCTION

In Chapter 1, I briefly described the basic properties of seismic waves in anisotropic solids. From now on, I shall concentrate on a detailed analysis of a series of Parkfield data, the aim being to establish a link between observed seismic anisotropy (shear-wave splitting) and geological, structural and geodynamic information. I will also discuss previous observations of seismic anomalies, which led to the earthquake prediction experiment (PPE) being set up at Parkfield. The Parkfield High Resolution Seismic Network (HRSN) was set up as a part of the PPE to monitor the expected intermediate-size earthquake (Bakun and McEvilly, 1984; Bakun and Lindh, 1985). In this Chapter I shall give all the necessary information about the study area, and discuss the usefulness of shear-wave anisotropy in earthquake prediction, in particular comparing the variation of shear-wave anisotropy with other methods which may be used to study precursors of large earthquakes.

2.2 THE ANOMALIES OF PREVIOUS OBSERVATIONS AND PARKFIELD HIGH RESOLUTION SEISMIC NETWORK

Since 1857, earthquake sequences with main shocks of magnitude 6 have occurred near Parkfield on 2 February 1881, 3 March 1901, 10 March 1922, 8 June 1934, and 28 June 1966 (Bakun and Lindh, 1985). The Parkfield area seismicity generally seems well described. It is characterized by a recurring moderate size earthquake, repeating the same epicentre, magnitude, seismic moment, rupture area, and southeast direction of rupture expansion (Bakun and McEvilly, 1984). Assuming the strictly periodic model and the absence since 1966 of the perturbations hypothesized for the 1922 to 1934 period, the next characteristic Parkfield earthquake

should have occurred between 1983 and 1993 (Bakun and McEvilly, 1984).

Wyss *et al.* (1990a) reported that only four earthquakes with $M \geq 2.5$ occurred on the Parkfield segment since January 1986, whereas twenty would have been expected, extrapolating from the mean background rate. Similar precursory quiescence has happened for the other six cases that preceded a main-shock happened in California, Hawaii and Alaska for earthquakes of magnitudes 3.6-8 (Stuart, 1990). Wyss *et al.* (1990a) suggested that the M = 5.7 earthquake should occur before 1992, rupturing the same 35 km fault segment that ruptured in 1966.

Wyss *et al.* (1990b) reported data from two geodetic lines crossing the San Andreas Fault (SAF) near Parkfield to investigate crustal deformations along the fault zone. The result was that the rate of shortening decreased by about 20% starting in August 1986. This change coincided with a rate decrease of 45% for earthquakes of $M_L \geq 2$ in the area. They interpreted the phenomenon as an intermediate-term precursor to the next Parkfield earthquake.

The average magnitude of earthquakes produced along the Parkfield segment of the SAF decreased significantly between late 1986 and late 1988 along with the seismic quiescence (Wyss, 1990). The change corresponds to an increase of the *b*-value from 1.1 to 1.4. During 1989 however, the average magnitude produced was approximately normal again corresponding to decrease of *b*-value. This same phenomenon had been identified before several other mainshocks, for example, in California (Wyss and Lee, 1973), in New Zealand (Smith, 1981) and in Japan (Imoto, 1991). It is also a feature of laboratory fracture tests (Main *et al.*, 1990a). Therefore it was considered that the unusually low *b*-value was a precursor to the predicted Parkfield mainshock.

The Parkfield prediction experiment (PPE) was launched in 1988 based on the above four anomalies. The Parkfield high resolution seismic network (HRSN) as a part of the PPE, was designed to monitor the expected M = 6 earthquake near Middle Mountain (MM) in the preparation zone at Parkfield (Bakun and McEvilly, 1984; Bakun and Lindh, 1985). Nine sites were installed with seismometers emplaced both in upholes (a few metres) and downholes (200 - 300 metres). The sensors for both

uphole and downhole are three component, 2 Hz Mark Products L22E seismometers. The triaxially mounted seismometer packages are locked in pressure-sealed packages, which are oriented by levelling gimbals in wire meshcages (Malin *et al.*, 1989). The triggered recording of the events were accomplished with General Earthquake Observation System (GEOS) event recorders on loan from the United States Geological Survey (USGS), Menlo Park (Borcherdt *et al.*, 1985).

Instruments deployed in boreholes penetrate below the weathered material of the near-surface thus potentially providing a considerably more transparent window through which to observe source processes and deeper path effects that may be masked by a strong near-surface transfer function. Recording in boreholes can also avoid problems with surface reflections or near-surface noise and attenuation from low-Q, low-velocity material. The difference between uphole and downhole seismometer results has been compared by calculating the stacked spectral ratio of uphole and downhole recordings (Aster and Shearer, 1991; Blakeslee and Malin, 1990) and it turns out that the site amplification between 1 Hz and 100 Hz varies greatly. Below a few tens of Hz, free-surface effects, low-impedance amplification, and near-surface reverberations play a dominant role in controlling spectral amplitudes (with larger amplification at uphole than that at downhole). Above these frequencies, exponential losses produced by anelastic attenuation overwhelms all other near-surface effects (seen at uphole). The detailed study of the Parkfield downhole recording is described in Sections 3.3, 3.4 and 3.5.

2.3 LOCAL GEOLOGY AND STRESS FIELD

The geology of the Parkfield area is dominated by the strike-slip plate boundary at the San Andreas Fault (SAF). Figure 2.1 shows the SAF and associated shallow thrust faults, and the station distribution of the Parkfield high resolution seismic network. The fault segment at Parkfield, central California, is generally understood to be the transition zone between the 170 km long creeping portion to the northwest and the 300 km long locked portion to the southeast, where the average

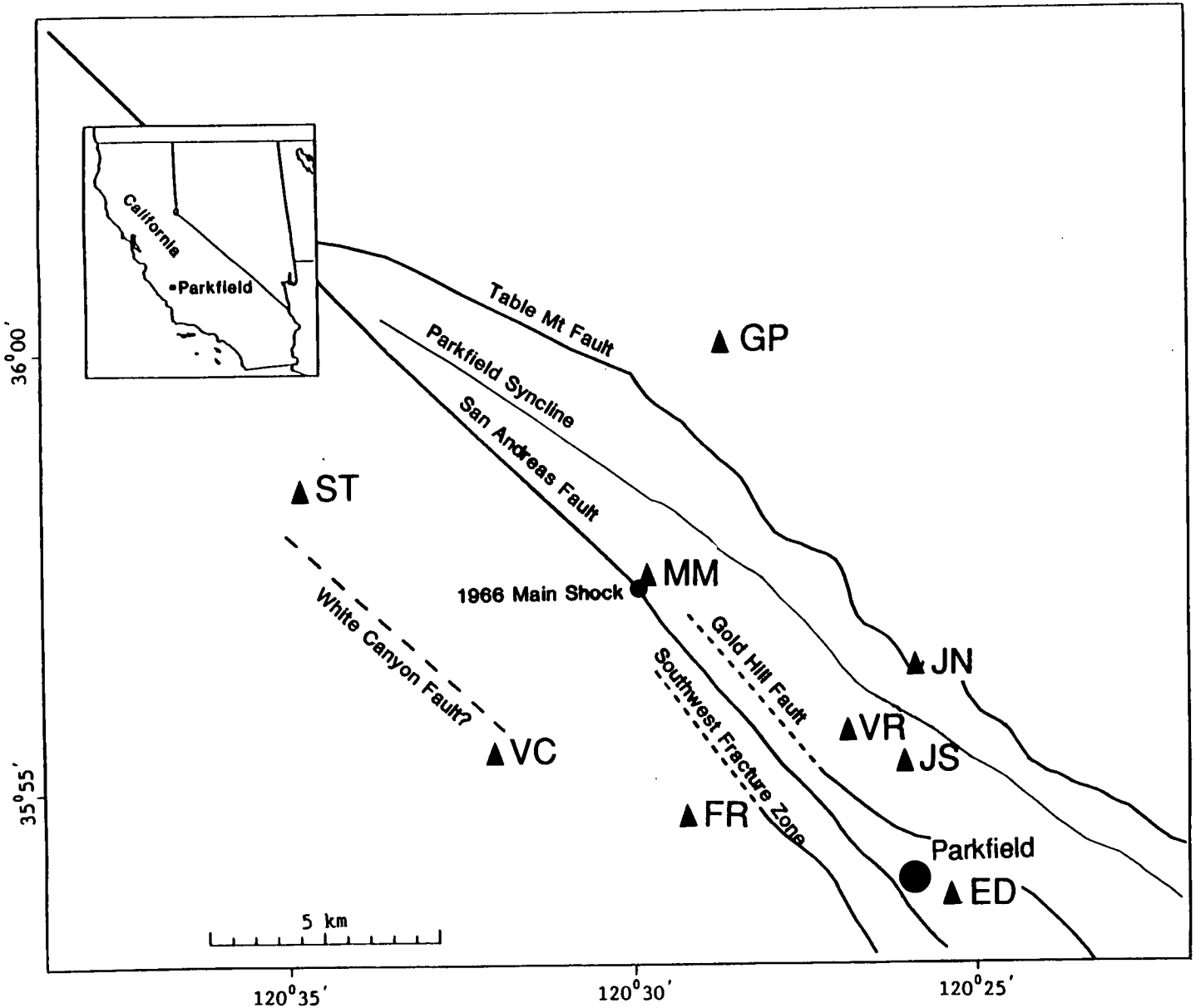

Figure 2.1. Map of major faults and seismometer distribution of the Parkfield downhole HRSN network. Triangles represent seismometer locations.

width of the fault-gouge varies from 100 to 200 m, with about 500 m of transition zone (Leary and Ben-Zion, 1992; Eberhart-Philips and Michael, 1993). The SAF at the Parkfield segment is characterized by a sharp cross-fault velocity gradient, with 5% to 20% lateral change in velocity observed in a 4 km width zone parallel to the fault trace (Michelini and McEvilly, 1991; Eberhart-Philips and Michael, 1993). Analysis of seismograms recorded at Middle Mountain (MM) in terms of fault zone trapped waves indicates that the shear wave velocity of the fault-gouge is about 1.1 km/s, and 1.8 km/s in the transition zone in the area of the 1966 M_L = 5.9 mainshock, while in the southeast segment approaching the locked portion of the SAF it is respectively 1.8 km/s and 2.5 km/s in the gouge and transition zone (Li and Leary, 1990; Leary and Ben-Zion, 1992). The fault is dipping steeply at 86°±1.1° to the southwest (Brown *et al.*, 1967; Nishioka and Michael, 1990).

The Salinian block on the southwest side of the SAF consists of Gabilan plutonic and metamorphic granite and granodiorite basement overlain by a maximum of 2 km of marine and nonmarine sedimentary and volcanic rocks of Tertiary age and Quaternary deposits (Brown *et al.*, 1967; Lees and Malin, 1990). These stratified rocks are tightly folded along northwest-trending axes near the fault zone, but a mile or so away from the fault zone the folds are open and generally dip away from the Cholame Hills high, on which station VC is located, which correspond to the basement uplift, parallels the SAF system several kilometres to its southwest, seen as a high velocity slice on the southwest block of the SAF (Eberhart-Philips and Michael, 1993). The northeast block of the SAF consists broadly of outcropping basement of Franciscan melange. Overlying this basement to the east are several kilometres of Cretaceous and younger sediments of the Great Valley sequence. This block is much more deformed than the Salinian block. It is complicated by numerous folds, thrust faults, and strike-slip tear faults which have undoubtedly caused much internal deformation during its evolution. In general, Franciscan rocks are moderately to strongly deformed and, in the fault zone, slivers of various crystalline rocks appear to have been trapped within older branches of the fault (Brown *et al.*, 1967). Some of the numerous thrust faults surrounding the SAF show Holocene movement (Sims, 1989).

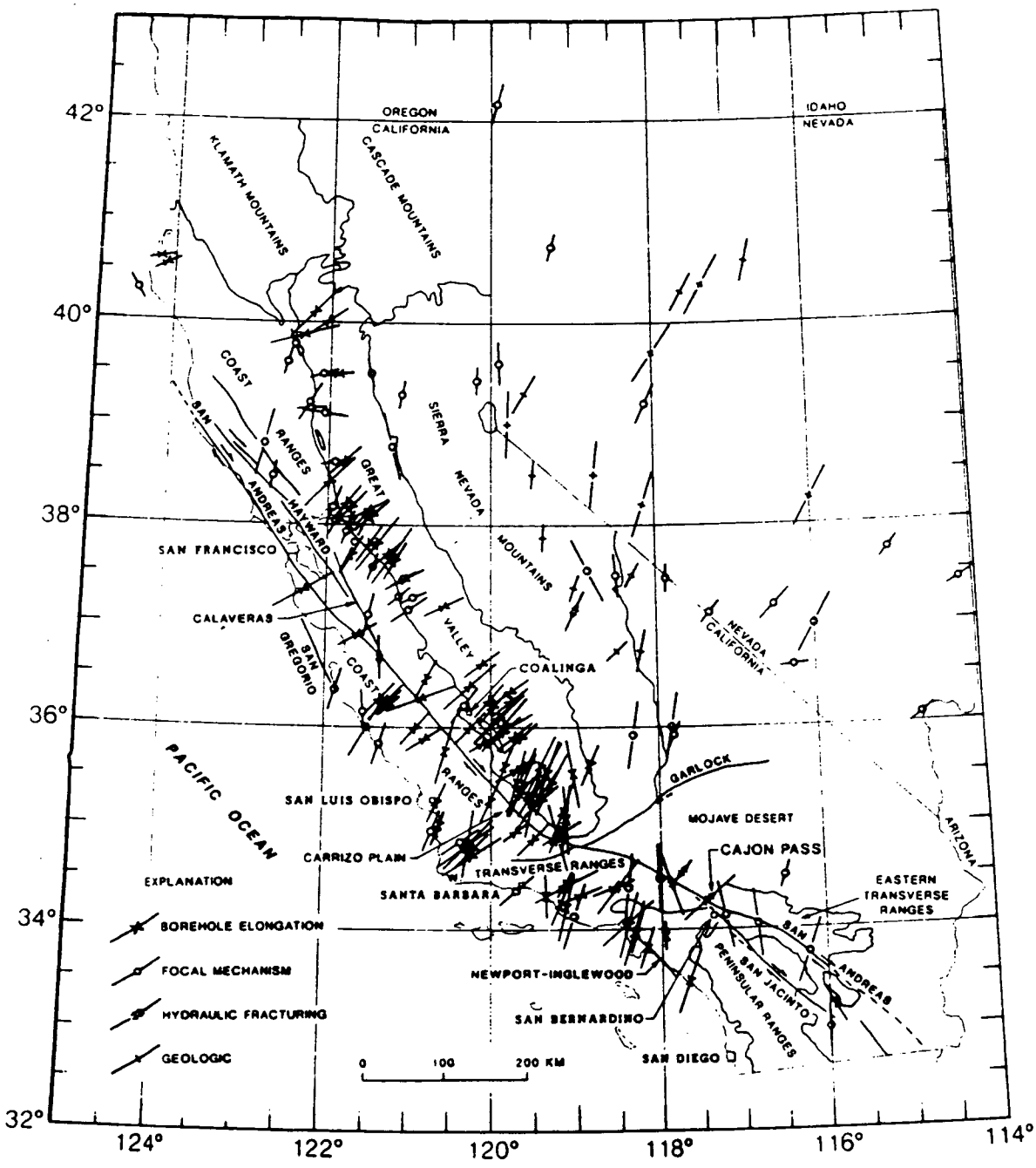

Figure 2.2. Directions of maximum principal stress in California. Note that the length of the arrows indicates the data quality and the symbols indicate different type of data (after Zoback et al., 1987).

Figure 2.2 presents the measurements of the orientations of the maximum principal tectonic stress in California (Zoback *et al.*, 1987). The data are from stress-induced wellbore breakouts, earthquake focal plane mechanisms, hydraulic fracturing *in-situ* stress measurements, and geologic volcanic alignments. We can see that the data density is very high in central California, and they are mainly derived from earthquake focal mechanisms and wellbore breakouts. The direction of maximum horizontal compressional stress is approximately perpendicular to the fault, which is consistent with all kinds of measurements. It has been suggested that a pervasive pattern of compressive stress nearly normal to the fault is a consequence of the weak SAF imbedded in strong crust in central California (Zoback and Zoback, 1991). The predicted coefficient of friction is so low that pore fluid pressure is likely to be a major cause of the weakness (Rice, 1992).

2.4 SURFACE TOPOGRAPHY NEAR STATION SITES

The surface topography in central California is variable, and includes mountains and horizontal plains. A large variation of topography can complicate a wavefield, and therefore affect the analysis of first shear-wave arrivals, even for seismometers located at depths of between 200 m and 300 m. Figure 2.3 shows the contour maps and cross-sections at seven stations along the SAF fault from northwest to southeast, and from southwest to northeast perpendicular to the fault. Solid triangles mark the position of the seismometers. Note that the contour interval for stations ST and VC is 40 feet, 80 feet for stations JN, ED, FR and VR, and section connects maps with contour intervals of 40 and 80 feet for station MM. The scale for altitude and horizontal distance for these cross sections is the same. It is seen that apart from two stations (ST and VC) all other stations were located at sites within 100 m or 200 m of either a horizontal or gently dipping plane.

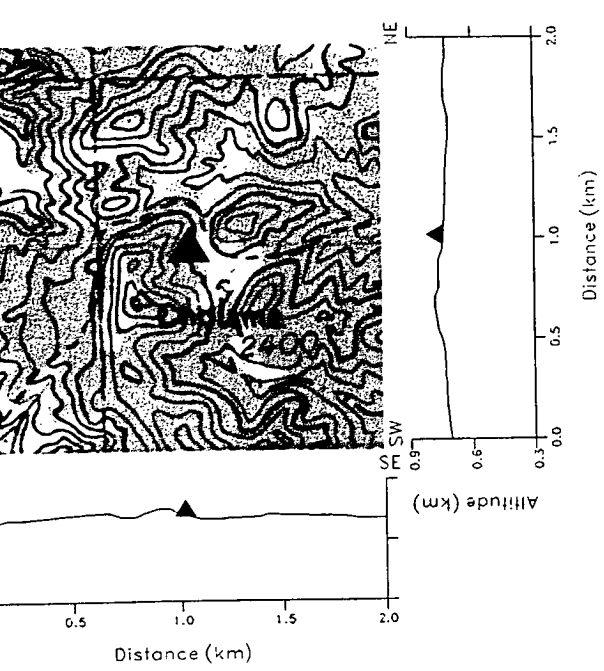

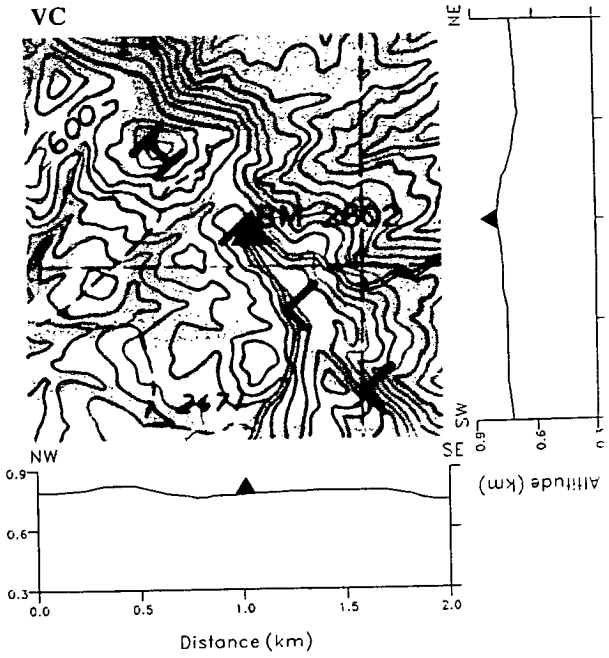

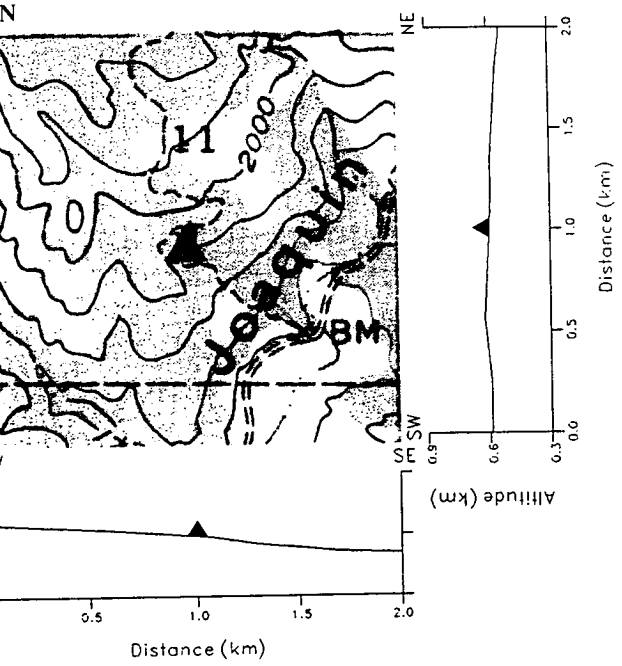

Figure 2.3. Topographic maps and cross sections from northwest to southeast along the SAF, and from southwest to northeast across the fault at seven stations. Solid triangles mark the positions of seismometers. Note that the contour interval for stations ST and VC is 40 feet, 80 feet for stations JN, ED, FR and VR, and for station MM the section connects maps with contour intervals of 40 and 80 feet.

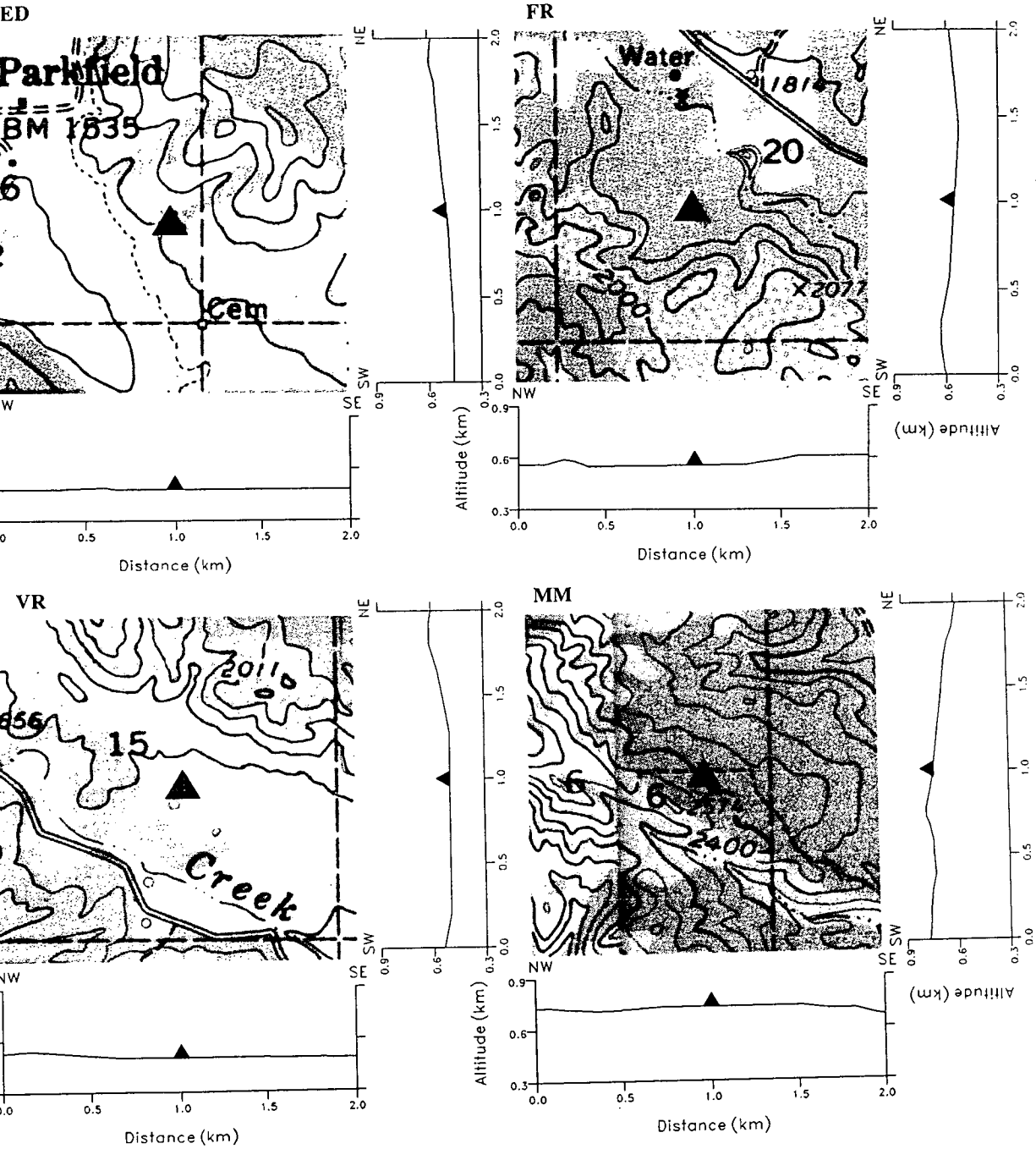

Figure 2.3 (continued)

2.5 EDA HYPOTHESIS AND EARTHQUAKE PREDICTION

2.5.1 Comparison of the *EDA* hypothesis and the conventional dilatancy diffusion model

Many solids show an increase in volume during deformation. The term 'dilatancy' was first used by Osbourne Reynolds in 1901 to mean the increase of volume of granular masses due to deformation, and it was first observed by Bridgman in 1949 that some rocks become dilatant when stressed to fracture. However, crustal-scale dilatancy has not been observed (Scholz, 1990). The validity of the conventional dilatancy model hinges on the assumptions that (1) *in-situ* stress near the earthquake source is large enough to cause rocks to dilate prior to the occurrence of the earthquake, (2) water is available in the brittle crust down to about ten kilometres, and (3) the permeability of rocks under crustal conditions is large enough to allow water to diffuse into the dilatant source region in relatively short lengths of time. By contrast, *extensive-dilatancy anisotropy* (*EDA* hypothesis): stress-aligned fluid-filled parallel vertical microcracks, which are caused by potential opening and growth of pre-existing cracks, exists throughout a large part of the volume of an earthquake preparation zone. The main difference is that *EDA* requires stresses one or two orders of magnitude less than those at which conventional dilatancy (Brace, Paulding and Scholz, 1966) occur. *EDA* therefore refers to phenomena occurring at comparatively low stresses throughout a large part of the preparation zone before an earthquake rather than locally high stresses near the nucleation point. The predominant cause of *EDA*-cracks (parallel saturated vertical cracks) is the anelastic subcritical growth of existing cracks and microcracks by stress corrosion at the crack tips (Rutter and Mainprice, 1978; Atkinson, 1982) at the low strain rates and low stresses expected throughout earthquake preparation zones. The elastic bowing of existing fluid-filled cracks and pores may also be important at low shear stresses on those, possible rare, occasions when the pore pressure is sufficiently high. Since stresses high enough to cause conventional dilatancy are restricted to the immediate focal zone of the impending earthquake, it is possible that these precursors may be caused by

modification to *EDA*-cracks initially aligned at lower stresses (Crampin *et al.*, 1984b).

2.5.2 Earthquake 'prediction'?

Earthquakes are the sudden release of stress accumulated over a period of time in a volume of rock related to the size of the eventual earthquake. Shimazaki and Nakata (1980) postulated a simple time-predictable model for earthquake recurrence based on elastic rebound. Figure 2.4 shows two examples of this time-predictable behaviour, given a constant breaking stress for (a) a constant residual stress level and (b) a variable residual stress level. Obviously, if earthquakes occurred as a simple process of elastic rebound following a slow build-up of stress to some critical breaking point, then the failure time could be predicted simply from the stress drop, or the amount of slip on a previous earthquake on the same fault as shown in Figure 2.4 (a) and (b) respectively. Figure 2.4 (c) shows another possible scenario where the residual stress level, which is held at a high level between earthquakes by friction, is a constant and the breaking stress may vary. In this case, the amount of slip which could be generated by an earthquake is predictable at any time, but the failure time is not inherently predictable. Main (1988) presented a theory which described the acceleration of a crack tip from initially slow (sub-critical) rates due to stress corrosion to rapid catastrophic rupture under conditions of gradually increasing stress. Failure times depended on initial conditions such as crack length, crack-tip velocity, residual frictional stress following a previous earthquake, stress-corrosion index and the rate of stress input. This means the process preceding a large earthquake is complicated and multiply variable.

Changes in stress can affect large volumes of rock around the focus of an impending earthquake, as indicated by changes in strain determined by geodetic surveys (Rikitake, 1976); changes in the coefficient b in the earthquake frequency-magnitude equation $\log N = a - bM$ (Smith, 1986) and other precursors (Dobrovolsky *et al.*, 1979) which can be detected hundreds of kilometres from the eventual epicentre. Precursory changes in the velocity ratio of *P*- and shear waves, Vp/Vs

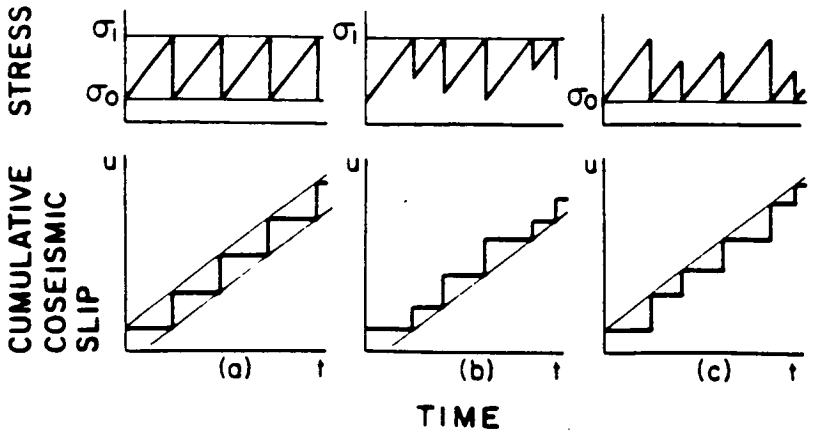

Figure 2.4. Schematic earthquake recurrence models after Shimazaki and Nakata (1980). (a) strictly periodic, (b) time-predictable and (c) slip predictable. σ_1 is the breaking stress and σ_0 is the residual static frictional stress.

(Semenov, 1969; Aggarwal *et al.*, 1973; Whitcomb *et al.*, 1973; Ohtake, 1973), and in seismic wave attenuation, have been attributed to crack growth under high stress (Mjachkin *et al.*, 1975; Sato, 1986) and movement of fluids in cracks (Scholz *et al.*, 1973), but since stresses high enough to cause conventional dilatancy are restricted to the immediate focal zone of the impending earthquake, it is more probable that these precursors are caused by modifications to *EDA*-cracks at low stresses (Crampin *et al.*, 1984b). Shear-wave splitting observed above small earthquakes in many parts of the world has been interpreted as being due to stress-aligned fluid-filled cracks or microcracks pervading the Earth's crust. Such a distribution of aligned cracks is effectively anisotropic to seismic waves and the study of shear-wave splitting may in principle be able to monitor the characteristics of the crack- and stress-geometry of the rockmass through which seismic body waves propagate, because changes in stress can cause changes in crack orientation, size, density and aspect ratio (Crampin, 1986). Following the observation of temporal variation in shear-wave splitting found by Peacock *et al.* (1988) and Booth *et al.* (1990), I have also detected a temporal variation of time delays before and after a $M_L = 4$ earthquake at Parkfield (see Chapter 4). Apart from these observations, laboratory measurements have shown that anelastic subcritical crack growth in response to stress change is rapid enough to cause detectable changes in crack size with a useful time interval for prediction (days, months or years, Crampin *et al.*, (1984b)). Systematic analysis of anisotropic changes in velocity and attenuation caused by changes in crack parameters may allow detection of stress changes in advance of a large earthquake (Crampin *et al.*, 1984; Crampin, 1987). However, as I will discuss in the interpretation of my results, the statistical significance of such precursors is still too low to establish whether or not earthquake prediction is a practical possibility.

2.6 SUMMARY

The Parkfield HRSN as part of the PPE project was set up in order to monitor the intermediate-sized characteristic earthquake expected, on the basis of a simple

time-predictable model before 1993. The geology at the Parkfield segment is complicated, characterised by the sharp velocity contrast across the SAF with a totally different geological structure and lithology on either side of the fault. The maximum horizontal compressive stress is almost normal to the fault, indicating that the SAF is a weak fault. The direction of the maximum horizontal compressive stress is consistent with my study of polarizations of leading split shear waves (see Chapter 4), as in many other cases observed in a wide variety of rocks in a wide variety of tectonic regimes in the world. It has been shown that the surface topography at each station site is generally not important, apart from at one station (ST). Shear waves recorded at depths of 200 to 300 m in borehole sites are even less affected by surface topography or any weathered layer.

It is interesting to note that the moderate sized earthquake expected before 1993 has still not occurred at the time of writing this thesis (December 1994). This implies that the simple time-predicable model does not apply, and draws a question mark over the data reported by Wyss *et al.* (1990a, 1990b) on seismic quiescence and crustal deformation. It has been further questioned by Savage (1993) whether the Parkfield prediction was plausible even in 1985 when it was first made. The dataset analyzed in this thesis sampled seismicity from 1988 to 1990 at the Parkfield network, so unfortunately we do not know how the response of shear-wave anisotropy continued to the present day. The 'small' study presented here (limited by the time constraints of a PhD and the data available) nevertheless shows that some interesting results can achieved when good quality borehole data are available.

CHAPTER 3

PARKFIELD: PRELIMINARIES TO THE DATA ANALYSIS

3.1 INTRODUCTION

To appropriately identify the first and the second shear wave arrivals the first step is to understand seismograms. There may be head waves, converted phases (*S-P*) and high energy *P*-coda waves preceding the first shear-wave arrivals. The geological structure at Parkfield is complex, and seismograms are sometimes so complicated that shear-wave first arrivals are severely contaminated with large amplitude *P*-coda waves, despite being recorded in boreholes at depths of 200 to 300 m. Furthermore, the orientations of horizontal component of seismometers, and the relative calibration of instruments are fundamentally significant in determining the orientation of shear-wave polarizations. In this chapter I shall study several factors that may affect the results of the measurements of the anisotropic parameters. These include the relative calibration and the orientations of borehole seismometers, site effects, head waves.

3.2 DATA PROCESSING

Data from the Parkfield HRSN network were written into TAR (Tape Archive) tape under UNIX system at USGS, Menlo Park. I processed three years' data from 1988 to 1990. There are 12 archives for each year. Each archive stores events sequentially in a binary format, with three component traces at the same length of 6025 samples for 9 stations in a fixed order. Relevant files, such as picking files, were included in each archive. The early part of processing was performed on a VAX machine, VMS system. It was moved onto a UNIX system when a UNIX machine became available; hence the processing became much faster and more convenient. However, due to the shortage of disc space disc files were not generated except to produce hardcopy of seismograms.

Data recorded from September 1989 to December 1990 were processed under the VMS system, which involves two procedures: reading UNIX TAR three component traces onto disc; and then reorganisation of the data of each earthquake recorded by 9 stations into a SEGY format file. Data from February 1988 to August 1989 were processed under the UNIX system, on which a program automatically read files to plot seismograms. Data recorded in January and December 1988 are unreadable because of a writing error and are therefore not included in this study. The major difference between processing under VMS and UNIX is that for all the events which are used in the analysis of shear-wave splitting *P*- and *S*-phase arrivals need to be picked manually under VMS system, whereas on a UNIX system, the arrival time of *P* and *S* phases are automatically identified by means of picking files.

Figure 3.1 (a) shows a three-component shear-wave record from station VC, which is located in intact rock on the southwest block of the San Andreas Fault (SAF). There is a high-frequency jitter disturbing the polarization diagrams. Figure 3.1 (b) shows the amplitude spectrum of the shear-wave signals. It shows that the dominant frequency of shear waves is between 1 and 35 Hz. Therefore, a bandpass filter of 1 to 35 Hz is applied in order to reduce background noise. Figure 3.1 (c) displays the original data in Figure 3.1 (a) after application of the filter, showing seismograms and polarization diagrams of the horizontal motion of the first three time-windows. It is seen in Figure 3.1 (c) that the bandpass filter of 1 to 35 Hz is necessary and important, in particular for noisy data.

3.3 BOREHOLE SEISMOMETERS

3.3.1 The relative calibration of components

The relative calibration of instruments is important because the analysis of shear-wave splitting is based on the relative amplitudes of three-component motion. The General Earthquake-Observation System (GEOS) mentioned in Section 2.4 has the function of self-calibration. To test the self-calibration capability of the GEOS under field conditions, time domain signals and their corresponding Fourier-amplitude

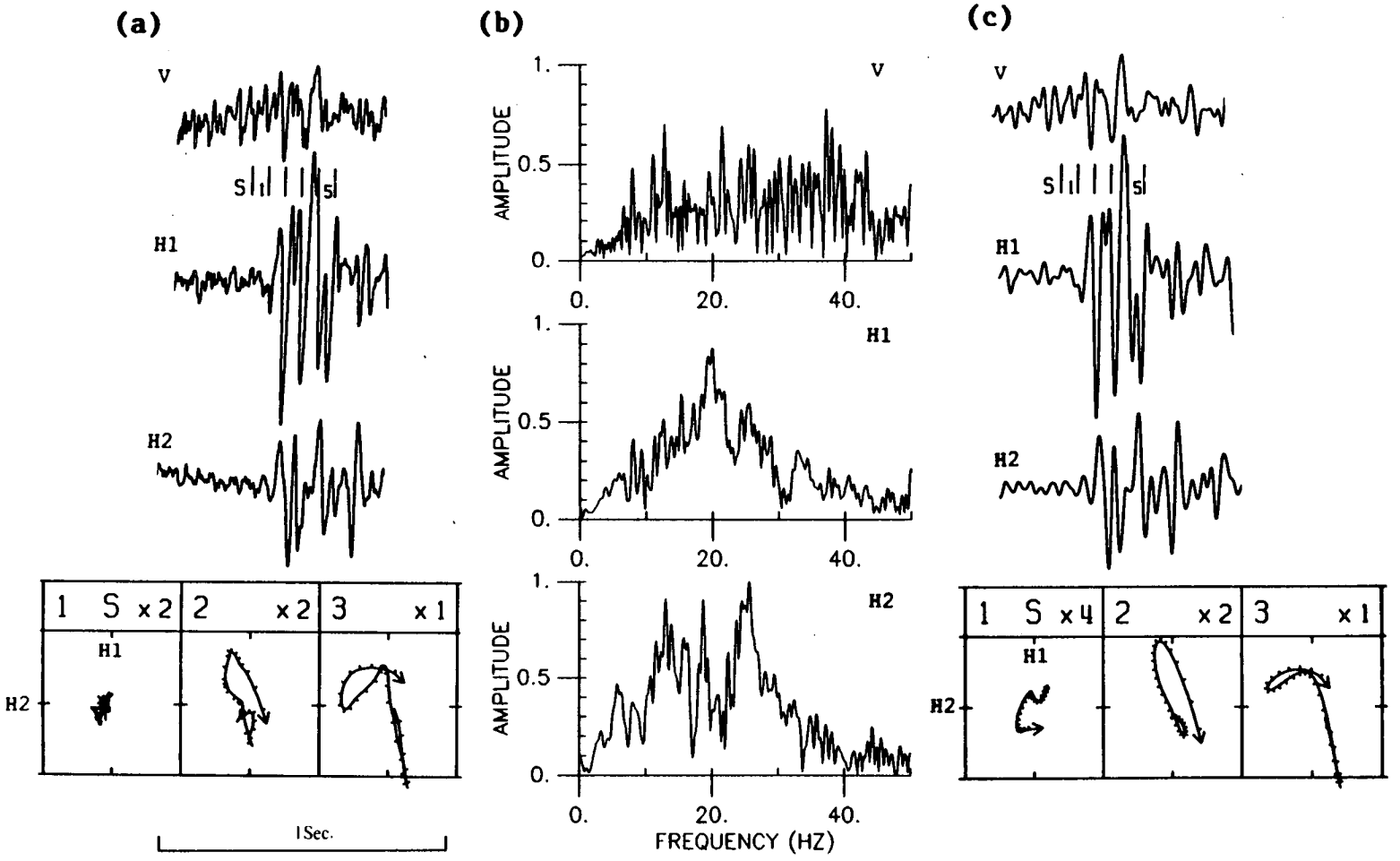

Figure 3.1. (a) An example of three-component shear-wave record from station VC showing seismogram and polarization diagrams of the horizontal motion in the first three time-windows, each window length is 60ms. (b) the amplitude spectrum of the shear-wave signals. The time window starts from the beginning of the shear-wave arrival and the window length is 2 seconds. Note that the dominant frequency of the shear-waves is between 1 and 35Hz. (c) compares the data after the 1-35Hz bandpass filter was applied to the original data in (a). Seismograms are plotted at the same scale on each component. The top line of the particle motion diagrams indicates the sequential number of the window (the first value) and the relative gain factor of the particle motions (the second value).

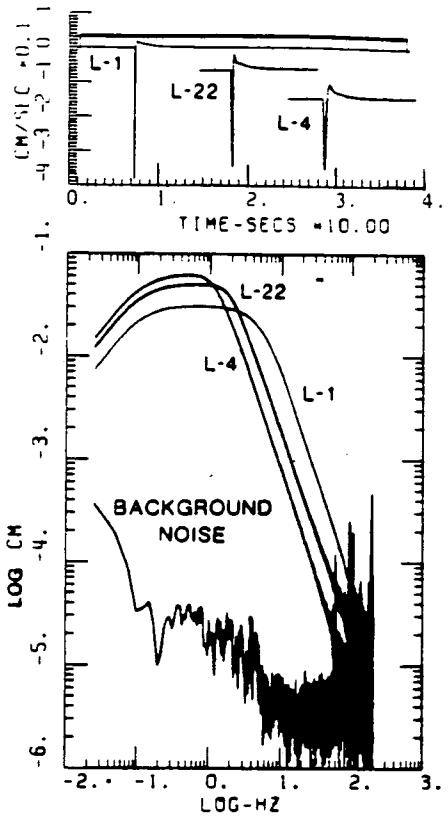

Figure 3.2. Self-calibration time history (upper) generated by the GEOS for three types of velocity transducers and their Fourier-amplitude spectra (lower). L-22 was used at Parkfield. The recordings of seismic background noise, using the L-4 sensors, were obtained within a few minutes of the time that the calibration signal for all the sensors were recorded at a site near Stanford University. These calibration signals generated by the GEOS permit accurate relative calibration of sensors in the field over bandwidths for which input signal is above background noise (from Borcherdt *et al.*, 1985).

spectra have been obtained for most of the applications (Borcherdt *et al.*, 1985). Figure 3.2 demonstrates that the calibration signals generated by the GEOS permit accurate relative calibration of sensors in the field over the bandwidth for which input signal is above background noise.

3.3.2 The orientations of horizontal components

Since the analysis of shear-wave splitting is based on particle motions in the horizontal plane, it is necessary to be certain that the orientation of the horizontal components of borehole seismometers are accurately known.

P-wave polarizations (available from September to December 1989) were used to orientate horizontal components. I use those data that have relatively longer wavepaths and clear onsets of direct *P* waves in order to reduce the effect of inhomogeneity of any local (smaller) scale disturbance on the wave propagation. It is expected that *P*-wave particle motions are along a raypath which is less affected by heterogeneity and anisotropy than the *S*-wave. If the orientation of horizontal components of each instrument is correct, the following equation holds:

$$H1 \pm R = AZI + m\pi \tag{3.1}$$

where *H1* is the orientation of the instrument; *R* is the polarization direction of a *P*-wave in a recording coordinate system of a seismometer (*V*, *H1* and *H2*), ranging from -360° to 360°; the plus sign ' + ' on the left side of the equation (3.1) represents right-hand system and the minus sign ' - ' represents left-hand system; *AZI* is the geographically-determined back-azimuth direction ranging from 0° to 360°; *m* takes 2, 1, 0, -1, -2, and is chosen by matching (3.1). All azimuths are measured from north through east. Figure 3.3 compares *P*-wave polarizations and back-azimuth directions at stations ST, VC, MM, FR, JN and VR, on the left, and the locations of the earthquakes used at each station, on the right. The earthquakes used in this analysis at each station are listed in Table 3.1. Note the range of azimuths is limited at most

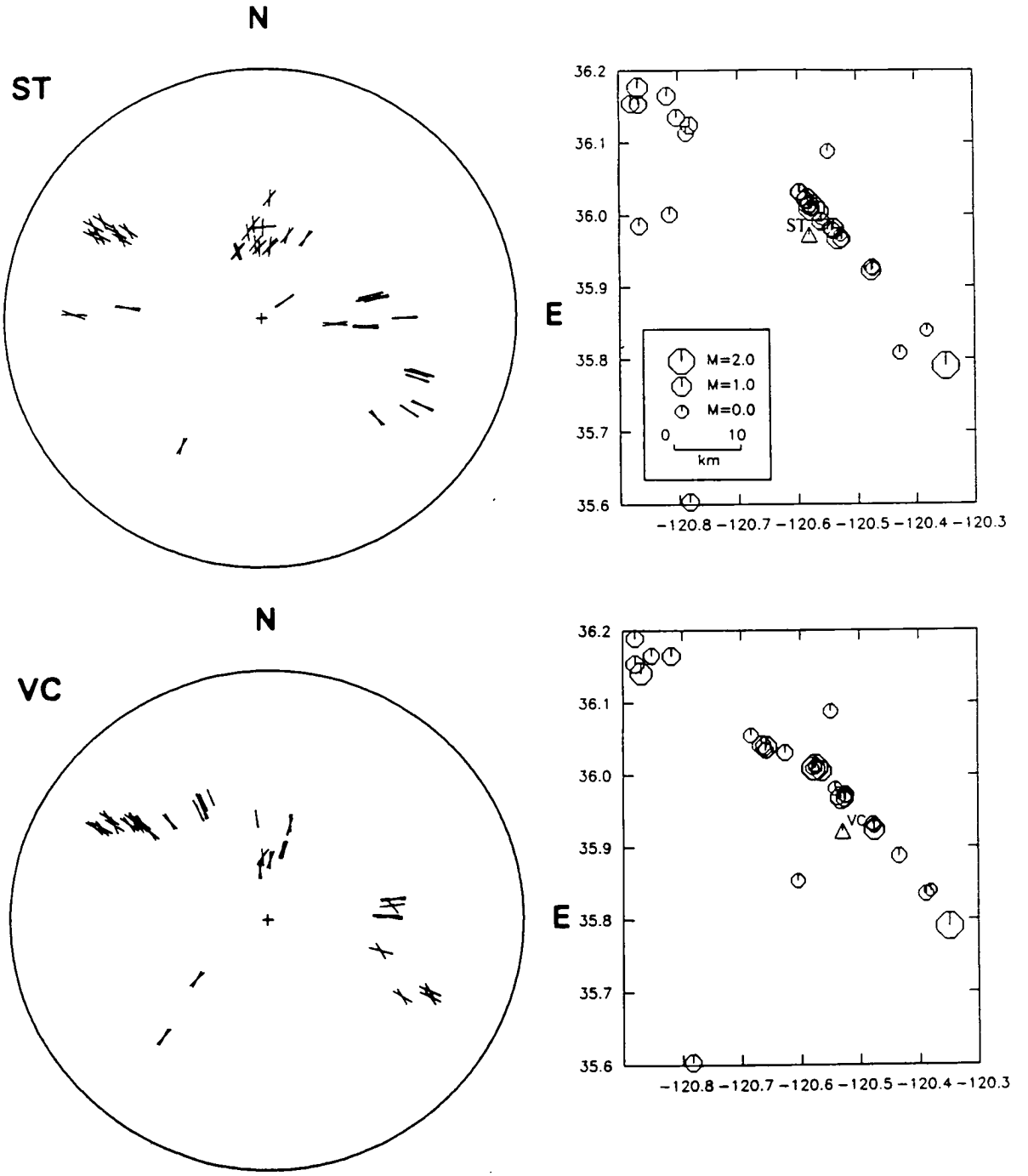

Figure 3.3. (left) Comparison of horizontal polarizations of *P*-waves with back-azimuths at six stations (ST, VC, MM, FR, JN and VR), in order to examine the orientation of horizontal components at each station. Diagrams are equal-area polar projections out to 90°. (Right) The locations of the earthquakes used at each station. Note all the maps having the same map key as shown in the first map at station ST.

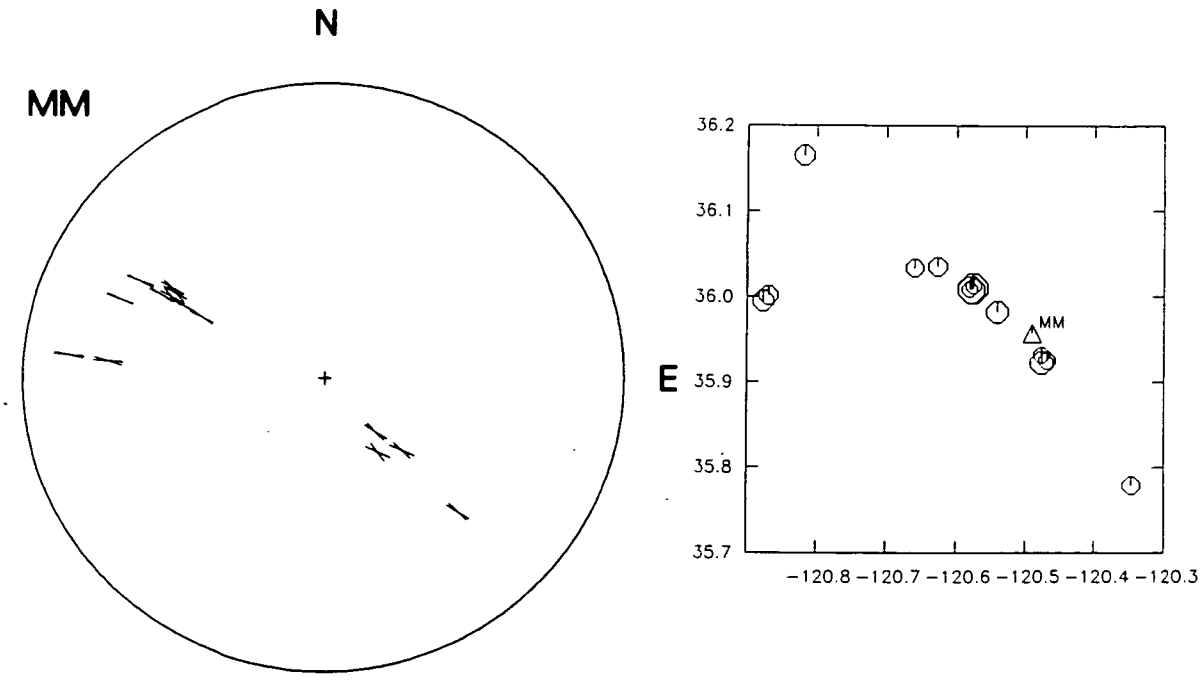
N
MM
E
36.2
36.1
36.0
35.9
35.8
35.7
MM
−120.8 −120.7 −120.6 −120.5 −120.4 −120.3

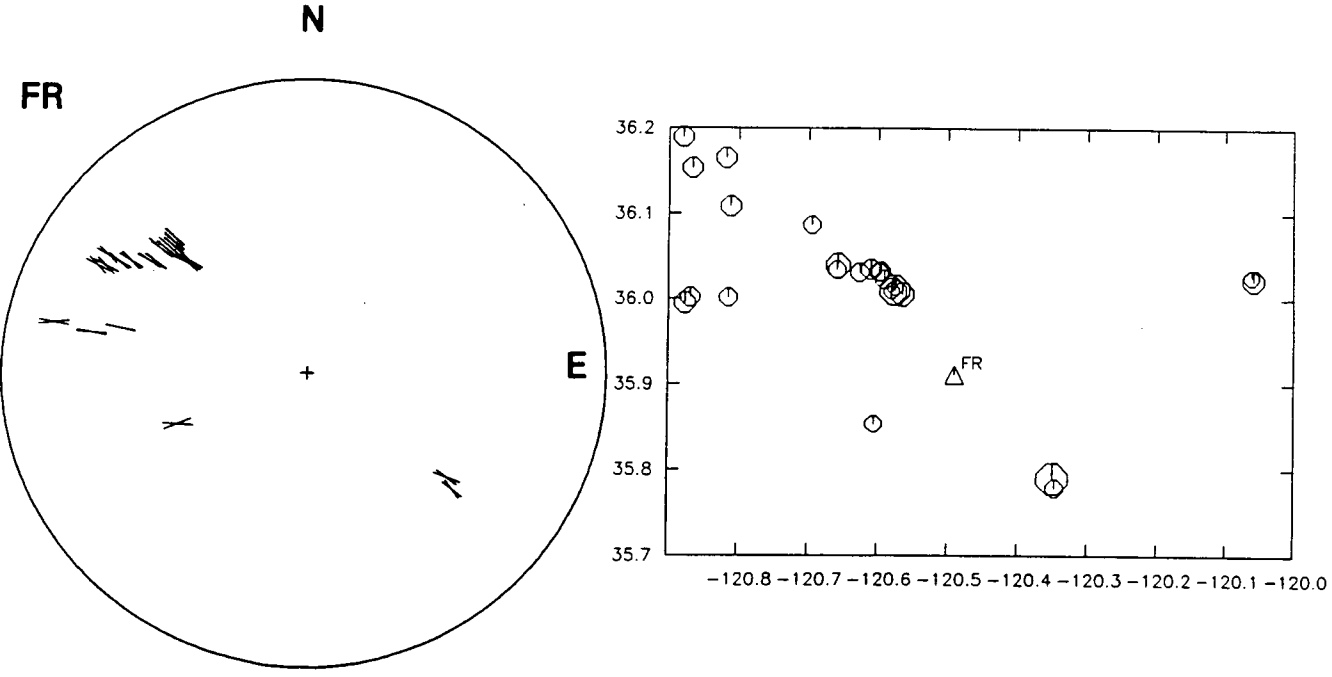
N
FR
E
36.2
36.1
36.0
35.9
35.8
35.7
FR
−120.8 −120.7 −120.6 −120.5 −120.4 −120.3 −120.2 −120.1 −120.0

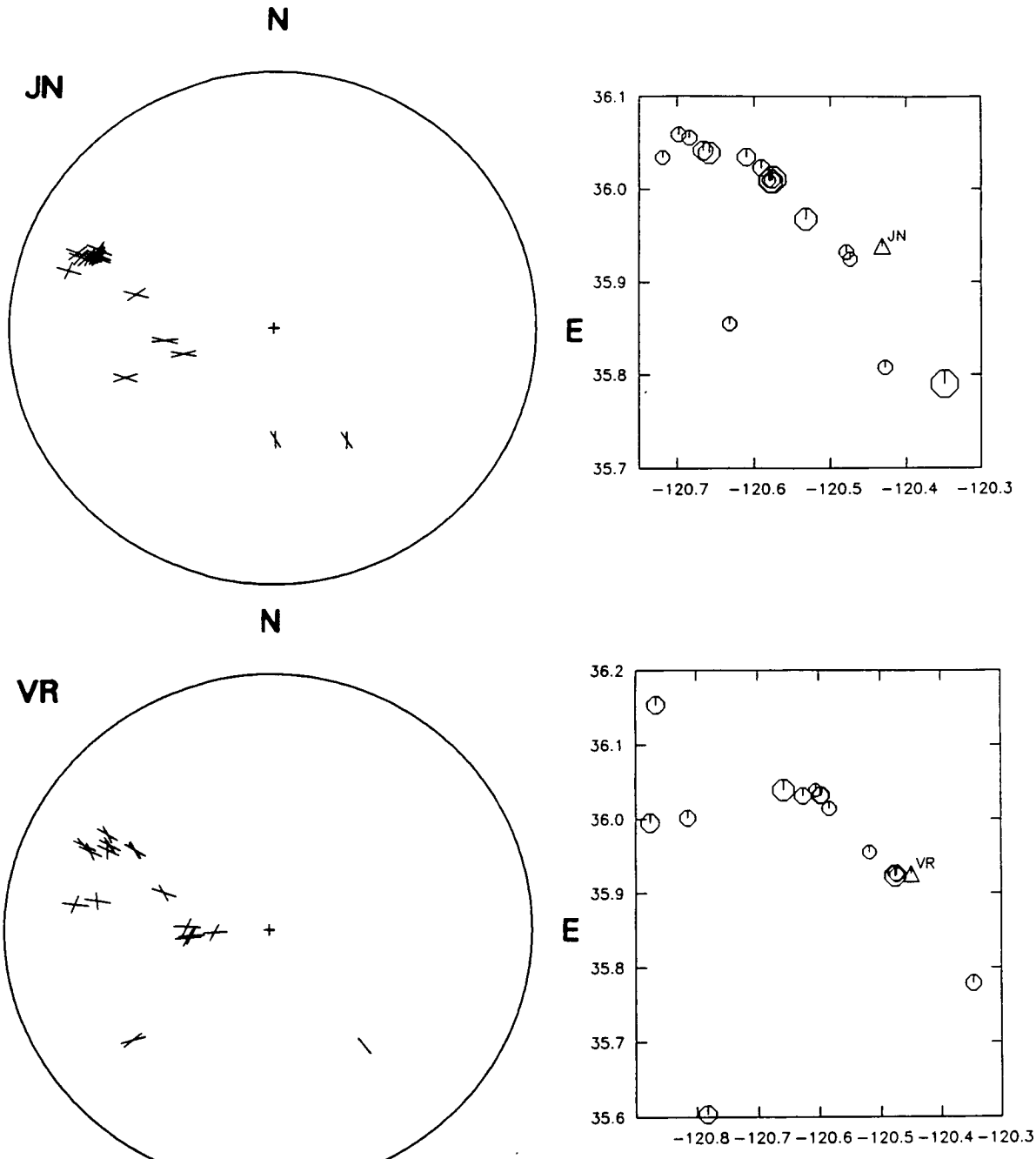
N
JN
36.1
36.0
35.9
35.8
35.7
E
JN
−120.7
−120.6
−120.5
−120.4
−120.3
N
VR
36.2
36.1
36.0
35.9
35.8
35.7
35.6
E
VR
−120.8
−120.7
−120.6
−120.5
−120.4
−120.3

Table 3.1 The dates of the earthquakes used in examing the orientations of horizonral component.

ST	VC	FR	JN	VR	MM
890806 2100	890802 0743	890802 1027	890806 2100	890802 0743	890802 1994
890806 2104	890802 1027	890806 2100	890806 2104	890808 0119	890806 2100
890808 0119	890806 2100	890806 2104	890807 0354	890809 2158	890806 2104
890809 2158	890806 2104	890807 0354	890811 1320	890810 2108	890807 0354
890810 2108	890807 0354	890807 0609	890904 1212	890811 1320	890807 0609
890811 1320	890807 0609	890810 2108	890904 1218	890901 0823	890808 0119
890812 1051	890808 0119	890812 1051	890906 1838	890903 0304	890811 0328
890903 1023	890808 0728	890901 0823	891003 0136	890904 1212	890901 0823
890903 1217	890808 1026	890904 1212	891003 1206	890917 1316	890904 1233
890904 1218	890812 0045	890904 1233	891117 0245	890924 0438	890924 0438
890906 1838	890812 1051	890917 1312	891117 1435	891001 1102	891004 2032
890917 1316	890903 1023	890917 1316	901025 1753	891003 1051	891224 0340
890921 0629	890903 1217	890922 0607	901026 0615	901008 0022	901006 1145
890924 0020	890904 1212	890924 0438	901026 1621	901021 1652	901022 1601
891001 0558	890904 1233	890926 0924	901028 1038	901023 0553	-
891002 0515	890906 1838	890928 1030	901028 1111	901024 0913	-
891002 1102	890919 0639	891001 1102	901028 2327	-	-
891002 1530	890920 0907	891003 1206	-	-	-
891003 1051	890921 0611	891004 2032	-	-	-
891004 1305	890928 1030	891115 1446	-	-	-
891004 1934	891003 0133	891117 0245	-	-	-
891004 2032	891003 1051	901008 0022	-	-	-
891111 2224	891004 2032	901022 1601	-	-	-
891117 0253	891004 2054	901023 0553	-	-	-
891128 0852	891223 1503	901026 0229	-	-	-
891210 1554	891225 0228	901026 1621	-	-	-
891220 2040	901006 0042	-	-	-	-
901006 1145	901006 2001	-	-	-	-
901006 1209	901023 0553	-	-	-	-
901006 2001	901026 1118	-	-	-	-
901008 0022	901026 1621	-	-	-	-
901018 1819	901028 1111	-	-	-	-
901026 0229	901028 1903	-	-	-	-
901026 0615	901028 2327	-	-	-	-
901026 1118	-	-	-	-	-
901026 1621	-	-	-	-	-

of stations because most earthquakes occurred on the plane of the SAF. It is seen that the difference between *P*-wave polarization and back-azimuth varies significantly between stations, and shows approximately azimuth-related particle motions at stations ST, VC and FR. Large deviations are shown at VR and JN on the northeast block of the SAF. Crampin *et al.* (1982) have examined *P*-wave polarizations in anisotropic media and show that the energy of seismic body waves in the Earth travelling along ray paths following the group-velocity vector, which deviates from the phase-propagation vector in approximately the same direction as the *P*-wave polarization. The apparent deviation of the polarization is the difference of the two individual deviations and this difference is negligible for up to 5% anisotropy in the Earth.

The anomalous *P*-wave polarizations for a given instrument orientation at each station has been reported to the relevant people in the installation group. The instrument orientation is determined in the field using a hammer to excite *P*-wave energy on the surface surrounding each borehole, and the accuracy of the orientation of the instrument is less than 5° (T.V. McEvilly, personal communication). This implies that the complicated local geology, and, presumably, strong lateral inhomogeneity may have severely distorted the wavepath, and hence shear wave studies may be obscured by the effect of scattering from geological inhomogeneity in the Earth. Table 3.2 lists the locations, the depths of borehole seismometers and the orientations of the component of seismometers at Parkfield.

3.4 COMPLEXITY OF WAVE PROPAGATION AND EARTHQUAKE LOCATION

Buchbinder and Haddon (1990) have demonstrated that local sloping topography can cause *P*-phase arrivals up to 40° off-azimuth. They also noted that shear-wave arrivals are an order of magnitude less affected by sloping topography than *P*-wave arrivals implying a worst case error of about 4°. The essential reason for this large difference of the effect of sloping topography on *P*- and *S*-wave is that *P*-wave motion parallel to the free surface depend on the sine of the angle of incidence,

Table 3.2. Parkfield HRSN instrumental description.

Station Name	Latitude °N	Longitude °W	Surface Elevation[1](m)	Sensor Elevation[1] (m)	Polarities[2] Z	H1	H2
ED	35.89522	120.42262	503	258	D	170°	260°
FR	35.91095	120.48688	549	265	D	338°	248°
JN	35.93897	120.43112	567	343	D	0°[3]	270°
JS	35.92117	120.43400	488	333	U	300°	210°
MM	35.95650	120.49600	735	514	D	175°	265°
GP	36.00087	120.47772	1198	1125	D	310°[3]	40°[3]
ST	35.97297	120.57988	732	450	D	120°	210°
VR	35.92608	120.44705	509	-63	U	15°	285°
VC	35.92162	120.53392	789	589	D	200°	290°

[1] Height above mean sea level. (conversion to height above ellipsoid: -34m)

[2] Direction of ground motion (east from true north) producing positive digital counts as recorded in field and as archived at Berkeley.

[3] These channel polarities are reversed on archive tapes generated by UCSB/Duke.

whereas in the case of *S*-wave they depend on the cosine (this is evident from the exponent decreasing of the maximum *P*-wave deviations with nominal angle of incidence). This agrees with Cormier (1984), who concluded that interaction with irregular internal interfaces can lead to distortions of shear-wave polarizations less than 10°.

The distinct difference between *P*-wave polarization and back-azimuth at some azimuths of stations ST, MM, VC, FR, and most of azimuths at JN and ED, seen in Figure 3.3, is consistent with the complicated geology at Parkfield. The SAF fault is the prominent feature in the Parkfield segment, marked by a large lateral velocity gradient. The segment of the fault zone where most of the HRSN stations are located (5 km northeast to 5 km southwest of station MM) shows an increase of about 15% in seismic velocity from northeast to southwest. From station MM to 5 km southeast along the fault, on the southwest block a body having relatively high velocity (Vp= 6.0 km/s) penetrates upwards to within about 3 km of the surface, showing an arch structure, which is consistent with other previous studies (McBride and Brown, 1986; Louie *et al.*, 1988) and is interpreted as Miocene and younger age sedimentary rocks which overlay a basement surface and arches upward towards the fault zone. The ratio of *P*-wave velocity to *S*-wave velocity (Vp/Vs) varies from 1.6 to 1.8 at depths of about 2 to 9 km, and a high Vp/Vs ratio of 1.9 has been detected in a 2 km-wide volume near station MM, close to the location of the 1966 main shock hypocentre. The northeast side of the fault is much more deformed than the southwest, complicated by numerous folds, thrust faults, and strike-slip tear faults which have undoubtedly caused much internal deformation during its evolution (Michelini and McEvilly, 1991; Eberhart-Phillips and Michael, 1993). Thus it appears that the high lateral inhomogeneity and the topography of subsurfaces surrounding the fault zone may distort some assumed straight line wavepaths defined by back-azimuth.

Figure 3.4 shows the 1-D velocity model (Poley, *et al.*, 1987) employed in the earthquake locations for the events used in this study. Nishioka and Michael (1990) modified the 1-D velocity model and applied station corrections, and relocated the earthquakes in the area of Middle Mountain. The seismicity was moved towards the

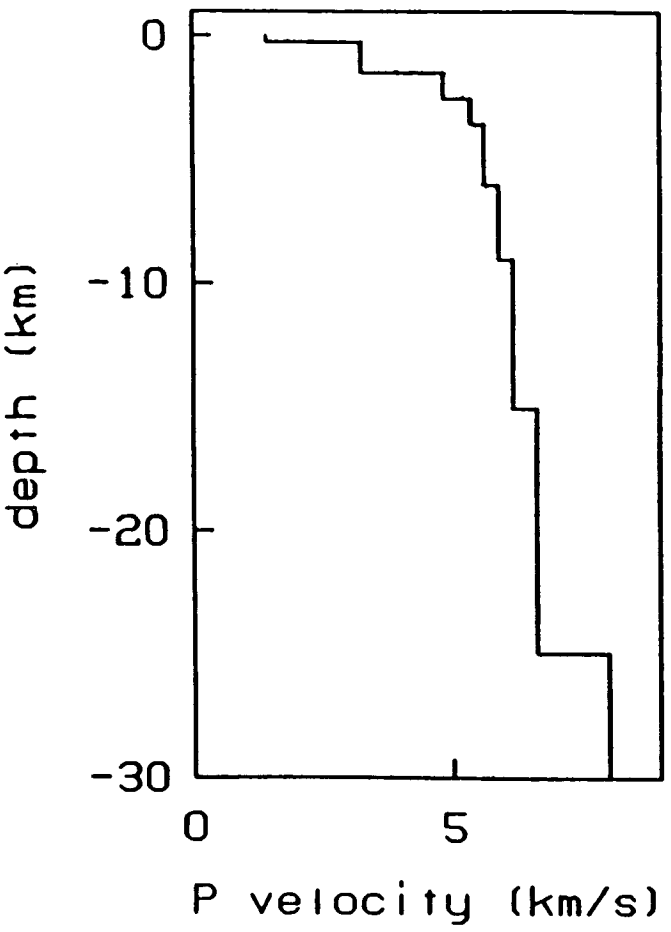

Figure 3.4. The velocity model used in earthquake locations (Poley *et al.*, 1987).

trace of the SAF. Michelini and McEvilly (1991) simultaneously inverted 3-D velocity structure and hypocentres using a cubic *b*-spline to interpolate between grid points. The relocated hypocentres are closer to the SAF plane. Similar work has also been done by Eberhart-Phillips and Michael (1993) using linear interpolation. Seismicity has clearly aligned along the SAF. The apparent velocity inhomogeneities have been shown up in their results.

Since the Parkfield network uses borehole recordings, it is inevitable that the interaction of upgoing waves and reflected downgoing waves from free-surfaces and the near-surface near the borehole seismometers may also contribute to more complicated seismograms. This site effect is discussed below.

3.5 SITE EFFECT ON BOREHOLE RECORDING

A number of investigators have studied the site effect, that is the effect on amplitudes of upcoming waves at the free-surface and the near free-surface. Results are often inconsistent or inconclusive. Examples are scattering from crustal irregularities due to local geology, even using careful statistical analysis (Aki, 1969; Aki and Chouet, 1975; and Phillips and Aki, 1986); studies that concentrated on local effects by comparison of recordings from surface and borehole seismometers have been more successful in discriminating site effects from path effects (Aster and Shearer, 1991; Abercrombie and Leary, 1993; Blakeslee, and Malin, 1990, 1991). Joyner *et al.* (1981) compared data recorded in two borehole sites located in bedrock and alluvium. The peak acceleration at the alluvial site was a factor of 2 larger than that at the bedrock site. Shearer and Orcutt (1987) presented a comprehensive theoretical study on borehole seismometer results. They showed that near-surface effects on upgoing body waves are complicated and are not always predictable from simple free-surface or impedance contrast relationships. Site amplifications can be very large, even without lateral heterogeneity or nonlinear effects. Seismometer sites will almost always give frequency-dependent response functions, for example, any velocity gradient or low-velocity zone near the surface will alter the site response. Borehole

seismometers at the depths from 200 to 300 m can escape some of the near-surface effects, but are still subject to interference between upgoing incident waves and reflected downgoing waves, which create borehole response functions that are often very complicated. This can probably explain in part why I observe complicated seismograms recorded in the shear-wave window at stations ST, FR and VR (shear-wave window is defined by the angle of $\sin^{-1}(Vs/Vp)$, within which the waveforms are preserved as incident waves). The near-surface geology at the receiver site and reflected downgoing waves may play an important role in producing a significant portion of the *P*-coda waves.

Some of the earthquakes recorded in the shear-wave window show considerable complexity due to scattering. At stations ST and FR, southwest of the SAF, and station VR on the block to the northeast, there are particularly large amplitudes of the *P*-wave coda. Thus direct shear waves have been strongly contaminated by the coda waves, which makes it difficult to analyze shear-wave splitting. Figure 3.5 displays typical seismograms showing such contamination at stations ST and FR. Seismograms recorded at stations VC, MM, JN and ED are relatively simple, but refracted shear wave head-waves propagating along the SAF may appear ahead of direct shear waves at the stations on the northeast block of the SAF, especially at MM, the closest station to the fault. Following this, I shall study head waves to assess their significance in the correct timing of the first onset of shear waves.

3.6 HEAD WAVES ON THE FAULT ZONE

3.6.1 Head waves

Ben-Zion (1990) presented numerical examples to demonstrate that when the media either side of the fault are dissimilar there are interface waves and *P*- and *S*-head waves which radiate from the interface into certain regions on both sides of the fault. In the faster medium, the head waves influence only the *S* pulse while in the slower medium both *P* and *S* pulses are affected. He found that the early parts of *P* and *S* pulses in the slower medium are head waves. He used the following parameters:

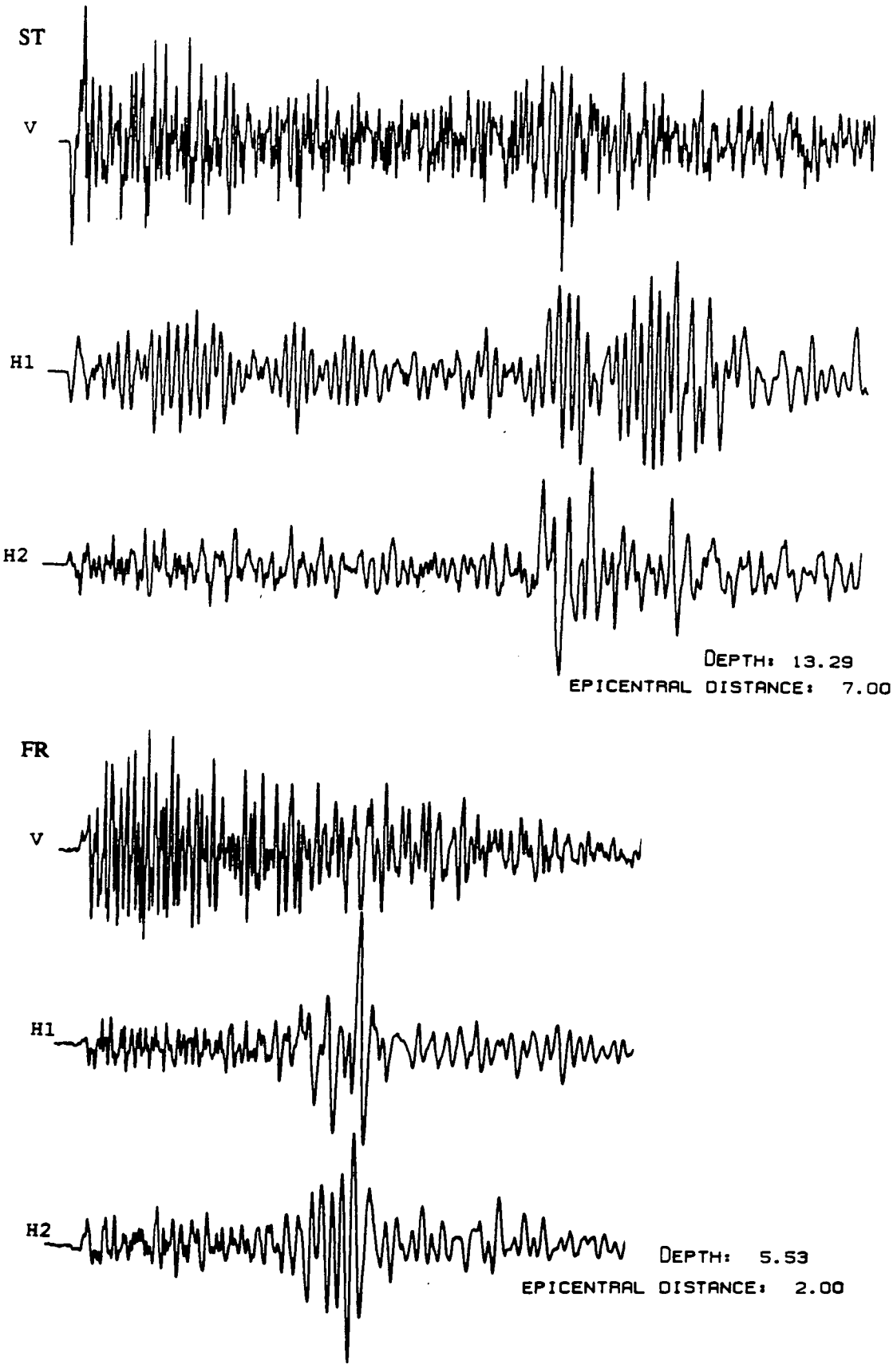

Figure 3.5. Examples of recorded first shear-wave arrivals contaminated by large *P*-coda waves at stations ST and FR.

Vp1=5.4 km/s, Vs1=3.3 km/s, and the rigidity of the medium $\mu 1=0.276 \times 10^{12}$ dyne/cm^2 on side 1 of the fault; Vp2=5.0 km/s, Vs2=3.1 km/s, $\mu 1=0.225 \times 10^{12}$ dyne/cm^2 on side 2; a typical 10 km focal depth for Parkfield earthquakes; and 4 and 14 km as the respective normal distances from the fault. This would also explain the commonly-observed emergent nature and relatively small amplitude of the wave preceding the direct *P* phase. Figure 3.6 shows corresponding direct wave and head wave paths for such source-receiver configuration. When the angle of incident θ is greater than $\theta_{Vs2Vs1} = \sin^{-1}(Vs2/Vs1)$ there are three head waves travelling at velocities of Vs1, Vp2 and Vp1, respectively. When θ is in the range $\theta_{Vs2Vs1} > \theta > \theta_{Vs2Vp2} = \sin^{-1}(Vs2/Vp2)$, there are two different head waves. When $\theta_{Vs2Vp2} > \theta > \theta_{Vs2Vp1} = \sin^{-1}(Vs2/Vp1)$ there is only one head wave before the geometrical arrival, corresponding to the disturbance that propagates along the interface with velocity Vp1.

Such emergent and small amplitude waves have been identified by Ben-Zion and Malin (1991) as *P* head waves (or diffraction or conical wave) preceding the direct *P* phases on stations MM, JN, VR, ED on the northeast block of the SAF. Modelling the characteristics of head waves will help to understand how large the influence of shear head waves may be in picking the first onset of shear waves. In the next section I shall describe a model incorporating shear-wave anisotropy on either side of the fault.

3.6.2 Modelling of head waves

A 2-D model was found to adequately reflect the geometry of the San Andreas fault, which dips almost vertically at 86° to the northeast. I calculated the shear-wave polarizations at the closest station (MM) to the fault. It is significant because its polarizations are nearly parallel to the fault. The fault and crack system were rotated so that the fault plane was a horizontal interface of two anisotropic halfspaces, with surrounding aligned crack planes dipping at 4°, having a symmetry axis 4° pointing outside of the paper, with aspect ratio AR=0.01 and crack density CD=0.05. Figure 3.7 shows the schematic geometry used for the modelling of head waves. Geophones

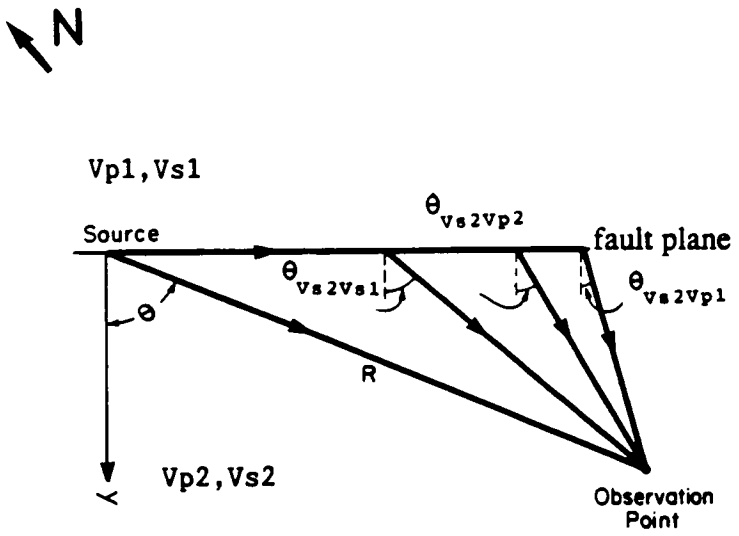

Figure 3.6. Schematic diagram in plan showing direct and head wave paths for an observation point with $\theta > \theta_{Vs2Vs1}$ assuming Vp1>Vp2>Vs1>Vs2. [after Ben-Zion (1990) with modifications]

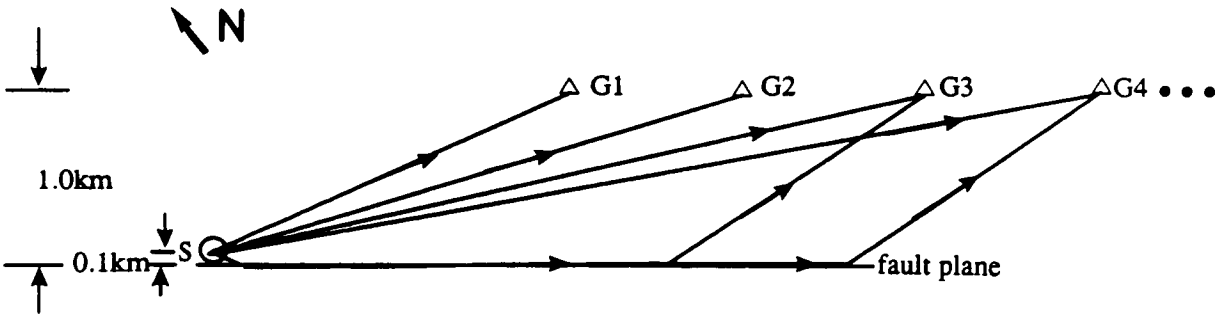

Figure 3.7. Schematic diagram in plan showing the geometry of the modelling of head waves. Note that the source is placed on the interface in model 2.

are placed in the upper halfspace in order to simplify the recorded wavefield (ignoring the effect of the free surface). Two models have been studied in order to examine the difference by changing the velocity contrast (Ben-Zion and Malin, 1991) and Vp/Vs ratio (Michelini and McEvilly 1991). Parameters used in the modelling are listed in Table 3.3. A horizontal force of SV22°SH polarized 22° from *SV*-wave towards *SH*-wave is used so that the *P* and *S* wave energy are similar. Figure 3.8 shows the synthetic seismograms of model 1 (a), and model 2 (b). Note that the amplitudes of the seismograms have been scaled to make all three-component traces to have the same maximum particle displacement so as to reveal the small features of the head waves. As indicated, phases 1, 2 and 3 represent the *P* head waves, head waves of fast arrivals of shear waves and head waves of slow arrivals, respectively. It is seen that the energy of both *P* and *S* head waves is small in comparison with the direct waves and characterised by its half cycle of waveforms with the same polarity as direct waves. In Figure 3.8 (b), it can be seen that a large velocity contrast can make a distinct difference in time delays between head waves and direct waves. Note that because the geometry of cracks is near horizontal (4° dip) the radial component is dominated by *P* wave energy, and the transverse component has mainly the energy of fast shear waves and the vertical component is dominated by slow shear waves.

The rock types are Gabilan granite with average Vp of 5.5 km/s on the southwest block of the SAF and slightly lower velocity Franciscan rock with Vp of 5.3 km/s on the northeast block. It may be expected that the time difference between head waves and direct waves is small when these two waves have not yet separated completely as shown at the 12 km and 14 km offsets in Figure 3.8 (a), and I may be able to reduce the possibility of misidentification of the onset of fast split shear waves by picking relatively sharp onsets as direct waves since head waves are emergent and have lower energy. Thus the model's predictions show that the occurrence of head waves may not produce crucial effects on the analysis of shear wave splitting, particularly, for the stations far from the fault because the waves would have small amplitude. In practice, the analysis becomes more complicated as head waves may be hidden in both the signal and noise-generated waves preceding the direct shear waves.

Table 3.3 Parameters used in modelling head waves at Parkfield.

Model	Halfspace	Vp (km/s)	Vs (km/s)	Vp/Vs	Density(g/cm^3)
1	Upper	5.3	3.06	1.732	2.4
	Lower	5.5	3.175	1.732	2.6
2	Upper	5.3	2.79	1.9	2.4
	Lower	6.0	3.16	1.9	2.65
	Aspect ratio AR=0.01		Crack density CD=0.05		

(a)

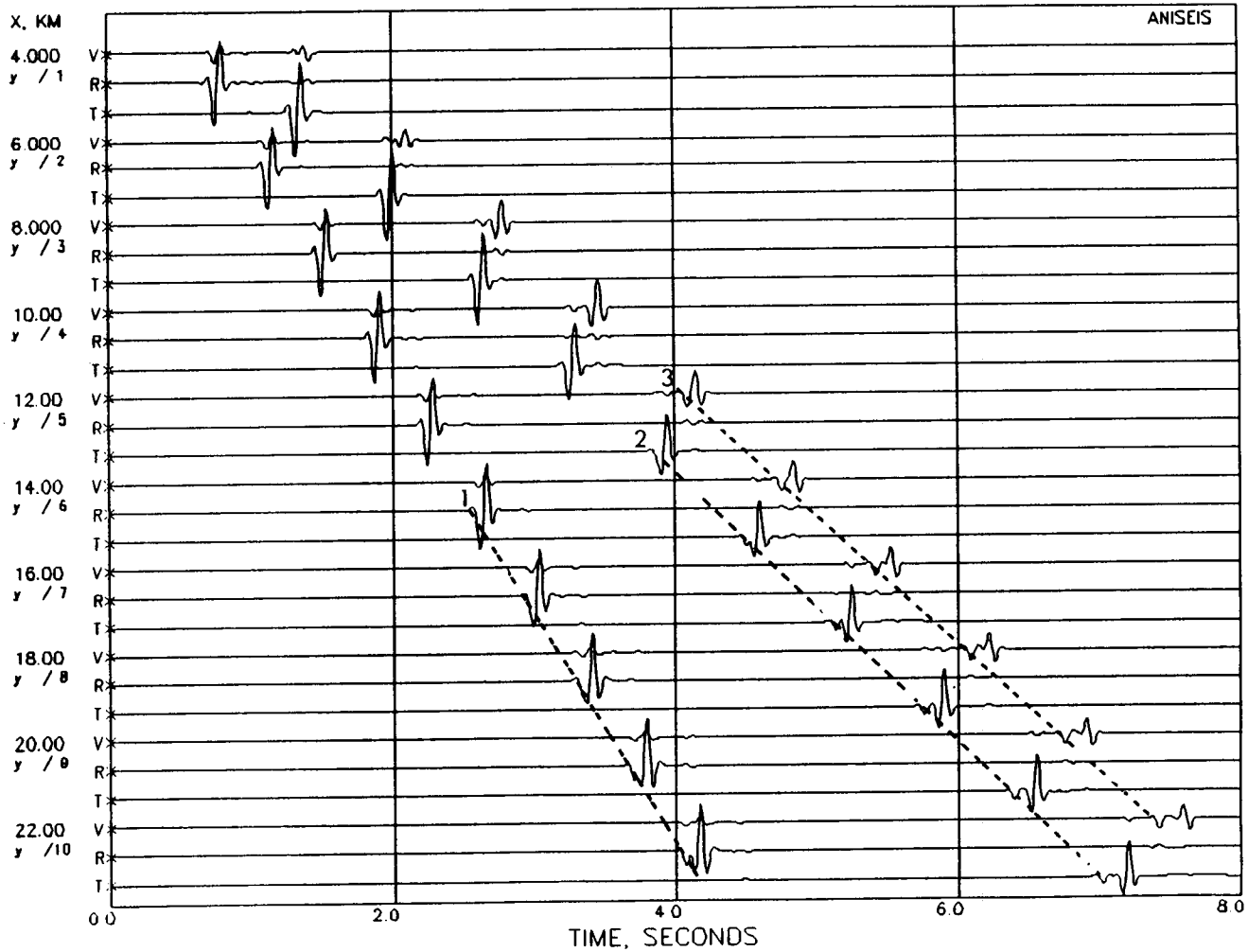

Figure 3.8. Synthetic seismograms of (a) model 1 and (b) model 2 described in the main text. The dashed lines marked 1, 2 and 3 represent respectively *P* refracted head waves, head waves of first split shear waves and head waves of second split shear-waves. In order to reveal the small features of head waves the amplitudes of the seismograms are normalised.

(b)

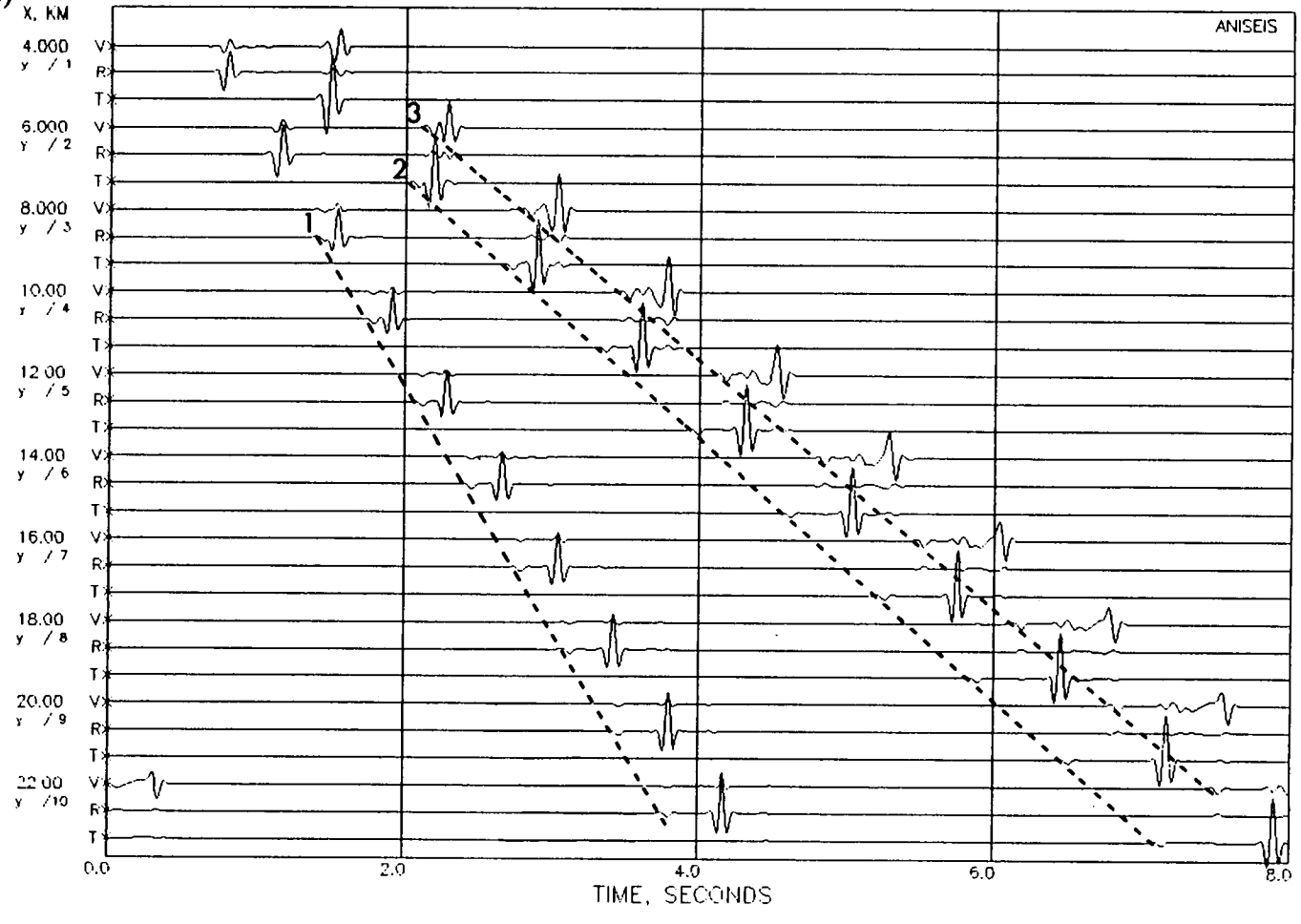
X, KM
4.000
y / 1
6.000
y / 2
8.000
y / 3
10.00
y / 4
12.00
y / 5
14.00
y / 6
16.00
y / 7
18.00
y / 8
20.00
y / 9
22.00
y /10
V
R
T
1
2
3
ANISEIS
0.0
2.0
4.0
6.0
8.0
TIME, SECONDS

3.7 THE EFFECTIVE SHEAR WAVE WINDOW

Evans (1984) studied the plane shear-waves scattered at the free surface and pointed out that when the angle of incidence is less than the critical angle, defined by $\alpha=\sin^{-1}(Vs/Vp)$, the reflection coefficients are real, there are no phase changes, and the waveforms are preserved as incident waves. This critical angle (35.3° when Poisson's ratio equals to 0.25) is defined as the shear wave window. Booth and Crampin (1985) investigated the behaviour of shear-waves with curved wavefronts incident on the free surface from a shallow point source by calculating synthetic seismograms using the reflectivity technique and found that shear wave particle motions become strongly elliptical at angles of incidence about 40°. Various studies have shown several features not present in plane-wave arrivals, such as *S* to *P* converted phases propagating parallel to the surface as a head-wave (known as the local *SP*-wave or the surface *P*-wave), and surface waves generated following the main shear arrivals. Reverberations also arrive before and after the main shear-wave arrivals. All the above effects may be severe for angles of incidence greater than the critical angle, but may occur at any angle of incidence if the surface topography or subsurface interfaces are sufficiently irregular both in-line and cross-line to the direct source-to-receiver path (Crampin, 1990).

Shear waves recorded at depths of 200 to 300 m at Parkfield may still suffer the effects generated from the near surface low-velocity layer or the free-surface, the effect of strong *P* coda waves has been observed on seismograms at most of the stations. Figure 3.9 shows an example of local *S*-to-*P* converted waves received at station VC. It is characterised by nearly horizontal propagation, and the energy is seen principally on the radial component. For this particular case it is not difficult to pick the true arrival of the shear wave since there are large enough delays between *S-P* phases and direct shear waves. In some other cases shear waves may be obscured by the converted waves, especially when the radial direction is about the same as that of the crack strike, and the time delays between the split shear waves will be increased. Therefore, shear-wave splitting with incidence in the shear wave window is still

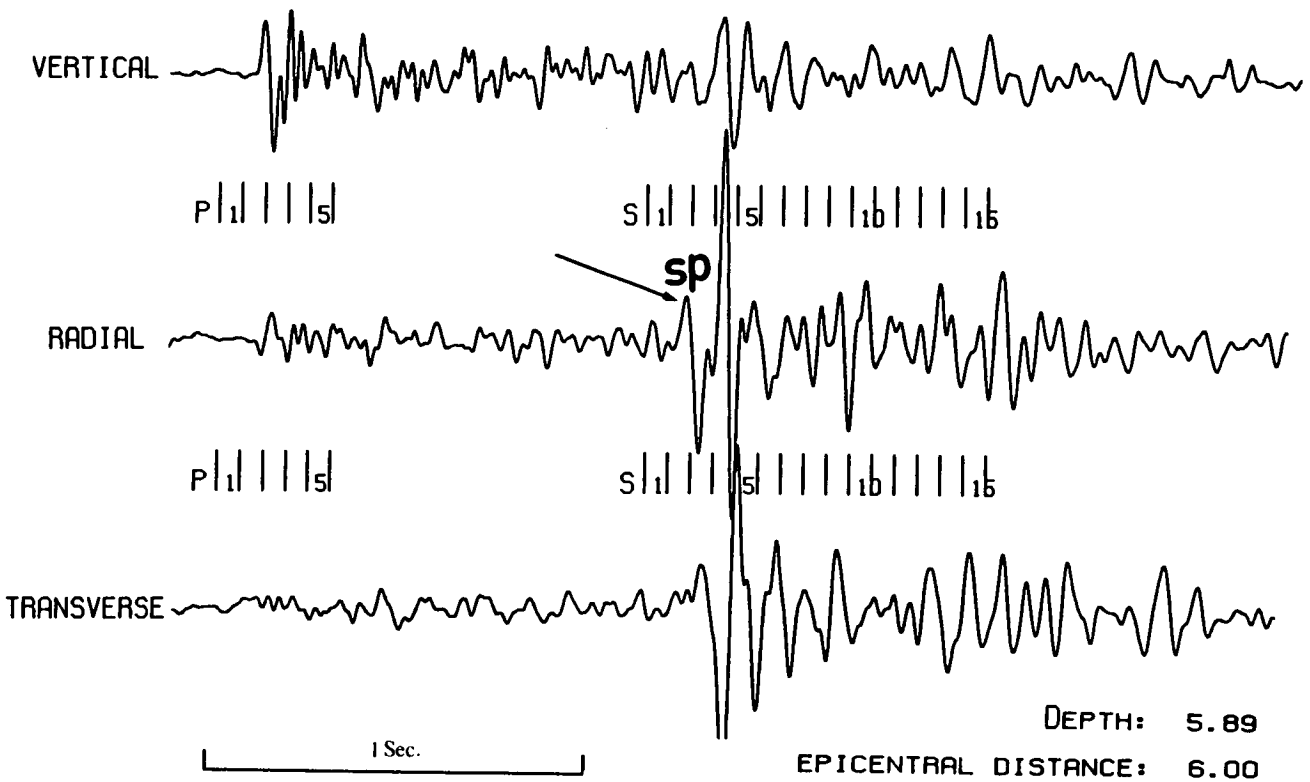

Figure 3.9. An example of an *S-P* converted phase observed at station VC. It is characterised by the dominant energy of the *S-P* phase on the radial component.

significant and necessary for data recorded at depths of 200 to 300 m at Parkfield.

Since we cannot properly include the effects of low-velocity near surface layers and subsurface irregularities of topography beneath the stations, the exact value of the critical angle is not available. However, it is reasonable to assume the arrivals are within the shear-wave window as long as the alignment of the shear-wave polarizations on the equal-area projections are consistent with the alignments of signals with small angles of incidence. In general, an effective critical angle of 45° appears to be appropriate for the Parkfield data because the regularity of the polarizations near the edge of the shear-wave window at 45° are not seriously distorted at stations MM, VC, JN, ED and VR.

3.8 CONCLUSIONS

The examination of the orientations of seismometers has led to the recognition of anomalous *P*-wave polarizations. This is principally due to scattering off the complicated local geology and deformation along the raypath. Site effects may be at least partly responsible for the greatly amplified energy of *P*-coda waves.

Shear-wave head waves propagating along the SAF are another potential source of ambiguity in the analysis of shear-waves, particularly at station MM, which is in the immediate vicinity of the fault. However, modelling the behaviour of head waves has shown that head waves are not significant sources of error because of their relatively small energy and half cycle of waveform. In practice, they are most likely to be hidden in much larger amplitude signal-generated noise preceding the direct shear-waves. It is also necessary to make allowance for the *S-P* conversions at the edge of the shear-wave window, though seismometers were located in boreholes at Parkfield. Any possible misidentification of the onset of the first split shear-wave is avoided by picking the sharp onset of the direct *S*-arrival.

CHAPTER 4

PARKFIELD: MEASUREMENT AND RESULTS OF SEISMIC ANISOTROPY

4.1 INTRODUCTION

Having investigated the factors that could affect the results of the measurement of shear-wave splitting in the previous chapter, I shall present the method of measurement and the results of shear-wave splitting with the Parkfield data in this chapter. First of all, I shall describe the method of extracting anisotropic parameters used in this study and summarise other techniques commonly used in the literature. I will then show the results of shear-wave polarizations and possible temporal change in time-delays between split shear waves. Finally, I shall examine the reliability of the temporal change in time-delays by the means of earthquake doublet (or multiplets), and its significance will be examined using error analysis. The depth extent of anisotropy is investigated in the fault zone in an attempt to examine the correlation between depth termination of the fault zone and seismic anisotropy.

4.2 MEASUREMENT OF ANISOTROPIC PARAMETERS

There are various techniques that are commonly in use in extracting anisotropic parameters. These include the aspect ratio method (Shih *et al.*, 1989; Shih and Meyer, 1990); the cross-correlation method (Bowman and Ando 1987); and the variance tensor method (Aster *et al.*, 1990), all of which have been used both for natural earthquake sources and artificial sources, such as vertical seismic profiles (VSPs). More recently, neural network methods have been attempted but are not yet proven. Next, I shall summarise the most useful methods.

4.2.1 Aspect ratio method

The aspect ratio method uses the aspect ratio of a window of data as a measure of the polarization linearity within the window. In this case only the horizontal components are considered. For a waveform with two orthogonal components X and Y, the total displacements (D_x,D_y) within a window having the number of N samples can be written as equation (4.1) and (4.2)

$$D_x=\sum_{i=1}^{N} |X_{i+1}-X_i| \ , \tag{4.1}$$

and

$$D_y=\sum_{i=1}^{N} |Y_{i+1}-Y_i| \ , \tag{4.2}$$

The aspect ratio A is given by

$$A(\phi)=D_x/D_y \ , \tag{4.3}$$

where ϕ varies from 0° to 180° in the window containing the shear-wave arrival. The shear-wave polarization θ relative to the North is given by

$$\theta=R\pm\tan^{-1}(1/A_{max})degrees \ , \tag{4.4}$$

where R is the rotation angle of the seismometer component. The plus sign ' + ' represents a right-hand system of a seismometer recording coordinate; minus ' – ' represents left-hand system; A_{max} is the maximum value of the aspect ratio $A(\phi)$ representing the largest linear motion in the window. After the polarization is estimated from equation (4.4), the horizontal seismograms are then rotated into 'fast' and 'slow' components, respectively parallel and perpendicular to the polarization

direction to measure time delays between fast and slow shear-wave arrivals which will yield the largest aspect ratio (A_{max}).

The advantage of the method is that it provides an objective estimate of shear-wave polarizations and the error of the measurement, which can exclude the less reliable data before conclusions are formulated, and it can be automated. However, this technique is very sensitive to both the start and the fixed length of the window chosen for the calculation of the aspect ratio. If the window is too short or too long, it will lead to unstable results and include both fast and slow split shear-wave arrivals, respectively. The window length limits the minimum linearity interval required before accurate polarizations can be measured to a few digital samples.

4.2.2 Cross-correlation method

The cross-correlation method is used to measure the delay time between the two split shear-waves. Once an estimate of the polarization of the first shear-wave arrival is available, the horizontal components of a seismogram are rotated into the fast and slow directions. The cross-correlations are then calculated in a window containing the first shear-wave arrival and the cross-correlation coefficient gives a measure of the reliability of the delay. Clearly, this technique (and to some extent the aspect ratio technique) requires the two wave pulses should be of similar shapes, otherwise, there will be no claim of observed shear-wave splitting. However, this is not always the case. Yao and Xiong (1993) have studied synthetic seismograms with a dislocation point source in an anisotropic medium and they found that source generated relative amplitudes of quasi-*P* wave (qP) and the two quasi-shear waves (qS1 and qS2), i.e. AqP/AqS1 and AqP/AqS2, depend on source behaviour and crack geometry surrounding the source. Moreover, near-surface layers and *P*-wave coda, etc, could also alter the waveform of the slow shear waves.

4.2.3 Variance tensor method

The variance tensor method can be considered as a generalization of the aspect ratio method. The variance tensor can be defined as the expectation over some time window:

$$V = \langle X(z,x,y) X(z,x,y)^T \rangle \ , \tag{4.5}$$

where the three-dimensional time series **X**(z,x,y) represents the response of three orthogonal, matched geophones to the motion of the ground. The diagonalization of this matrix yields an estimate of the polarization direction in the three dimensions based on the components of the eigenvector associated with the largest eigenvalue. A measure of the linearity of the signal in the window can be calculated from the eigenvalues. Aster *et al.* (1990) took this process a step further by defining an orientation matrix **M**, based on the results of the polarization measurements on N earthquakes:

$$M = \sum_{i=1}^{N} L_i L_i^T \ , \tag{4.6}$$

where,

$$L_i = l e_i \ , \tag{4.7}$$

and e_i is the polarization direction of earthquake i, and l is the linearity measure of the observation. Analysis of the properties of this matrix allows contours to be determined for a distribution of polarization measurements to be plotted on an equal-area projection.

Aster *et al.* (1990) adopt this method to estimate the linearity interval of the shear-wave arrivals, which can be interpreted as a measure of the delay between the split shear-waves. However, it suffers the same windowing problem as the aspect ratio

method, and the linearity interval does not necessarily measure the time delay and may only indicate the period of time before scattering dominates. Crampin *et al.* (1991) showed that some results of this technique published by Aster *et al.* (1990) were dramatically incorrect. Consequently, the use of this technique is not suggested for measuring parameters of shear-wave splitting.

4.2.4 Method used in this study

The visual method of extracting anisotropic parameters used in this study has been described in detail in the appendix of Chen *et al.* (1987). It is preferred to rotate the recorded horizontal seismograms into radial and transverse components with respect to the earthquake-to-seismograph azimuth as it is convenient to monitor *P*-wave energy of possible *S* to *P* converted waves on the radial component, as shown in Figure 3.9 of chapter 3. The plots of both *P*-phase and *S*-phase arrivals are produced on three planes, they are the radial-transverse horizontal plane, vertical-radial and vertical-transverse vertical planes. The particle motion diagrams of *P*-phase arrivals are checked on the sagittal (vertical-radial) plane to ensure that the apparent incident angle is within the shear-wave window, and on the radial-transverse and vertical-transverse planes to estimate the possible errors of shear wave polarizations caused by ray travelling off azimuth as discussed in Section 3.4.

All shear-wave splitting measurements are made on the particle motion diagrams. Seismograms are referenced to identify the onset of the first shear-wave arrival and sometimes possible for the second shear-wave arrival. The most important step is the identification of the onset of the first shear-wave arrival. Care must be taken to make sure that late *P*-phases, or *S*-to-*P* conversions and shear-wave head waves on specific stations, are not misidentified as shear-wave arrivals preceding the true arrival. This is particularly so if the motion is dominated by the radial component. The first motion of the shear-wave arrival is usually sufficiently linear for the polarization direction to be identified; if it is not, no measurement is made. The initial motion is picked as a polarization direction for a slightly elliptical motion of the first

shear-wave arrival, strongly elliptical arrivals are not measured. Where possible vector polarizations are determined by assessing the polarity of the first motion, and a weight of each measure is given by the quality of the data or the reliability of the measurement.

Measurement of the time delay requires the identification of the onset of the second shear-wave arrival. This is more difficult and may be less reliable as the second split shear-wave may be obscured by both signal-generated and background noise, and it is possible that multiple splitting will further complicate the identification. Furthermore, the focal mechanism of the earthquake may not excite both possible polarizations equally, so that either of the split shear-waves may be small,. or absent, along a particular raypath. Despite these constraints, an attempt is made to identify the second arrival by searching for an abrupt change in polarization, followed by significant energy in a direction orthogonal to the first arrival. Studies of synthetic seismograms show that the onset of the second split shear-wave is marked by an abrupt change in the direction of the particle motion, or by the increasing ellipticity of the motion. A weight is assigned in terms of the relative reliability of the measurement.

Data are weighted from 1 to 3 according to both the quality of seismogram (signal to noise ratio) and particle motion diagram. Weight 1 is given to the polarizations and the time delays if the particle motions display clearly the onset of the first shear-wave and the second shear-wave arrivals, which is identified by a sufficient large linearity between the first and the second arrivals and a large energy on the orthogonal direction for the second arrival; weight 2 is assigned for polarizations that represent the apparent onset of the first arrival but particle motions displaying either an elliptical motion or complicated by a background noise, and also in the case if the arrivals of the slow waves are identified by an orthogonal energy that is not large enough to show the abrupt change of the motion. Time delay in this case is usually weighted by 2. If the onset of the first split shear wave can be identified, but may be obscured by P-coda waves, then weight 3 is usually given to polarizations, and the same weight of the time delays is used generally if there is a

small energy of orthogonal motion so that the picking of the second split shear-wave is doubtful. Such weights provide some information about the reliability of the measurements of anisotropic parameters, although in practice it may be far more complicated, and it is inevitably to some extent subjective.

This method certainly has the advantage of providing a graphical means of identifying shear-wave splitting parameters, and it does not suffer from the problems of automated techniques, such as the start time and length of the window of aspect ratio method. However, it may be subjective in measuring shear-wave splitting parameters and the estimate of error, although a weight has been given to each measurement according to its reliability. It is necessary to point out that whatever technique is used it always has the similar result for good quality data, and this has been compared by Gledhill (1991).

4.3 SHEAR-WAVE POLARIZATIONS

4.3.1 Observation of shear-wave splitting

Shear-wave splitting has been subsequently observed in many parts of the world in a wide variety of rocks for a wide variety of tectonic regimes over the last 15 years (Crampin, 1987; Crampin and Lovell, 1991). In particular, shear-wave anisotropy has been observed in plate boundary tectonic regimes in California (Li *et al.*, 1988; Daley and McEvilly 1990; Karageorgi *et al.*, 1992; Liu *et al.*, 1993; Li *et al.*, 1994; Zhang and Schwartz, 1994). Figure 4.1 displays typical examples of shear-wave splitting observed at five stations of the HRSN network at Parkfield. Note that the horizontal components of each seismogram have been rotated to 'fast' and 'slow' directions respectively parallel to, and orthogonal to, the polarization direction of the leading split shear waves in order to present clear delay times between the fast and slow waves.

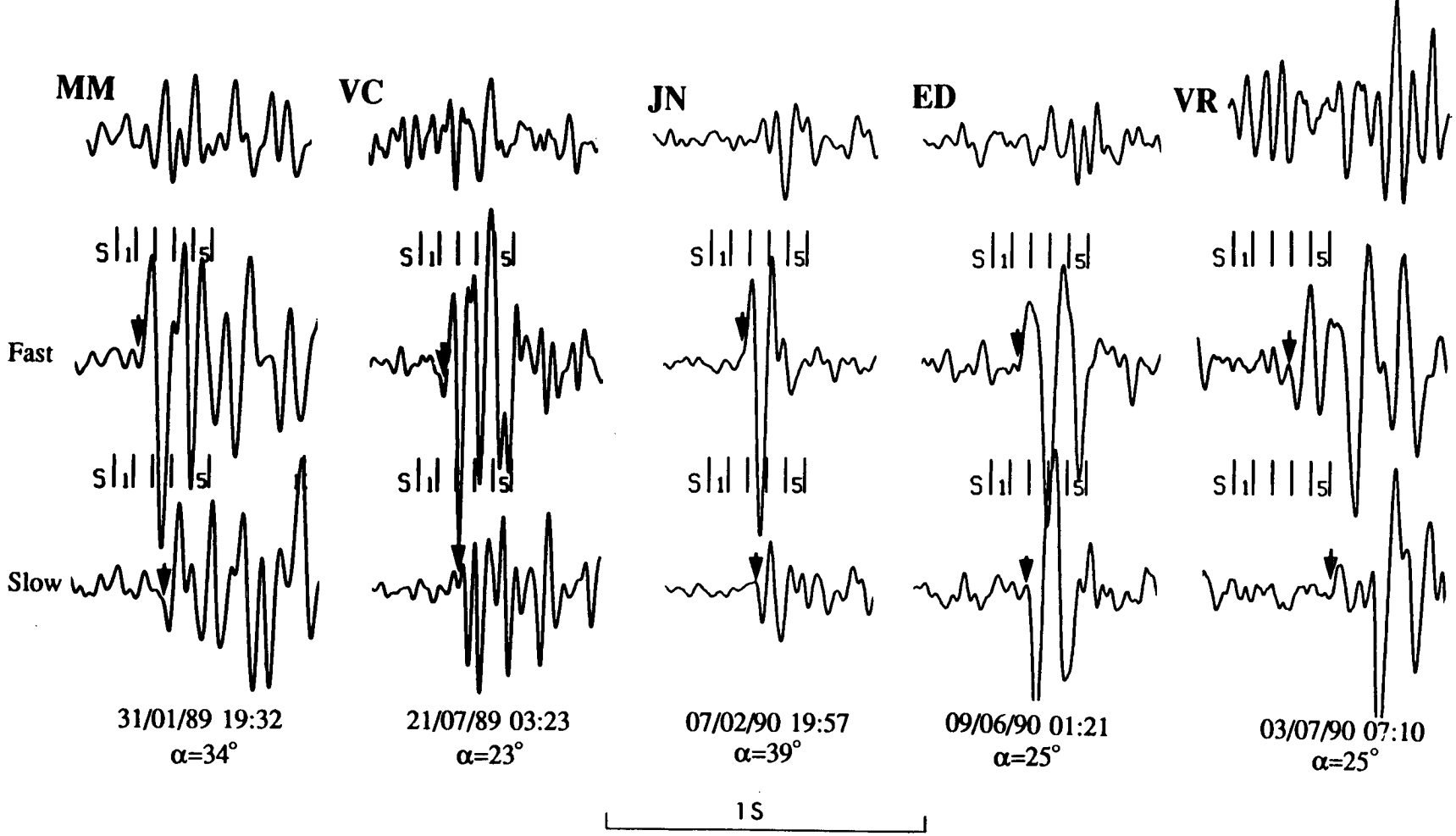

Figure 4.1. Examples of seismograms showing shear-wave splitting at stations MM, VC, JN, ED and VR. Note that the horizontal components have been rotated to make 'fast' and 'slow' components respectively parallel to, and orthogonal to, the polarization direction of the leading split shear waves; arrows mark the onset of fast and slow waves, each window length is 60ms and the amplitudes of components for each earthquake are normalised with respect to the maximum amplitude of the three components. Earthquake origin time and the angle of incidence, α, for each event at corresponding station are indicated at the bottom of each seismogram.

4.3.2 Equal-area projection of lower-hemisphere

A convenient way of displaying three-dimensional variations of shear-wave propagation is to project a hemisphere surrounding either a source or station onto a plane. Equal-area projections (polar projections or polar maps) are preferred to display shear-wave polarizations and time-delays.

Figure 4.2 (a) shows the construction of equal-area polar projections (polar maps) of a hemisphere of directions. Ray directions are projected onto a horizonal plane at the same azimuth, and distance $2\alpha\sin(\theta/2)$ from the centre, O, where θ is the incidence angle of the ray and α is the distance of the source from the projection plane. Figure 4.2 (b) shows the map resulting from the construction in (a), which has the property that equal solid angles are transformed to equal areas on the plane.

4.3.3 Polarizations

Daley and McEvilly (1990) have investigated shear-wave anisotropy in the Parkfield Varian Well (VR) VSP. The VSP survey was run to 1334 m depth and the controlled sources are at three different offsets. They found about 8% velocity difference below the depth of about 400 m, and the polarizations of fast and slow split shear-waves are parallel to and perpendicular to the San Andreas fault. However, they found that polarizations become elliptical at deeper levels indicating a possible change in orientation of the axis of symmetry of cracks pervading in the rockmass. Another study of seismic anisotropy at Parkfield was completed by Karageorgi *et al.* (1992), using repeated Vibroseis sources and the Parkfield HRSN receivers. They observed shear-wave splitting for some source-receiver paths and the results of shear-wave polarizations were the same as Daley and McEvilly (1990).

Here, the distribution of shear-wave polarizations within the shear-wave window (45°) at each station are plotted in Figure 4.3 in both (a) equal-area rose diagrams and (b) equal-area projections. Inverse weights 1 to 3 have been linearly applied to each measurement, which means weight 1 is the most reliable data

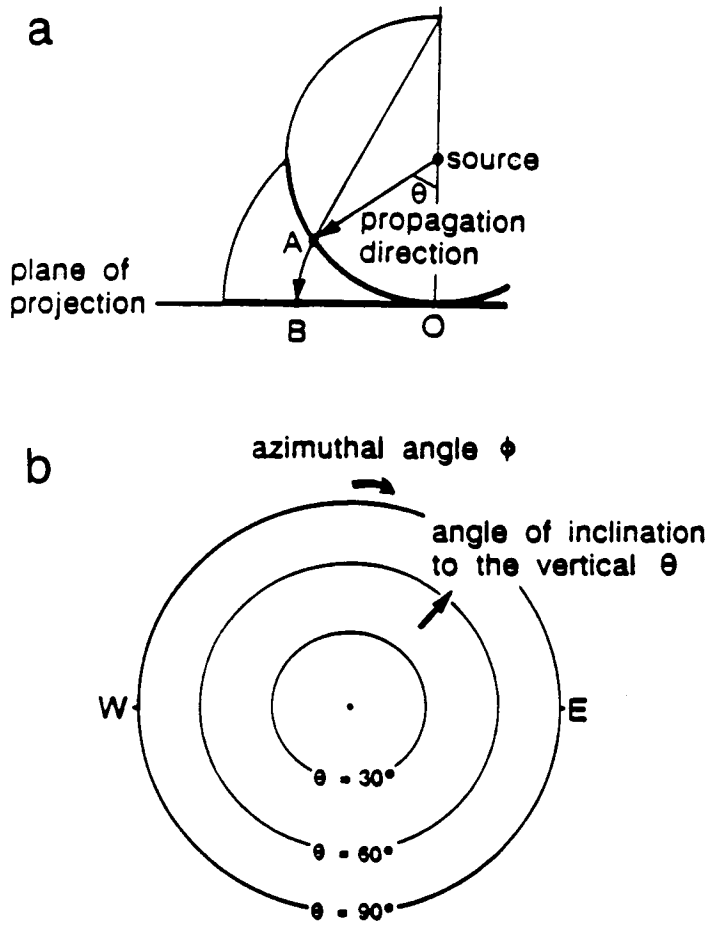

Figure 4.2. (a) Geometry of an equal-area polar projection. A direction from a source to a point A on a hemisphere is mapped to a point B on the plane of projection, where OA=OB=2αsin(θ/2) and the azimuth, ϕ, is preserved, where α is the distance from the source to projection plane, and θ is the angle of incidence. (b) Equal-area projection of directions, with angle of incidence from 0° to 90° and azimuths from 0° to 360° (after Wild and Crampin, 1991).

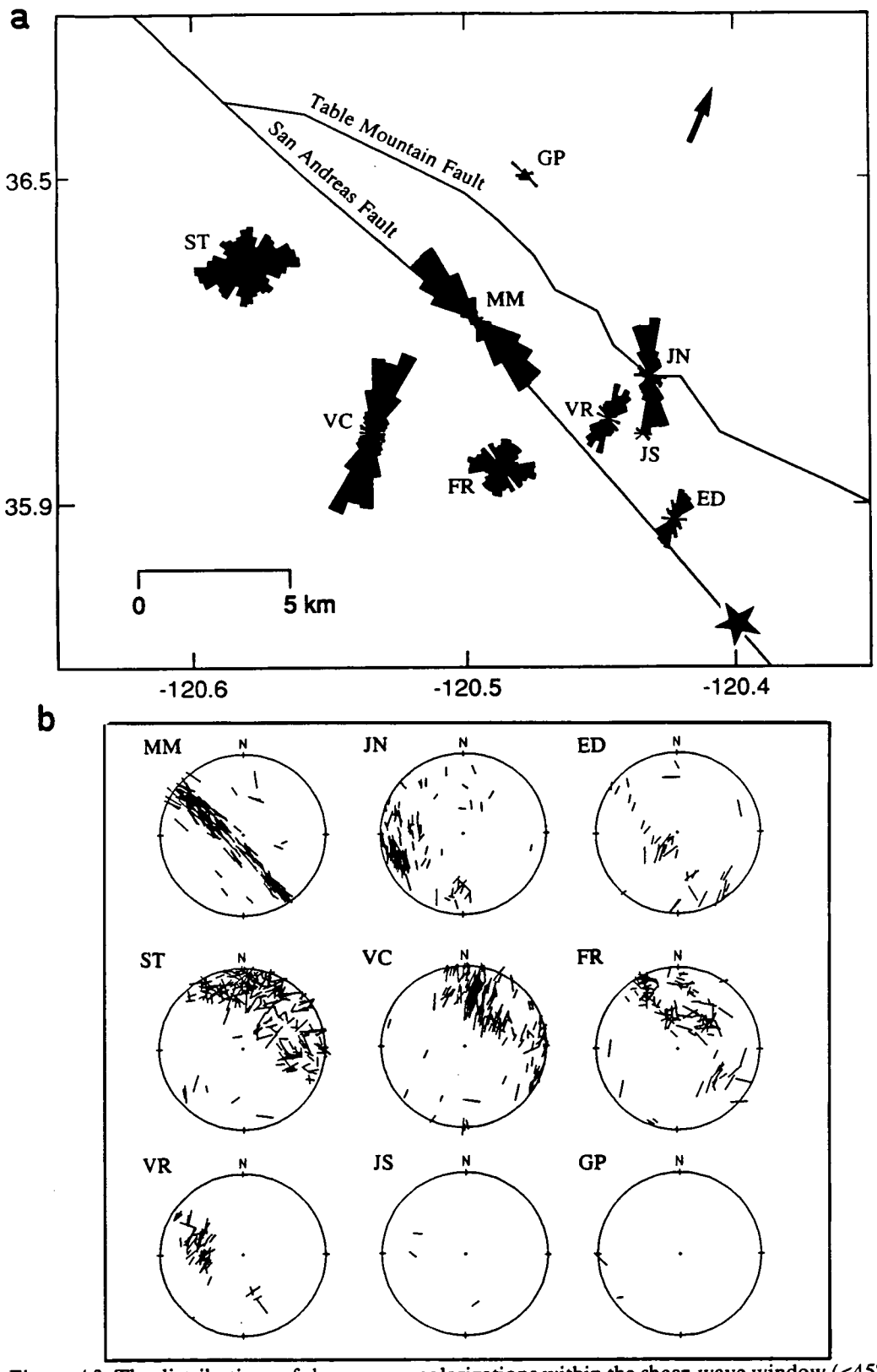

Figure 4.3. The distributions of shear-wave polarizations within the shear-wave window (<45°) in (a) equal-area rose diagrams and (b) equal-area projections at the corresponding stations in (a). A heavy arrow in (a) marks the direction of regional maximum horizontal principal stress. The star indicates the M_L=4 earthquake which occurred on May 25th, 1989. Note the length of bars in the equal-area projections in (b) indicates the reliability of the measurements, i.e. weight 1 is the most reliable data representing by a long bar, weight 3 is less reliable representing by a shortest bar and weight 2 is in between in reliability representing by a medium length of a bar.

representing by a long bar, weight 3 is less reliable representing by a shortest bar and weight 2 is in between in reliability representing by a medium length of a bar. The polarizations of the fast split shear-waves display approximately parallel alignments at stations MM, VC, JN, VR and ED, as was typically observed elsewhere (Crampin and Lovell, 1991). The directions of the polarizations are scattered at stations ST and FR with little evidence of any preferential alignment. Polarizations at stations VC, VR and ED are distributed about N30°E direction, which is approximately parallel to the direction of maximum principal stress near the San Andreas Fault (SAF) in central California (Zoback *et al.*, 1987), shown as a heavy arrow. The alignment at JN is approximately North-South, and is about N40°W at MM, approximately parallel to the SAF. Note that there are very few data at stations GP and JS, because station JS was not working properly most of the time between 1988 and 1990, and there are actually few data recorded in the shear-wave window at station GP.

At station VR, the borehole seismometer was located at the depth of 572 m, therefore the seismic anisotropy detected at this station reflects the property of the medium deeper than this depth in the upper crust. Thus, polarizations from earthquake sources may be different from VSP observation, and Daley and McEvilly (1990) have pointed out that the polarizations become elliptical with the increase in depth. This implies that the orientation of the axis of symmetry of cracks pervading the rockmass might have changed because of near-surface effects. As discussed in Chapter 3, the near-surface and site or path effects can be very large at this site, especially with relatively shallow VSP data. Furthermore, this is supported by the results of Karageorgi, *et al.* (1992). Since the receivers were located at a depth between 200 m and 300 m and the sources (Vibroseis) were at the surface (Karageorgi, *et al.*, 1992), the observed direct shear wave splitting is caused by near-surface layers, and hence it may show different shear-wave polarizations from my results (interpretation in next chapter), which are derived from natural earthquake sources, and represent the properties deeper in the upper crust.

Since crustal earthquake are thought to be stress-induced phenomenon and the changes in crack orientation have been identified before and after hydraulic pumping

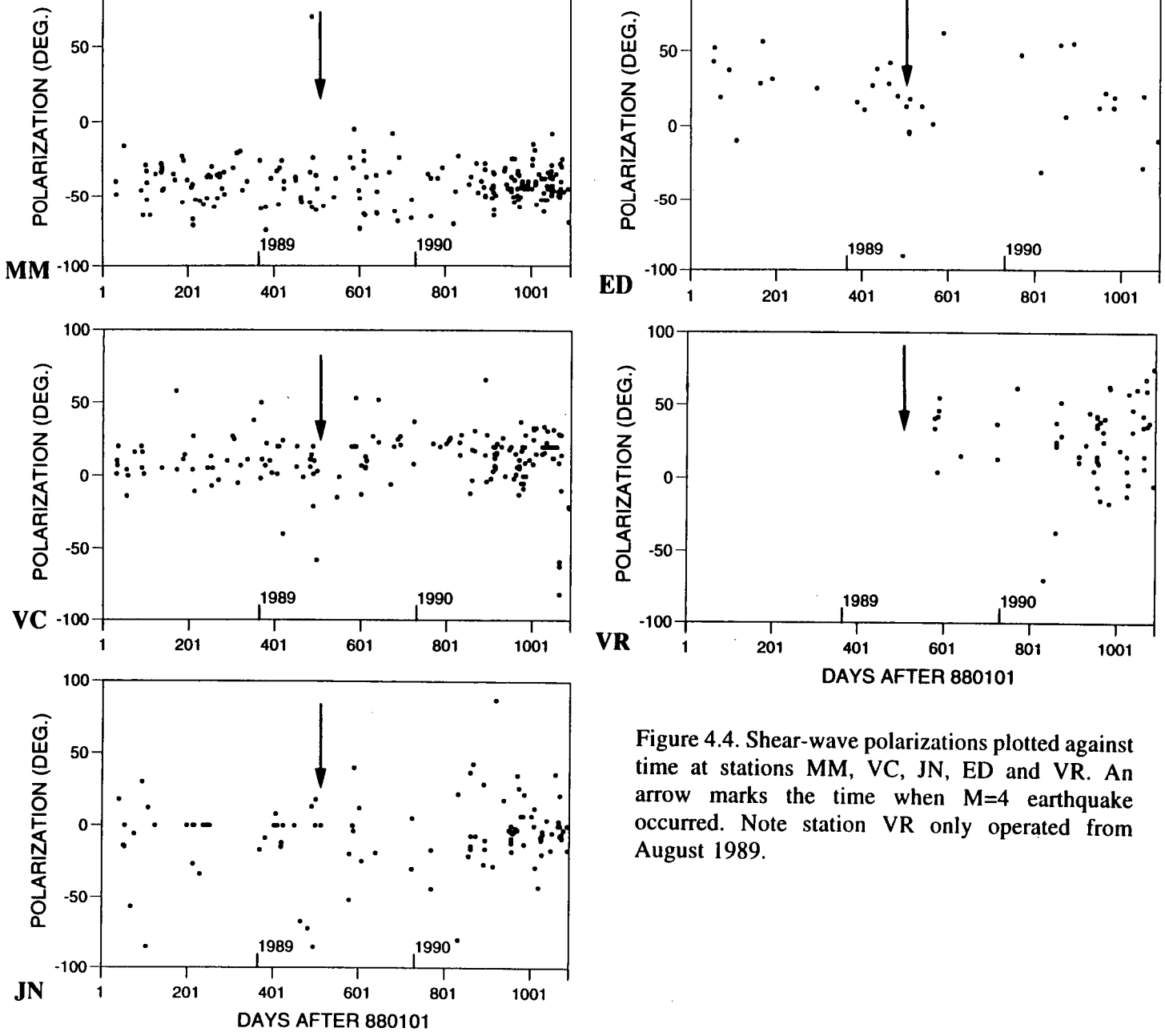

Figure 4.4. Shear-wave polarizations plotted against time at stations MM, VC, JN, ED and VR. An arrow marks the time when M=4 earthquake occurred. Note station VR only operated from August 1989.

(Crampin and Booth, 1989), it is possible there are temporal variations of shear-wave polarizations associated with the M=4 event. Figure 4.4 is plotted at the stations MM, VC, JN, ED and VR. The shear-wave polarizations appear to be uniformly scattered around a consistent direction, and there is no significant change in alignment at any of the stations at the time of the M=4 earthquake.

4.4 POSSIBLE TEMPORAL CHANGE OF TIME DELAYS AT PARKFIELD

The greatest time delay between the fast and slow waves is about 72 millisecond near the fault zone, at station MM, and 70 millisecond at station VC, on southwest block, 5 km from the SAF, which corresponds to about 3% and 2% of differential shear-wave anisotropy at the two sites, respectively. An increase in time-delays followed by a pronounced decrease before and after the largest earthquake M=4 is observed at Parkfield, as observed at Anza, California by Peacock *et al.* (1988) and, Crampin *et al.* (1990), and at Enola, Arkansas by Booth *et al.* (1990). Possible temporal change of time-delays and its significance are examined in detail by the means of doublet and the error analysis. The differential shear-wave anisotropy decreasing with depth is observed at the 2 out of 4 stations which are near to the SAF.

4.4.1 Seismicity and the largest earthquake

Figure 4.5 shows the seismicity of earthquakes recorded by the Parkfield network from 1988 to 1990. It has been mentioned in Section 2.2 that the seismicity of earthquakes with magnitudes greater than 2.5 has declined about 25% (Wyss *et al.*, 1990) since the last M=6 earthquake occurred at Middle Mountain (MM) in 1966. In general, earthquakes recorded by the network occurred close to the fault plane with depths between 4 km and 15 km, and magnitudes in the range of $-0.5 \leq M_L \leq 2.0$. The largest earthquake during the period studied was a M_L=4 event recorded on 25th May 1989 in the Parkfield segment. It was located at a depth of 8.25 km, south of the town of Parkfield and near the southeast extremity of the network (marked by an asterisk

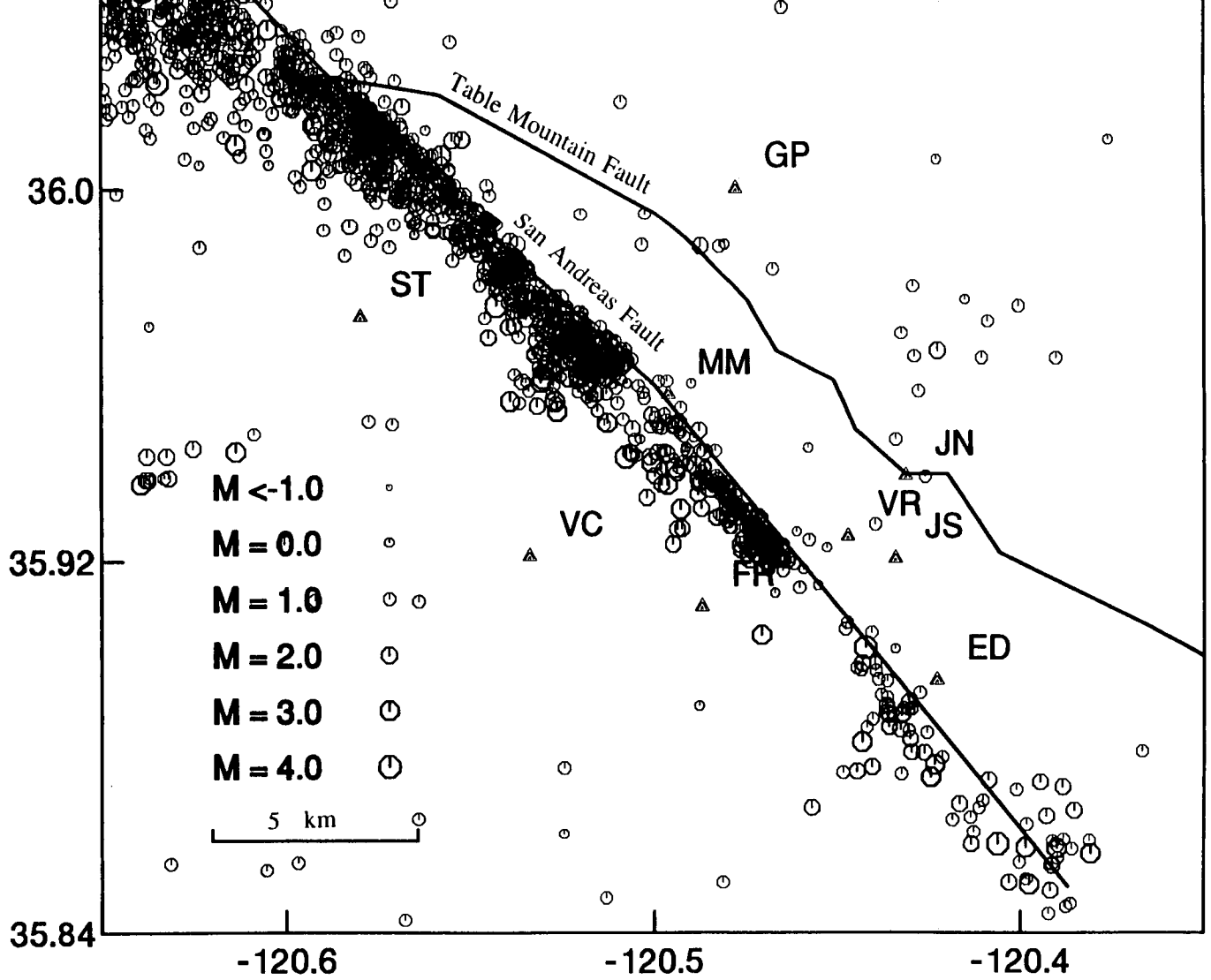

Figure 4.5. The seismicity of earthquakes recorded by the Parkfield network from 1988 to 1990. The epicentres of the earthquakes are the locations using the 1-D velocity model shown in Figure 3.4. Note the largest M=4 earthquake is at the southeast end along the San Andreas Fault. The triangles represent the corresponding locations of seismometers.

in Figure 4.3) about 15 km away from stations MM and VC, and resulted in a C level alert. Coincident with this earthquake, small co-seismic steps were recorded at 9 of the 13 Parkfield creepmeters. It also generated static steps on all dilatometer and tensor strain instruments. A preliminary inversion of these steps indicates a moment of 1.2×10^{22} dyne cm. (Lindh and Estrem, 1989).

4.4.2 Time delays

Time-delays between the split shear-waves are more difficult to estimate than polarizations of the leading split shear-waves, and scattered polarizations usually indicate disturbances to the wavetrain which make it impossible to estimate time-delays reliably. I have concentrated the analysis on the stations MM, VC, JN, ED and VR, where shear-wave polarizations exhibit approximately parallel alignment.

If the anisotropy is uniform then it is expected that in a given direction, the time delay will increase with hypocentral distance, assuming wave propagation in a straight line from source to receiver, although for each ray path, delay time depends upon the direction of wave propagation with respect to the hexagonal symmetry axis of an azimuthal anisotropic medium. The variations of time delays with hypocentral distance at the five stations are plotted in Figure 4.6. The approximately linear variation of the maximum at any particular distance in Figure 4.6 allows us to normalise time delays. Figure 4.7 shows the variations with time of time-delays normalized to a hypocentral distance of 1 km at the five stations. The arrow marks the time of the M=4 earthquake. Note that station VR was installed after all other stations, and started to function from the middle of 1989. There are insufficient data at stations JN and ED to make reliable assessment of the significance of variations in time-delay before and after the time of the M=4 earthquake. However, it can be seen at stations MM and VC that there is an apparent increase of time-delays of the earthquakes before the time of the M=4 earthquake, and a decrease after the time of the M=4 event followed by an irregular increase. A nine-point moving average of the data has been calculated at the two stations and plotted in Figure 4.8. It is seen that the

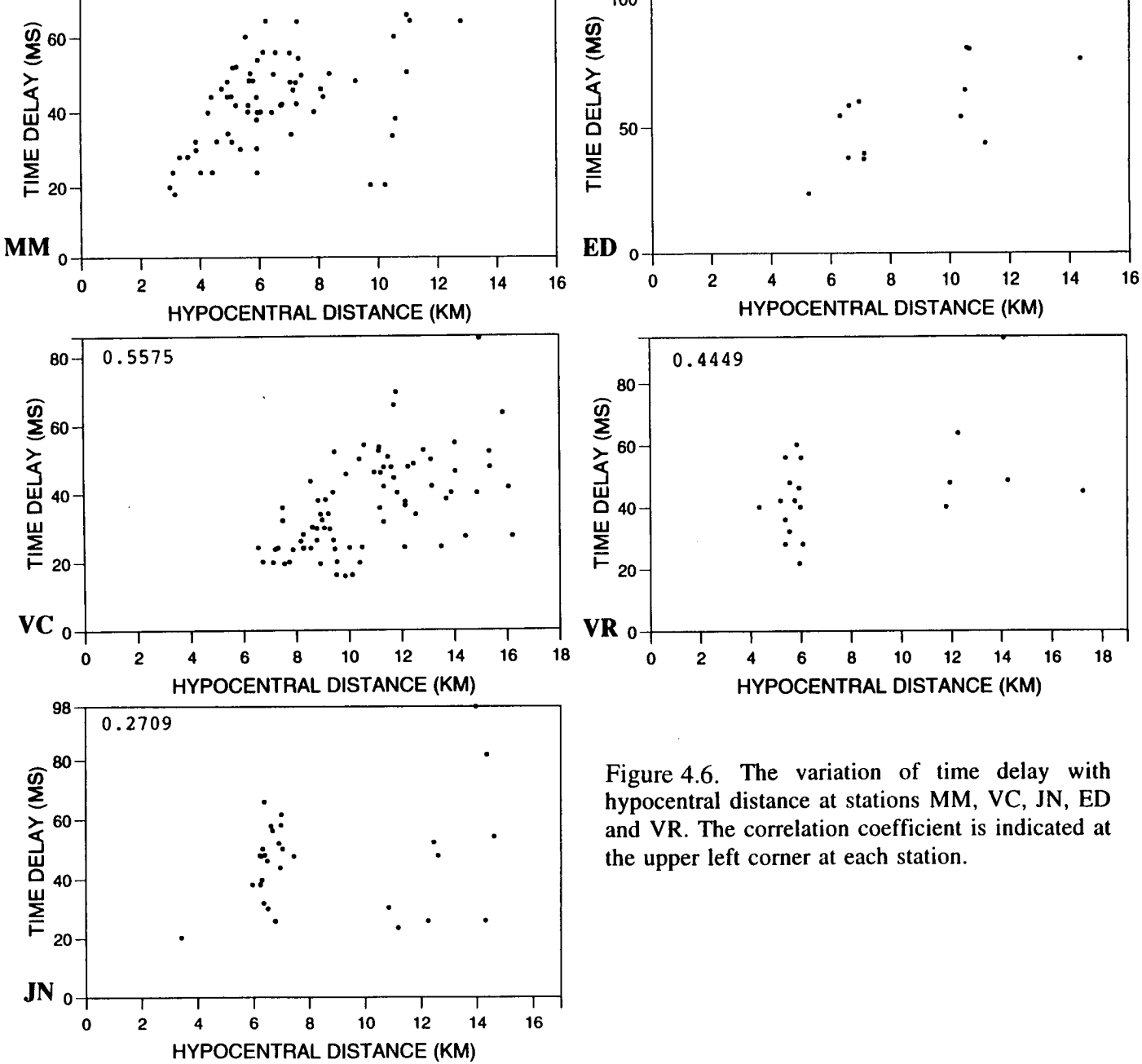

Figure 4.6. The variation of time delay with hypocentral distance at stations MM, VC, JN, ED and VR. The correlation coefficient is indicated at the upper left corner at each station.

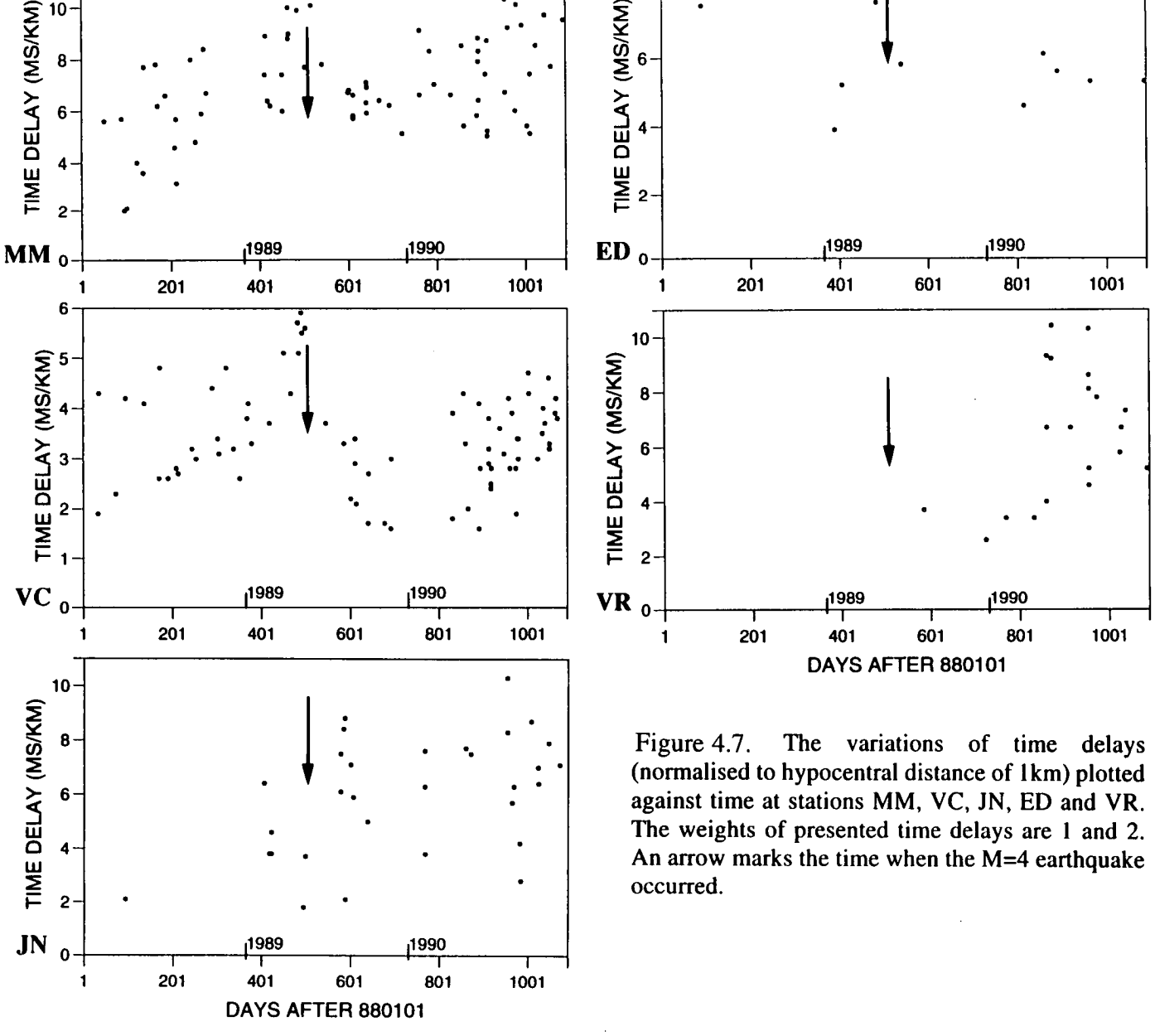

Figure 4.7. The variations of time delays (normalised to hypocentral distance of 1km) plotted against time at stations MM, VC, JN, ED and VR. The weights of presented time delays are 1 and 2. An arrow marks the time when the M=4 earthquake occurred.

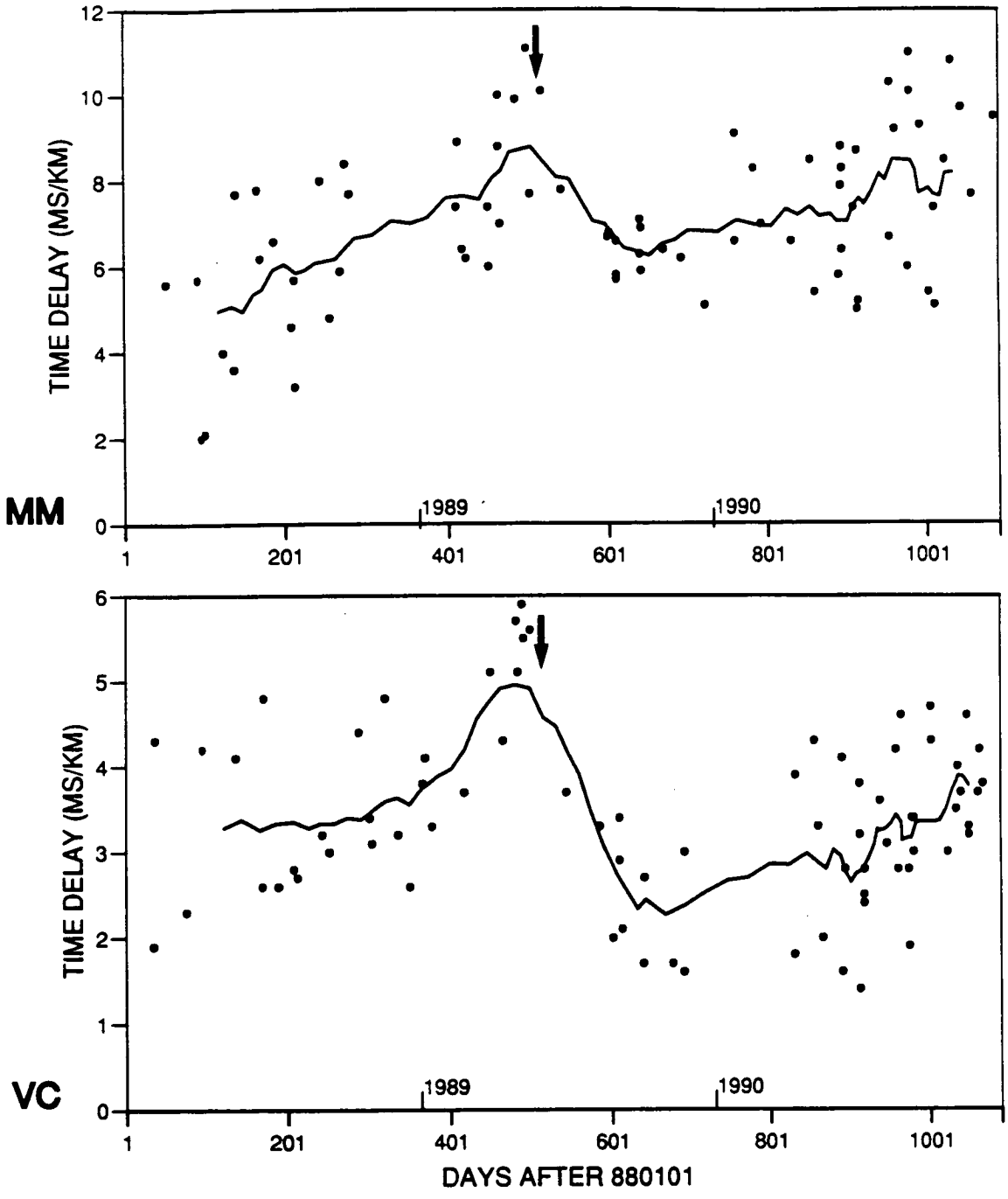

Figure 4.8. The diagrams of Figure 4.7 at stations MM and VC with a 9-point moving average. An arrow marks the time when the M=4 earthquake occurred.

scattered trend of the variation of increase and decrease before and after the largest earthquake has been clearly observed and the delays at MM are about twice as large as those at VC. Note that the possible significance of this earthquake was not recognised initially, and only came to my attention after I had observed the possible temporal change in time-delays. This behaviour is similar to that seen in previous studies which showed similar variation in time-delays before and after a M=6 earthquake (Crampin *et al.*, 1990); and before and after the time of a M=3.5 earthquake (Booth *et al.*, 1990).

The observed possible temporal change in time-delays is based on analysis of a large set of seismic events, as are the other studies of shear-wave splitting. Each event has different raypaths and with different angles between the raypath and the symmetry axis of parallel vertical cracks, which is assumed to cause the effective anisotropy. It has been shown in Section 1.3 that different angles between the wavepath and the symmetry axis will produce different values of time delays. This would explain a certain degree of scattering of the observed time delays, shown in Figure 4.8, which will be further examined in the next chapter. Furthermore, studies of shear-wave splitting have displayed spatial variations due to different distributions of data sets (Gledhill, 1993a; Kaneshima, 1990; Liu *et al.*, 1993). Earthquake doublets are one method of avoiding such wavepath variations and spatial variations, and may be able to provide more reliable evidence of temporal variation of time-delays. In order to do this, I need to find such doublets or multiplets that are separated in time. Note that the detailed studies of time-delays are only made at stations MM and VC since they are the only stations with sufficient data, and the only stations where the shear wavetrain signal-to-noise ratio permits secure identification and timing of the second split shear-wave.

4.4.3 Earthquake doublets

Doublets are neighbouring earthquake pairs with similar waveforms, and by implication, similar source properties including focal mechanism. Poupinet *et al.*

(1984) and Aster *et al.* (1990) have used microearthquake doublets to measure accurately seismic velocity changes. Got and Fréchet (1993) have used seismic doublets to measure temporal variations of attenuation in the crust before earthquakes of large magnitudes. More recentaly, Nadeau *et al.* (1994) have defined some 80 clusters of from 2 to 12 events during the period 1987 to 1989 at the Parkfield segment, and a full-scale study of fault-zone dynamics is underway. Here, I use earthquake doublets to investigate and check the temporal changes in time-delays observed at Parkfield.

4.4.3.1 Observation of earthquake multiplets

I concentrate my analysis on those events for which time-delays were picked at stations MM and VC. Earthquakes are chosen for each group with a difference in depth at less than 1 km, and differences in both incidence and azimuth to station MM and VC of less than 5°. Every pair of events is examined for similar waveforms. For the collected similar events cross-correlation of each three-component traces are calculated with a 0.24s and 0.3s window length at MM and VC, respectively, starting from the beginning of the shear-wave arrival. Five distinct clusters of up to 5 event multiplets are eventually selected with average maximum correlation coefficient greater than 0.63 at station MM, and 0.51 at VC. Here it is noticed that the waveforms of shear waves are expected to be different to a certain extent caused by a variable delay time for each individual event since time delays are expected to vary with time. The central event with respect to which the correlation coefficient is calculated is chosen because this event was located at the centre in each cluster. Cluster multiplets shared by both stations have been examined, but none has been used because they are either located outside the shear-wave window (45°) or show complicated or poor quality shear wavetrains with no satisfactory measurement of time-delay at one of the stations. The similarity of the source mechanism of the events in each cluster family is examined by examining waveforms at all other stations in the network. Table 4.1 lists the multiplets of each cluster family and the corresponding parameters of each

Table 4.1 List of the parameters of earthquake multiplets used at stations MM and VC

GP.	No.	Stn	Date	Time	Maxc	Dep	Azim	Ainc	M_D	Pol	Del
A	1	MM	890216	0456	0.958	4.55	-57.0	36	0.77	123	7.4
	2*	MM	890409	1918	0.799	4.74	-57.0	34	1.59	129	8.8
	3	MM	891004	1725	0.938	3.95	-59.0	37	0.57	116	6.9
	4	MM	891223	1503	0.664	5.11	-56.0	30	0.82	113	5.1
	5	MM	900703	2055	0.638	4.09	-55.0	36	0.13	115	8.7
B	1	MM	890218	0055	0.831	4.88	-21.0	9	1.55	149	8.9
	2	MM	901110	1437	0.851	4.65	-20.0	12	0.52	143	9.7
	3*	MM	901111	0254	0.841	4.85	-18.0	12	-0.17	145	9.7
C	1*	MM	890223	1807	0.885	5.55	-32.0	39	1.56	154	6.4
	2	MM	900813	0536	0.885	4.79	-36.0	40	0.71	143	10.3
D	1	MM	881006	1741	0.867	4.85	-63.0	35	0.29	135	7.7
	2*	MM	890327	1426	0.867	6.32	-57.0	31	0.85	143	7.4
E	1*	VC	880727	0301	0.658	10.5	4.0	22	-0.22	4	2.8
	2	VC	881117	0022	0.727	9.73	9.0	21	0.29	7	4.8
	3	VC	890106	0323	0.513	12.1	4.0	19	1.11	11	4.1
	4	VC	890515	2252	0.733	11.1	0.0	19	0.52	3	5.6

Maxc: maximum correlation coefficients of the inter-event wrt the one marked by an asterisk (*), the underlined value is the average Maxc in the group; Dep: depth in kilometres; Azim and Pol: azimuth and polarization angles of events from north to east; Ain: angle of incidence in degree; M_D: coda-duration magnitude; Del: time delays normalised to hypocentral distance of 1 kilometre in millisecond.

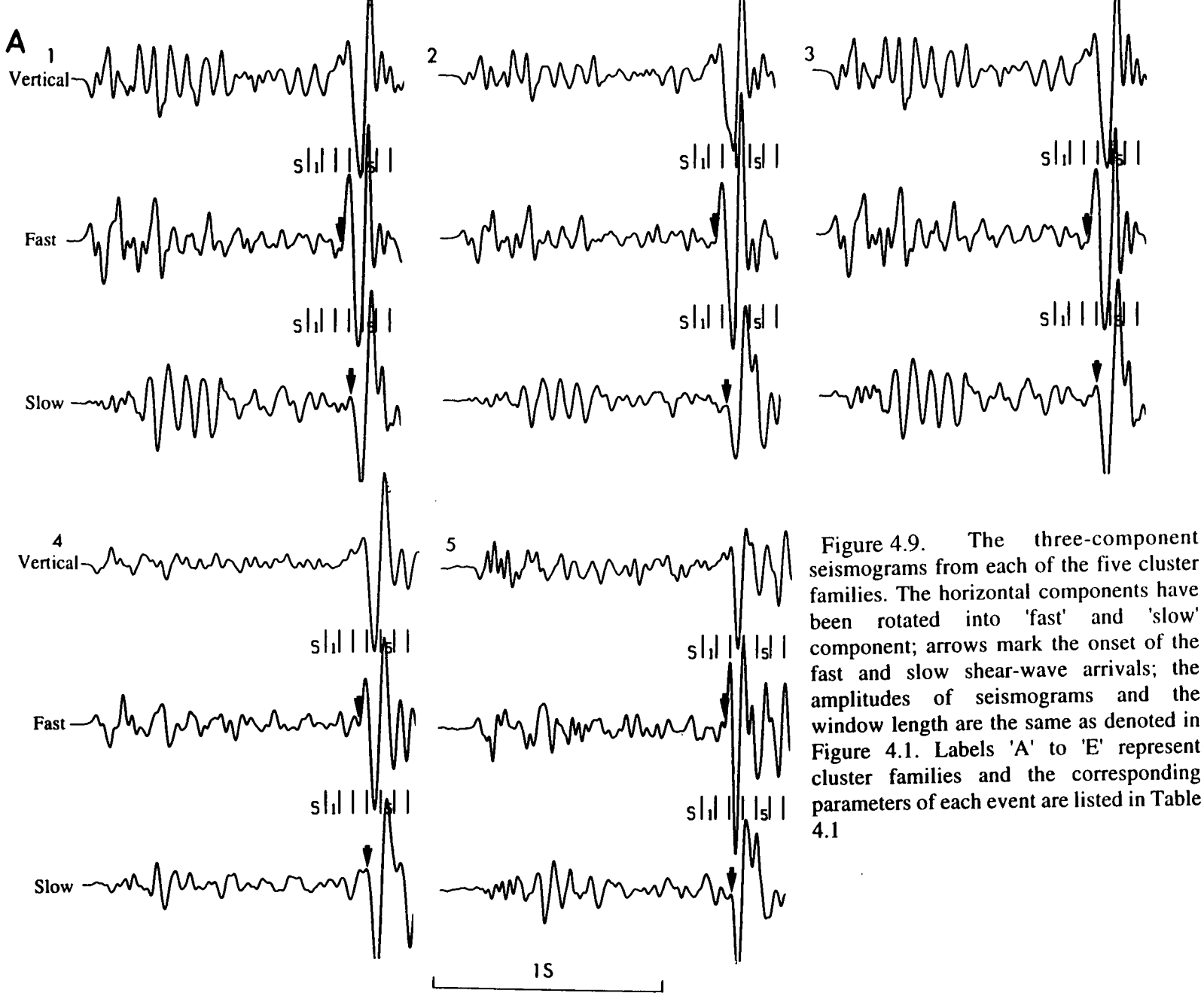

Figure 4.9. The three-component seismograms from each of the five cluster families. The horizontal components have been rotated into 'fast' and 'slow' component; arrows mark the onset of the fast and slow shear-wave arrivals; the amplitudes of seismograms and the window length are the same as denoted in Figure 4.1. Labels 'A' to 'E' represent cluster families and the corresponding parameters of each event are listed in Table 4.1

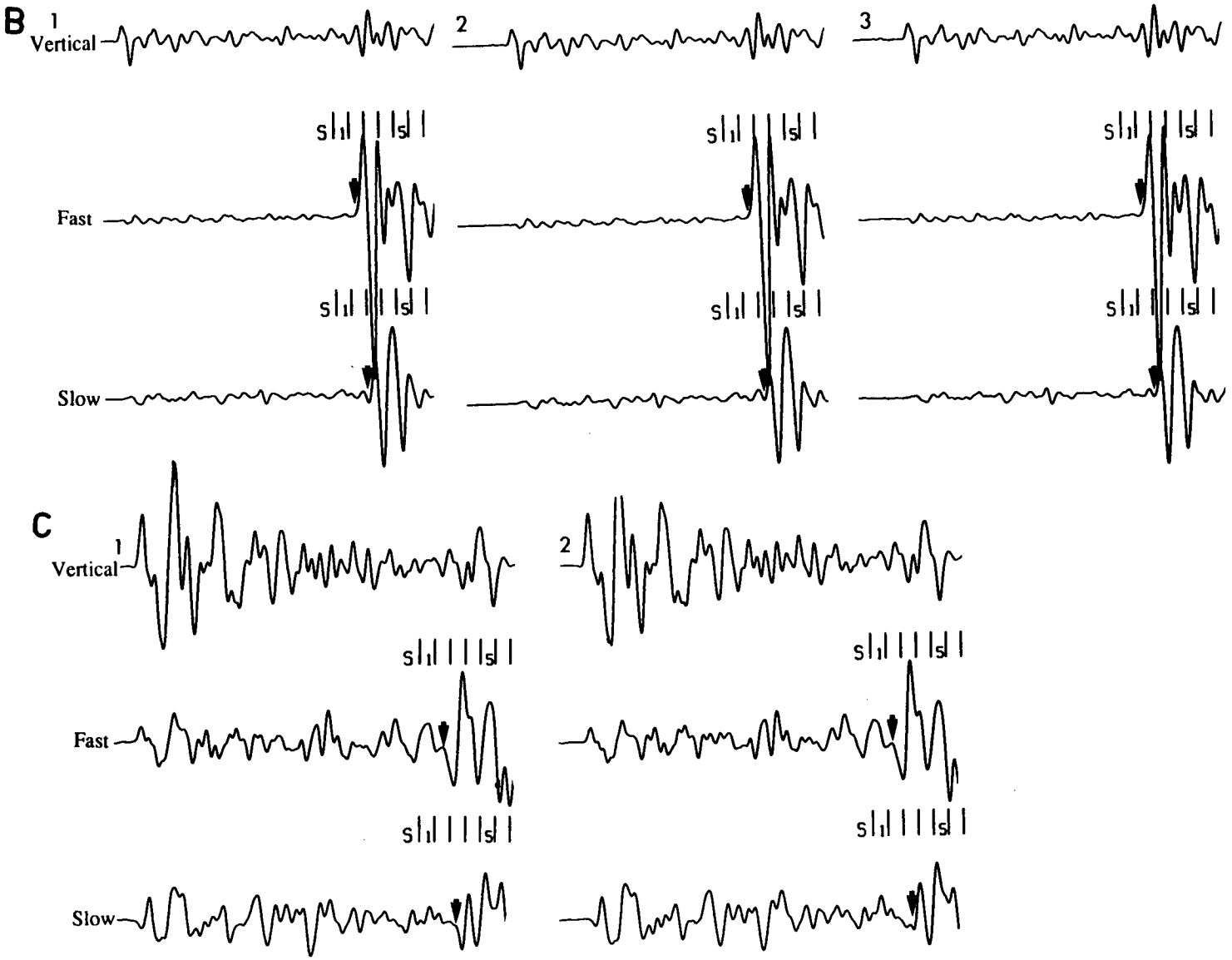

Figure 4.9 (continued)

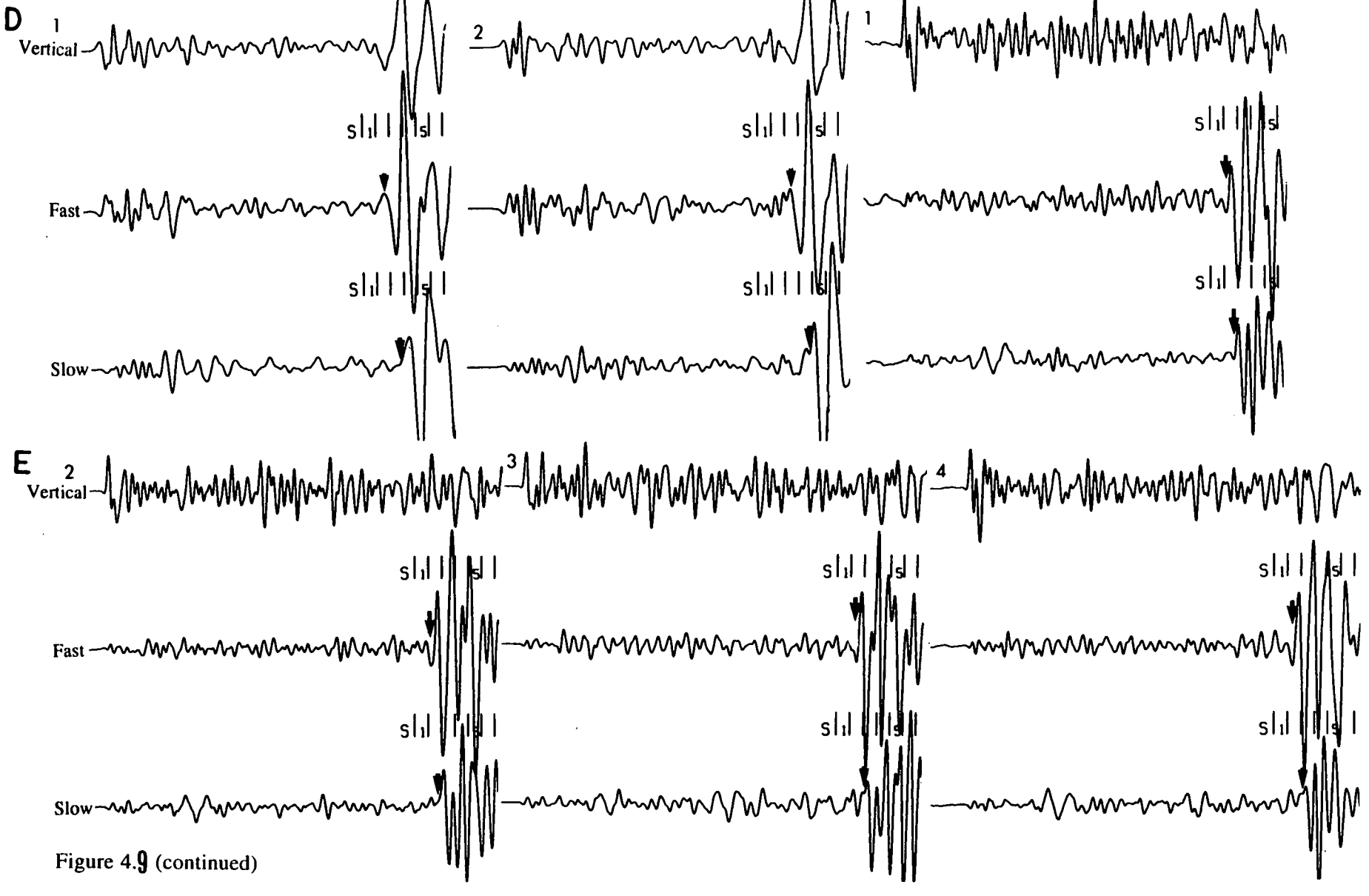

Figure 4.9 (continued)

event. Figure 4.9 displays the three-component seismograms from each of the collected five cluster families. Note that the horizontal components have been rotated to fast and slow directions in order to present clear time-delays between fast and slow waves. The arrows mark the start time of the two waves. Figure 4.10 shows the locations of the cluster events at MM and VC. It is seen that earthquakes in each cluster family have highly similar *P* and *S* waveforms with average maximum correlation coefficient of shear wavetrain greater than 0.54; similar raypaths; similar polarization directions and inter-event distance varies from a few tens of metres to hundreds of metres. The quality of these data is good enough to make reliable measurements of time delays.

4.4.3.2 Time delays of multiplets

The variation with time of normalised time-delays of the multiplets of each cluster family are plotted at the two stations in Figure 4.11. As above, the arrow indicates the time when the largest earthquake M=4 occurred, and each cluster family has a different symbol. Cluster 1 at MM shows the variation of time delays which was observed with the whole dataset -- the increase and decrease of delays before and after the time of the M=4 earthquake, respectively. At VC, we can only see the distinct increase of delays since there is only one cluster of 4 events selected and they all occurred before the time when the M=4 event occurred. Combining the two stations we see a change of time delays before and after the time when the M=4 earthquake occurred. The quality of the data, shown in Figure 4.9, is convincing that the observed temporal variation at Parkfield reflects the change of the properties of media, and the temporal change is associated with the time when the M=4 occurred. However, it is important to examine whether the variation of temporal change is physically and statistically significant.

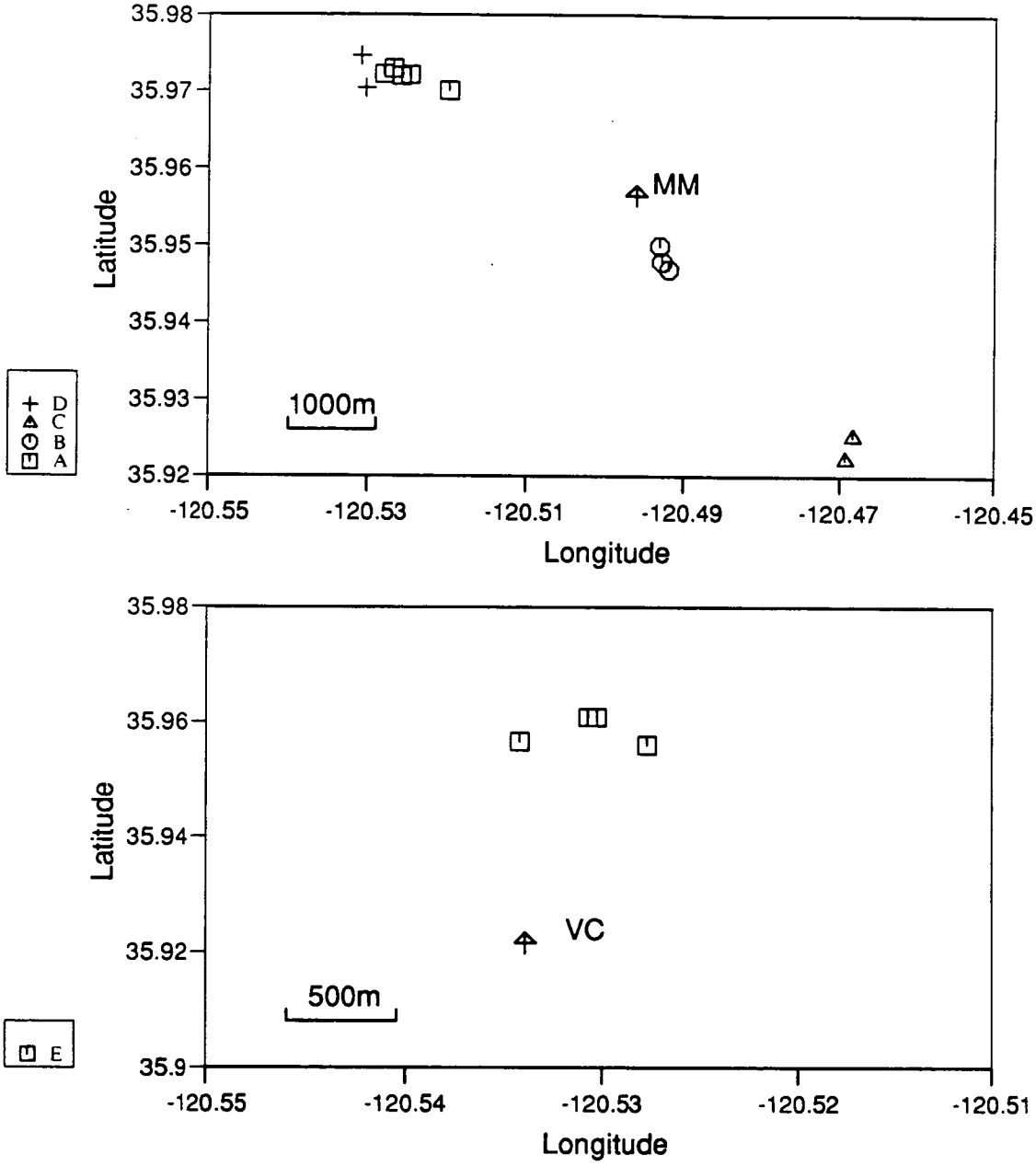

Figure 4.10. The locations of the cluster events at stations MM and VC. Same symbols represent the same cluster events.

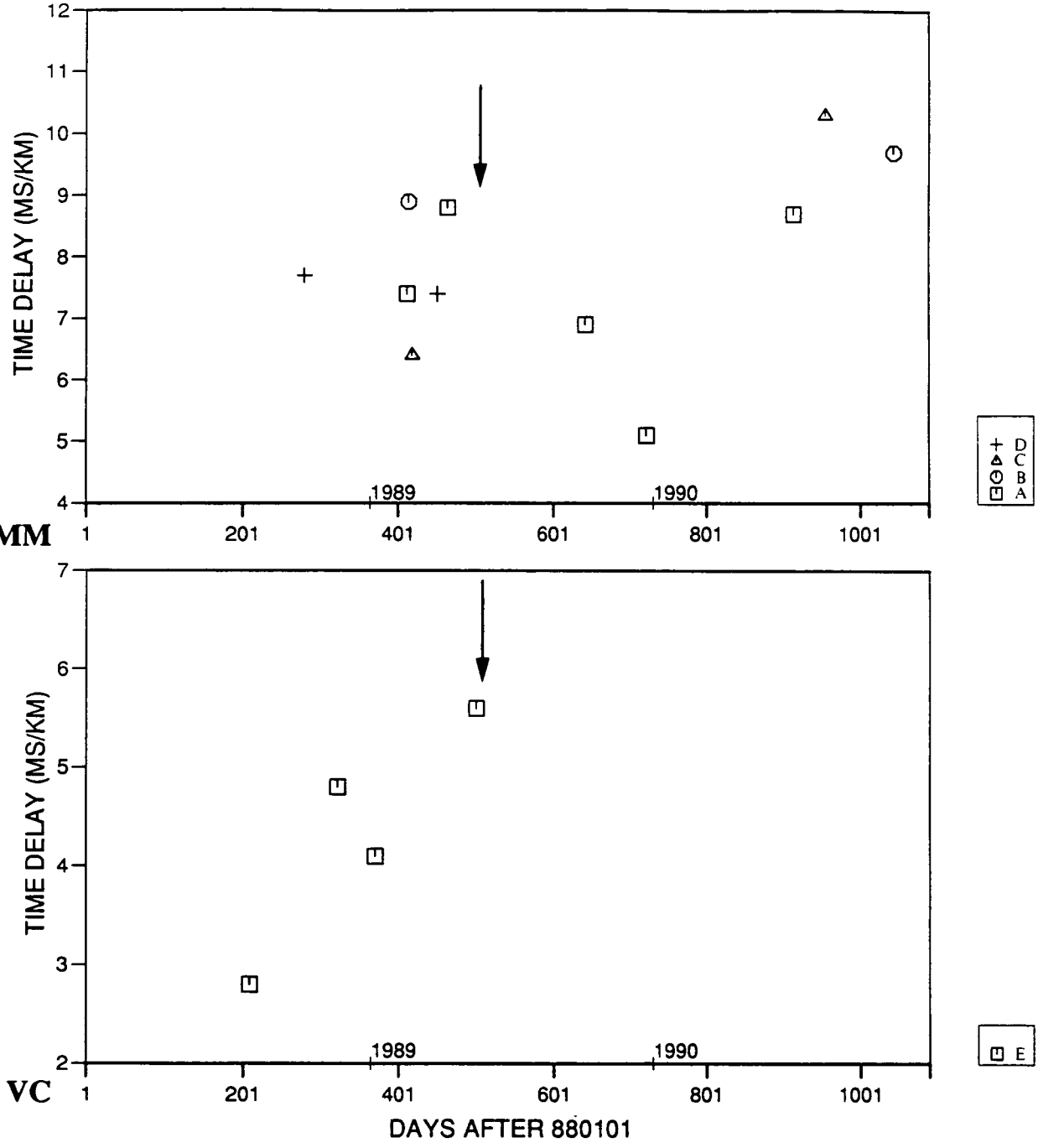

Figure 4.11 The variation with time of normalized time delays of the multiplets at stations MM and VC. Different symbols represent different groups of multiplets shown in the legend. An arrow marks the time when the M=4 earthquake occurred.

4.4.4 Significance of temporal change in time delays

The significance of the temporal change in time delays may be analyzed by the reliability of the estimated time-delays indicated by weight and the possible maximum error, which may be considered as experimental error. As discussed above, the estimate of errors can be obtained quantitatively when the time delay is derived by automated techniques. However, the error analysis for the method used in this study may only be performed on the basis of the data that have shown clear shear-wave splitting. In practice, the estimate of the errors of time-delays are only performed on the data that are of weight 1, because the errors are strongly dependent on the uncertainty of determining the onset time of the second arrival for the data of weight 2 and 3, as discussed in section 4.2.4. The errors may be caused by two circumstances. The first is the miscounting of sample intervals at the two extreme ends of the start time of the first and the second shear-wave arrivals. This can occur since both the fast and slow arrivals are superimposed on the *P*-wave coda and signal generated noise, respectively, and the energy of the initial arrival may not be large enough to produce an obvious abrupt change of motion and so become obscured. The second is the uncertainty in the correct start time of second split shear-waves because the second arrival might be marked by a start of an elliptical motion when the time delay is not large enough to separate the fast and slow waves completely. Under these circumstances, a measurement in samples of time-delays and its corresponding error may be estimated as:

$$N = 0.5[(N_{max} + N_{min}) \pm (N_{max} - N_{min})] \tag{4.8}$$

where N_{max} is the number of samples of possible maximum time-delays; N_{min} is the number of samples of possible minimum time-delays. Figure 4.12 shows the variation of normalised time-delays with time at stations MM and VC, with weight linearly applied from 1 to 3. It is seen that the majority of the data are of weight 2 (medium size), and the general variations of time delays with weight 1 (the largest size), 2 and

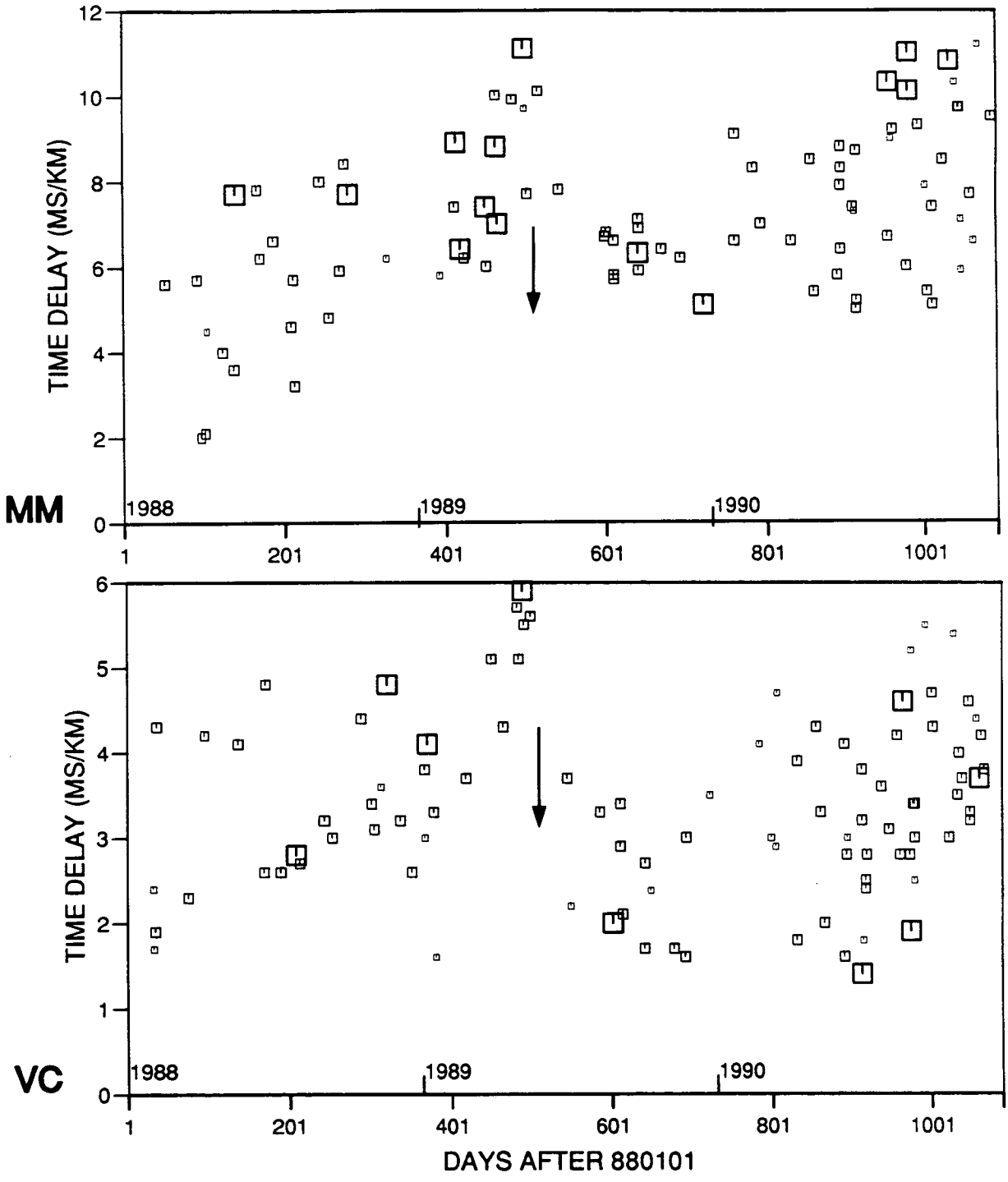

Figure 4.12. The variation with time of normalized time delays at stations MM and VC with the weight of the data from 1 to 3. The size of each square is inversely proportional to its weight as denoted in Figure 4.3, and an arrow marks the time of the M=4 earthquake.

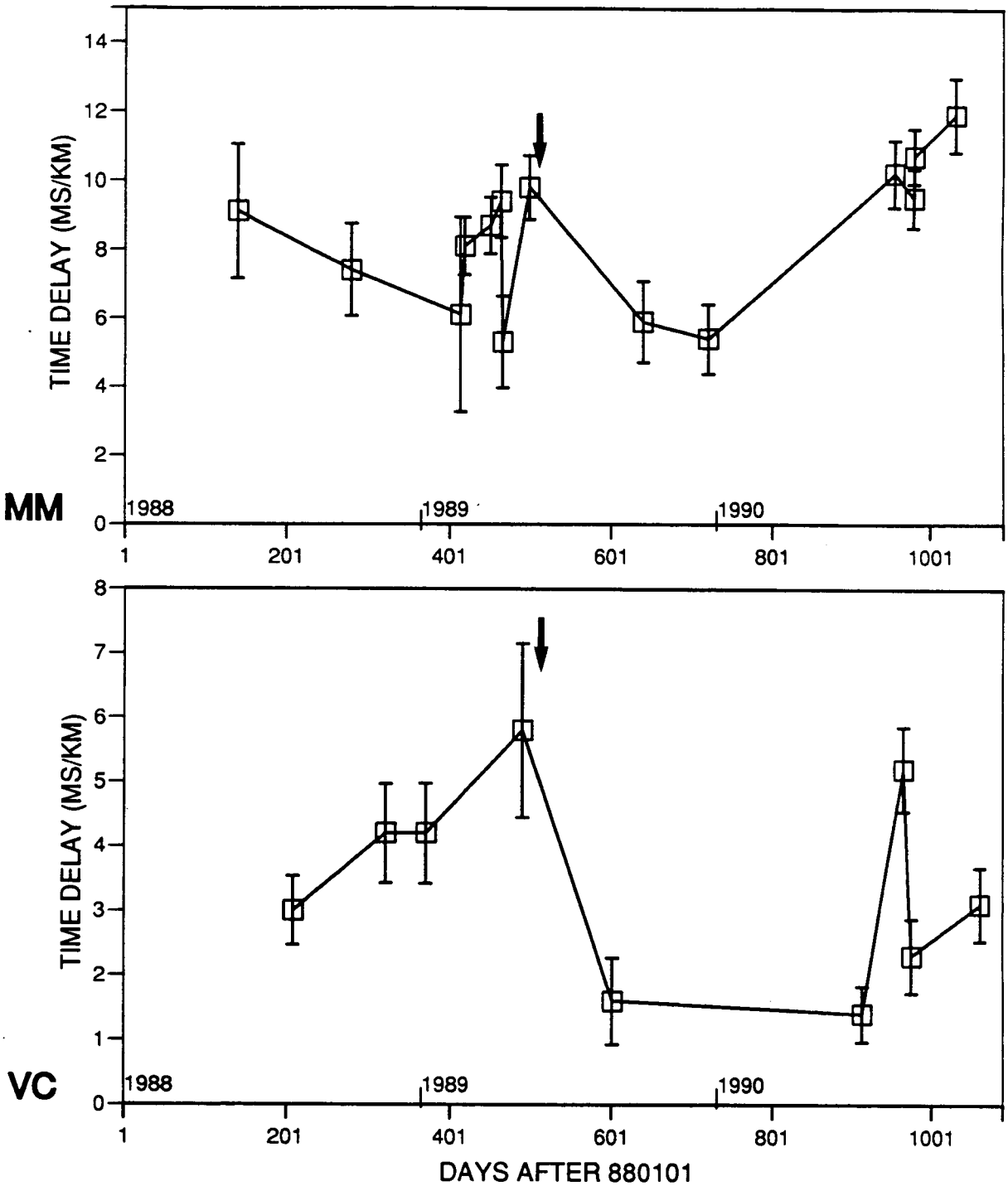

Figure 4.13 The variation with time of normalized time delays of the data of weight 1. Each error bar measures the possible maximum error for each event; the arrow marks the time when the M=4 earthquake occurred.

3 (the smallest size) are the same, except for the more scattered variations of delays with data of weight 3 at VC. Figure 4.13 exhibits the variations with time of normalised time-delays of the data with weight 1 and the corresponding possible maximum error for each measurement at stations MM and VC. Note here the time-delays presented in Figure 4.13 may not be the same values as presented in Figure 4.12 since the error analysis based on equation 4.8 was done independently after the shear-wave analysis as described in section 4.2.4 with the whole dataset. We can see that the possible temporal change in time-delays at MM and VC may be significant as indicated by the reliability of the data and their error bars before and after the M=4 earthquake. The earthquakes used in the error analysis are listed in Table AI-1, together with their corresponding seismograms and particle motion diagrams presented in Appendix I.

Since one and two standard deviations represent 68% and 95% confidence respectively, one and two standard deviations of 9 points moving average are calculated for stations MM and VC. Figure 4.14 shows the variation of time delays against time with a smooth curve of 9 points moving average and one (dense dotted lines) and two (dotted lines) standard deviations. The standard deviation of 9 points moving average is 0.972 and 1.61 for stations VC and MM, respectively. It is seen that the confidence is greater than 68% and less than 95% at VC; at MM, the confidence is about 68%, or maybe slightly lower. Therefore, the observations of an increase followed by a decrease in time delays is statistically significant at one standard deviation, and such temporal variation is associated with the time of the M=4 earthquake.

4.5 DEPTH EXTENT OF ANISOTROPY IN THE FAULT ZONE

Studies of the depth extent of seismic anisotropy (Kaneshima *et al.*, 1988; Kaneshima and Ando, 1989) have shown that the azimuthal velocity anisotropy is probably restricted to the top 10 to 15 km of the crust. However, their data did not allow them to reject the possibility that the anisotropy is concentrated in a much

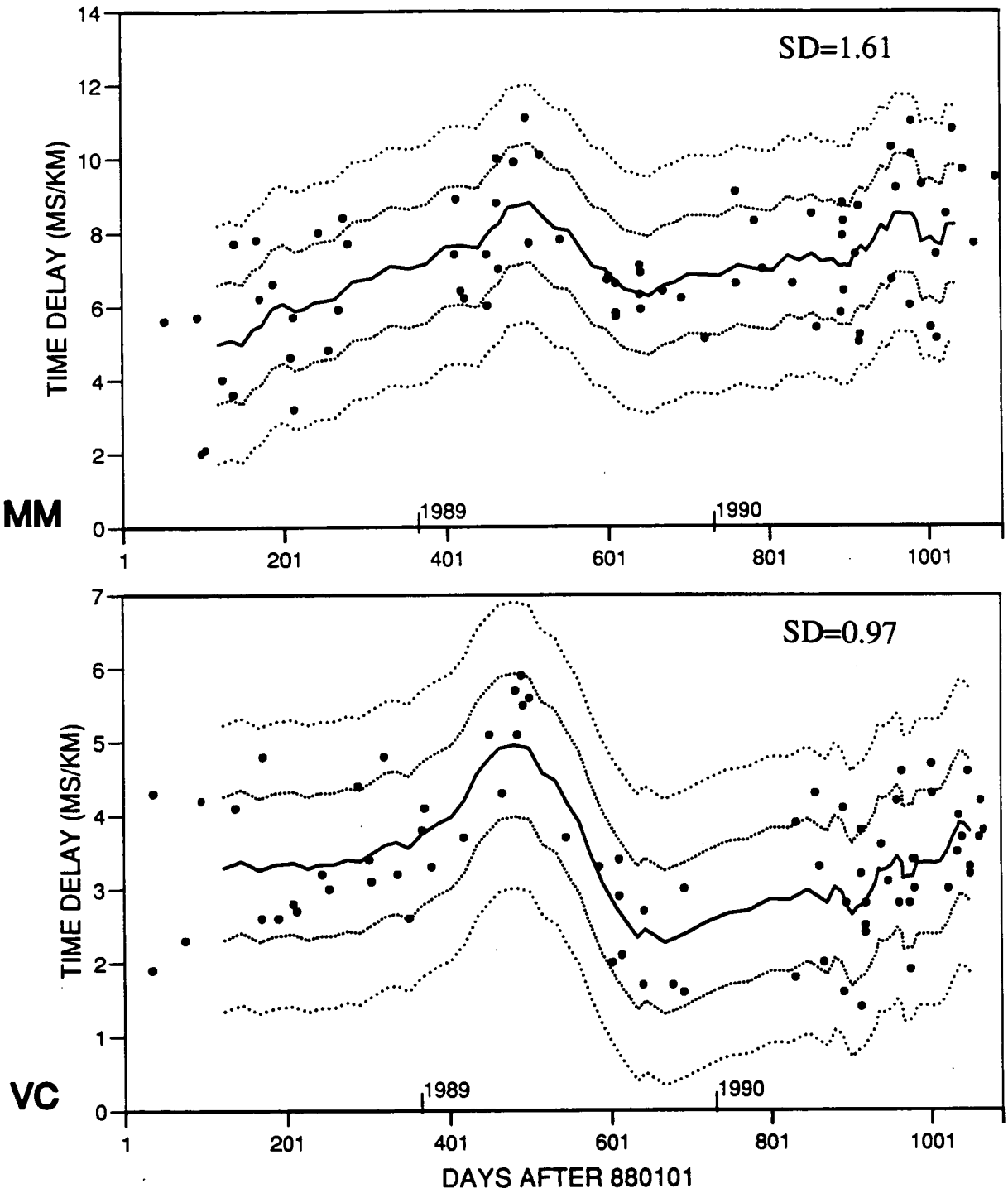

Figure 4.14. One (dense dotted) and two (dotted) standard deviation of a 9-point moving average (solid line) showing the confidence of temporal variation of Figure 4.8 at stations MM and VC. Statistically, one and two standard deviations represent 68% and 95% confidence, respectively. The numerical value of the standard deviation of a 9-point moving average is indicated at the upper right corner at each diagram.

thinner surface layer. Kaneshima (1990) correlated data from shear-wave splitting studies carried out in Japan, and suggested that the observed crustal anisotropy in Japan may be concentrated in the upper 15-25 km of the crust. Graham and Crampin (1993), in an examination of shear-wave splitting observed by the Turkish Dilatancy Project Network (Crampin and Booth, 1985), found evidence that shear-wave splitting was present in the lower crust with similar polarizations to those in the upper crust. Shih and Meyer (1990) have found clear evidence that split shear-wave delays increase with hypocentral distance, in the South Moat of Long Valley Caldera of California. However, Savage *et al.* (1990) found no evidence for pervasive anisotropy using stations located as close as seven kilometres to those used by Shih and Meyer (1990), and concluded that near-receiver anisotropy was dominant in their study.

Since the HRSN stations at Parkfield are closely spaced, the depth extent of seismic anisotropy may be confirmed from combinations of stations. Figure 4.15 presents the variations of normalised time-delays, which represent the degree of seismic anisotropy, with focal depth at stations MM, VC, ED and VR. Note station JN is omitted here because the correlation between time delays and hypocentral distance, shown in Figure 4.6 is weak. It is seen at station VC that delays are uniformly scattered, as would be expected if the anomalies in the temporal variation of time-delays shown in Figure 4.8 were caused by the decrease in focal depth. However, at stations MM, and VR, on the northeast block of the SAF, there are pronounced decrease of time-delays with focal depth, which means a decrease of focal depth would tend to increase the time delays. Station MM is about 0.5 km away from the SAF; and is probably on the transition zone of the fault between the fault gouge zone and the surrounding rocks, and the shear-waves used in this study actually sampled the medium of the fault zone (Li and Leary, 1990; Leary and Ben-Zion, 1992). The observed seismic anisotropy at MM will be attributed principally to the fractures or microcracks in the fault zone, and hence the termination of the SAF beneath MM may be indicated by the remarkable change of seismic anisotropy. It is seen that the normalised time-delays have a pronounced increase for earthquakes with focal depth above about 8 km at MM. The possible depth of 8 km is in broad

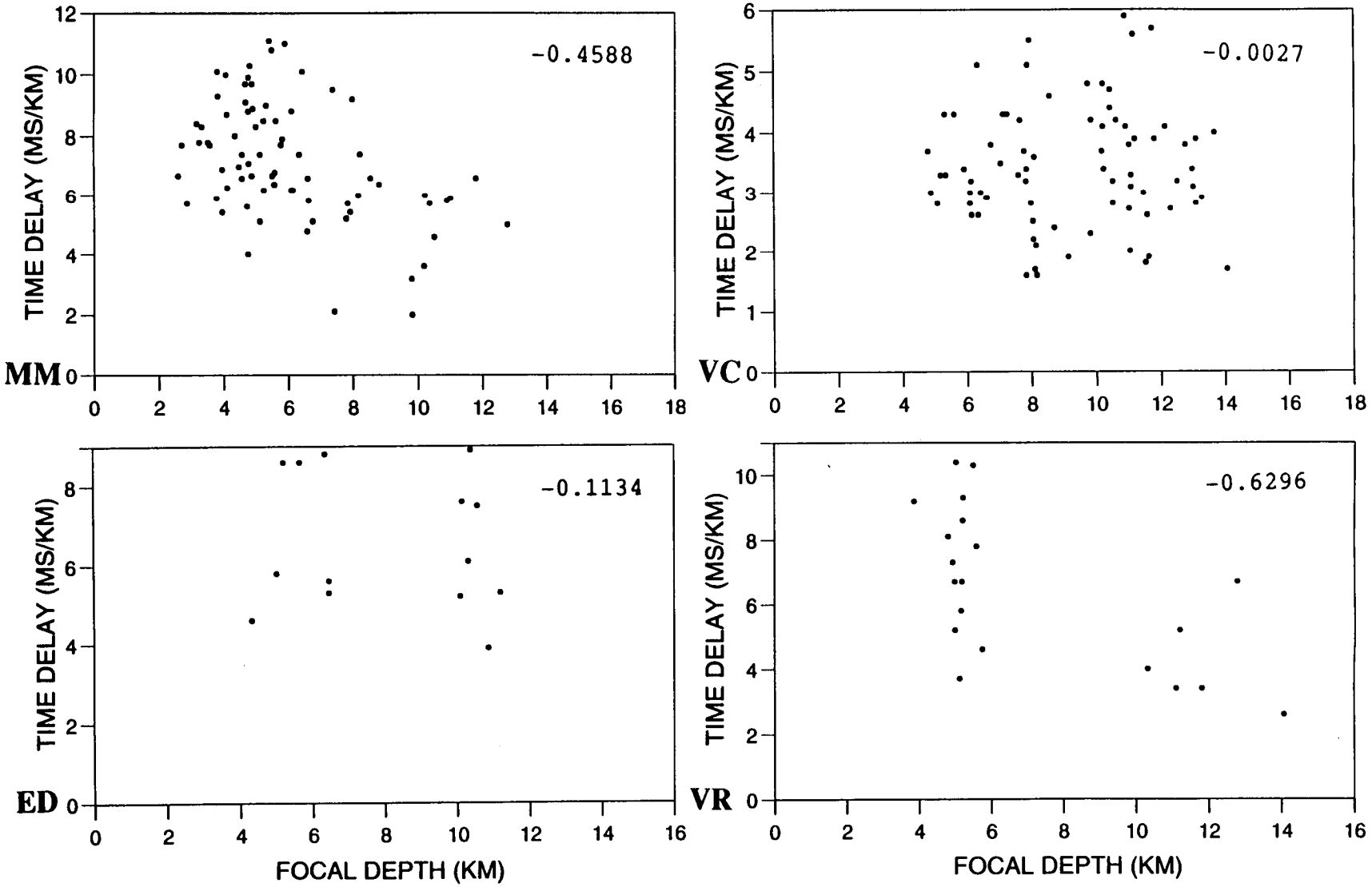

Figure 4.15. The variations of normalised time delays with focal depth at stations MM, VC, ED and VR. The weights of presented time delays are from 1 to 2. The correlation coefficient is indicated at the upper right corner at each station.

agreement with the results of Malin *et al.* (1989) and Li *et al.* (1992) who suggest that the fault gouge may extend from the surface to 10 km depth at the locked portion towards southeast of the Parkfield segment and about 5 km at the creeping portion towards the northwest of the segment in the fault zone. At station VR, there is a shortage of data at the range of depths between 6 and 10 km, but normalised time-delays below the depth of 10 km decline about 50% in comparison with average delays at the depth above 6 km, which means the differential shear-wave anisotropy beneath VR may be concentrated above the depth of 10 km. At station VC, on the southwest block of the SAF, the uniformly scattered distribution of normalised time delays means that shear-wave anisotropy extends to at least 14 km deep. I shall discuss this observation further in the next chapter.

4.6 CONCLUSIONS

I have presented the observations of shear-wave polarizations and time-delays between the fast and slow split shear-waves. The reliability and the significance of the observed temporal variations of time-delays have been examined independently by the study of earthquake multiplets, the analysis of possible maximum error and one and two standard deviations, respectively. The results of the observed seismic anisotropy, shear-wave polarizations and time delays, will be interpreted in the next chapter. Here I will summarise the observed phenomena and suggest conclusions.

The shear-wave polarizations at VC, ED and VR are aligned approximately NNE, which is approximately parallel to the direction of regional principal stress. Shear-wave first motions at station JN are aligned approximately North-South; at MM polarizations are probably controlled by the internal fault structure with an alignment of about N40°W, parallel to the fault.

Temporal variations of time-delays before and after the time of the M=4 earthquake have been observed at stations MM and VC. The study of the cluster of multiplets at MM shows an increase of delays before the time when the largest earthquake occurred and a decrease after it, as observed with whole dataset. At station

VC an increase in delays is apparent before the time when the largest earthquake occurred. The analysis of possible maximum error to the high quality data of weight 1 demonstrates that the temporal variation of time-delays is physically significant. Statistically, the temporal variation is significant at the 68% confidence, corresponding to one standard deviation. It has been seen that the normalised time-delays at MM are about twice as great as those at VC, which would be consistent with the fluid-filled microcracks and fractures within the fault zone being more extensive than in the surrounding crust.

The degree of seismic anisotropy, shown by the normalised time-delays, displays a significant decrease with focal depth at two stations MM and VR. Station MM is on the transition zone of the SAF. The clearly decreasing time delays below 8 km suggest that the fault gouge of the SAF may be terminated at the depth about 8 km beneath MM, and this is consistent with other studies. Beneath station VR, on the northeast block of the SAF, shear-wave anisotropy may be concentrated at the depths above 10 km. Beneath station VC, on the southwest block of the SAF, the differential shear-wave anisotropy extends to the depth deeper than 14 km.

CHAPTER 5

PARKFIELD: INTERPRETATION OF POLARIZATIONS AND POSSIBLE TEMPORAL CHANGE IN TIME DELAYS

5.1 INTRODUCTION

Shear-wave splitting, implying some form of effective elastic anisotropy, and observed along almost all shear-wave raypaths in the Earth's crust, has been interpreted as the effects of stress-aligned fluid-filled cracks, microcracks, and preferentially oriented pore-space. Such splitting is routinely observed in the shear-wave window above small earthquakes in a very wide range of igneous, metamorphic, and sedimentary rocks in a variety of tectonic regimes, and in reflection surveys, vertical seismic profiles (VSPs), reverse VSPs, and crosshole surveys in seismic exploration of sedimentary basin. Kaneshima (1990) and Crampin and Lovell (1991) are recent reviews of such observations. Variations in the stress-field may modify the geometry of the fluid-filled cracks (known as EDA-cracks), and as a consequence, temporal changes in the orientation and the differential of shear-wave splitting may occur, for example, Crampin and Booth (1989) identified changes in orientation of shear-wave polarizations induced by hydraulic pumping in a granite batholith, and there are several occasions that show the possible temporal change in time delays (Crampin *et al.*, 1990; Booth *et al.*, 1990; Liu *et al.*, 1993). However, there are some observations, for instance at station KNW at the Anza seismic network, Southern California, where there is an argument (Crampin *et al.*, 1991) about the interpretation. Peacock *et al.* (1988) speculated that the observation of shear-wave polarizations and temporal change in time delays at KNW might be the result of a build up of stress before an impending M=6 earthquake. This was further confirmed with more data (Crampin *et al.*, 1990), while Aster *et al.* (1990) studied the same dataset using automated technique and found no evidence of temporal variation of time delays. Note

here, some examples of delay times analysed by automated technique have been proven incorrect by Crampin *et al.* (1991). They interpreted shear-wave polarizations at KNW caused by palaeostrain alignment of fabric and/or microcracks (Aster and Shearer, 1992). Shear-wave polarizations near fault zones at most seismic stations in central California (Zhang and Schwartz, 1994) are aligned parallel or subparallel to the fault, almost normal to the maximum horizontal compressive stress direction. Similar observations also observed at several seismic stations in Japan (Kaneshima, 1990). In this chapter, I shall attempt to interpret the shear-wave splitting at Parkfield reported in the previous chapters, and investigate the other possibilities that could be associated with the observed temporal change in time-delays. I shall start with the factors that could affect the observed shear-wave polarizations.

5.2 EFFECTS ON SHEAR-WAVE POLARIZATIONS

5.2.1 Comparison of source polarizations

In an isotropic medium the shear-wave polarization recorded within the shear-wave window at a seismograph station should depend upon the source mechanism of the earthquake, modified only by interaction with internal interfaces and topography (Booth and Crampin, 1985; Liu and Crampin, 1990). However, shear-wave polarizations in anisotropic media typically exhibit parallel or subparallel alignment with the direction of maximum horizontal compressive stress. A number of studies (Crampin *et al.*, 1986; Kaneshima *et al.*, 1987; Gledhill, 1991; Zhang and Schwartz, 1994) have compared the differences between observed polarizations and those expected from earthquake sources, and have found that in general shear-wave polarizations are consistent with regional maximum horizontal compressive stress.

Here I examine 11 Parkfield earthquakes with sufficient arrivals to derive source mechanisms. I adopt a method which uses *P*- and *S*-wave relative amplitudes and polarities (Pearce, 1977; Pearce and Rogers, 1989) to determine fault plane solutions. The method and detailed studies of the source mechanisms are described in Appendix II. Six out of eleven events have well constrained solutions listed in Table

Table 5.1 Events for which well-constrained fault plane solutions have been derived.

No.	Date	Time	Latitude	Longitude	Depth	M_D	Strike	Dip	Rake
1	890218	0055	35.9500°	120.4930°	4.88	1.55	205°	75°	165°
2	890223	1807	35.9222°	120.4692°	5.55	1.56	25°	50°	140°
3	890327	1426	35.9747°	120.5308°	6.32	0.85	255°	60°	150°
4	890825	0408	35.9545°	120.5172°	8.05	0.73	165°	75°	165°
5	901110	1437	35.9470°	120.4918°	4.65	0.52	135°	60°	180°
6	900907	0915	35.9748°	120.5310°	6.41	1.09	60°	65°	145°

M_D: Coda-duration magnitude; depth is in kilometres.

5.1.

Errors could arise in determining fault plane solutions due to inaccuracy of hypocentre locations and calculated *P*-wave takeoff angles caused by differences between the true velocities of waves in the rocks at Parkfield and the assumed homogeneous one layer velocity model. Since the takeoff angles from the location files are not available, they are calculated by 180°-$\tan^{-1}(x)$, where x is the epicentral distance/focal depth. The lack of station coverage on the focal sphere may also affect the estimate of the fault plane solutions. Nevertheless, it is still useful to make general comparison of source and observed polarizations.

Figure 5.1 compares the theoretical shear wave radiation vectors at the source (Aki and Richards, 1980) with the observed polarization vectors at the indicated stations. The equal-area projections of upper hemisphere are plotted out to 45° of angle of incidence. Since fault plane solutions are derived from *P*- and *S*-wave relative amplitude method (Pearce, 1977; Pearce and Rogers, 1989), rather than conventional method of using *P*-wave polarity, the fault plane solutions presented in Figure 5.1, on the left, are plotted without stations that were used in determining the fault plane solutions. The detail studies of source mechanisms are presented in Appendix II. It is seen that both direction and polarity of the observed shear-wave polarizations show a marked difference from the theoretical radiation vectors of the shear waves for each earthquake mechanism. Shear-wave polarizations for these events are reliable since these events are of high signal-to-noise ratio and show clear shear-wave splitting. This suggests that anisotropy of the medium through which seismic waves propagate probably control the orientation of the first motion of the shear-waves, and modelling the polarization of the shear-waves may provide further evidence of such interpretation.

5.2.2 Possible near-surface and near-source effects

The geometry of cracks in near-surface layers, caused by the particular stress configuration, may be different from that below the surface layer (Crampin, 1993).

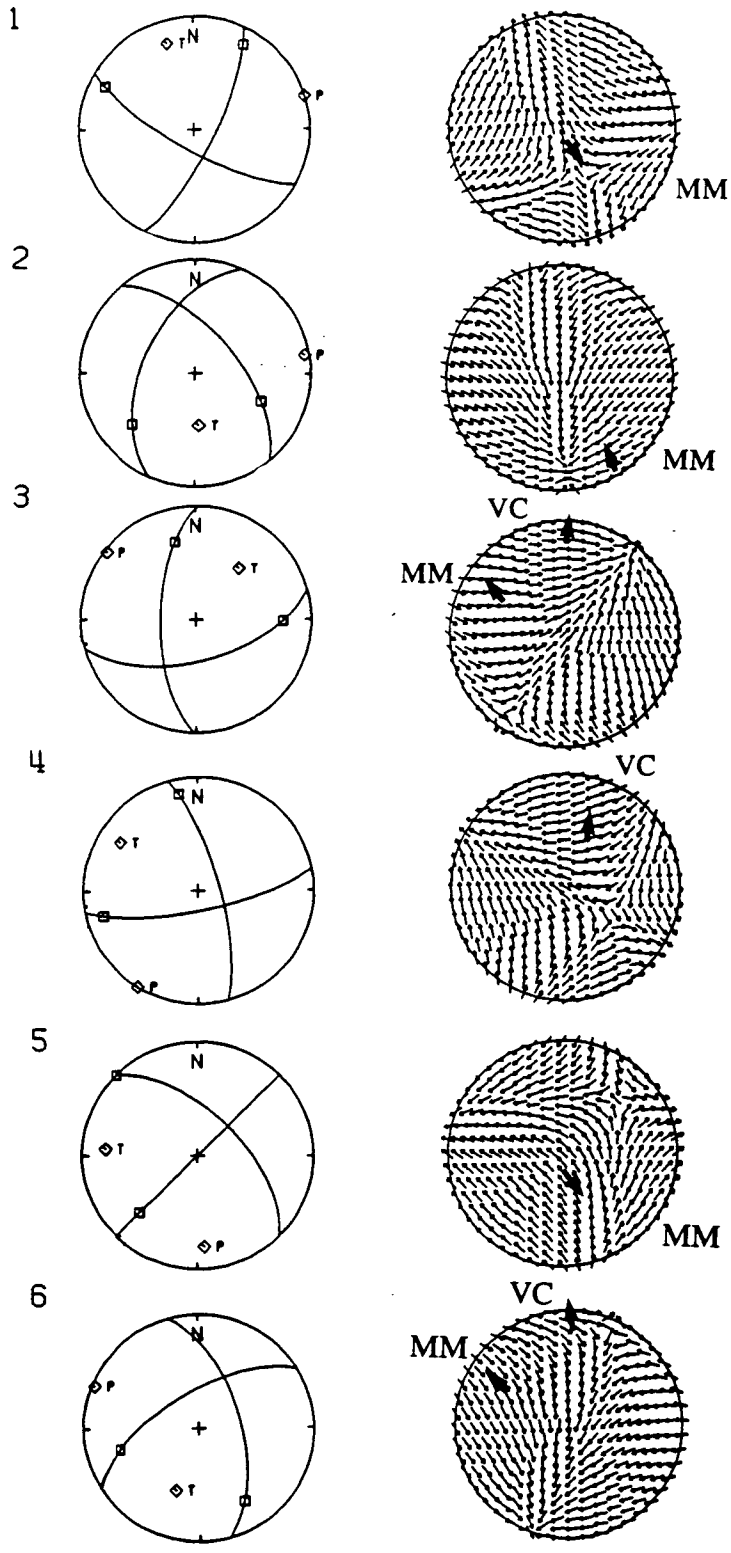

Figure 5.1. Comparison of theoretical shear-wave radiation vectors at the source with the observed shear-wave polarizations marked by the heavy arrows at the indicated stations. The equal-area projection of upper hemisphere is plotted out to 45° of angle of incidence.

The behaviour of split shear waves may be distorted by near-surface crack anomalies. Similarly, the geometry of the cracks in the vicinity of a source may also differ from that in the upper crust due to the stress concentration, so that the polarizations of the split shear waves inside and outside of the source regions may be well different. As a result, multiple shear-wave splitting and converted shear waves, *P* to *S*, may be generated at the boundary of the source region. However, for a sufficiently small earthquake the source region containing the anomalous cracks will be small, and the original split shear waves in the vicinity of the source will by dominated by the split shear waves in the upper crust.

Yao and Xiong (1993) have calculated synthetic seismograms for both near-surface and near-source effects to compare with those for a half-space. They found that the major features of the shear-wave splitting for the three cases are almost the same. They noticed that when the time delays produced in a thinner layer is shorter than a quarter of the visual period of the incident shear-wave, further splitting in the thinner layer will be merged with the incident split shear waves at the bottom of the thinner layer. Since 98% of the earthquakes used in this study are small earthquakes with M<2.0, and they were recorded at depths of 200 to 300 m, shear-wave splitting is expected to be less affected by both near-source and near-surface effects than in many previous studies.

5.2.3 Other effects: surface topography, site effect and instrumentation

It has been found that the effect of the surface topography is particularly important for free-surface recording (Kaneshima *et al.*, 1987; Chen *et al.*, 1987). At Parkfield, the dominant frequency of shear-waves is about 20 Hz, but the depths at which the seismometers were buried between 200 m and 300 m is probably not sufficiently deep to remove the effects of surface topography (Shearer and Orcutt, 1987). This could cause misinterpretation of the first arrivals of the shear waves by focusing reflected waves if there exists an appropriate variation of topography near receivers. In Figure 2.3 of Chapter 2, I have shown that the surface topography within

a few hundred metres of each station is relatively smooth and flat apart from at station ST. Consequently, shear-wave signals are not expected to be distorted by surface topography at stations other than ST.

Site effects on borehole recordings, discussed in Section 3.5, may be another source that distorts shear-wave polarizations. In practice, the effects of these anomalies can be reduced to a certain extent simply by discarding poor quality data. However, the effects could be much stronger at some specific stations (see Section 5.3.1 below).

The HRSN borehole seismometers are General Earthquake Observation System L22E products, which have the function of self-calibration. The relative calibration of the instruments has already been investigated in Section 3.3.1. It is expected that the relative calibration of sensors are accurate in the field over the frequency bandwidth for which the input signal is above background noise. Thus, It is concluded that the observed phenomenon of shear-wave splitting is not likely to be affected by the instruments.

5.3 INTERPRETATION OF SHEAR-WAVE POLARIZATIONS

The shear-wave splitting phenomenon has been observed at all stations of the Parkfield HRSN network. At MM, shear-wave first motion is polarized parallel to the SAF fault; at JN, the direction of polarizations is approximately North-South; at stations VC, ED and VR, polarizations are aligned in the direction parallel or subparallel to the maximum horizontal compressive stress direction at central California; and at the other two stations ST and FR, very scattered orientations are observed. In this section I shall interpret the polarizations observed at each station.

5.3.1 Shear-wave polarizations at stations ST and FR

Shear-wave first motions at stations ST and FR, southwest block of the SAF, are very scattered. The geology on the southwest side of the SAF consists of Gablian plutonic and metamorphic basement rocks covered by a maximum of 2 km of Tertiary

and Quaternary sediments. These deposits generally dip away from the Cholame Hills high, on which station VC located and where polarizations display a good alignment. There are 47 (20%) out of 233 and 78 (63%) out of 124 earthquakes that share the same events within the shear-window at VC and at stations ST and FR, respectively. Figure 5.2 (a) shows locations of the earthquakes common with VC at stations ST and FR, and comparison of shear-wave polarizations corresponding to these events at (b) ST and VC, and (c) VC and FR. It is seen that the scattered polarizations at ST and FR are not observed at VC. Since surface topography at station ST is relatively irregular, as shown in Figure 2.3, the scattered polarizations observed at ST are thought to be caused by either local topography or inhomogeneity of the sediments beneath the station, or both. At Station FR the scattering of the polarizations is likely to be caused by the inhomogeneity of the sediments beneath the station. This could produce the complicated scattering wave-field characterized as a large amplitude *P*-coda wave, and/or the topographic irregularities of the subsurfaces of the sediments, which in turn could alter the internal shear-wave window (Liu and Crampin, 1990), and hence distort the shear-wave polarizations. On the other hand, as I have shown in Section 3.5, site effects such as the near-surface geology at the receiver site and reflected downgoing waves may be partly responsible for the greatly amplified *P*-coda waves, which interact with the first shear-wave arrivals and therefore distort the shear-wave polarizations at both ST and FR.

5.3.2 Shear-wave polarizations at stations VC, VR, ED and JN

Shear-wave first motions are aligned approximately in directions between N20°E and N30°E at stations VC, VR and ED, and about N5°E at JN. These large angles to the SAF are approximately parallel or subparallel to the direction of maximum horizontal principal stress near the SAF in central California (Zoback *et al.*, 1987). Station VC is about 5 km away from the SAF, on the southwest block. ED, VR and JN are about 0.7 km, 1 km and 3.5 km from the fault, respectively, on the northeast side. The local geology on the either side of the fault is entirely different

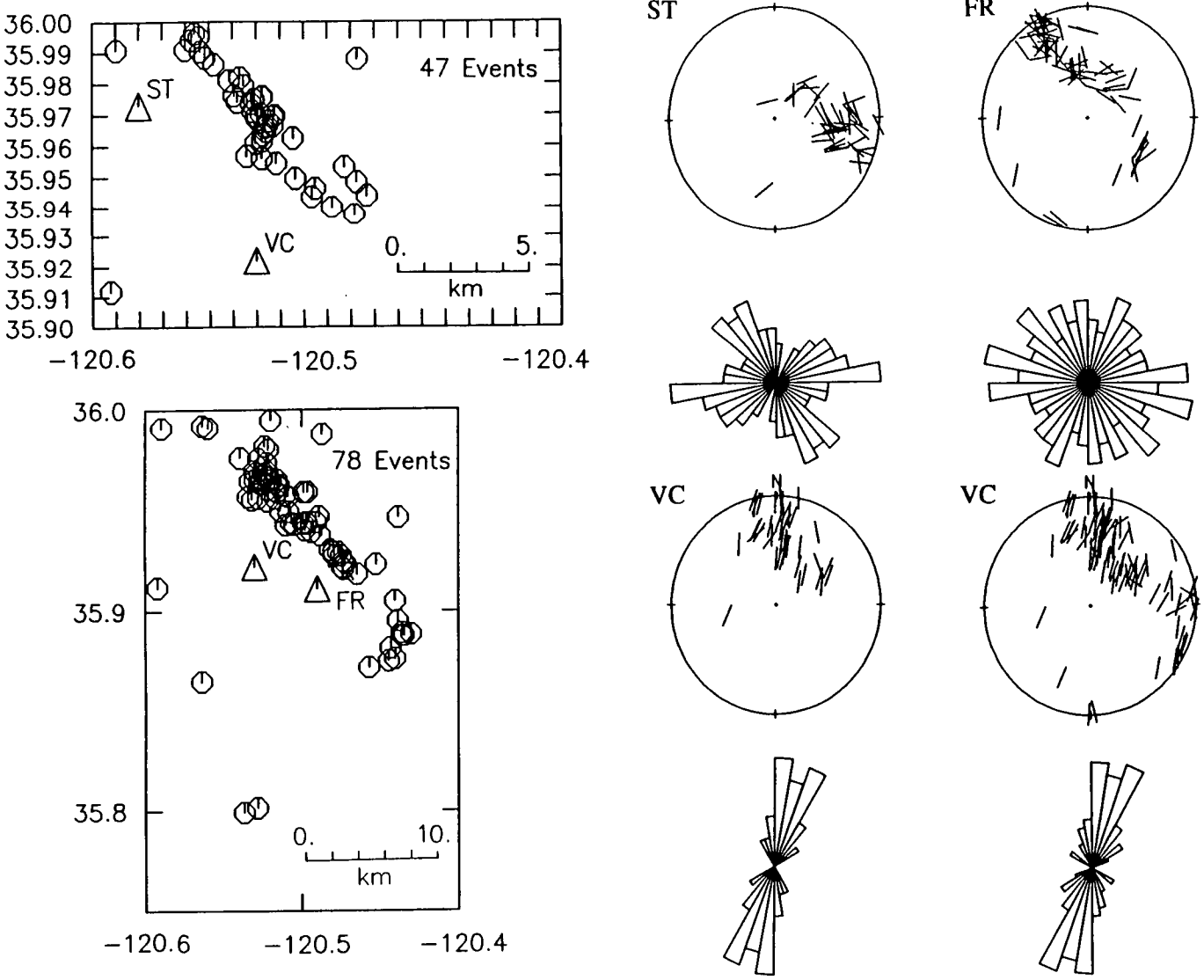

Figure 5.2. (a) The locations of the events common to stations ST and VC, and VC and FR; and comparison of polarizations of these events at (b) ST and VC, and (c) VC and FR. The polarizations are displayed as equal-area projections and equal-area rose diagrams.

(Chapter 2). However, the polarizations of the first split shear waves are observed to display an essential common pattern indicating that the cause is undoubtable not local geology.

As many studies have suggested (Crampin *et al.*, 1986; Kaneshima *et al.*, 1987; Peacock *et al.*, 1988; Gledhill, 1990, and in Section 5.2.1 of this chapter) the alignment of shear-wave polarizations is not due to the source polarizations, and is unlikely to be caused by all other effects discussed above. It could be attributed to the effective anisotropy of stress-aligned vertical inclusions. Shear-wave polarizations appear in most cases to be aligned parallel to the direction of local maximum horizontal compressional stress or, perpendicular to the minimum horizontal stress direction which is expected to control the orientations of fluid-filled inclusions in the crust (Crampin and Atkinson, 1985). Note that such parallelism constrains the type of anisotropic symmetry to hexagonal symmetry with a horizontal or subhorizontal symmetry axis. This strongly suggests a distribution of subparallel vertical cracks as the source of the anisotropy since such a structure is the only common source of hexagonal symmetry found in the crust (Crampin, 1993). I have offered in Section 1.1.2 the five possible causes of shear-wave splitting. They are direct stress-induced anisotropy; aligned crystals; lithologic anisotropy; structural anisotropy; and stress aligned crack-induced anisotropy.

Direct stress-induced anisotropy has to be rejected as the cause of the observed shear-wave splitting because the stresses required to cause anisotropic effect in seismic wave propagation are too great to produce observable seismic anisotropy in the Earth (Dahlen, 1972). All other possibilities except stress aligned crack-induced anisotropy are also rejected because on the southwest block of the SAF, beneath VC, there is no evidence of crystalline rocks of aligned minerals or rock fabrics. The basement of granite rocks is covered by maximum 2 km marine and nonmarine sedimentary and volcanic rocks of Tertiary and Quaternary ages. These stratified sedimentary rocks are tightly folded along northwest-trending axes near the SAF, but a mile or so away from the fault zone the folds are open (Brown *et al.*, 1967). Therefore, the N20°-30°E alignment of the shear-wave polarizations at VC can not be interpreted by the

possibilities of aligned crystals, lithologic anisotropy, with a horizontal symmetry axis, and structure anisotropy, but only stress aligned crack-induced anisotropy. Furthermore, in seismic exploration modelling including reflection surveys, VSPs and reverse VSPs (reviewed by Crampin and Lovell, 1991; Crampin, 1993), the assumed model that parallel vertical water-filled (EDA) cracks are responsible for the effective shear-wave anisotropy allows the observed seismograms and shear-wave polarizations to be matched well with the synthetic data. Modelling shear-wave waveforms and polarizations with earthquake sources performed in this study in Section 5.5 also support this model.

On the northeast block of the SAF, beneath stations ED and VR, there is evidence of a far more complex geologic history. Crystalline rocks of varied composition and origin that crop out along the northeast side of the SAF are probably slivers enclosed by older branches of the SAF. Structure relations in the northeastern block are complex. The rocks are moderately to strongly folded along northwest-trending axes. The intensity of deformation increases towards the southwest, and near the SAF overturned folds and folded structural trends are common (Brown *et al.*, 1967; Eberhart-Philips and Michael, 1993). However, none of the crystalline formations or structural deformations are trending in the direction of N20°-30°E. Thus stress aligned crack-induced anisotropy is probably the only possible interpretation of the shear-wave polarizations at stations ED and VR.

Station JN is located on the Table Mountain Fault, northeast block of the SAF. The 20°-30° deviation of the polarizations with respect to VC, VR and ED is probably due to local geologic structure. The Parkfield syncline is located between the Gold Hill fault, which is subparallel to the SAF, and Table Mountain fault (Figure 2.1). Seismic waves received at JN will penetrate the southwest wall across the axis of the syncline (Eberhart-Phillips and Michael, 1993), which means steeply dipping sediment layers towards the southeast will bend wavepaths and effectively enlarge the shear-wave window at the interfaces, known as the internal shear-wave window (Liu and Crampin, 1990). Figure 5.3 is the schematic diagram showing the enlarged shear-wave window at the dipping interfaces ($\alpha_e > \alpha$). Where α is the predicted angle of incidence

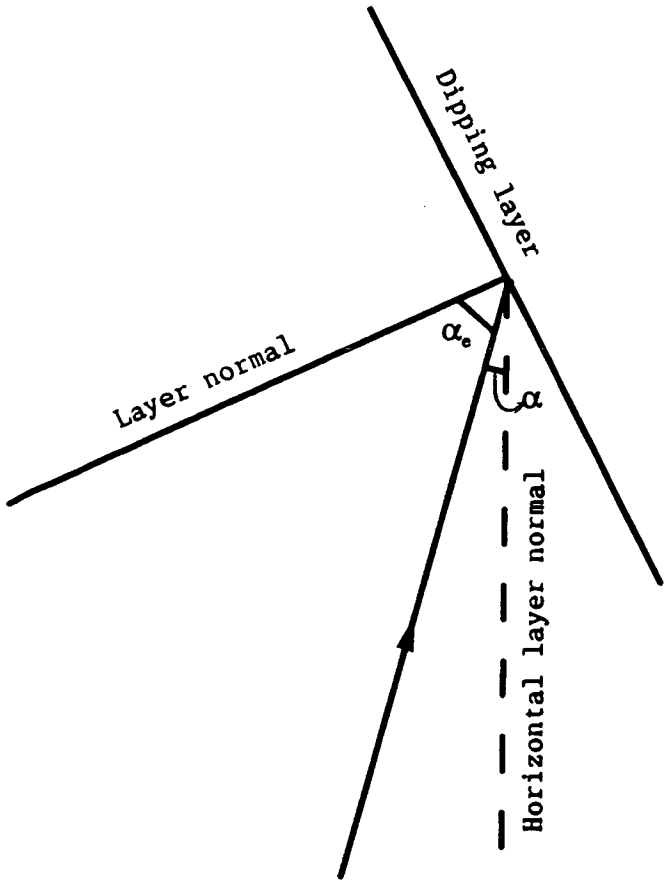

Figure 5.3. Schematic diagram showing the enlarged shear-wave window at the dipping interfaces. Note that the angle of incidence changes from predicted α (assuming horizontal layers) to α_e, which is the effective angle of incidence, where $\alpha < \alpha_e$.

calculated by $\tan^{-1}(x)$, x is epicentral distance/focal depth; α_e is the effective incidence. In some cases, subsurface topography could cause parallel polarizations to be systematically rotated by up to 90° (Chen *et al.*, 1987; Graham and Crampin, 1993). This is likely to be the reason why shear-wave polarizations observed at JN are rotated systematically by approximately 20° to 30°.

5.3.3 Shear-wave polarizations at station MM

Shear-wave first motions at MM show pronounced alignment in the direction of N40°W, approximately parallel to the SAF. If we accept the hypothesis of shear-wave splitting caused by aligned fluid-filled EDA-cracks, the polarizations at MM suggest that the cracks' strike is parallel to the fault. Studies of shear fracture failure suggest the development of fault parallel or subparallel fractures (King, 1983; Wang and Sun 1990), and observations of the shear-waves polarizations especially associated with fault zones, such as at seismic station KNW on the San Jacinto Fault, California (Crampin *et al.*, 1990) and seismic stations in the Loma Prieta segment of the SAF for the shear-wave anisotropy study of aftershocks of the 1989 Loma Prieta earthquake (M_w=7.0) (Zhang and Schwartz, 1994) show the same result.

Station MM is situated immediately in the vicinity of the SAF. 95% of the shear-waves from the earthquakes recorded within the shear-wave window (taken as 45°) at this station propagate within an angle of less than 15° to the proposed vertical crack plane. The average width of the fault-gouge of the SAF in the Parkfield segment varies from 200 to 400 m, with about 400 m of transition zone on both sides of the fault (Li and Leary, 1990; Leary and Ben-Zion, 1992). Thus the internal structure of the fault (fault-gouge and transition zone), and its nearby subparallel folds and crystalline rocks (Brown *et al.*, 1967) are probably dominant factors in the shear-wave polarizations beneath this station. It is likely that the gouge of the fault zone plays the most significant role on controlling shear-wave polarizations at MM.

5.4 SCATTERING OF POLARIZATION ALIGNMENTS

There are five out of seven stations showing essentially parallel alignments of shear-wave polarizations. The cause of the alignment is interpreted as due to propagation through the fluid-filled vertical parallel EDA-cracks in the upper crust. The scattered alignments at stations MM, VC, JN, ED and VR, which are obviously second order of disturbances, are likely to be due to seismic wave scattering by an irregular subsurface topography. This has been investigated in a number of studies (for example, Boore *et al.*, 1981; Ohtsuki and Harumi, 1982). Existing theoretical models of scattering by topographic irregularities do not yet permit prediction of scattering effects in complicated terrain, but it has been generally agreed that such effects are the largest when the incident wavelengths are comparable to the dimensions of the topographic features (Booth *et al.*, 1985). In such cases, components of the incident shear-wave motion may be amplified, or attenuated, and result in different alignment of shear-wave polarizations.

5.5 SYNTHETIC SEISMOGRAMS

I attempt to model the observed seismograms using synthetic seismograms with an aim of examining my interpretation of shear-wave polarizations. Since synthetic seismograms are calculated in displacement, whereas observed data are velocity recordings at Parkfield, therefore, for the consistency of a comparison, I first convert the velocity records to displacement records.

5.5.1 Integration of velocity traces

The integration is performed in the frequency domain, where it is a simple multiplication manipulation, given by the following general equation:

$$F'(\omega) = iF(\omega)/\omega \tag{5.1}$$

where ω is the angular frequency, i is the imaginary unit, and $F(\omega)$ and $f(t)$ are Fourier transform pairs related through the equation:

$$f(t) = (1/2\pi)\int F(\omega)\exp(-i\omega t)d\omega$$

in the time domain (Bracewell, 1965). $F'(\omega)$ is Fourier transform of displacement. Since the right hand side of equation (5.1) is divided by ω the integration of the velocity seismograms has a severe low-pass filtering effect on the signals. However, the comparisons of the shear-wave polarizations measured on velocity and predicted velocity recordings calculated from acceleration seismograms of rockbursts (Graham, *et al.*, 1991) have shown that this filtering has very little effect on the observed polarization directions of the shear-waves. Figure 5.4 compares the seismograms and particle motion diagrams of the velocity and the calculated displacement records of events 4 and 5 (in Figure 5.1). The directions of polarizations are marked by small arrows on the particle motion diagrams on both velocity and displacement records. It is seen that shear-wave polarizations remain unchanged although the low-pass filtering effect has altered the waveforms and the pattern of the particle motions. This effect probably explain the mismatch of the waveforms between the calculated displacement record and the synthetic seismograms of event 5 in the following section.

5.5.2 Modelling

Events 4 and 5 of Figure 5.1 recorded at stations VC and MM, respectively, are modelled by assuming that water-filled parallel vertical (EDA) cracks are responsible for the observed polarization alignment. The anisotropic reflectivity technique (Booth, 1982; Booth and Crampin, 1985) is used, together with derived earthquake double couple sources. The elastic constants for the cracked medium are derived using the method of Hudson (1980, 1981) for thin liquid-filled cracks in an intrinsically isotropic background solid. Figure 5.5 shows the variations of body waves in the modelled anisotropic media for events 4 and 5 respectively. Stations are

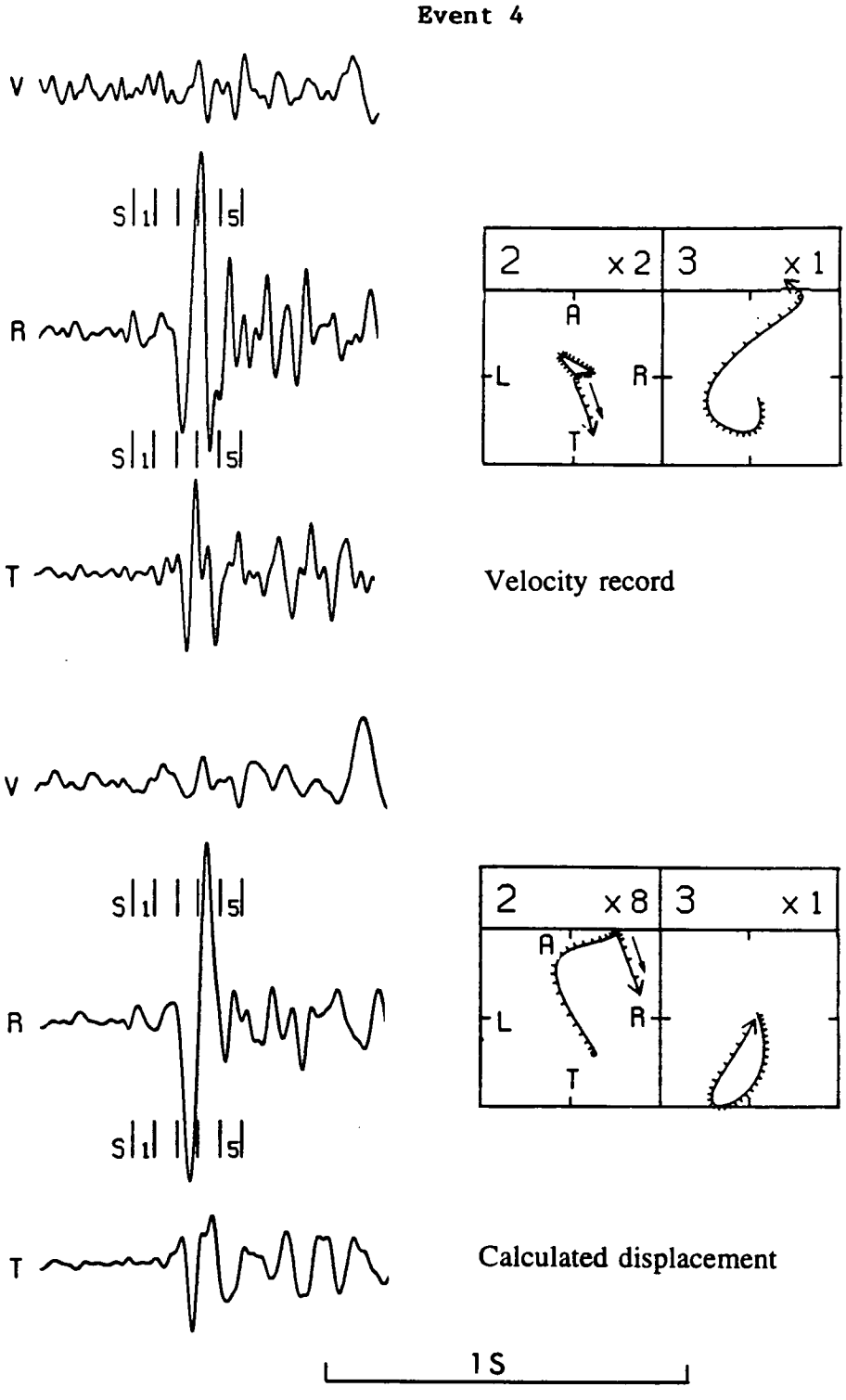

Figure 5.4. Comparison of seismograms and particle motion diagrams for the velocity and the calculated displacement records of events 4 and 5 in Table 5.1. Each time window represents 60ms. Small arrows indicate the direction of shear-wave polarization.

Event 5

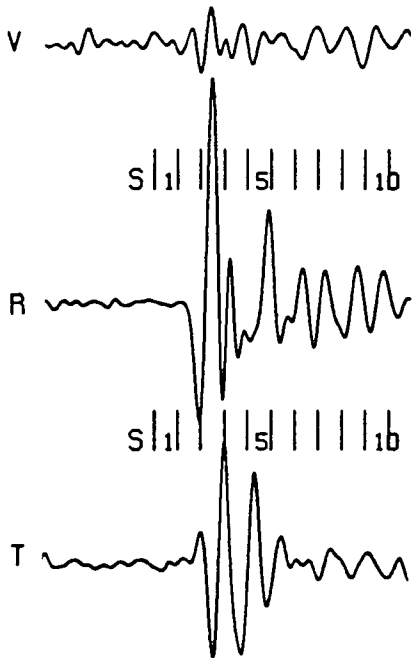

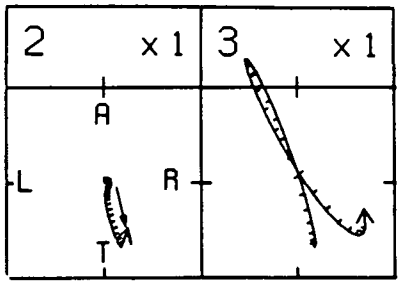

Velocity record

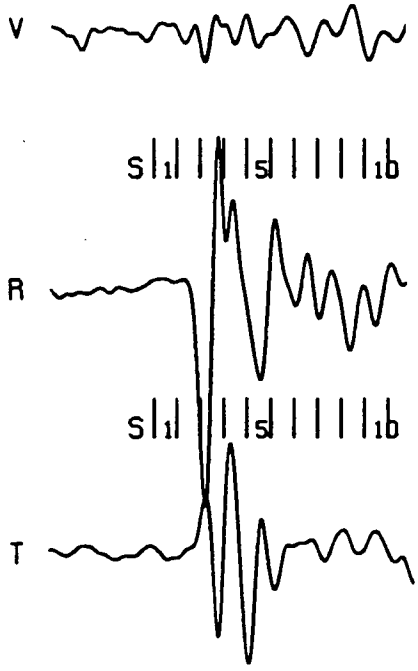

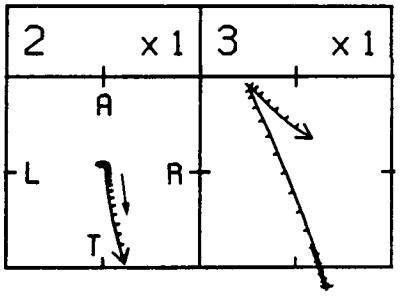

Calculated displacement

(Figure 5.4 continued)

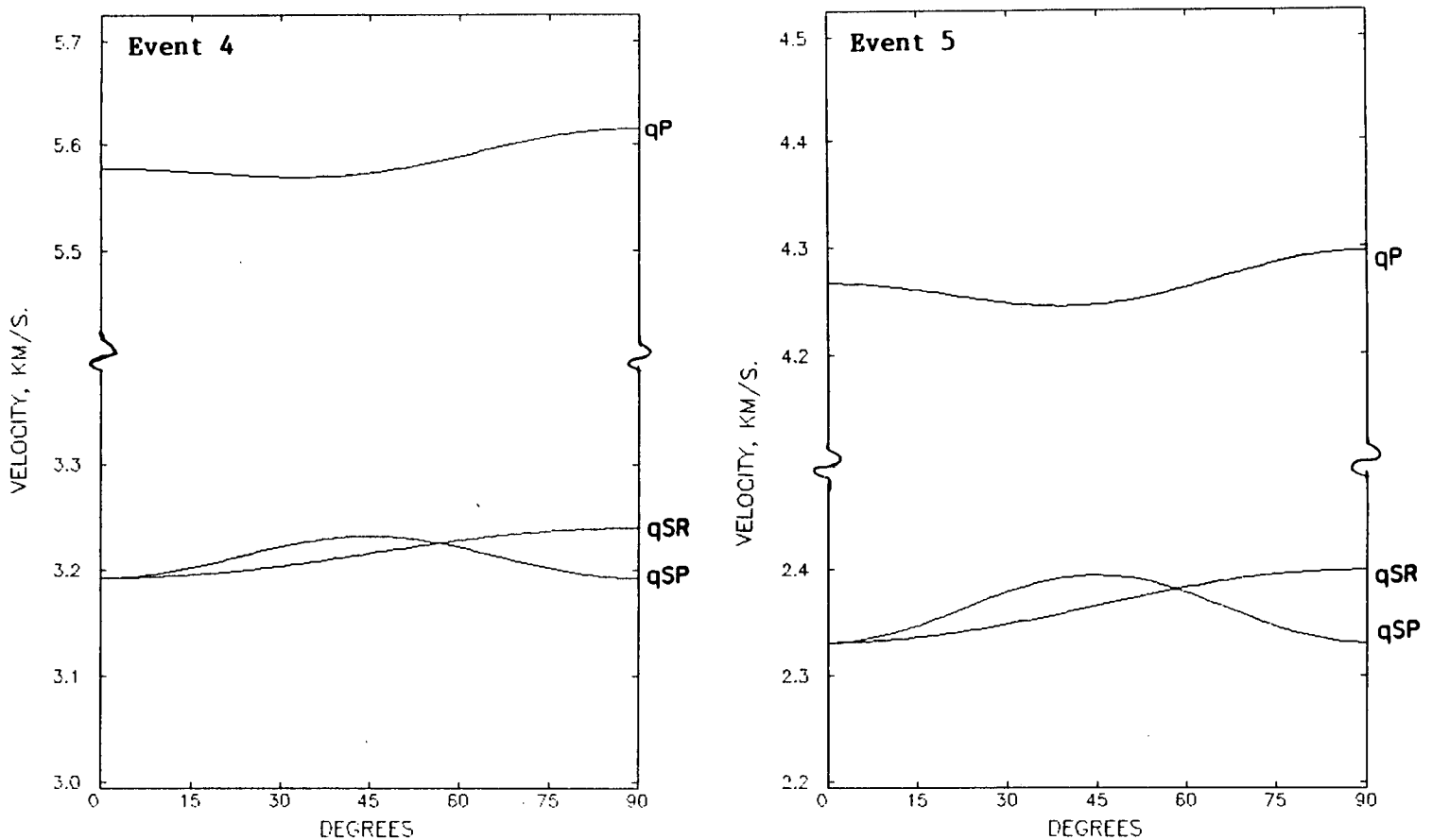

Figure 5.5. The angular variation of body wave velocities in the modelled anisotropic medium for events 4 and 5, respectively. For the isotropic rockmass, Vp=5.62km/s, Vs=3.24km/s, ρ=2.39g/cm^3, and crack density equals 0.013 for event 4; Vp=4.30km/s, Vs=2.40km/s, ρ=1.9g/cm^3, and crack density equals 0.026 for event 5.

Table 5.2 Parameters of models for synthetic seismograms.

	Event 5 at MM	Event 4 at VC
Observed Depth	4.65 km	8.05 km
Azimuth to Station	340°	203°
Epicentral Distance	1.00 km	3.80 km
Observed S-wave Polarization	143°	187°
Focal Mechanism: Strike, Dip, Rake	150°, 65°, 175°	330°, 75°, 165°
Dominant Frequency of Shear Waves	10 Hz	10 Hz
Model:		
Layer Thickness	4.65 km	8.05 km
Type	Anisotropic: Vertical Aligned Cracks, Crack Density: 0.026 Strike: N143°E	Anisotropic: Vertical Aligned Cracks Crack Density: 0.013 Strike: N187°E
Density	1.9 g/cm^3	2.39 g/cm^3
Vp, Vs	see Figure 5.5b	see Figure 5.5a
Halfspace		
Type	Isotropic	Isotropic
Density	1.9 g/cm^3	2.39 g/cm^3
Vp	4.30 km/s	5.62 km/s
Vs	2.40 km/s	3.24 km/s

assumed to be at the free surface, but its effect has been ignored. The source is located at the top of the lower isotropic halfspace; and seismic waves generated from the source propagate through a homogeneous anisotropic medium. The parameters used in the modelling for the two events are listed in Table 5.2.

The choice of events to model are restricted to those in Figure 5.1, since these events are simple in waveform and there are clear shear-wave arrivals and well-constrained fault plane solutions at stations MM and VC. Events 4 and 5 are selected for VC and MM, respectively. A adjustment has been made for fault plane solutions at both stations in order to improve the match of relative amplitude of the synthetic seismogram at MM for event 5 and the polarity of the synthetic seismogram at VC for event 4, respectively. Figure 5.6 is the adjusted focal mechanisms and the radiation patterns of the shear waves for events 4 and 5. The observed polarizations are superimposed on the theoretical radiation pattern. Figure 5.7 compares the synthetic and calculated displacement seismograms at station MM for event 5 and station VC for event 4. The small arrows mark the directions of the polarizations. It can be seen that the major features of the shear-wave waveforms are matched at VC on event 4, and polarizations can be modelled accurately for both events. The waveform on radial component of event 5 could not be matched well. This is probably due to the low-pass filtering effect when integrate velocity record to displacement record. The distortion of the waveform can been seen in Figure 5.4 on event 5. Note that the sampling rate is not the same as that of the observed data as the theoretical calculation of the frequency of the source pulse is a function of the window length and the number of data points. My intention here is to model the waveforms and polarizations, thus time delays are matched by estimating the time interval between the first and second arrivals in the windows. There appears to be about 2.6% (CD=0.026) and 1.3% (CD=0.013) differential shear-wave anisotropy at the site of MM and VC, respectively. These are within the limits of shear-wave anisotropy expected for intact rocks (Crampin, 1994).

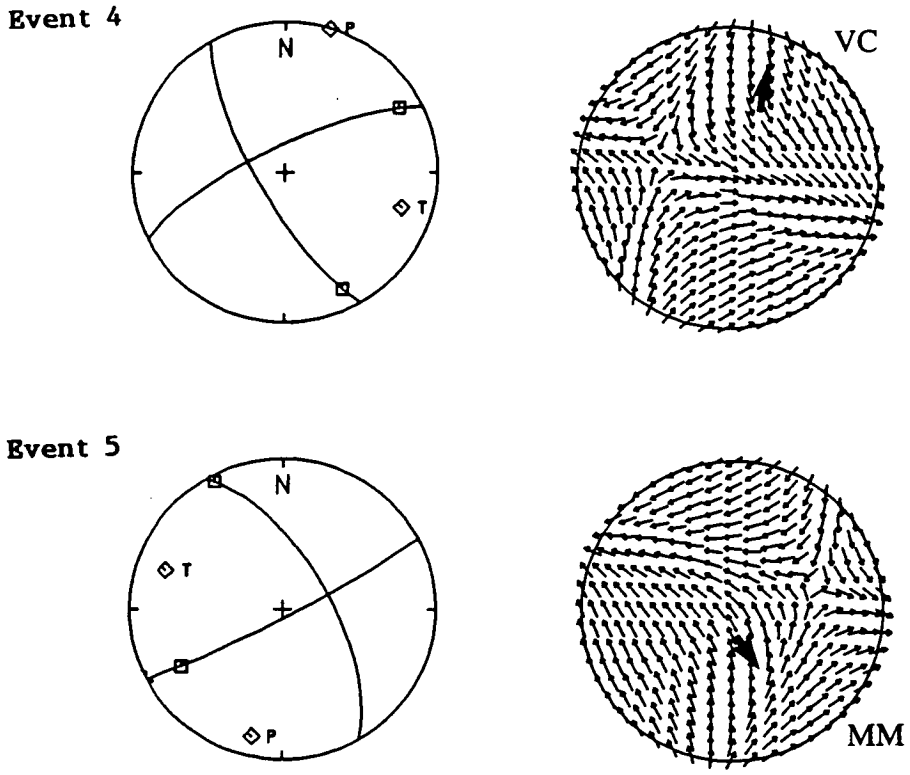

Figure 5.6. The adjusted focal mechanisms and the radiation patterns of the shear-waves out to 45° of angle of incidence for events 4 and 5. Note that the heavy arrows mark the observed shear-wave polarizations at the indicated stations.

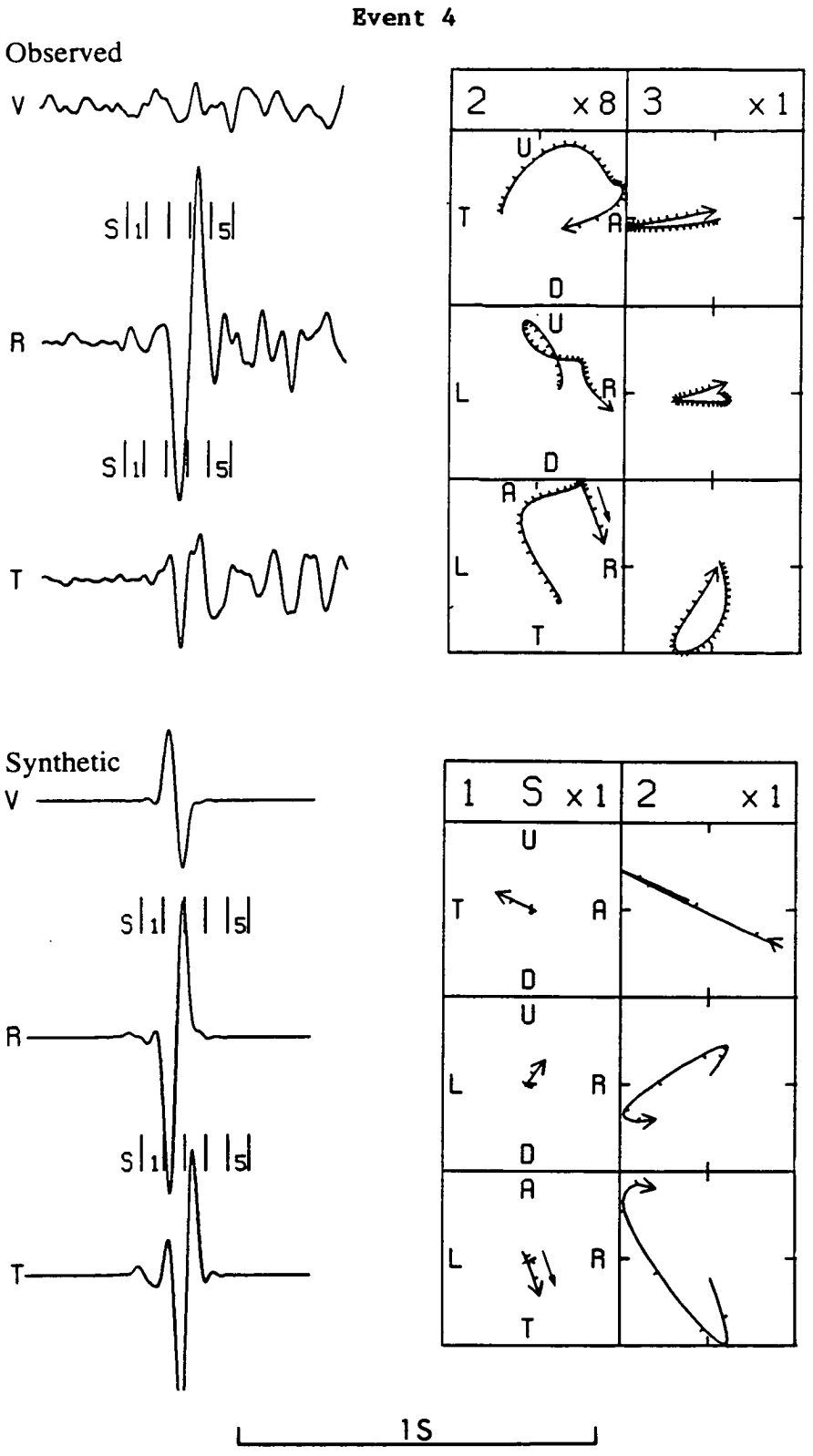

Figure 5.7. Comparison of synthetic seismograms and particle motion diagrams with the calculated displacement records for event 5 at station MM and event 4 at station VC. Each window length is 60ms. Small arrows indicate the direction of shear-wave polarization.

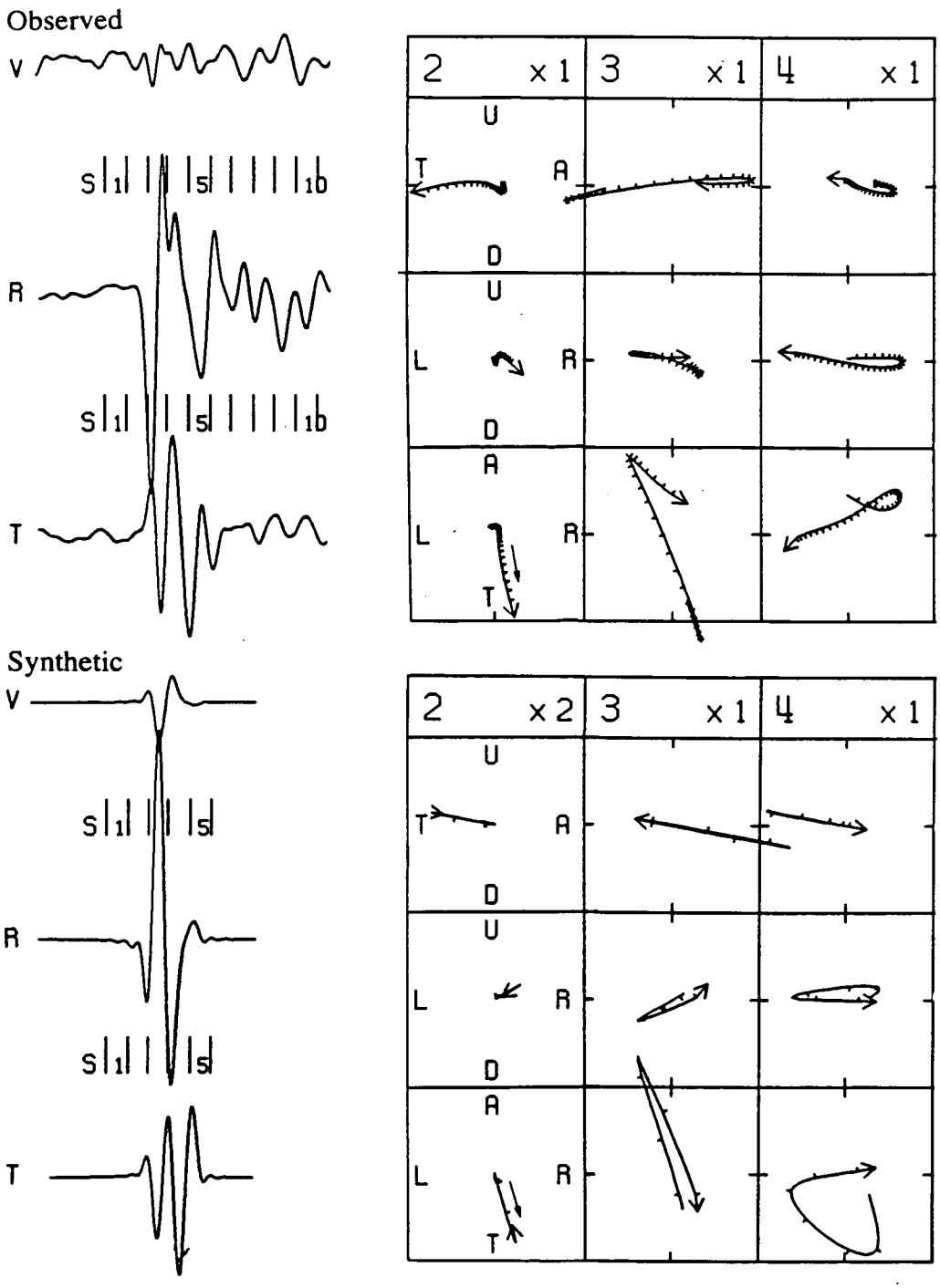

(Figure 5.7 continued)

5.6 INTERPRETATION OF TIME DELAYS

The possible temporal change in time delays and the further examination through the study of earthquake doublets and the analysis of the possible maximum error have been presented in Chapter 4. The similar observations have been observed on two occasions previously, at station KNW in Anza network (Crampin *et al.*, 1990) and in the Enola swarm in Arkansas (Booth *et al.*, 1990). Gledhill (1991) has studied the variation of time delays with the earthquake source parameters, such as seismic moment, stress drop and source size. He found no evidence of any correlation between scattered time delays and source parameters. This might be due to no relatively large earthquakes occurred in the time when the data were collected. In the following sections I shall examine the possibilities that may be relevant to the variation of temporal change.

5.6.1 Correlation of time delays with seismic moment

The information I have relevant to source parameters is the coda-duration magnitudes M_D, which have been routinely published by U.S. Geological Survey for earthquakes in central California. In order to find the relationship between time delays and the source parameters, I used the result from Bakun (1984). He investigated the relationship of seismic moment (M_o) and local magnitude (M_L) and the relationship of M_o and M_L to the coda-duration magnitude M_D, and found that $\text{Log}M_o$ can be estimated to a precision of 0.2 for $1.0 \leq M_D \leq 3.5$ for earthquakes in central California by applying $\log M_o = 1.2M_D + 17$. Thus it can be examined if time delays are correlated to seismic moment. I calculated $\log M_o$ through M_D for earthquakes with $1.0 \leq M_D \leq 3.5$ according to the above equation.

Figure 5.8 presents the variation of time delays with $\log M_o$ at the two stations. It is seen that the patterns basically show scattered at both sites and there is no clear sign of correlation between the two variables. Figure 5.9 compares the variations of $\log M_o$ against time with the variations of time delays against time at stations MM and

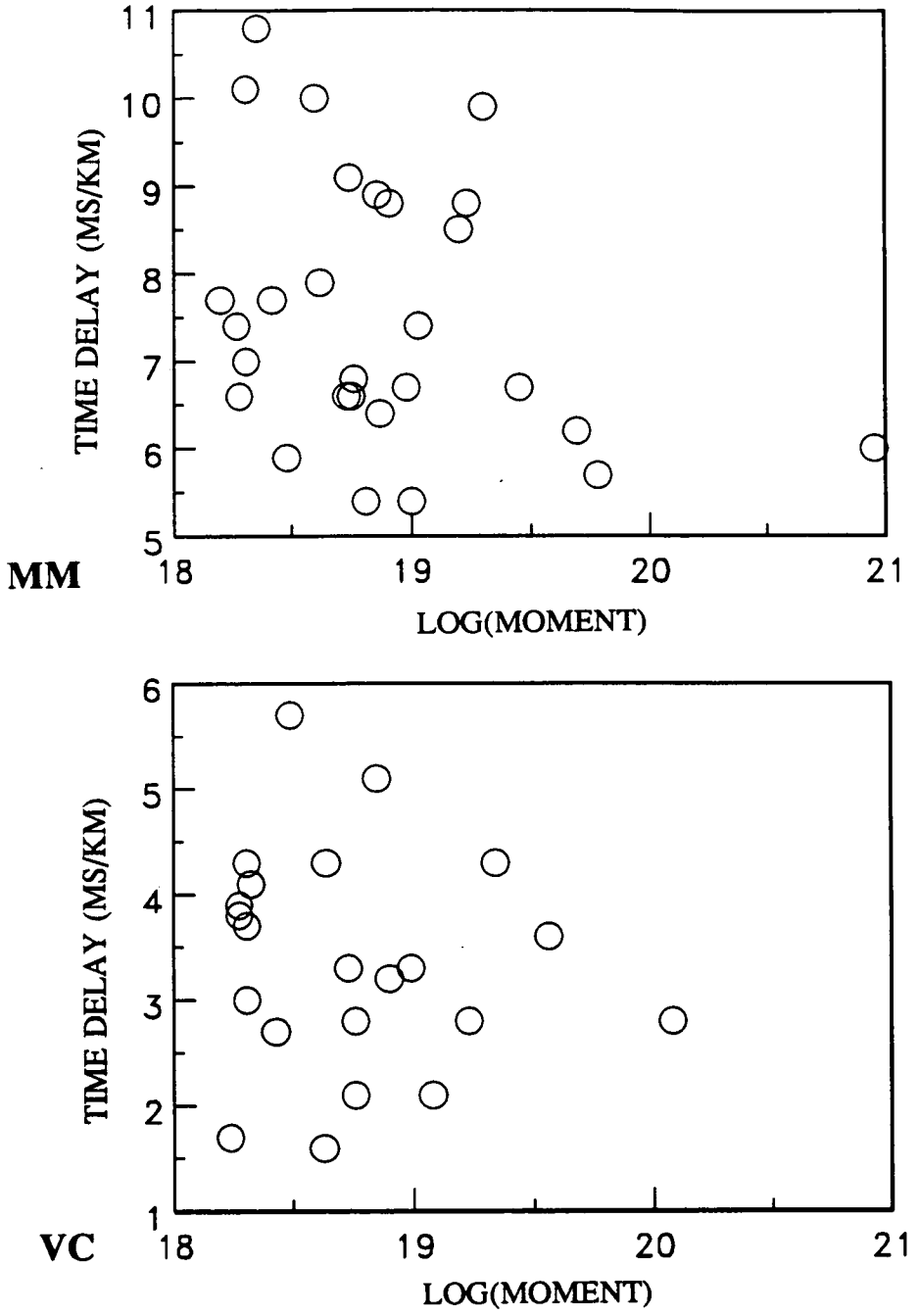

Figure 5.8. Variations of time delays against $\log M_o$ for events with magnitude $1.0 \leq M_D \leq 3.5$ at stations MM and VC.

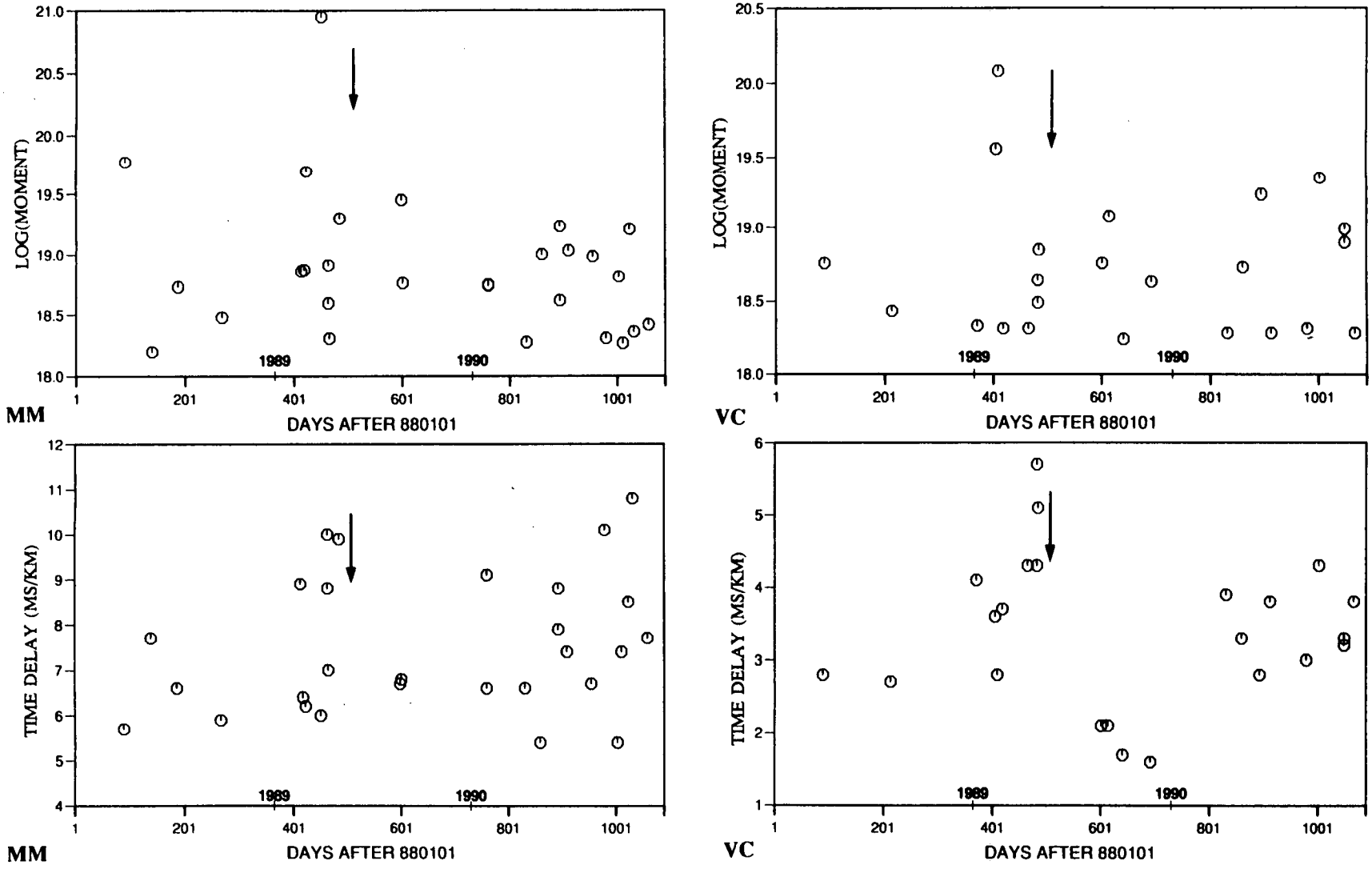

Figure 5.9. Comparison of $\log M_o$ against time with the variations of time delays against time for the earthquakes with weights of time delays from 1 to 2 and magnitude of $1.0 \leq M_D \leq 3.5$ at stations MM and VC. Arrow marks the time when the M=4 event occurred.

VC. Note that these two diagrams plot the same events, corresponding with time delays of weight 1 and 2 and magnitudes in the range of $1.0 \leq M_D \leq 3.5$, for which $\log M_o$ were calculated. Arrows mark the time when the $M_L=4$ earthquake occurred. It is seen that the variations of both time delays and $\log M_o$ are scattered at MM and no clear sign of correlation between them. At VC, time delays show marked increase and pronounced decrease before and after the marked time, respectively, whereas there is no such variation for $\log M_o$ but only a scattered distribution, so there is no sign of correlation between time delays and seismic moment at VC as well. I therefore conclude that the observed temporal variation of time delays is unlikely to be related to the seismic moments, in other words, it is probably not attributable to the differences between source time functions.

5.6.2 Variation of time delays with focal depth

It is seen in Figure 4.15 that in general normalised time delays at station MM decreases with increase in earthquake focal depth. So it is important to examine whether there is any correlation of temporal variation of time delay with focal depth. This investigation is done only at stations MM and VC. Figure 5.10 shows the variations of focal depths with time. At station MM, observations are scattered before the time of the M=4 event and there is no evidence of a temporal decrease of focal depth, corresponding to the increase of time delays which is shown in Figure 4.15 at MM. After the M=4 event there is an decrease in focal depth for about 100 days, which suggests that the decrease of time-delays could be caused by migration of focal depths (note though there are only three events involved). However, the decrease of focal depth, as mentioned above, would tend to increase the normalised time-delays. Thus the temporal decrease at MM is unlikely to be caused by depth migration. In Figure 5.10 at station VC, earthquake focal depths distribute uniformly over the whole period as the distribution of normalised time delays shown in Figure 4.15. The temporal variation of time delays is not observed to correspond with the variation of focal depth. Thus the observed temporal variation is also unlikely to be caused by

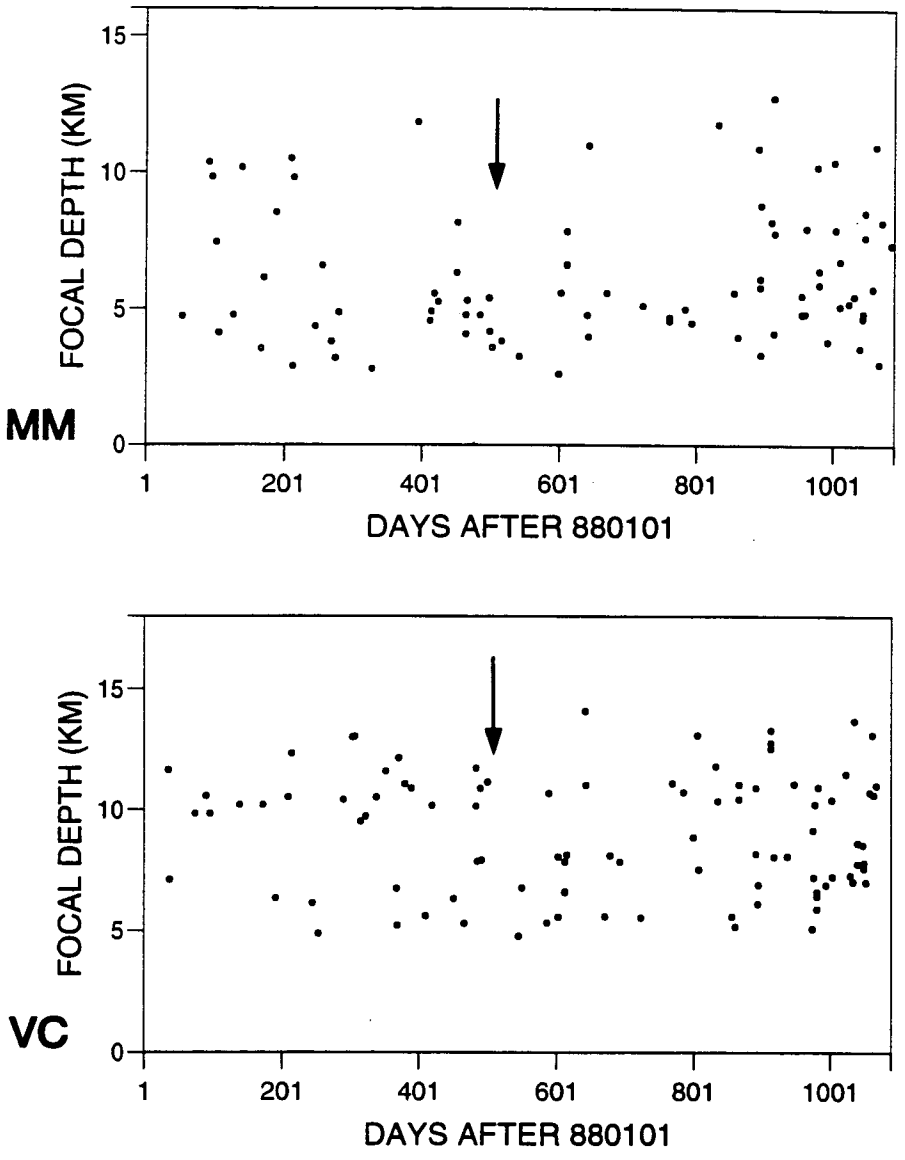

Figure 5.10. The variation with time of focal depth at stations MM and VC. The arrow marks the time of the M=4 earthquake.

depth migration at VC. I therefore conclude that the observed temporal variation at Parkfield is unlikely to be caused by depth migration.

5.6.3 Variation of time delays with raypath

Vavryčuk (1993) has examined directional variation of delay time in West Bohemia, Czech Republic. He found that the observed data can be well matched using Schoenberg-Douma's theoretical crustal anisotropic model (En=0.4, Et=0.2). In this model, the computation of elastic coefficients of effective anisotropy involves the elastic coefficients λ and μ of an isotropic background, and two fracture parameters En, Et. The fracture parameters are dimensionless constants characterizing the response of fractures to the normal and shear stress, respectively. By contrast, Hudson's ellipsoidal inclusion model (Hudson, 1980, 1981) characterizes the fracture parameters by aspect ratio and crack density.

Chapter 1 summarised the theoretical behaviour of seismic body waves in crack-induced anisotropic media (Hudson, 1980, 1981). It has been seen from Figure 1.2 that the velocity difference between split shear waves varies with the angle between wave propagation and hexagonal symmetry axis of the vertical cracks. Near-vertical propagation wave paths (waves propagating along symmetry plane) have the largest delay time. Figure 5.11 displays directional variation of observed normalised time delays (squares), least square fit curve (dashed line) and the optimum fit of theoretical curve (solid curve), at stations MM and VC. Note that the time period of observed data is chosen from January to December 1988 at VC and from July to December 1989 at MM, based on time delays being constant during the time period because the observed delay times are the function of time. The theoretical curve assumes that time delays are independent of time. The symmetry axis is taken as N40°W at MM and N15°E at VC. *P*-wave velocity in the isotropic medium is assumed to be 6km/s, which is the major layer in earthquake location; the ratio of *P*- and *S*-wave velocities Vp/Vs=1.9 (Michelini and McEvilly, 1991) at MM and Vp/Vs=1.732 at VC; density ρ=2.65kg/m^3. The well-matched theoretical curves are of aspect ratio

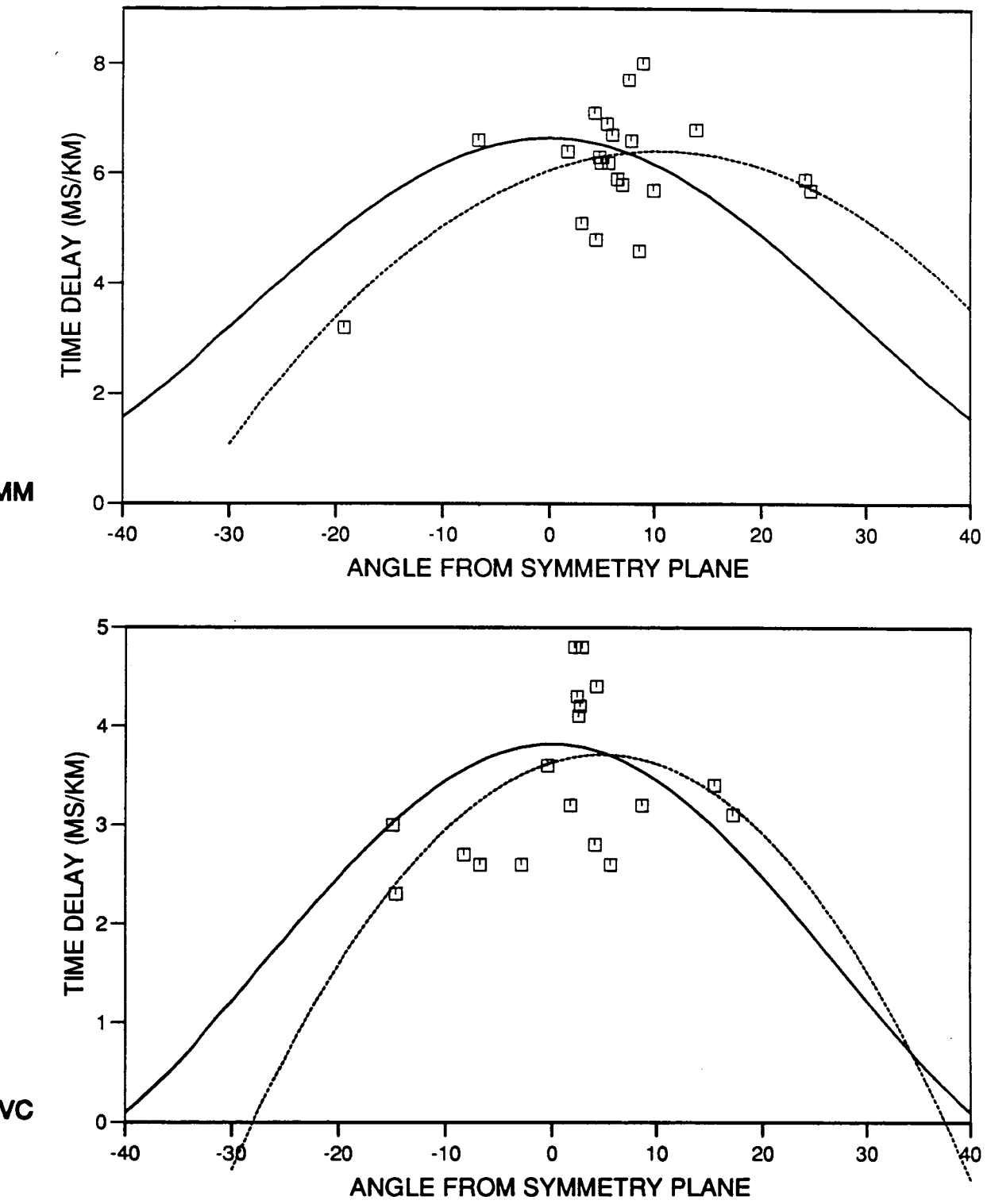

Figure 5.11. Directional variation of time delays at stations MM and VC. Squares are the observed data, the dashed line is the least square fit curve of the observed data and the solid line is the optimum fit of the theoretical curve (Hudson, 1980,1981). The *P*-wave velocity in the isotropic media is assumed to be 6km/s, which corresponds to the major layer in the earthquake location velocity model (poley *et al.*, 1987), ρ=2.65g/cm^3, Vp/Vs=1.9 at MM (Michelini and McEvilly, 1991) and Vp/Vs=1.732 at VC. The symmetry axis is taken at N40°W and N15°E; aspect ratio and crack density are 0.1, 0.019 and 0.03, 0.0115 at MM and VC, respectively.

AR=0.1 and crack density CD=0.019 at MM; AR=0.03 and CD=0.0115 at VC. It is seen that there are about 5° and 10° shift of symmetry axis between fitted theoretical curve and least square fit curve at VC and MM, respectively. Since earthquakes were along the SAF plane, and under the limitation of shear-wave window, raypaths are not optimally covered. The standard deviation of the least squares fit is 0.71 at VC and 0.84 at MM.

In Figure 5.11 the observed time delays can basically be fitted by a second-degree curve that is comparable with the theoretical curve calculated by Hudson's ellipsoidal inclusion model, although the observed data are scattered and raypaths are not well covered. Here I have shown that directional variation of time delays can be basically matched using Hudson's model at Parkfield, Next I shall investigate the interpretation of change of crack density and aspect ratio.

5.6.4 Change of crack density and aspect ratio

Crampin *et al.* (1990) have observed a temporal variation of time delays at station KNW of Anza network, Southern California. They found a remarkable increase of delays before an M=6 earthquake and a decrease after the earthquake. Figure 5.12 shows the theoretical behaviour of the velocity of shear waves propagating through parallel water-filled microcracks for a range of crack densities from CD=0.015 (modelling observations at Anza) to CD=0.03 with aspect ratio AR=0.001, to the left, in an isotropic matrix (ρ=2.7gm/cm^3, Vp, Vs=6.3, 3.643 km/s), and on the right, with crack density CD=0.015 and aspect ratio from AR=0.001 to 0.05. The constant pore-fluid is water with velocity of 1.5 km/s (after Crampin *et al.*, 1990). Note that only an increase of aspect ratio as three times as normal may be realistic (Crampin, 1993). For the range of ray paths between 50° to 75.5° to the crack normal, the velocity variations are shaded in both diagrams. It is seen that the increase of crack density, caused either by increase in number of cracks or by an increase of (radius) the size of cracks, will effectively increase the velocity difference between fast and slow split shear-waves, whereas an increase of aspect ratio will effectively enlarge the central

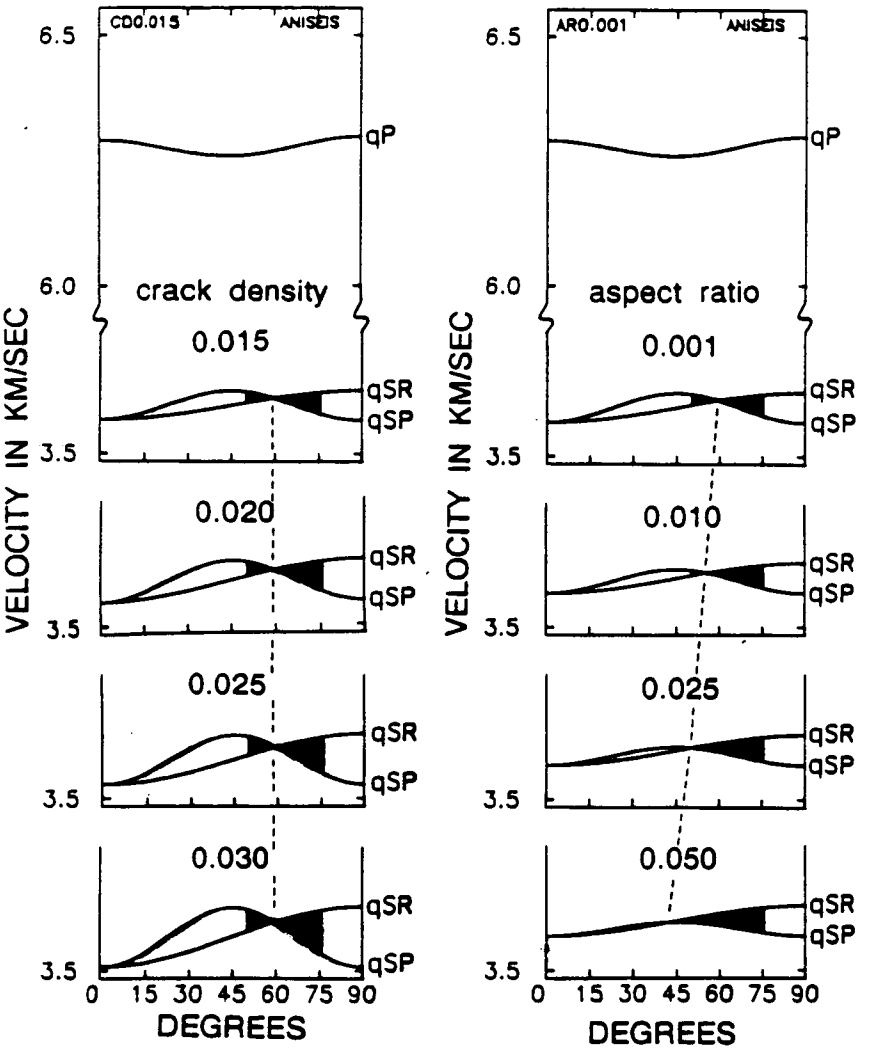

Figure 5.12. Theoretical behaviour of the velocities of shear waves propagating through parallel liquid-filled microcracks; on the left, for a range of crack densities from CD=0.015 (modelling observation at Anza) to CD=0.03 with aspect ratio AR=0.001 and water as the pore-fluid with velocity of 1.5km/s. In an isotropic rockmass (ρ=2.7gm/cm3, Vp=6.3, Vs=3.643km/s); on the right, with crack density CD=0.015 and aspect ratio varying from AR=0.001 to 0.05 with the same rock matrix. Note that for the range of ray paths between 50° and 75.5° to the crack normal, the velocity variations are shaded. With the increase of crack density the velocity difference of qSR and qSP is remarkably increased; the increase of aspect ratio will only slightly modify the velocity difference, but the intersection point of the split shear-wave velocities effectively moves towards the left (after Crampin *et al.*, 1990).

band toward the intersection point, and only slightly increase the velocity difference. In order to examine whether the temporal variation observed at Anza was caused by a change of crack density or aspect ratio, ray paths were split into two bands, with 50° to 75.5°, and 75.5° to 90° to the symmetry axis. The interpretation of the observed temporal variation at Anza was then made as the combined effects of small increase in crack density and the increase of aspect ratio (bowing) of the supercritical fluid-filled EDA cracks throughout the rockmass as the stress builds up before the earthquake. The rapid decrease of aspect ratio (flattening), and a more gradual reduction of crack density by partial healing, occurred as stress was released by the earthquake.

Here, I examine delay variations by splitting the data into two parts, data propagating at an angle to the symmetry axis of greater than 77° and those of angles less than 77°. Note this angle varies little with different dataset, and 77° is found to be appropriate angle at Parkfield to examine whether the temporal variation is caused by a change of crack density or aspect ratio (Figure 1.2). As mentioned in the last section, 95% data received at MM are of waves propagating within 75° to 90° to symmetry axis. Therefore, this examination is only applied to the data recorded at station VC. Figure 5.13 shows equal-area projections of time delays and the variations of time delays against time, with data in which rays propagate within the angle of 77° to 90° in (a), and 50° to 77° in (b), to the symmetry axis. Solid lines are a 5-point moving average. Figure 5.13 (a) shows a large range of scattering, but the tendency of the delay times to increase before the time of the M=4 earthquake is still visible, so is the marked decrease in delay values after the earthquake. This indicates that crack density may have increased slightly beneath VC before the M=4 earthquake happened, then cracks started to heal up, not necessarily immediately after the release of strain energy. The data here suggest that healing probably took about three to four months. Figure 5.13 (b) exhibits an increase and decrease before and after the earthquake, although there are not many data in this band. It suggests that the cracks pervading the rockmass may have increased their aspect ratio (bowing) due to stress concentration before the earthquake, and decreased (flattened) after the earthquake. It

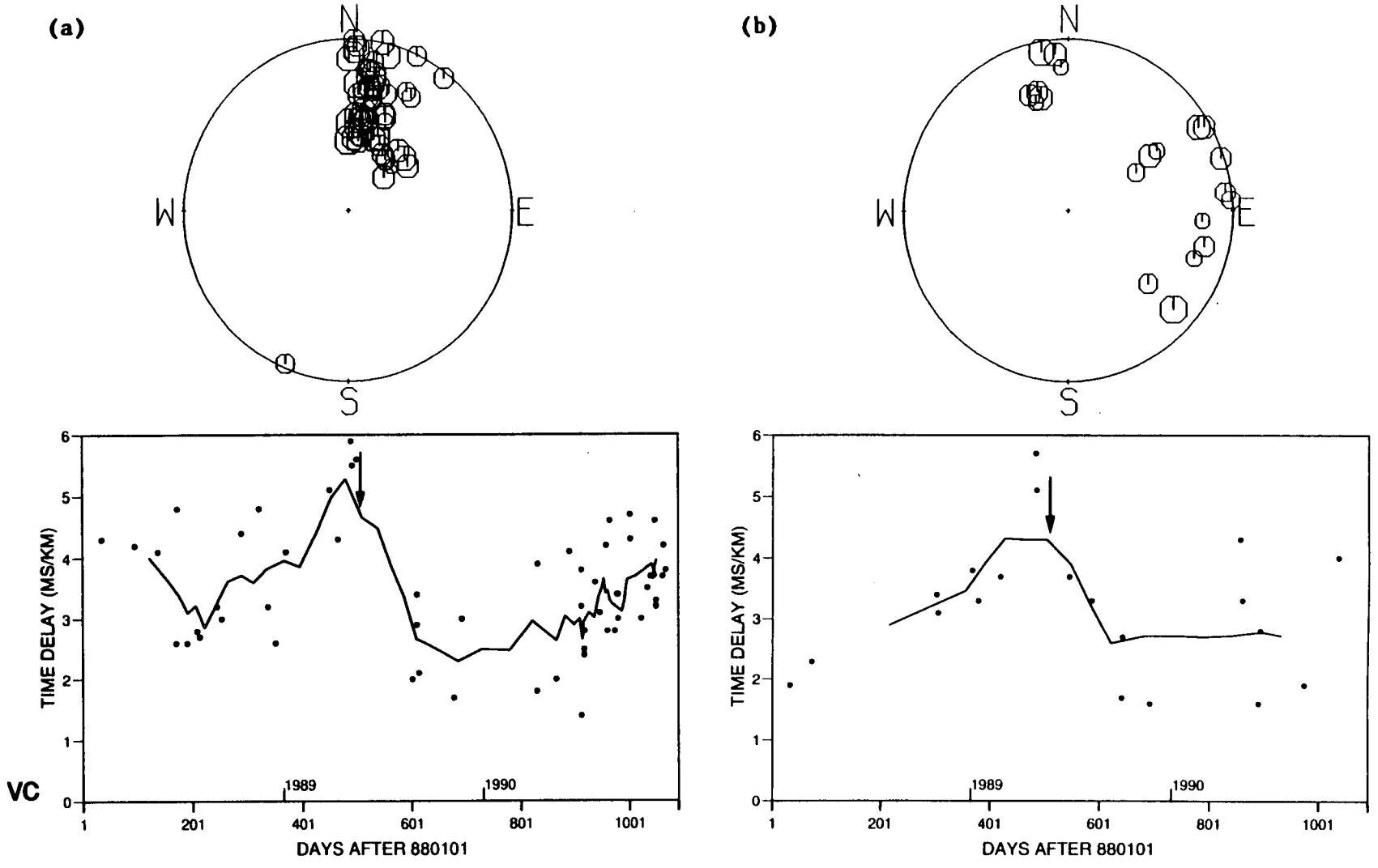

Figure 5.13 Equal-area projections of time delays out to 45°of incidence, and the variation of time delays with time for raypaths within the angle of (a) 77° to 90°, and (b) 50° to 77° to the symmetry axis of N110°E. The solid line is the 5-point moving average, and the arrow marks the time when the M=4 earthquake occurred.

is also seen on the upper plots of the polar maps that time delays towards the edge of shear-wave window are not decreasing to zero, that may be explained by the intersection point of the split shear wave velocities moving to smaller angle (to the left) with the increase of aspect ratio, seen in Figure 1.2. In the fault zone, beneath station MM, fluid at higher pore pressure (Rice, 1992) may be indirectly responsible for the increase of crack density because it accelerates stress-corrosion cracking during stress concentration before the impending earthquake. This interpretation has recently been confirmed by Zatsepin and Crampin (1995) through modelling of the deformation of rocks in the brittle crust. Their results suggests not only that the microcrack geometry responds to changes in stress and can be monitored by appropriate observations of shear-wave splitting, but that modifications to microcrack geometry can be numerically modelled and the physical behaviour of the rockmass predicted.

5.7 PROBABILITY OF DETECTING TEMPORAL VARIATIONS AND SEISMIC ANISOTROPY IN THE FAULT ZONE

It may be doubtful whether the M=4 earthquake, with seismic moment about 1.2×10^{22}dyne cm, and presumably a low stress drop (<50 bars), can cause the observation of temporal variations in time-delays at seismograph stations around 15 km away from the epicentre. This doubt could be true for the dilatancy-diffusion hypothesis, which is that the changes in density, distribution and saturation of cracks near earthquake source are responsible for most precursors (Scholz *et al.*, 1973; Byerlee, 1978b; Simpson and Richards 1981). This hypothesis may explain the behaviour of the cracks in the immediate vicinity of an impending earthquake, but the behaviour of the cracks remote from the source cannot be explained by conventional dilatancy. However, the EDA hypothesis refers to phenomena occurring at comparatively low stresses throughout a large part of the preparation zone before an earthquake, possible many tens of kilometres from the impending epicentres, because water-filled cracks are expected to be common at all depths in the crust, and the weakening effects of subcritical crack growth by stress-corrosion can take place at low

stress and strain rate. It does not depend on the behaviour within the immediate focal zone (Crampin *et al.*, 1984). In this aspect it differs from many other suggested earthquake precursors. Furthermore, the direct evidence recorded from all dilatometer and tensor strain instruments indicates that the observed temporal variation probably reflect the change of the properties of fluid-filled cracks in the crust due to stress concentration before the impending earthquake and stress release after the earthquake (Lindh and Estrem, 1989). Recent results from Zatsepin and Crampin (1995) shows that the mechanism of deformation of a pre-stressed fluid-saturated rockmass is fluid-migration along pressure gradients between neighbouring EDA-microcracks at different orientations to the stress field. This microscale fluid migration can take place at very low values of differential stress (Zatsepin and Crampin, 1995).

Rice (1992) postulated that pore-pressure distributions are high and near to the fault-normal compressive stress within the fault zone, but decrease rapidly with distance into the adjacent crust. This is consistent with the fact that the San Andreas fault is weak in both absolute sense and relative sense. The 'absolute' means that the SAF moves under shear stresses far smaller than implied by the most obvious reading of laboratory friction results; the 'relative' is indicated by that the adjoining crust seems to be mechanically stronger, this is implied by the stress state having a horizontal maximum principal direction that makes a steep angle to the trace of the fault. Such high pore-pressure in the fault zone tends to increase the rate of stress-corrosion since the propagation of pre-existing cracks is expected to be dominant. The development of the pre-existing cracks is caused by for example stress-corrosion, dissolution and, diffusion in the fault zone. All of these mechanisms are influenced by the chemical effects of pore water in the crustal environment, and water is a major factor in the above mechanisms. Presumably, the propagation rate of the cracks in the fault zone is greater than that in the contact rocks, beneath VC. It is consistent with the observation that the differential shear-wave anisotropy at MM is about twice as large as that at VC, shown in Figure 4.8. This suggests that the fluid-filled fractures within the fault zone are more extensive than that in the surrounding crust.

5.8 SUMMARY AND CONCLUSIONS

I have compared the observed polarizations with the earthquake source radiation patterns, and shown that the directions of the shear-wave polarizations are not the same as those of the earthquake sources. Shear-wave splitting is less affected by near-source and near-surface effects because most the earthquakes used in this study are microearthquakes and the seismograph stations are in boreholes between 200 m and 300 m deep at Parkfield. Other effects, such as surface topography, site and instrument effects have also been investigated, but none of them could produce a large effect on the observed polarizations.

At stations ST and FR on the southwest block of the SAF, the heterogeneities and/or the irregularities of the sedimentary layer are probably responsible for the scattered polarizations. Local topographic irregularities surrounding station ST may also distort shear-wave first motions. At stations VC, ED, and VR, shear-wave polarizations are aligned at about N20°-30°E, parallel or subparallel to the direction of maximum compressive horizontal stress. It is found that there is no other mechanisms which could be responsible for the observed shear-wave splitting such as aligned crystals, lithologic anisotropy or structure anisotropy other than stress-aligned parallel vertical (EDA) cracks. Polarizations at stations MM and JN are well aligned, but orientated at N40°W and N5°E, respectively. The deviated polarizations at JN are explained by the distortion of the shear-waves, due to an effectively enlarged shear-wave window. At station MM shear-wave polarizations are parallel to the fault trace, as observed at stations close to the fault zone at other places. It is concluded that fault parallel fractures and probably rock fabrics are responsible for the observation of shear-wave splitting there, because there is geologic evidence showing that some crystalline rocks and intensive folds are trapped along the fault trace near the fault zone. By modelling events 4 and 5, it is further demonstrated that stress-aligned fluid-filled vertical (EDA) cracks are probably the only suitable model that can interpret shear-wave splitting in the upper crust at Parkfield.

In order to find any associated cause of the observed temporal variation I

investigated the relationship of time delays with seismic moment. It has been shown that time delays are not correlated with seismic moment, or in other words, the observed temporal variation is not related to the earthquake source time function.

I have demonstrated that the temporal variation of time-delays is not associated with a variation of earthquake focal depth. By examining the delay variation with the wavepaths. I found that the delay variation with raypaths at MM and VC is basically matched by Hudson's ellipsoidal inclusions model, which gives elastic constants using isotropic matrix properties, crack density, and aspect ratio. However, there is a lack of data coverage over a wide range of angles. It is expected in terms of theoretical behaviour of shear-wave anisotropy that the change of crack density and aspect ratio will effectively alter the duration of time delays. This has been investigated for observed data, and it is suggested that stress concentration before the M=4 earthquake probably slightly increased the number of cracks and bowed them. After the release of strain energy, stress reduced to a lower level, accompanied by healing and flattening of the cracks. The fact that the differential shear-wave anisotropy at MM is about twice as large as that at VC suggests that fluid-filled microcracks and fractures within the fault zone are more extensive than those in the surrounding crust. This can be explained by the development of pre-existing cracks in the fault zone. After investigating and examining the aspects relevant to the phenomenon of shear-wave splitting, I find that EDA cracks is the most appropriate model responsible for the observation of shear-wave splitting, and hence the temporal variation of time delays is probably precursory to the M=4 earthquake at Parkfield.

CHAPTER 6

FURTHER EVIDENCE OF SEISMIC ANISOTROPY FROM DOWNHOLE RECORDINGS AT THE CAJON PASS SCIENTIFIC BOREHOLE, SOUTHERN CALIFORNIA

6.1 INTRODUCTION

My study on shear-wave anisotropy in the previous chapters was based on data recorded at depths between 200 m and 300 m at the Parkfield HRSN network. The data exhibit distinct shear-wave anisotropy, although the analysis of shear-wave splitting becomes difficult, and may be obscured in some cases, due to the complexity of the scattering wavefield. The complexity could be caused by topography of free surface and subsurfaces, and the inhomogeneity of the crust, particularly the near-surface shallow crust. Data from Cajon Pass recorded at a depth of 2.5 km is expected to be free of near-surface effects, and the analysis of this data forms the subject of the present chapter. Seismic waves recorded under these conditions are very 'clear' (Abercrombie and Leary, 1993), and hence provide high quality data for the study of shear-wave splitting.

The fact that polarizations of the leading split shear waves travelling within the shear-wave window to the surface usually display parallel alignments, approximately orthogonal to the direction of minimum horizontal compressional stress (Crampin and Lovell, 1991), may be used to determine directions of the maximum horizontal stress in the seismogenic zone near Cajon Pass. The mechanism driving the right-lateral movement of the San Andreas fault (SAF) in southern California has been widely discussed. The measured *in-situ* maximum horizontal stress in the deep Cajon Pass borehole measured using wellbore breakouts (Shamir *et al.*, 1988; Shamir and Zoback, 1992) and hydraulic fractures (Healy and Zoback, 1988; Zoback and Healy, 1992) is approximately in the direction of N57° E ± 19°, which does not support the movement of the major fault. The maximum regional

stress orientation inferred from focal mechanism studies is around the direction of N17°W, which is consistent with the motion on the major fault (Jones, 1988) but cannot explain the existence of fault normal extension or compression close (< 15 km) to the SAF. Thus it is actually not clear whether the SAF is driven by deep stresses caused by plate tectonics or a modified stress field which is suggested by the secondary structure seen at the surface. This is also closely related to the problem in fault mechanics (the stress/heat flow paradox described in the next section), the resolution of which was one of the principal objectives of the Cajon Pass drilling project (Zoback *et al.*, 1988).

The distributions of fractures or microcracks are of further significance, not only because such features correlate with the stress field, but also because they control the fluid flow and permeability of rocks. These parameters are important for the study of fault mechanics, and particularly for improved recovery techniques in sedimentary oil reservoirs by the oil industry. In this chapter, I shall apply the method described and used with the Parkfield dataset to the data recorded in the Cajon Pass borehole at a depth of 2.5 km. This is a high quality dataset with a high signal to noise ratio (on account of the quiet recording location) which in principle will resolve the configuration of cracks and the direction of *in-situ* maximum horizontal stress down to a certain depth in the seismogenic zone and possibly, the crack dimensions in the upper crust near Cajon Pass.

6.2 SCIENTIFIC BOREHOLE PROJECT AND GEOLOGY AT CAJON PASS

One of the principal scientific objectives of the Cajon Pass borehole was to address a long-standing problem in fault mechanics sometimes referred to as the stress/heat flow paradox. There is a contradiction between the average shear stress acting on the San Andreas fault (SAF) inferred from the measurements of conductive heat flow, which suggests that the average shear stress acting on the SAF is less than about 20 MPa, and the direct prediction from laboratory-derived friction coefficients and *in situ* stress measurements, which suggest that the average shear stress should

be about 100 MPa. The resolution of this paradox is crucial to understanding the nature of deformation along major plate boundaries, the relevance of laboratory rock-friction experiments to crustal faulting, and the balancing of forces that drive the plate motion (Zoback *et al.*, 1988; Zoback and Lachenbruch, 1992).

A three-component seismometer installed in the Cajon Pass borehole at 2.5 km downhole (surface recording run for three months) started to function from April 1992 to July 1993. The downhole instrumentation is a three component set of 10 Hz L15 velocity transducer. Data are sampled at the rate of 500 Hz and all recordings are for 60 seconds. The amplitude response of the horizontal component H2 decayed slowly with time, presumably due to the high temperature in the borehole (105°C at 2.5 km). This will be further discussed in Section 6.3.1

The location of the Cajon Pass deep borehole was chosen principally due to a good exposure of local geology and moderate topographic relief at a site about 4 km from the SAF. Figure 6.1 shows the location of the Cajon Pass deep borehole relative to major faults and physical features in southern California. The drilling site is on the southwest edge of the Mojave Desert and at the west end of the San Bernardino Mountains. This range and the San Gabriel Mountains west across the SAF are rising rapidly (1-3 km relief) in apparent response to SAF transpression (Silver and James, 1988). Recent studies by Weldon and Sieh (1985) and Meisling and Weldon (1988) indicate a combined right lateral rate of motion on the San Andreas and San Jacinto faults of about 37 mm/year.

The Cajon Pass drill hole penetrates a late Tertiary basin developed on crystalline basement in the southwest Mojave desert. All the crystalline rocks are foliated, ranging from weak alignment of mafic minerals in the granodiorites to strong preferred orientation of minerals and compositional layering in paragneisses and migmatitic gneisses. Foliation dips are generally low (< 30°). The San Bernadino Mountains contain a variety of Mesozoic to Precambrian granitic rocks and the remains of Cordilleran miogeoclinal sedimentary formations. The San Gabriel Mountains are comprised of tectonically stacked Mesozoic granitoids and Precambrian orthogneisses resting on a great mylonite zone above Pelona Schist.

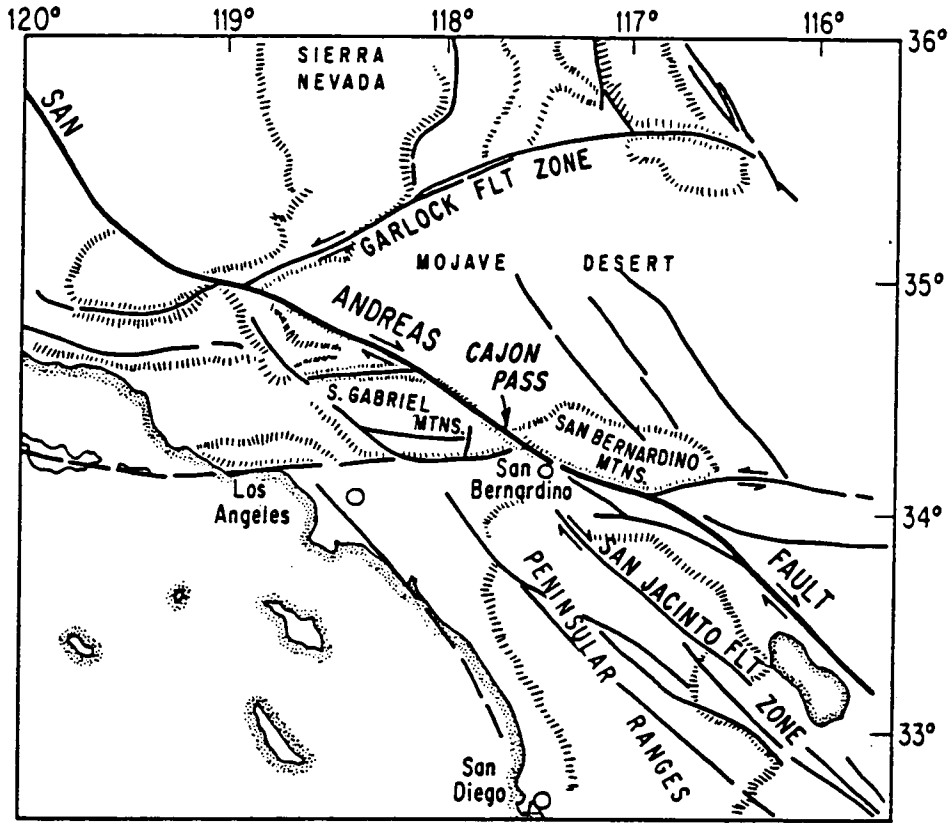

Figure 6.1. Location of the Cajon Pass deep drillhole relative to major faults and physical features in southern California (after Silver and James, 1988).

This complex tectono-stratigraphic assemblage is exposed across the SAF west of the Cajon Pass deep drill hole in the eastern San Gabriel Mountains (Silver and James, 1988).

Figure 6.2 shows the generalised local geological map near the Cajon Pass scientific drill hole. The basement is widely exposed southeast of the drill hole. The nearest exposure is a fault-bounded mass of granodiorite on Squaw Peak. Further southeast, granodiorite crops out continuously for a distance of at least 12 km on east-west trending Cleghorn Ridge. Sandstone of the Miocene non-marine Crowder Formation overlies the granodiorite along the north side of Cleghorn Ridge and locally along the south side where it has been dropped down along the Cleghorn fault. South of Cleghorn Ridge is a large area of exposed basement consisting of migmatitic gneiss and lesser amounts of marble, other metasedimentary rocks, metagabbro, dioritic gneiss and granitic rocks. The granodiorite is typically medium-grained, and faintly foliated in most outcrops. Foliation is produced by subparallel alignment of biotite plate, the broad faces of plagioclase crystals and lens-shaped blobs of quartz. Some outcrops also display vague banding caused by slight variations in composition and grain size. Lineation is locally present and is produced by the preferred orientation of elongate minerals and aggregates of quartz. Gneiss predominates in the area around Cajon Mountain between Cleghorn Ridge and the SAF, and on Circle Mountain between the Cajon Valley fault and the SAF, and some occurs on the southwest side of Whale Mountain. Much of it has well developed compositional layers suggestive of relict bedding and contains interlayered marble and other rock types diagnostic of a sedimentary origin. In some areas, particularly between Cleghorn Ridge and Cajon Mountain, the granitic masses are so intermingled and deformed with more mafic gneissic layers that the rock is most appropriately referred to as a migmatite (Ehlig, 1988).

The area contains significant folds and faults. Faults and alteration zones bound several rock units with low apparent dips. Folds in the layered metamorphic rocks are recumbent isoclinal with axes parallel to the foliation. Basement cores are typically cut by steep fractures, less than 1 mm wide. Fractures and faults

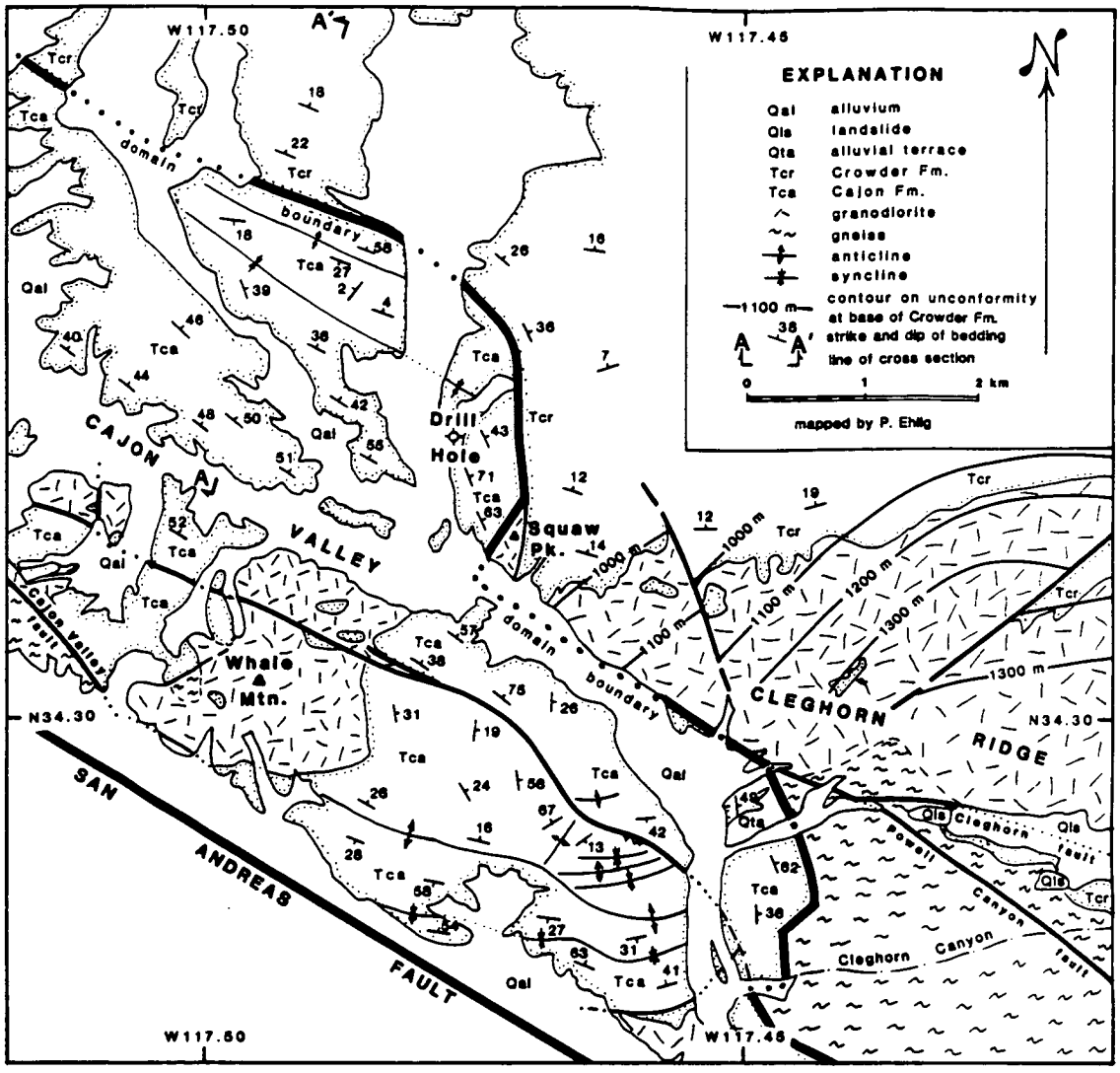

Figure 6.2. Generalised geological map of the area surrounding the Cajon Pass deep borehole. The detailed illustration of the map is at the top right of the map (after Ehlig, 1988).

decrease in abundance with depth (Silver and James, 1988; Zoback and Healy, 1992).

6.3 DATA AND PROCESSING

Seventy-one events written in *ASCII* format were collected at Edinburgh via anonymous File Transfer Protocol (*FTP*) from University of Southern California. Figure 6.3 shows the locations of these events. They include 46 events located by stations of southern california seismic network and 25 events located by the single three component downhole seismometer at Cajon Pass (Abercrombie, 1994). The sixty-seconds long three-component traces for each event were cut into 8 seconds intervals, centred at the major shear-wave train, and rewritten as *SEGY* format files.

As noted previously the second horizontal component *H2* decayed slowly in amplitude and geophone resistance response, but there is no decay in the frequency response. The corrections for *H2* was worked out by measuring resistance and calculating daily correction for decay. An independant estimate of correction was also calculated by comparing amplitude of late coda on three component. The comparison of the two methods showed that the corrections made by two ways were consistant and stable (Abercrombie, 1994). I have examined that the two ways of correcting for *H2* only make minor ($< 5°$) differences to the measurement of shear-wave polarization.

P-wave polarizations were first checked based on the known direction of arrival from each event similar to my analysis of the Parkfield dataset, in order to minimize the errors of shear-wave polarizations. If the orientation of a component of a seismometer is accurately determined, *P*-wave polarizations are expected to be aligned radially in the horizontal plane since in a homogeneous anisotropic medium the effect of seismic anisotropy on *P*-wave is small (Crampin *et al.*, 1982; see Section 3.3.2). It is found that *P*-wave particle motions are correctly aligned at both radial component on radial-transverse (*R-T*) horizontal plane and vertical component on vertical-transverse (*V-T*) normal plane for more than 92% of the events. This

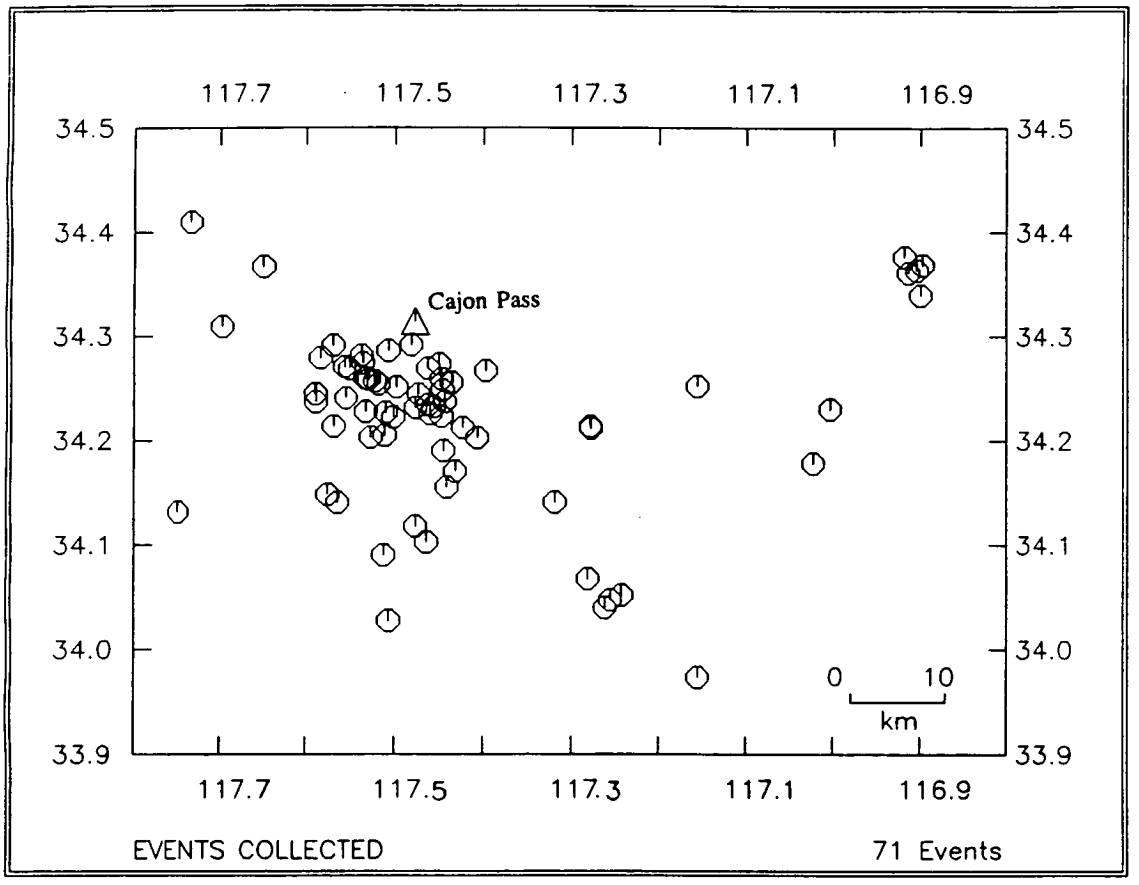

Figure 6.3. Locations of the events used for this study.

suggests that the orientations of the horizontal components of the seismometer as estimated by Abercrombie (1994) are essentially accurate, and there exists a relatively uniform medium at the scale of the average *P*-wave wavelength. Thus errors of measurement of shear-wave polarizations caused by misalignment of instruments are expected to be small for the Cajon Pass data. In practice, the angle of incidence is measured on the sagittal vertical-radial (*V-R*) plane.

Figure 6.4 shows an example of a three-component seismogram and the shear wavetrain amplitude spectrum on each component. It is seen that in the frequency domain there exists some resonance at about 55 Hz on the horizontal components. This is common for the data collected at Cajon Pass, and corresponds to resonance of the seismometer package. A band pass filter of 1-45 Hz is therefore applied to all the data used in this analysis in order to avoid high frequency noise. Seismograms generally display clear onsets of shear-wave arrivals which are not seriously affected by coda waves, confirming the expectations outlined in the introduction. Shear wave energy, in general, is in the frequency band of 10 to 40 Hz, as shown in Figure 6.4, indicating smaller attenuation below 2.5 km in the crust (Abercrombie and Leary, 1993).

6.4 SHEAR-WAVE PROPAGATION IN ANISOTROPIC SOLIDS

In anisotropic solids, two shear-waves propagate in every direction of phase velocity with the faster qS_1-, and slower qS_2-waves, having mutually orthogonal polarizations. The difference in velocity and polarization between the two waves leads to the phenomenon of shear-wave splitting. Phase velocity is seldom measurable, as traveltimes estimated from field observations are measured along seismic rays propagating at the group velocity. The variation of shear-wave velocities can be described by two surfaces corresponding to phase and group velocity. In anisotropic solids, the group velocity diverges from the phase velocity both in magnitude and direction. Consequently, the polarizations of the two split shear waves are no longer strictly mutually orthogonal for propagation along seismic rays at the

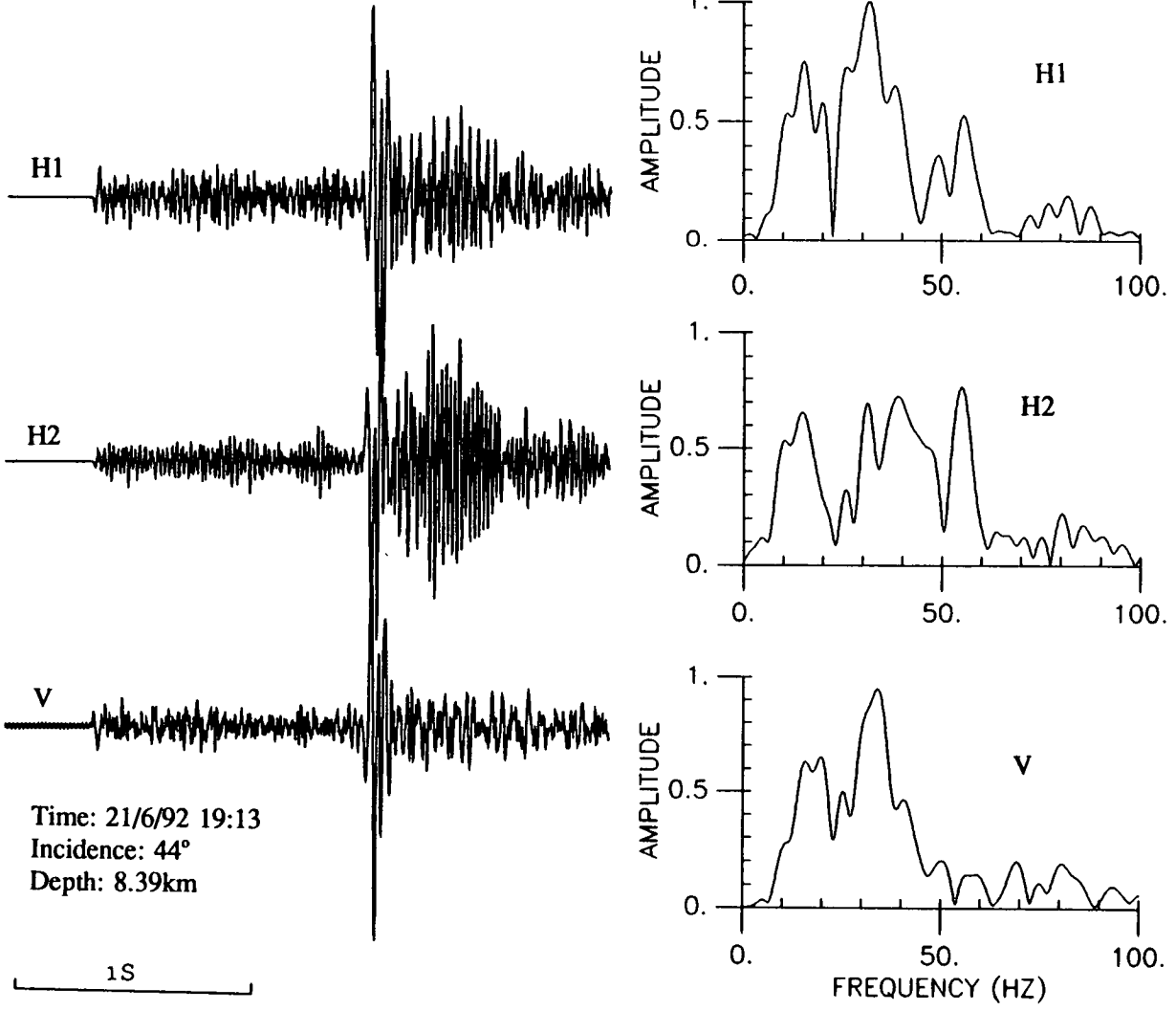

Figure 6.4. An example of a three-component seismogram recorded at 2.5km depth in the Cajon Pass drillhole and the spectrum of shear waves of each component. The window length for the spectra is 0.3s, which starts from the beginning of the shear-wave arrival. The orientations of horizontal components, H1 and H2 are at N15°E and N105°E, respectively.

group velocity except in certain symmetry directions (Crampin, 1981, 1989).

6.4.1 Singularities

There are directions of propagation, known as shear-wave singularities, where the split shear-waves have the same phase-velocities. There are three types of singularities. These are: a line singularity, where the velocity surfaces of qS_1- and qS_2-waves may be considered as intersecting, which can only occur in systems with hexagonal symmetry, where the line singularities are circular, concentric with symmetry axis; a kiss singularity, where the two velocity surfaces touch tangentially; and a point singularity, where the two shear-wave surfaces touch in isolated directions at the vertices of convex and concave cones on the shear-wave velocity surfaces. Kiss singularities always occur along the symmetry axis in hexagonal symmetry and may occur occasionally in other anisotropic symmetry depending on specific elastic constants; Figure 6.5 shows the schematic illustration of the three types of singularities on the two shear-wave phase velocity sheets. Kiss and line singularities generally cause little disturbance to rays of shear waves along neighbouring ray paths (propagating at the group velocity), but the presence of the most frequent occurring singularity in sedimentary basins, the point singularity can significantly disturb the behaviour of shear waves along neighbouring ray paths at the group velocity, more than 10° either side of the singularity (Crampin, 1991).

Point singularities cannot occur in hexagonal symmetry, but can in all other systems of anisotropic symmetry because of symmetry properties. Crampin (1991) investigated in detail the effects of point singularities on shear-wave propagation in sedimentary basins using synthetic seismograms. He found that the polarizations of the leading split shear waves in directions near point singularities may swing through 90° for small changes in ray path direction, while still retaining significant time delays between the split shear waves. This is a result of the complicated relationship of phase and group velocities near directions of point singularities. Bush and Crampin (1987) and Bush (1990) have shown that *PTL*-anisotropy (caused by

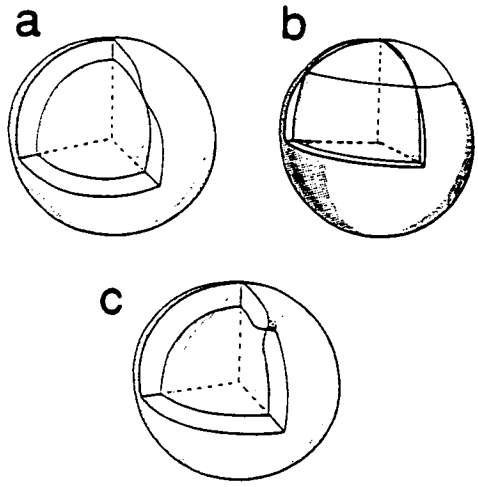

Figure 6.5. Schematic illustration of the three types of singularities on the two shear-wave phase velocity sheets: (a) kiss singularity, where the two sheets touch tangentially at a point; (b) line singularity, where the two sheets may be considered as intersecting; (c) point singularity, where the two sheets touch at the vertices of shallow cones (here much exaggerated) [after Crampin and Yedlin (1981), modified by Crampin 1991].

periodic thin-layers or lithology of mineral grains) has to be taken into account in sedimentary basins. The combinations of *EDA*- and *PTL*-anisotropy lead to orthorhombic symmetry.

6.4.2 Shear-wave splitting in Plate Carée projection

The distinctive feature of shear-wave splitting in parallel vertical cracks displayed on equal-area polar projections displayed for shear-wave recorded at the surface (Figure 1.2) is that the faster shear-wave is polarized parallel to the strike of the vertical cracks for a broad band of directions across the centre of the projection, including almost the whole of the shear-wave window (the effective window is usually 35° or greater at the free surface). This diagnostic feature is seen in almost all observations of shear waves along nearly vertical raypaths in the crust (Crampin, 1987; Crampin and Lovell, 1991). Time delays between the split shear-waves reach maximum values within the same broad band. Equal-area polar projections are usually used to display shear waves with near vertical propagations and recorded at the surface, but it is appropriate to use Plate Carée projections to display polarizations and time delays for raypaths with a wide range of azimuths and dips (Liu *et al.*, 1989; Baptie *et al.*, 1993; Holmes *et al.*, 1993) recorded at subsurfaces in crosshole surveys and offset VSPs. In sedimentary basins, the symmetry (known as *PTL*-anisotropy) is generally found to be azimuthally transversely isotropic (hexagonal symmetry with a vertical symmetry axis), caused by periodic thin-layers or lithology of mineral grains in rocks such as shales. This kind of anisotropy has to be taken into account in interpreting shear-wave splitting (Bush and Crampin, 1991).

Figure 6.6 displays Plate Carée equal-area cylindrical projections of predicted polarizations and time delays of split shear waves propagating along rays at the phase velocity through (a) *EDA*-anisotropy with crack density $CD = 0.01$ and aspect ratio $AR = 0.001$; (b) *PTL*-anisotropy with 1% differential shear-wave anisotropy and (c) the anisotropy of a combination of the material in (a) and (b). The combined

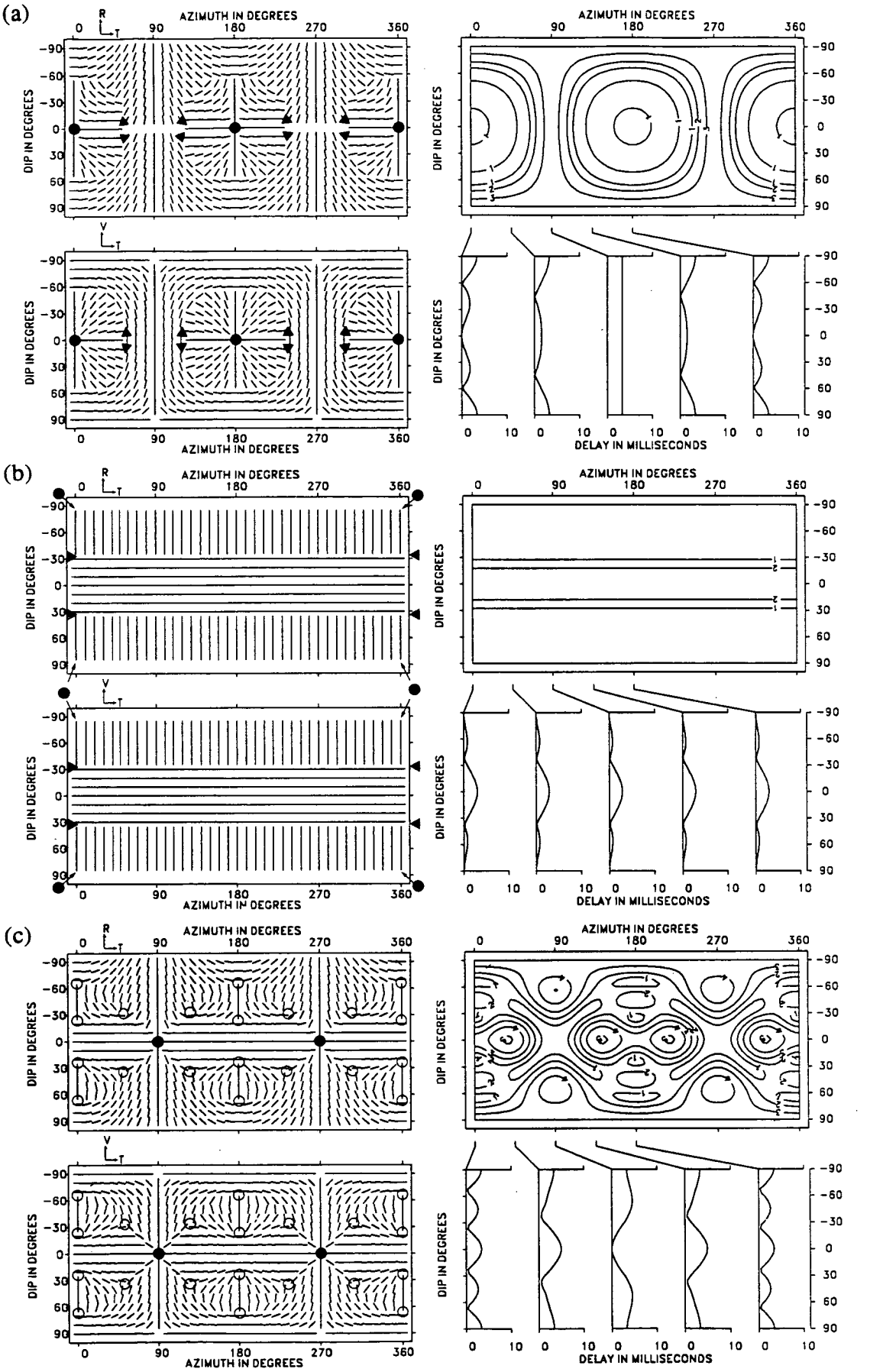

Figure 6.6. Plate Carée equal-area cylindrical projections of predicted polarizations and time delays of split shear waves propagating along rays at the phase velocity through (a) EDA- anisotropy, with crack density CD=0.01 (1% shear-wave anisotropy), aspect ratio AR=0.001; (b) PTL-anisotropy with 1% differential shear-wave anisotropy and (c) the combined anisotropy of (a) and (b). Arrows, solid circles and open circles indicate directions of line singularities, kiss singularities and point singularities, respectively.

material in (c) is of orthorhombic anisotropic symmetry. The four sections of each figure are: polarizations of leading split shear waves projected onto, top left, radial-transverse (*R-T*) plane and, bottom left, vertical-transverse (*V-T*) planes; and, top right, contours of the time delays in millisecond normalised over 1 km and, time delay cross sections of the contours at indicated azimuths. Arrows, solid circles and open circles indicate directions of line singularities, kiss singularities and point singularities, respectively. Note that point singularities cannot occur in hexagonal symmetry, but are present in all other anisotropic symmetries. For example, in Figure 6.6 (a) and (b), with hexagonal symmetry, horizontal and vertical symmetry axis, respectively, there is no point singularities. A full range of raypaths is covered by 360° azimuths and dips from -90° to + 90° indicating upwards to downwards propagation. The features of Plate Carée projections are generally the same as for polar projection. For example, for a fixed aspect ratio, the increase of crack density will not change the pattern of the projection (nor is it changed in a polar projection) but will instead increase the values of time delays for a given model. An increase of aspect ratio increases the width of the broad band of parallel polarizations in polar projection and increases the diameter of the circular features in the cylindrical projection.

6.4.3 Observation of shear-wave splitting

Li *et al.* (1988) have studied shear-wave splitting generated by mode conversion of *P*-waves from surface compressional sources and recorded by orientated geophones at depths from 1300 m to 1820 m at Cajon Pass. They found clear shear-wave splitting with the alignment of polarizations orientated N70°±10°E and an estimated differential shear-wave anisotropy of about 2% to 3%. Daley *et al.* (1988) reported a study of 9-component VSP data recorded at depths between the free surface and 1000 m at Cajon Pass, they documented that shear wave polarizations vary with depth, and at increasing depth the anisotropy changed to a pattern suggesting a maximum horizontal compressive stress direction, normal to the

SAF. This is consistent with the low shear-stress or low frictional coefficient predicted by the heat flow paradox, i.e. the SAF is a weak fault and can be moved by a force field acting almost orthogonally (Zoback *et al.*, 1987; Zoback and Lachenbruch, 1992; Rice, 1992).

Data recorded at the 2.5 km borehole depth have a range of incidence angles from 40° to 80° and about 180° azimuth coverage. It is appropriate and convenient to display the shear-wave polarizations and time delays on Plate Carée cylindrical projections. There are 53 out of 71 events analyzed for shear-wave polarizations and, among them, time delays of 32 events can be positively identified. The events discarded are those which are too small or which provide a poor first split shear-wave arrival, in which case the measurements of polarizations cannot be made positively. Polarizations are weighted from 1 to 3 in term of reliability. Weight 1 is defined with an apparent error less than 5°, weight 2 less than 10° and weight 3 less than 20°. The hypocentral distances range from 5 to 25 km, and time intervals between the split shear waves from 14 ms to 44 ms. They are measured and assigned with an error bound following the same method described in Section 4.4.4 and Appendix I. There are some events that display no clear linearities after the first shear-wave arrivals. This implies that either the time delays are too small and contaminated by noise or late arrivals or that shear waves are travelling near the directions of singularity (Crampin, 1991; Wild and Crampin, 1991; Baptie *et al.*, 1993). Figure 6.7 presents two events displaying shear-wave splitting. Seismograms are plotted with vertical, radial and transverse components; particle motion diagrams are presented on V-T (upper) and R-T (lower) planes; arrows mark the identified first and the second shear-wave arrivals; the relevant parameters regarding the earthquakes are given below each event.

6.5 INVERSION

The high quality data recorded at Cajon Pass deep borehole allow me to measure reliably shear-wave polarizations although the azimuth and incidence angle

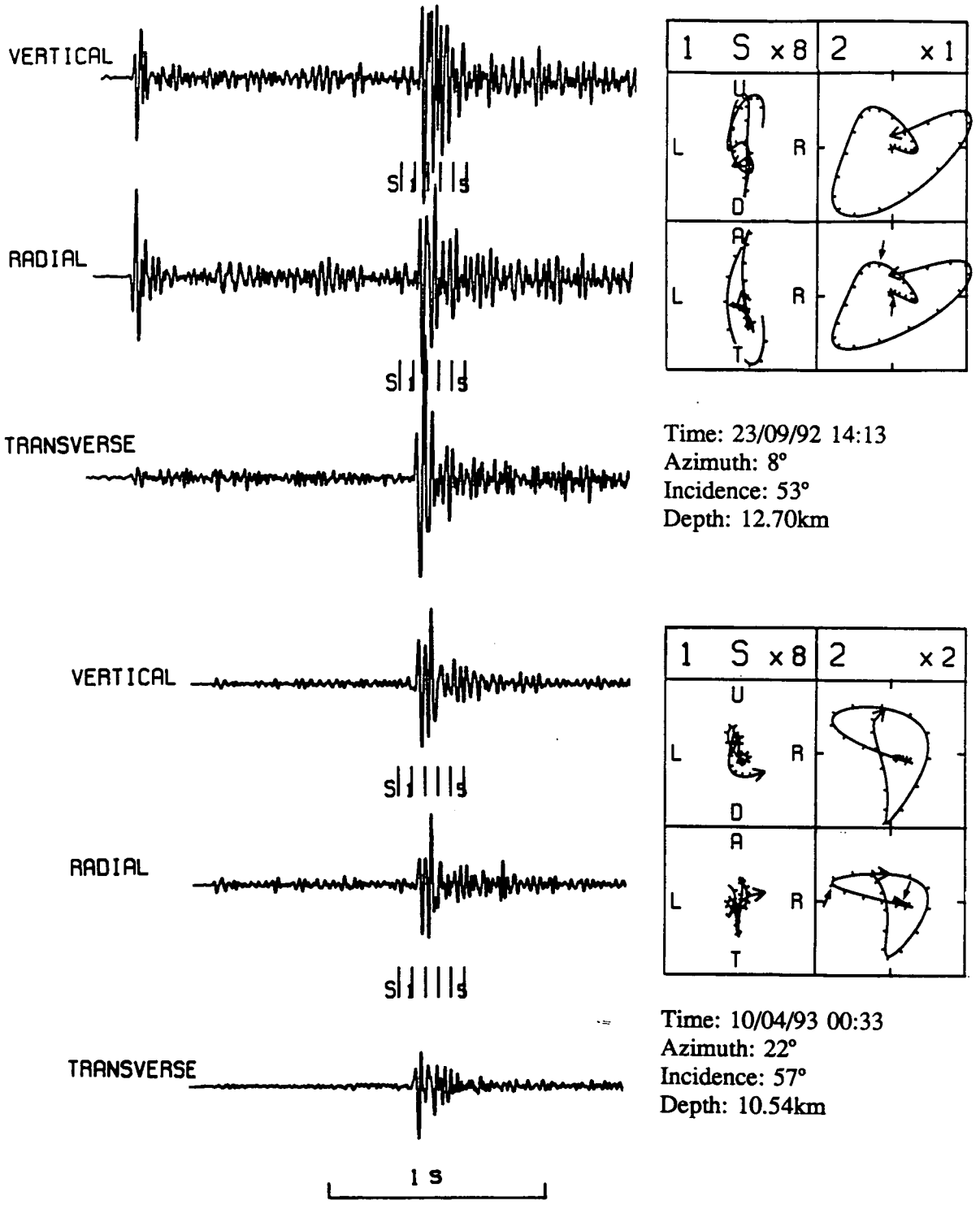

Figure 6.7. Examples showing observed shear-wave splitting. Seismograms are presented with vertical, radial and transverse components. Particle motion diagrams are shown on vertical-transverse and radial-transverse planes. Arrows on the Radial-Transverse particle motion diagrams mark the identified first and second shear wave arrivals. The notations for seismograms and particle motion diagrams are the same as Figure 3.1.

coverage are not good. Here, I attempt to invert a symmetry structure that best matches the observed data using Genetic Algorithms (GA)(Horne and MacBeth, 1994). The advantage of inversion using Genetic Algorithms in comparison with trial and error matching with visualisation is that it objectively relies on the observations and their reliability, which is made by an error bound according to a weight. Genetic Algorithms, which are thought to be non-linear global optimization schemes, are considered as directed searches guided by random processes. Once the predicted velocities and polarizations have been calculated a misfit function between the predicted and observed estimates is evaluated in the form of (Horne and MacBeth, 1994):

$$f(M, \tau^o, p^o) = \frac{1}{2N}\left(\sum \frac{|\tau_i^o - \tau_i^m|}{\delta_{\tau_i}}\right) + \frac{1}{2N}\left(\sum \frac{|p_i^o - p_i^m|}{\delta_{p_i}}\right);$$

where τ^o is a component of the vector of the observed time delays, τ^m is a component of the vector of model estimates for time delays. Similarly p^o and p^m are components of the vectors of the observed and model estimates of polarizations, respectively, δ_i is the error assigned for polarizations and time delays for each observation i. The summations are over the number of polarization and time-delay observations N. More specifically, the vector of model parameter M is a set of crack and orientation values corresponding to one of the chromosomes in the GA's population. Thus, the model is optimised according to the degree of fit of the observed parameters with those predicted by the model.

The best model consistent with the data is of orthorhombic symmetric structure, which is represented as two orthogonally intersecting crack sets, consisting of (1) saturated vertical parallel cracks striking N13°W±10° (mean measure error), which is consistent with the maximum horizontal compressive stress inferred from focal mechanisms at Cajon Pass, and (2) saturated parallel horizontal cracks. The first set has a crack density of $CD_1 = 0.01$ representing about 1% differential shear-wave anisotropy and aspect ratio of $AR_1 = 0.155$, and for the second set, $CD_2 =$

0.015 (1.5% anisotropy) and $AR_2 = 0.155$. The horizontal crack set represents the existence of *PTL*-anisotropy, or the existence of anisotropy induced by either lithology aligned mineral grain or aligned crystals. This most appropriate model gives a misfit value of 2.46, while the maximum misfit value is 30.38 in the models that GA searched. The average *P*-wave velocity (V_p) is taken as 6.0 km/s and the ratio of *P*-wave and *S*-wave velocity (V_s), V_p/V_s as $\sqrt{3}$, with density $\rho = 2.65$ g/cm^3 for the isotropic rockmass used in the inversion, following the values used in earthquake location by a single station (R. Abercrombie, personal communication). Figure 6.8(a) displays the equal-area cylindrical projections of polarizations and time delays inverted from the observations of 53 polarizations and 32 time delays, and (b) is the polarizations with superimposed observations and the observed contour projection and cross sections of time delays. Note that time delays are plotted with inversion symmetry, which mirror reflects the observations in the upper projection and effectively doubles the data so as to image time delays properly. Open circles mark the approximate locations of point singularities. Note that the patterns of the observed time delays in the contour map shown in Figure 6.8 display far more complexity and irregularity than that of the model predicted. This is probably attributed to the difficulties in the identification of the second split shear waves, and therefore, time delays are scattered at a certain level. However, the general features of the distribution of time delays, for example, large delays in the central band, shown in the model predicted, can be seen in the patterns of observations, although there are some local irregularities, including large values of observed delays at large dips. The agreement of the general features is also seen in the plot of cross sections of the observations.

Another medium which could model the observed polarizations and time delays is a dipping orthorhombic structure. The symmetry class is identical to that of orthorhombic symmetry but an additional degree of freedom is required to specify the orientation of the symmetry axis from the vertical. The inversion gives the model parameters $CD_1 = 0.005$, $AR_1 = 0.155$; $CD_2 = 0.01$, $AR_2 = 0.155$; the strike of the saturated parallel vertical cracks is in the direction of N7°W ± 10° (mean measure

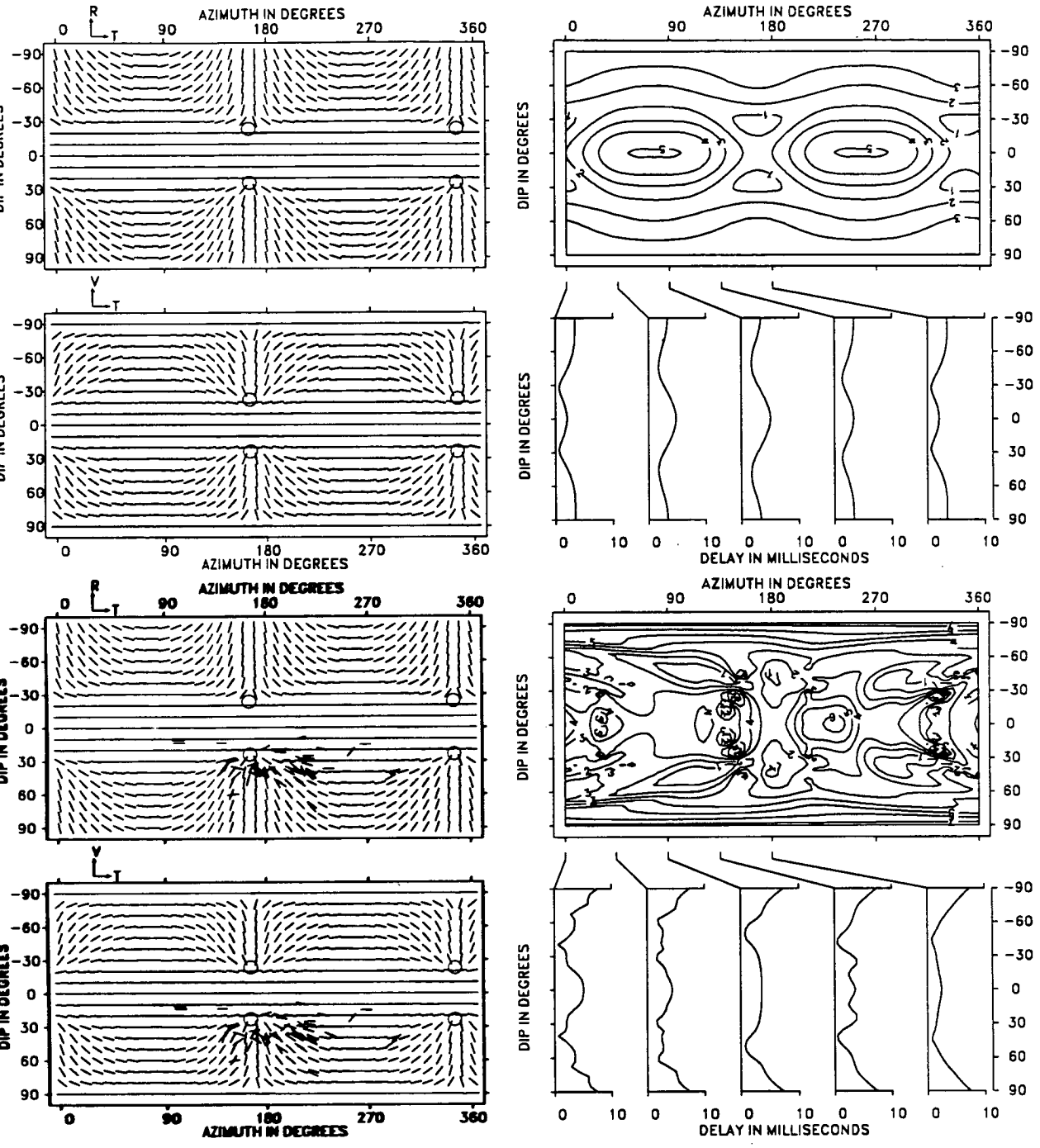

6.8. The best model consistent with the observations of polarizations and time delays calculated by Genetic Algorithms. The model orthorhombic symmetry, representing the combination of (1) EDA- and (2) PTL-anisotropy, with crack density CD_1=0.01, aspect AR_1=0.155, and CD_2=0.015, AR_2=0.155 for orthogonally intersecting crack sets respectively. The cracks representing EDA- and nisotropy are saturated. The strike of the vertical parallel cracks is in the direction of N13°W. The isotropic rockmass is of *P*-wave ty Vp=6.0km/s, *S*-wave velocity Vs=3.46km/s, and density ρ=2.65g/cm^3. (a) equal-area cylindrical projections of polarizations (left), e projections of time delays shown in contour and cross sections at indicated positions (right). (b) the model with superimposed vations of polarizations (left), and observed time delays in contour map and cross sections (right). Note time delays are plotted using ion symmetry. Open circles mark the approximate locations of point singularities.

error), and the saturated two orthogonal crack sets (or the orthorhombic structure) dip 21° to the southeast. Note that this model has smaller crack densities than the previous model, and the orientation of the vertical cracks is modified from N13°W to N7°W. The misfit value is 2.41 for this model, corresponding with the maximum misfit value of 38.83 in the models that GA searched. The decreased misfit value in comparison with the previous model do not necessarily mean the increase of significance since an extra degree of freedom (dip) introduced will tend to decrease the misfit value. Figure 6.9 (a) shows the inverted model with dipping orthorhombic structure and (b) with superimposed observed polarizations; time delays are the same as in Figure 6.8, plotted with inversion symmetry. We can see that the characteristics of the cylindrical projections on *R-T* and *V-T* planes become asymmetric between upwards and downwards propagation.

I have also investigated other possible symmetric systems that could model the observed data, for example, the simplest hexagonal anisotropic symmetry, which is transverse isotropy with horizontal symmetry axis (*TIH*) for vertical parallel cracks; and dipping hexagonal symmetries. It is seen in Figure 6.8 and 6.9 that when dips are less than about 20°, particularly when dips closer to 0°, shear waves polarized horizontally on both *R-T* and *V-T* planes. This means the existence of *PTL*-anisotropy has to be taken into account so as to model these horizontally polarized observations. The inversion for the *TIH* and dipping *TIH* symmetries verified such prediction, demonstrated by the mismatch with the horizontally polarized observations.

Figure 6.10 displays the velocity variations in the three mutually-perpendicular symmetry planes, *x-y*, *y*-z and *z-x*, for the first model in Figure 6.8. The y-z plane is parallel to the strike of the *EDA* cracks and the z-x plane perpendicular. The point singularity is marked by a black dot. Note that the anisotropy is so weak, about 1% *EDA*-anisotropy and 1.5% *PTL*-anisotropy, and the phase- and group-velocity lines are indistinguishable on all three planes. Note here, I do not attempt to investigate the depth extent of shear-wave anisotropy because time delays are more complicated than that in the hexagonal symmetry, in particular,

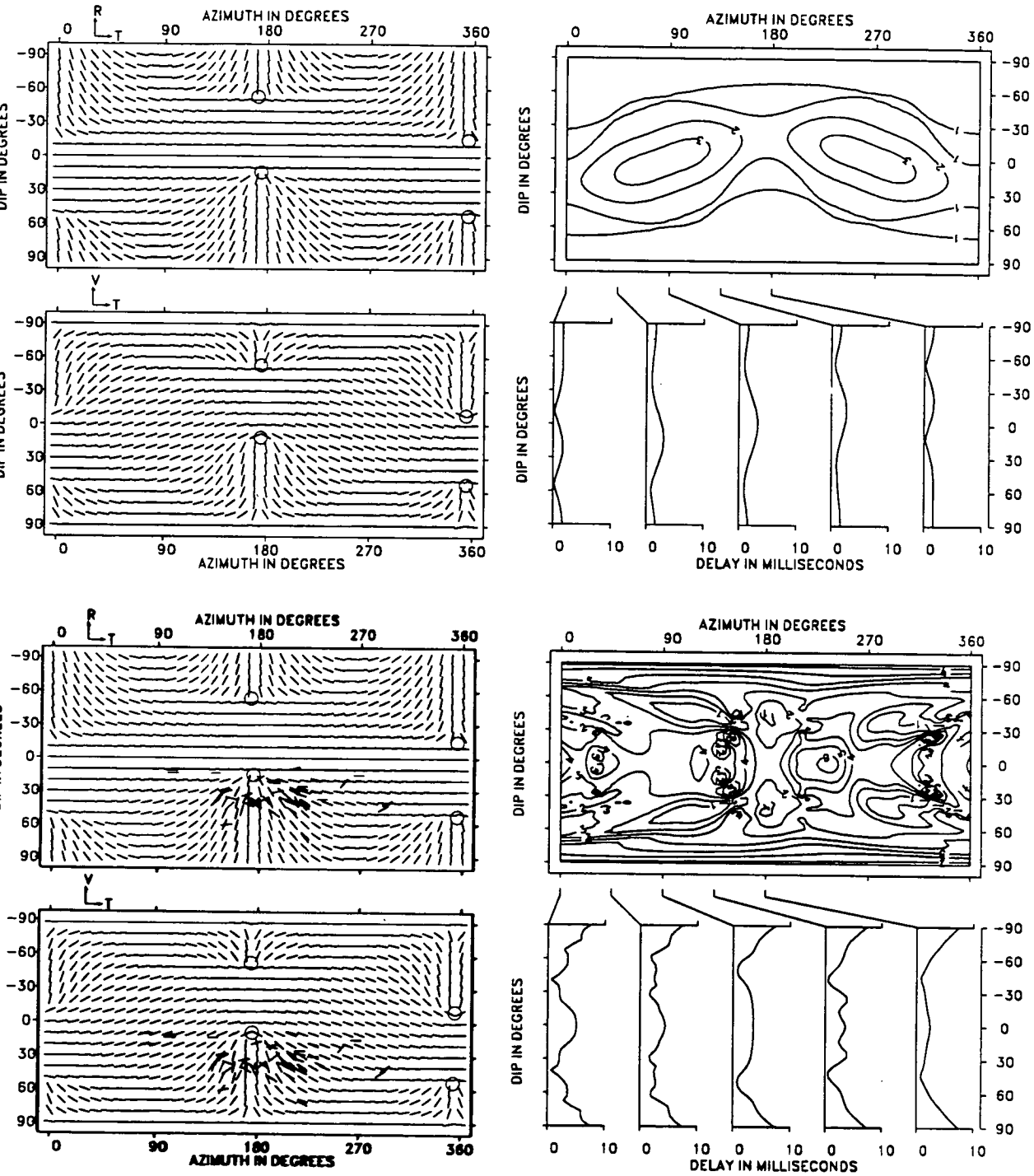

e 6.9. The model consistent with the observations of polarizations and time delays inverted with dipping orthorhombic anisotropic etry. The symmetry class is identical to that of the orthorhombic symmetry as shown in Figure 6.8, but an additional degree of om is required to specify the orientation of the symmetry axis from the vertical. (a) equal-area cylindrical projections of polarizations and the projections of time delays shown in contour and cross sections at indicated positions (right) (b) the model with mposed observations of polarizations (left), and observed time delays same as in Figure 6.8 (b), plotted using inversion symmetry. otation of this diagram is the same as in Figure 6.8.

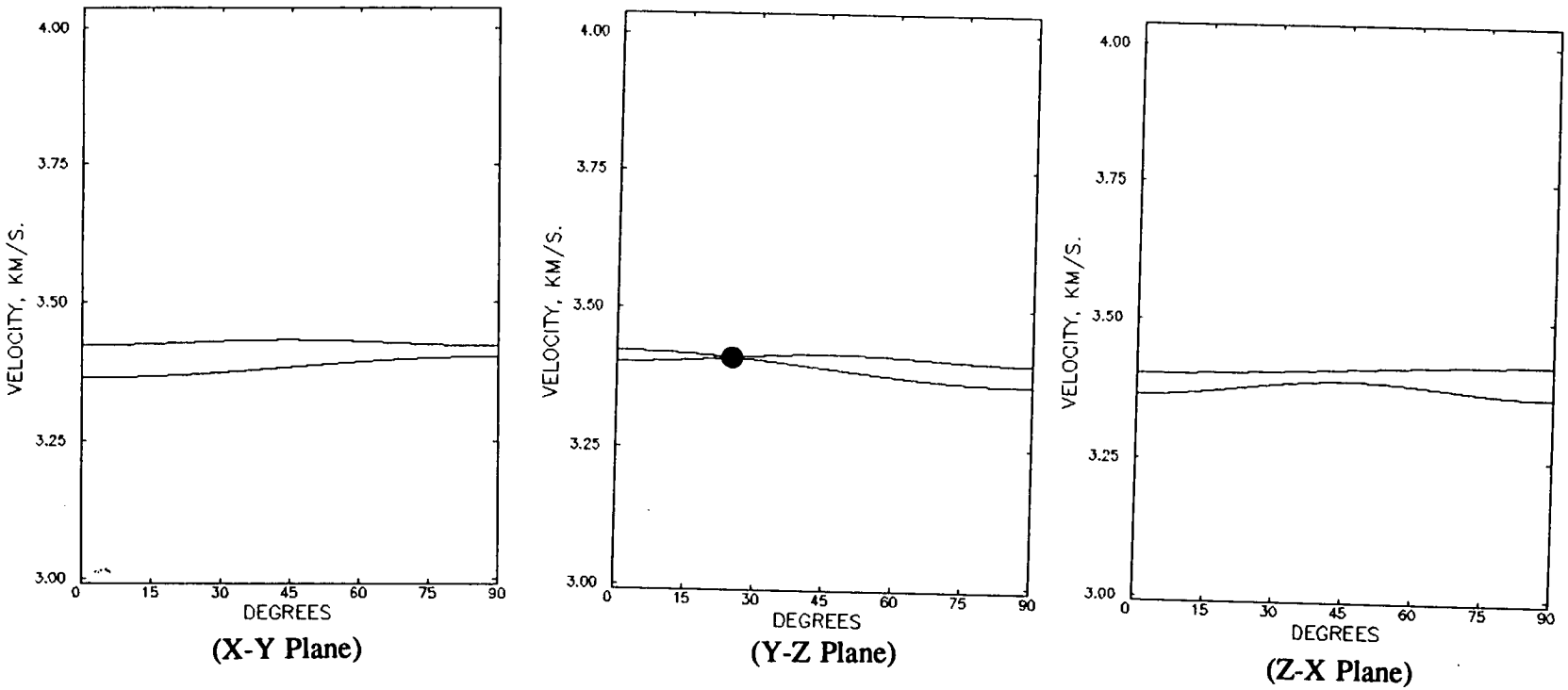

Figure 6.10. Velocity variations in the three mutually perpendicular symmetry planes, x-y, y-z and z-x, for the medium corresponding to the best fitted model (Figure 6.8). The y-z plane is parallel to the strike of the EDA cracks and z-x plane perpendicular. Note the anisotropy is so weak that the phase and group velocity lines are indistinguishable on all three planes.

when waves travellling near the direciton of point singularities. In the next section I shall interpret how the maximum horizontal stress inferred from this model relates to the geology at Cajon Pass, and present supporting evidence for such orthorhombic symmetry.

6.6 INTERPRETATION

6.6.1 Stress field near Cajon Pass

Wellbore breakouts (Shamir *et al.*, 1988; Shamir and Zoback, 1992) and hydraulic fractures (Healy and Zoback, 1988; Zoback and Healy, 1992) suggest that the direction of the maximum horizontal stress at Cajon Pass is about N57°E ± 19° almost orthogonal to the SAF, which is consistent with the results of seismic anisotropy measured at depth between 1000 m and 1820 m (Li *et al.*, 1988). Wang and Sun (1988) examined cores under both optical and electronic microscopes sampled from 745 to 1742 m at Cajon Pass and found three sets of microcracks, all dipping subvertically. The oldest set (set to 2) consists of mineralized microfractures with an orientation of N40° - 50°W. A younger set (set to 3), less prominent in appearance, consists of mineralized microfractures with an orientation of N68° - 76°E and the most recent set (set 1) consists open microcracks with fresh walls, with orientation of N14° - 28°W. Based on the elementary consideration in fracture mechanics, they concluded that the second and the last sets (set to 3 and 1, respectively) of microcracks are consistent with a mean orientation of present state of stress at N70°E. However, the maximum horizontal stress inferred from earthquake focal mechanisms at Cajon Pass is N17°W, which is consistent with the direction of N13°W derived from this study. In contrast to the study of shear-wave splitting made by Li *et al.* (1988), the inferred maximum horizontal stress from my study probably represent the property of the seismogenic zone, whereas their result might reflect the stress field of shallow crust. The average orientation of the maximum horizontal stress along the southern SAF, determined from earthquake focal mechanisms is N5°W (Jones, 1988), which generally agrees with previous focal

mechanism studies (Zoback and Zoback 1980; Pechman, 1983; Webb and Kanamori, 1985). The orientation of principal horizontal strain determined from geodesy (Savage *et al.*, 1986) is remarkably consistent with the stress orientation derived from seismicity. This is consistent with essentially pure strike-slip motion all along the southern SAF.

Weldon and Springer (1988) studied the relationship between active faulting and the stress orientation near Cajon Pass. They pointed out that the overall pattern of faulting in southern California, dominated by northwest striking right-lateral faults, northeast striking left-lateral faults, east striking thrust faults, and north-south striking normal faults, suggests a regional stress regime dominated by north-south shortening, which is supported by regional studies of seismicity. However, active secondary faults and folds are very common within 15 km of the entire southern SAF, and the movement of these active secondary faults are consistent with having maximum horizontal stress at the direction of about N57°E ± 19° determined by *in-situ* stress measurement in the borehole. They typically exhibit fault normal extension and compression (Weldon and Springer, 1988). This is inconsistent with the strike-slip on the SAF or other faults beyond 15 km. Since these secondary faults and folds are only found close to the SAF and do not seem to be responding to stresses inferred from focal mechanism studies that reflect the stresses near the base of the seismogenic zone, it was deduced by Weldon and Springer (1988) that there is a fault-localised, depth-dependent influence on the regional stress caused by the presence of the SAF. If the stresses near the base of seismogenic zone are different from those measured in the well, the SAF may be driven by deeper stresses than the secondary structures (Weldon and Springer, 1988).

Weldon and Springer's inference is supported by the result of this study. Firstly, the maximum horizontal compressive stress inferred from the alignment of parallel vertical cracks is consistent with the movement on the major SAF; Secondly, Since the alignment of parallel vertical cracks is almost the same as the maximum horizontal stress in the seismogenic zone inferred from focal mechanisms, and the focal depths of the earthquakes used for shear-wave polarization measurements are

between 5 km and 20 km, it is likely that the phenomenon of shear-wave splitting is attributed to the seismogenic zone although we cannot rule out the possibility that a particular thick layer at a certain depth below the receiver could be the cause because the theoretical concept of a shear wave propagation in an anisotropic medium (Hudson, 1980) takes a long wavelength approximation, which is equivalent a mean effective medium in which shear waves sampled.

6.6.2 Interpretation of orthorhombic symmetry

The best model consistent with the observed data is an orthorhombic anisotropic structure. The polarization of the saturated parallel vertical cracks suggests that the maximum horizontal compressive stress is approximately in the direction of N13°W, which is consistent with the results inferred from earthquake focal mechanism studies. Both *EDA*-anisotropy and *PTL*-anisotropy are weak, about 1% and 1.5% respectively. From geologic evidence, *PTL*-anisotropy could be induced by both lithology mineral grains and aligned crystals. The Cajon Pass drill hole located on the southwest Mojave desert. The basement consists of crystalline foliated rocks, ranging from weak alignment of mafic minerals in the granodiorates to strong preferred orientation of minerals and compositional layering in paragneisses and migatitic gneisses. Apart from lithologic variation, such as compositional layering in paragneisses and migatitic gneisses, there is also some evidence which indicates a sedimentary origin in some local areas (Ehlig, 1988). Therefore, the crystallized lithology of mineral grains and crystals could be responsible for the observed *PTL*-anisotropy. The alignments of foliated rocks are locally variable, striking about northwest in granodiorite rocks, and striking from northeast to east in gneiss dominated rocks. However, the alignment of vertical cracks inferred from this study seems not associated with the directions of rock foliation. It is suggested, as studied and discussed in the previous chapters and in literatures by many other investigators, that stress-aligned *EDA* cracks are responsible for the hexagonal symmetry with horizontal symmetry axis. The combination of *PTL*-anisotropy

induced by the lithologic mineral grains and crystals with *EDA*-anisotropy induced by stress-aligned vertical parallel cracks leads to the orthorhombic anisotropy structure which is difficult to explain by any other mechanisms.

6.7 CONCLUSIONS

The relatively 'quiet' Cajon Pass deep drill hole provides a good opportunity to study shear-wave anisotropy in the crust under conditions of enhanced signal/noise ratio. The high quality data used in this study permits the reliable measurement of shear-wave polarizations and hence allows a statistically-significant model to be inverted by the Genetic Algorithms despite the comparatively narrow angular range of azimuths.

The resulting model is of an orthorhombic anisotropic symmetry, comprised of two hexagonal anisotropic symmetries, interpreted as *EDA*-anisotropy induced by stress- aligned saturated vertical parallel microcracks and *PTL*-anisotropy induced by the aligned lithologic mineral grains and crystals. The differential shear-wave anisotropy derived by this model is weak, approximately, 1% and 1.5% for *EDA*- and *PTL*-anisotropy respectively. Such weak crack-anisotropy is compatible with the general impermeable metamorphic rock type at Cajon Pass.

The strike of the parallel vertical microcracks suggests that the maximum horizontal compressive stress is approximately in the direction of N13°W ± 10° (mean measure error), consistent with results of earthquake source mechanisms. This direction supports the pure right-lateral strike slip motion on the major SAF, and hence, it is suggested from this study that the SAF is probably driven by deeper stresses rather than the secondary structure, and the active secondary faults and folds are probably driven by the relatively shallow stresses as measured in the borehole. The study of shear-wave splitting at Cajon Pass is further evidence of seismic anisotropy on the SAF, following that at Parkfield, which has been discussed earlier in this thesis.

CHAPTER 7

CONCLUSIONS, DISCUSSIONS AND SUGGESTED FUTURE WORK

7.1 MAIN RESULTS FROM THIS THESIS

I have so far completed the answers to the questions proposed in Chapter 1. Firstly, shear-wave splitting has been identified clearly at both Parkfield, central California and Cajon Pass, southern California. I have shown in Figures 4.1 and 4.9 and in Appendix I, that the data that were used in deriving the results are of sufficiently high quality that the analysis of shear-wave splitting is reliable. I have also demonstrated (in Chapter 3) that neither shear head waves travelling along the fault zone nor converted waves are crucial to the analysis of data, although care should be taken in the analysis for shear-wave splitting.

Shear-wave polarizations in the intact rocks at Parkfield generally exhibit parallel alignment with ±20° deviations (at stations VC, VR and ED), as normally observed in many other studies. This alignment is consistent with the direction of maximum horizontal compressional stress. In the fault zone, shear-wave polarizations (at station MM) are aligned parallel or subparallel to the fault as they are at several stations elsewhere located near or on fault zones, which shows the influence of fault internal structures and the irregularity (localization) of the stress field in the fault zone. Polarizations are systematically rotated up to 90° due to local geologic structure, such as dipping subsurface layers. At station JN, the dipping subsurface layers have effectively enlarged the internal shear-wave window so that shear-wave polarizations are about 20° -30° deviated from other stations (VC, VR and ED). The irregularity of surface and subsurface topography can severely distort shear-wave polarizations. This may explain in part the irregular shear-wave polarizations observed at stations ST and FR. Secondly, parallel or subparallel fluid-filled vertical cracks (*EDA*-cracks) are found to be the general cause of shear-wave splitting in this study (exclude station MM).

Modelling the waveforms and shear-wave particle motions using derived earthquake sources has encouraged further confidence in such interpretation (Chapter 5).

Thirdly, temporal variations of time-delays between faster and slower shear-waves are observed before and after a M_L = 4 earthquake (Liu *et al.*, 1993). This observation has been examined in detail through error analysis and earthquake multiplets. The analysis of possible maximum error based on the best quality data shows that the temporal variation is clearly visible with significance at the 68% confidence level. This temporal variation is also demonstrated through the study of earthquake multiplets. This means that there was probably a change in stress, which modified the geometry of cracks or microcracks pervading the crust before and after this event, so that the time delays between faster and slower shear-waves for the similar events travelling along nearly the same wave paths and occurred at different times display a distinct increase before the time of the M_L = 4 earthquake, and a decrease afterwards. It is found that normalised time delays in the fault zone (at station MM) are about twice as large as those in the intact rocks, 5 km away from the fault (at station VC). This suggests that fluid-filled cracks and fractures within the fault zone are more extensive than those in the surrounding rocks. This is consistent with the explanation that fault parallel polarizations of leading split shear-waves at station MM are attributed to the fault internal structures, as observed in other cases near fault zones (Aster and Shearer, 1992; Zhang and Schwartz, 1994).

To find out the cause of such temporal variation I have examined the correlation between time delays and seismic moment, earthquake focal depth, raypaths and change in crack density and aspect ratio of cracks. I find that temporal variations are unlikely to be related to the seismic moment. In other words, they are unlikely to be caused by the differences in source time functions, nor caused by depth migrations of earthquake foci. The observed time delays can be basically matched with the theoretical curve calculated by Hudson's ellipsoidal inclusion model, which calculates elastic constants of a medium containing cracks given isotropic matrix properties, crack liquid infill, crack density, and aspect ratio of the cracks. Study of the change in crack density and aspect ratio for the observed temporal variation in time delay suggests that

stress concentration before the M_L = 4 earthquake probably slightly increased the number of cracks or the radius of the cracks, and bowed the cracks; after the release of strain energy after the earthquake, stress reduced to a lower level, accompanied by healing and flattening of the cracks. The change of crack density and aspect ratio associated with the M_L = 4 earthquake is interpreted to have caused the observed temporal variations. Such interpretation has recently been quantified by Zatsepin and Crampin (1994).

The study of the Cajon Pass dataset recorded in a 2.5 km deep borehole shows distinct shear-wave splitting. The high quality of this dataset allows the reliable measurement of shear-wave polarizations, and a statistically-significant model to be inverted by Genetic Algorithms. The resulting model is of an orthorhombic anisotropic symmetry, with a combination of approximately 1% and 1.5% respectively of crack-induced (*EDA*) and fine layer-induced (*PTL*) anisotropy. The *PTL*-anisotropy can be explained by the aligned lithologic mineral grains and crystals, which is supported by the geological evidence. The strike of the parallel vertical microcracks suggests that the maximum horizontal compressive stress direction is approximately N13°W, which is consistent with the results from earthquake source mechanisms, and supports the pure right-lateral strike slip motion on the San Andreas fault. It is suggested from this study that the San Andreas fault is driven by deeper stresses rather than the secondary structure close to the fault, and the active secondary faulting and folding are probably driven by the relatively shallow stresses as measured in the deep borehole.

At last, investigation of the depth of the observed anisotropy suggests that shear-wave anisotropy is probably concentrated in the top 10 to 15 km of the Earth's crust at Parkfield. In the fault zone (at station MM), the degree of seismic anisotropy decrease with earthquake focal depth suggests that the fault gouge of the San Andreas fault is probably terminated at a depth about 8 km, which is consistent with other studies (Malin, *et al.*, 1989; Li *et al.*, 1992).

7.2 DISCUSSION

7.2.1 Polarizations

It seems clear now that study of shear-wave splitting can provide useful information about the crustal structure and current stress field in a region. However, It has to be noted that in a complicated area, such as near or in a fault zone, shear-wave polarizations often display anomalous alignments, implying that it is fault internal structure of microcracks and faults or rock foliation that controlled fault parallel alignment, for example, at station MM in this study, at station KNW on the San Jacinto fault; California (Crampin *et al.*, 1990); at several stations in the Loma Prieta segment of the San Andreas fault (Zhang and Schwartz, 1994); and in Japan (Kaneshima, 1990). In a complicated subducting zone (Gledhill, 1993a, b), shear-waves sampled two different anisotropic regions, so that shear-wave polarizations vary significantly between nearby stations (only 2 to 3 km apart). These anomalies imply that a rockmass with hexagonal symmetry will be effectively anisotropic, and the leading shear-wave polarizations may not necessarily be determined by stress-induced aligned cracks. Any rocks with vertical or near-vertical bedding or cleavage planes have hexagonal symmetry about a horizontal or near-horizontal axis, similar to the observed symmetry of *EDA*-cracks (Crampin and Booth, 1985). Therefore, the interpretation of shear-wave polarizations has to be accompanied with the local geological evidence. The combination of aligned microcracks and aligned rock fabric in different planes would generally cause orthorhombic anisotropy symmetry as demonstrated in Chapter 6, and monoclinic symmetry or triclinic symmetry in the extreme case of an intrinsically anisotropic rock pervaded by two or more non-orthogonal sets of aligned cracks (Crampin, 1978; Liu *et al.*, 1993). We have been trying to understand the nature of these anomalous polarizations which reveals the geologic structure. It is clear that no study of crustal structure can now claim to be complete without considering the effects of anisotropy.

7.2.2 Time delays

There has been argument about whether time delays can be used to monitor the intrinsic stress field of crustal rocks. The question was raised first from the reliability of the measurement of time delays, then the complexity and large uncertainties in the process involved. It appears that all published shear-wave time delays, no matter what the measurement technique employed, show large scatter (Peacock *et al.*, 1988; Aster *et al.*, 1990, Crampin *et al.*, 1990; Booth *et al.*, 1990; Kaneshima, 1990; Shih and Meyer, 1990; and also this study). For the studies that claimed to be observations of temporal variations (including this study, and also Peacock *et al.*, 1988; Booth *et al.*, 1990; Crampin *et al.*, 1990) the argument focused on the techniques that were used in measurement of the parameters of shear-wave splitting. In this study, I aimed to reveal the measurement to convince and let others judge for themselves the reliability of my measurements, and through detailed examination to understand whether the observed temporal variation is statistically significant (Figures 4.1, 4.9 and Appendix I). I have demonstrated, through various studies based on the quality of these datasets, that the detected temporal variations at Parkfield are statistically significant. It is probably firm evidence that further proves the *EDA* hypothesis as a new physical basis for earthquake prediction research proposed by Crampin *et al.* (1984b).

7.3 SUGGESTED FUTURE WORK

Nadeau *et al.* (1994) found 80 microearthquake clusters during the period 1987 to 1989 in the Parkfield segment. Each cluster occupies a small region, typically about 100 to 200 m in extent within the fault zone (note earthquakes were located simultaneously using a three-dimensional velocity structure). These cluster events are invaluable in the detailed study of shear-wave temporal variation as they were in my study in Section 4.4.3. I may be able to use these cluster events to confirm the observed temporal variation of time delays found in this study.

The investigation of observed temporal variation suggests that the aspect ratio

of cracks and crack density have probably increased due to stress concentration before the M_L = 4 earthquake, and after the release of strain energy cracks start to close and heal, which effectively decreases crack density and aspect ratio. Numerous studies have shown that scattering attenuation (Q^{-1}) is related to the crack density (Hudson, 1981; Lerche and Petroy, 1986) and viscosity of the fluid filling the cracks or pore space (White, 1965). It has been suggested by Jin and Aki (1989) that Q^{-1} is more sensitive to fractures than the seismic velocity. There have been many papers reporting changes in coda Q^{-1} associated with the occurrence of major earthquakes since temporal change in coda Q^{-1} was first observed by Chouet (1979) at Stone Canyon, California. Recently, Su and Aki (1989) studied coda Q^{-1} for earthquakes occurring in the vicinity of the North Palm Springs earthquake of 1986, and reported a significant temporal change in coda Q^{-1}, although they had paid careful attention to the factors that could introduce systematic changes in coda Q^{-1}, such as source mechanisms of earthquakes, epicentres and focal depths, selected time window and the selected stations used for coda analysis. Therefore, it may be possible to verify the observations and interpretation of temporal change of my results by studying coda Q^{-1} of local earthquakes at Parkfield, preferably by using the same dataset as used in this thesis.

Shear-wave splitting has clearly become a useful tool in understanding the geometry and geologic structure of the subsurface in exploration seismology. Various studies on seismic exploration have shown that polarizations are consistent with the maximum horizontal stress in the oil field, and differential shear-wave anisotropy, indicating aligned cracks, correlates with rates of hydrocarbon production, for example: by Lewis *et al.*, (1991), using three-dimensional three-component reflection surveys in the Silo field, in Wyoming; and (Li *et al.*, 1993) three lines of three-component shear-wave reflection surveys in an area without many producing wells, on the edge of a producing field and in the middle of a producing field, respectively; and also (Yardley and Crampin, 1993) in VSPs in Texas. Similarly, Cliet *et al.* (1991) correlate the percentage of shear-wave splitting noted on two VSPs in the Romashkino oil field, Tatarskaya, Russia with hydrocarbon production rates, and estimating the properties from the cores of reservoir rock, Brodov *et al.* (1991) were able to correlate the rates

of production almost exactly with reservoir properties derived from the analysis of cracks within cores examined in the laboratory. All the above evidence indicates that shear waves carry much information about cracks and fluid in the crust, and fully understanding the propagation of shear waves has potential applications. Recently, scientists have drawn attention to the delays of arrival time in a VSP recording which continuously recorded shear-waves with the increase of water injection in a well (Queen, 1994). This phenomenon is consistent with the observation of temporal change in time delays detected in this study. Obviously, with the increase of injection of water in the oil field the stress field probably has been modified. Water as an effective agent at crack tips has speeded up stress corrosion, and has potentially increased crack density and aspect ratio.

Earthquake prediction has experienced a long period of decline largely because of the complexity and uncertainties in the rock failure process. The decline involves not only the study of shear-wave temporal variation as a precursor of large earthquakes, but also other methods including variations in attenuation, *b*-value, and other phenomena. Clearly, 68% confidence for temporal variation as a precursor is still too low to establish whether or not earthquake prediction is a practical possibility. However, the identification of temporal variation based on sufficiently high quality data has produced positive and interesting results in this study, which is limited by the time constraints of a PhD and the data available. The subject of seismic anisotropy is still relatively young, and the application of shear-wave anisotropy to earthquake prediction is even younger. What we are doing now, I believe, is accumulating basic data on earthquake occurrence from the seismic activity of different geological structures throughout the world.

APPENDIX I

SEISMOGRAMS AND PARTICLE MOTION DIAGRAMS FOR THE DATA OF WEIGHT 1 AT STATIONS MM AND VC

There are 14 events given weight 1 at station MM and 9 events at VC, which are used in the experimental error analysis. They are listed in Table AI-1. In order to clearly visualise the delays between the split shear waves I have rotated seismograms to make the 'fast' and 'slow' direction respectively parallel to, and orthogonal to, the polarization direction of the leading split shear-waves.

As I have described in Section 4.2.4 that Weight 1 is given to the polarizations and time delays if the particle motions display clearly the onset of the first shear-wave arrival and there is a sufficient large linearity interval between the two split shear waves, and a large energy on the orthogonal direction of the leading shear-wave polarization for the second arrival. In the cases when time delays are not large enough to separate the two split shear waves, the second shear wave arrival is marked by the start of ellipticle motion followed by a large energy of motion on orthogonal direction. This is the behaviour of shear-wave splitting in an ideal homogeneous anisotropic halfspace. However, in practice, the second arrival becomes difficult to identify because it superimposed on both signal generated and background noise. Here I use an arrow head to mark the onset of either the first or the second shear-wave arrival with misidentifying sample intervals less than 2 or 3 (4ms or 6ms); use a small fine arrow to indicate the possible earliest arrival of either the first or the second shear wave; use a heavy large arrow to indicate the possible latest onset for both shear waves. This means the time interval between the possible earliest and latest arrival for either the first or the second split shear wave is considered due to the effect of noise. The procedures for the analysis of possible maximum errors of time delays have been described and formulated in Section 4.4.4 of Chapter 4. The seismograms and particle motion diagrams are presented here.

Table AI-1: List of the events of weight 1 used at stations MM and VC.

No.	Stn	Date	Time	Dep	Azim	Ainc
1	MM	880519	1349	2.70	110°	29°
2	MM	881006	1741	4.85	117°	35°
3	MM	890218	0055	4.88	339°	9°
4	MM	890223	1807	5.55	328°	39°
5	MM	890327	1426	6.32	123°	31°
6	MM	890409	1918	4.74	123°	34°
7	MM	890411	1329	5.29	122°	28°
8	MM	890514	1932	5.39	335°	34°
9	MM	891003	1934	4.10	122°	36°
10	MM	891223	1503	5.11	124°	30°
11	MM	900813	0536	4.79	324°	40°
12	MM	900907	0915	6.41	123°	32°
13	MM	900907	0924	5.88	120°	34°
14	MM	901029	1109	5.47	117°	10°
15	VC	880727	0301	10.50	344°	22°
16	VC	881117	0022	9.73	189°	21°
17	VC	890106	0323	12.12	184°	19°
18	VC	890505	0504	10.86	181°	23°
19	VC	890825	0408	8.05	203°	25°
20	VC	900702	1728	13.29	224°	17°
21	VC	900823	0122	11.18	191°	24°
22	VC	900902	1147	9.13	236°	29°
23	VC	901128	0059	13.10	220°	21°

Stn: station name, Dep: depth in kilometres, Azim: azimuth from the north to the east; Ainc: angle of incidence.

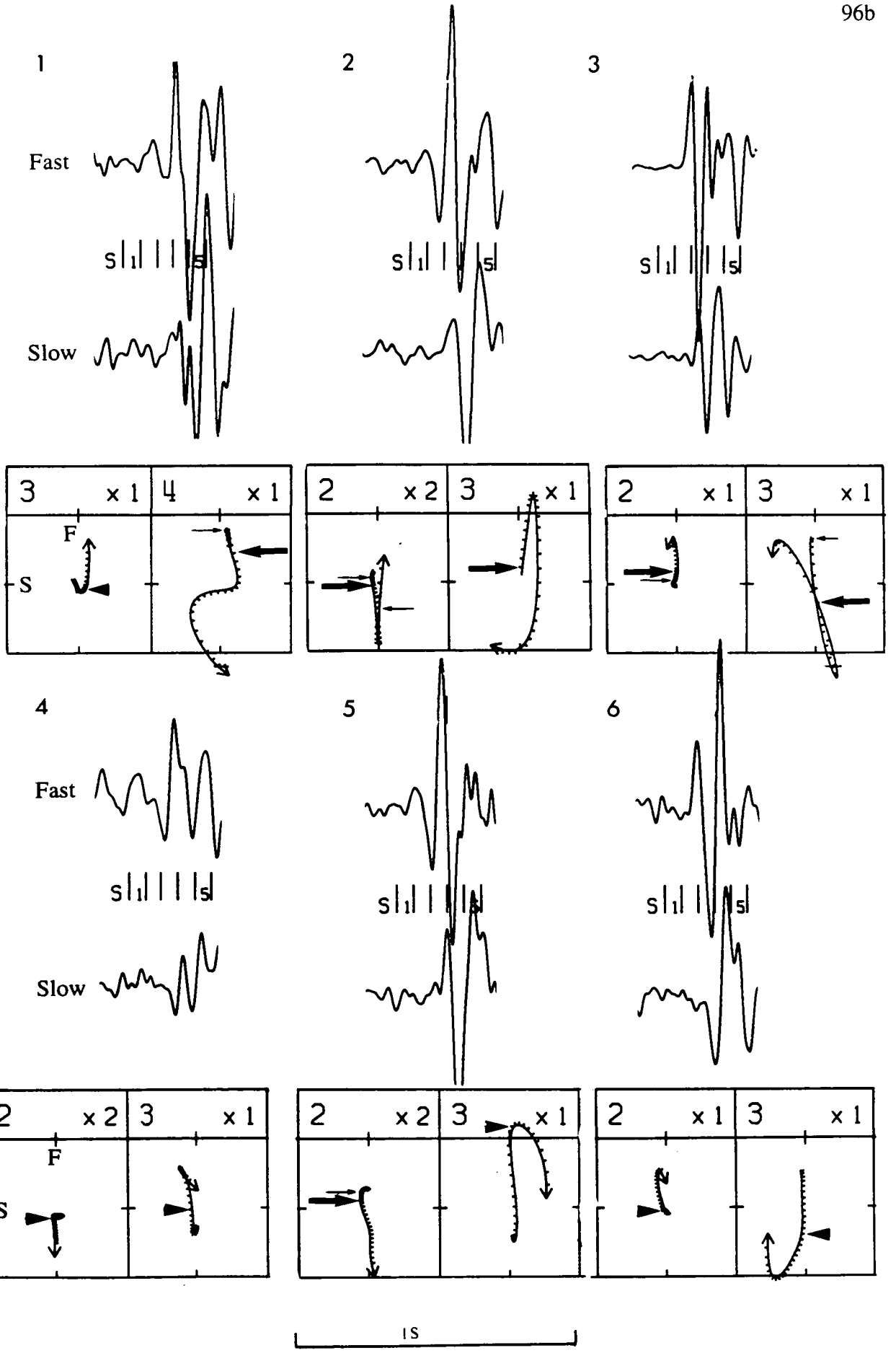
1
Fast
Slow
2
3
3 x 1
4 x 1
F
S
2 x 2
3 x 1
2 x 1
3 x 1
4
Fast
Slow
5
6
2 x 2
3 x 1
F
S
2 x 2
3 x 1
2 x 1
3 x 1
1S

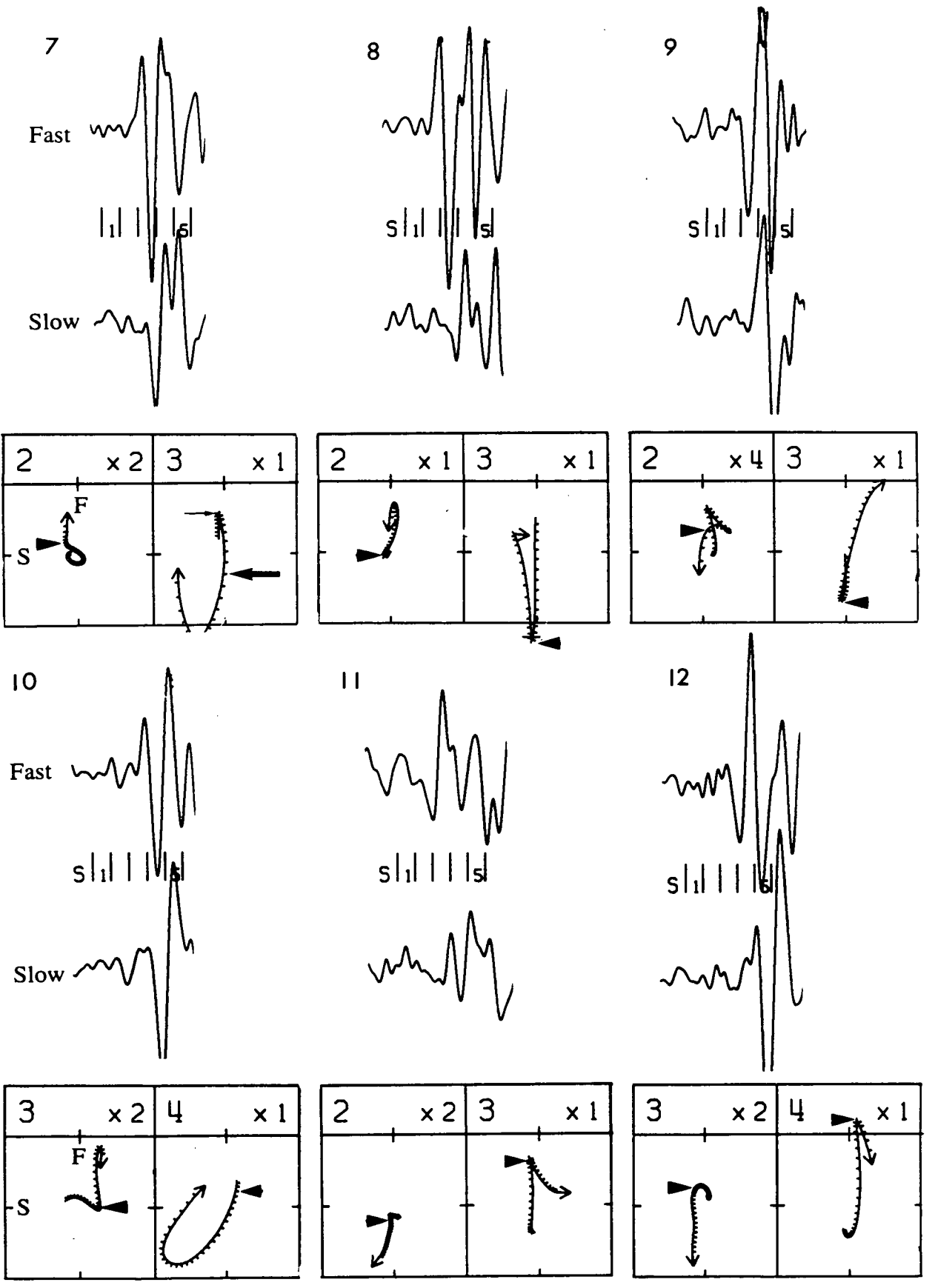
7
Fast
Slow
8
9
2 x 2 3 x 1
F
S
2 x 1 3 x 1
2 x 4 3 x 1
10
Fast
Slow
11
12
3 x 2 4 x 1
F
S
2 x 2 3 x 1
3 x 2 4 x 1

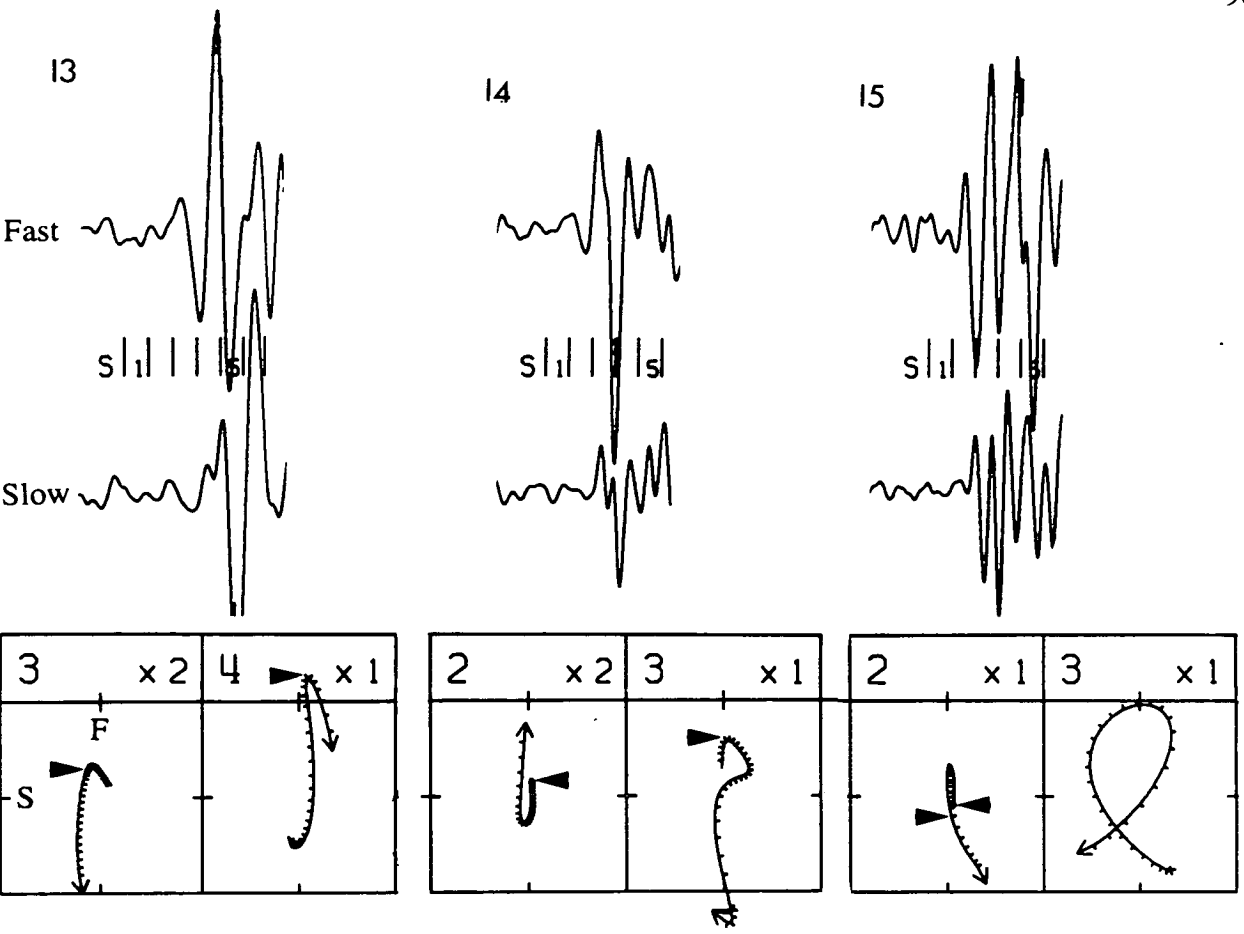
13
Fast
S
Slow
14
S
15
S
3 x 2
4 x 1
F
S
2 x 2
3 x 1
2 x 1
3 x 1

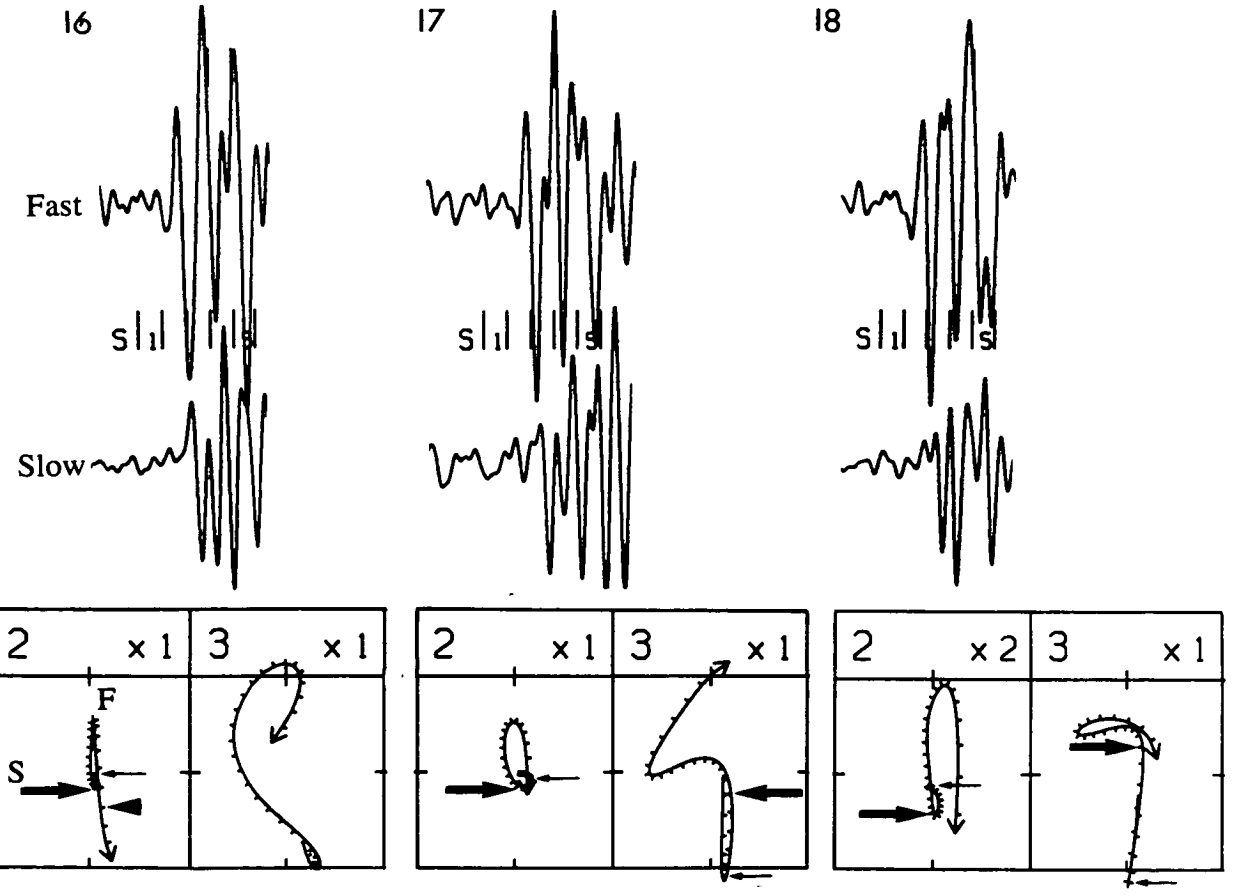
16
Fast
S
Slow
17
S
18
S
2 x 1
3 x 1
F
S
2 x 1
3 x 1
2 x 2
3 x 1

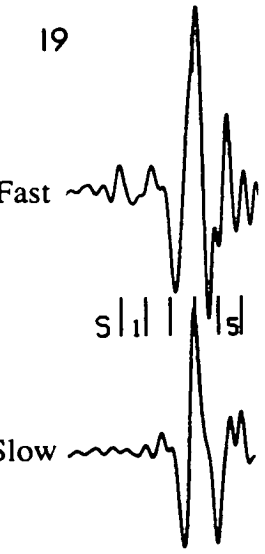
19
Fast
S
S
Slow

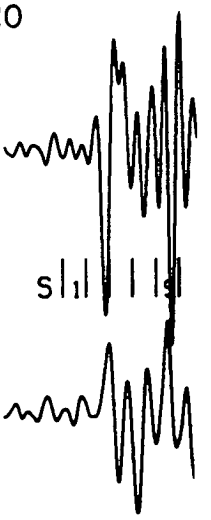
20
S
S


21
S
S

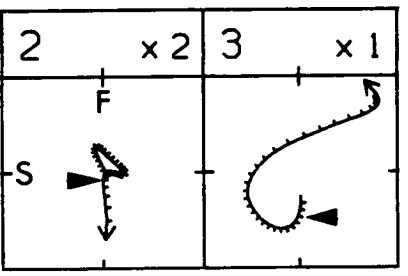
2
x 2
3
x 1
F
S

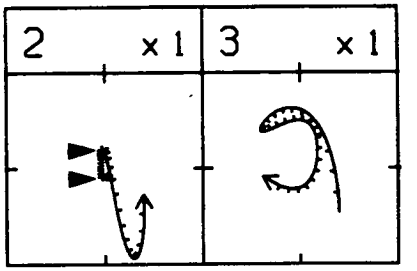
2
x 1
3
x 1

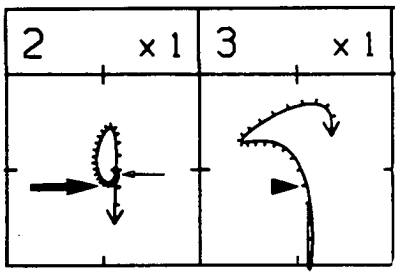
2
x 1
3
x 1

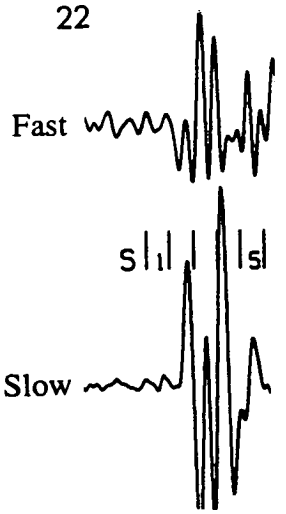
22
Fast
S
S
Slow

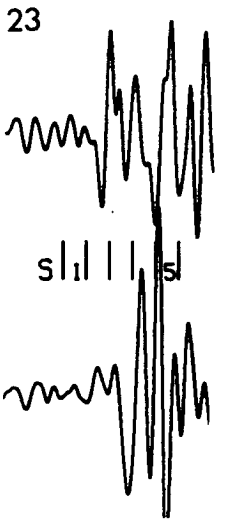
23
S
S

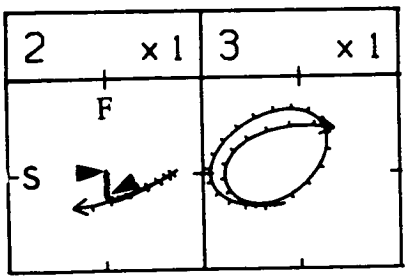
2
x 1
3
x 1
F
S

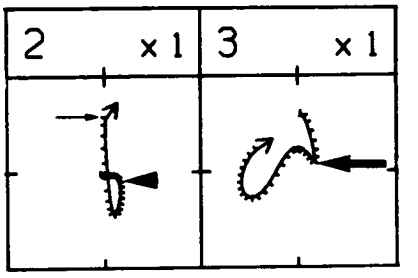
2
x 1
3
x 1

APPENDIX II

METHOD AND STUDIES OF EARTHQUAKE SOURCE MECHANISMS

The method of using *P*- and *S*-wave relative amplitudes and polarities (Pearce, 1977, 1980; Pearce and Rogers, 1989) in the determination of earthquake source mechanisms is adopted so as to obtain well-constrained and reliable solutions. I do this as the clear polarities and relative amplitude of shear waves on three component-seismograms, such as the events shown in Figure 4.1 and Appendix I, can be used in this method to play a significant role in constraining solutions in contrast with the conventional method of using *P*-wave polarity only. This technique was developed by Pearce (1977; 1980) for teleseismic earthquakes by using the relative amplitude of *P, pP and sP* phases, assuming a double couple source. It was further developed by Pearce and Rogers (1989) to make it available for other variable source mechanisms in terms of a moment tensor, which expresses the forces acting at the source as a 3x3 matrix. It is now available for local earthquakes, for which it makes use of both *P*- and *S*-wave polarities and *S*-wave relative amplitudes.

The method requires bounds to be placed on the observed amplitudes of *P*- and *S*- phases so as to be certain that the true amplitude of the phase lies between the bounds specified. The polarity of *P*- and *S*- phases can be specified as being positive, negative or unknown. The units used for amplitude measurement are arbitrary, but must be consistent within each seismogram; no absolute measurements are made. It allows for the case where a phase cannot be clearly observed, which may be a very significant observation, pointing to the proximity of a node in the radiation of either *P* or *S*. It calculates theoretically all the possibilities of source orientations in the combination of strike, dip and slip (the number of possibilities investigated depends on the increment of strike, dip, and slip). For each orientation, the relative amplitudes of *P* and *S* are predicted and checked for compatibility with the observed amplitude bounds. Since no absolute amplitude measurements are made, the compatibility is checked for each "phase pair"; that is, the predicted ratio of amplitudes is checked

against the limits of the amplitude ratio permitted by the observed bounds for each possible combination of phases observed on a particular seismogram. The solutions are therefore deduced according to the compatibilities of predicted and observed "phase pairs".

Seismic anisotropy has to be taken into account in the measurement of shear-wave relative amplitudes, since the measurement of amplitude is likely be the interaction of two split shear waves (qS1 and qS2) and, on the other hand, to study source properties the medium effect need to be taken into account. The effective anisotropy of the medium is considered by rotating seismograms into 'fast' and 'slow' components for the measurement of *S*-wave relative amplitudes corrected for an isotropic medium. A double couple source is assumed in this study.

There are 6 out of 11 events having well constrained solutions. Events 4 and 11 chosen from earthquake doublets in Table 4.1, corresponding to B(1) and B(2), have very similar solutions. These well constrained fault plane solutions all have dip fault planes ($\geq 60°$), and large components of strike slip motion with small portions of thrust movement, which is consistent with other studies of source mechanism (Nishioka and Michael, 1990). So they are basically considered to be reliable, and some of my studies have been based on these results. Table AII-1 lists the events used in this study. Table AII-2 lists the input data used in the determination of fault plane solutions. The fault plane solutions determined are plotted on equal-area projections of lower hemisphere.

Table AII-1. Events used in deriving fault plane solutions.

No.	Date	Time	Latitude	Longitude	Depth	M_D
1	881117	0022	35.9560°	-120.5277°	9.73	0.29
2	890106	0323	35.9608°	-120.5303°	12.12	1.11
3	890216	0456	35.9730°	-120.5268°	4.55	0.77
4	890218	0055	35.9500°	-120.4930°	4.88	1.55
5	890223	1807	35.9222°	-120.4692°	5.55	1.56
6	890327	1426	35.9747°	-120.5308°	6.32	0.85
7	890409	1918	35.9720°	-120.5258°	4.74	1.59
8	890825	0408	35.9545°	-120.5172°	8.05	0.73
9	900813	0536	35.9252°	-120.4682°	4.79	0.71
10	900907	0915	35.9748°	-120.5310°	6.41	1.09
11	901110	1437	35.9470°	-120.4918°	4.65	0.52

M_D: Coda-duration magnitude; depth is in kilometres.

Table AII-2. Data used in the determination of earthquake source mechanisms

Event 1: 35.9560 -120.5277
Time: 17/11/88 00:22
M_D : 0.29 Depth: 9.73

Station		Polarity	Amplitude	Rotation
		P-WAVE		
FR		-	0.0001 - 1000.0	0.0
ST		-	0.0001 - 1000.0	0.0
VC		-	0.0001 - 1000.0	0.0
JN		+	0.0001 - 1000.0	0.0
		S-WAVE		
VC	N	+	2.0 - 10.0	189.0
VC	E	+	2.0 - 8.0	189.0
VC	V	U	0.5 - 1.00	0.0
ST	E	-	0.0001 - 1000.0	120.0
FR	N	-	0.0001 - 1000.0	248.0

Event 2: 35.9608 -120.5303
Time: 06/01/89 03:23
M_D : 1.11 Depth: 12.12

Station		Polarity	Amplitude	Rotation
		P-WAVE		
FR		-	0.0001 - 1000.0	0.0
ST		+	0.0001 - 1000.0	0.0
VC		-	0.0001 - 1000.0	0.0
JN		+	0.0001 - 1000.0	0.0
		S-WAVE		
VC	N	-	32.0 - 42.0	200.0
VC	E	O1	23.0 - 33.0	200.0
VC	V	U	3.0 - 30.0	0.0
FR	N	-	2.0 - 10.0	248.0
FR	E	U	2.0 - 10.0	248.0
ST	N	U	2.0 - 10.0	120.0
ST	E	-	2.0 - 10.0	120.0

Event 3: 35.9730 -120.5268
Time: 16/02/89 04:56
M_D : 0.77 Depth: 4.55

Station		Polarity	Amplitude	Rotation
		P-WAVE		
JS		+	0.0001 - 1000.0	0.0
FR		-	0.0001 - 1000.0	0.0
ST		+	0.0001 - 1000.0	0.0
VC		-	0.0001 - 1000.0	0.0
JN		+	0.0001 - 1000.0	0.0
MM		U	0.000 - 0.5	0.0
		S-WAVE		
VC	E	+	0.0001 - 1000.0	200.0
MM	N	+	1.0 - 10.0	123.0
MM	E	-	1.0 - 10.0	123.0
MM	V	U	1.0 - 10.0	0.0

Event 4: 35.9500 -120.4930
Time: 18/02/89 00:55
M_D : 1.55 Depth: 4.88

Station		Polarity	Amplitude	Rotation
		P-WAVE		
FR		-	0.0001 - 1000.0	0.0
ED		-	0.0001 - 1000.0	0.0
ST		+	0.0001 - 1000.0	0.0
VC		+	0.0001 - 1000.0	0.0
JN		+	0.0001 - 1000.0	0.0
		S-WAVE		
VC	N	-	2.0 - 20.0	200.0
VC	E	+	2.0 - 20.0	200.0
VC	V	U	0.1 - 4.00	0.0
MM	N	+	2.0 - 20.0	175.0
MM	E	-	2.0 - 14.0	175.0
MM	V	U	0.1 - 4.00	0.0

Event 5: 35.9222 -120.4692
Time: 23/02/89 18:07
M_D : 1.56 Depth: 5.55

Station		Polarity	Amplitude	Rotation
		P-WAVE		
FR		+	0.0001 - 1000.0	0.0
JS		+	0.0001 - 1000.0	0.0
GP		-	0.0001 - 1000.0	0.0
ED		+	0.0001 - 1000.0	0.0
ST		+	0.0001 - 1000.0	0.0
VC		+	0.0001 - 1000.0	0.0
		S-WAVE		
VC	N	-	2.0 - 20.0	200.0
VC	E	U	0.0001 - 4.00	200.0
VC	V	U	0.0001 - 1.00	0.0

Event 6: 35.9747 -120.5308
Time: 27/03/89 14:26
M_D : 0.85 Depth: 6.32

Station		Polarity	Amplitude	Rotation
		P-WAVE		
FR		-	0.0001 - 1000.0	0.0
ST		+	0.0001 - 1000.0	0.0
VC		-	0.0001 - 1000.0	0.0
JN		+	0.0001 - 1000.0	0.0
MM		+	0.0001 - 1000.0	0.0
		S-WAVE		
VC	N	U	2.0 - 20.0	200.0
VC	E	U	2.0 - 20.0	200.0
VC	V	U	1.0 -10.0	0.0
ST	N	-	2.0 - 20.0	120.0
ST	E	-	2.0 - 20.0	120.0
MM	N	-	2.0 - 20.0	143.0
MM	E	+	2.0 - 20.0	143.0
MM	V	+	2.0 - 16.0	0.0

Event 7: 35.9720 -120.5258
Time: 09/04/89 19:18
M_D: 1.59 Depth: 4.74

Station		Polarity	Amplitude	Rotation
		P-WAVE		
JS		+	0.0001 - 1000.0	0.0
FR		-	0.0001 - 1000.0	0.0
JN		+	0.0001 - 1000.0	0.0
VC		-	0.0001 - 1000.0	0.0
		S-WAVE		
GP	N	-	0.0001 - 1000.0	130.0
GP	E	+	0.0001 - 1000.0	130.0
MM	N	+	1.0 - 6.0	129.0
MM	E	-	1.0 - 6.0	129.0
MM	V	U	1.0 - 6.0	0.0

Event 8: 35.9545 -120.5172
Time: 25/08/89 04:08
M_D: 0.73 Depth: 8.05

Station		Polarity	Amplitude	Rotation
		P-WAVE		
ED		+	0.0001 - 1000.0	0.0
FR		+	0.0001 - 1000.0	0.0
VR		+	0.0001 -1000.0	0.0
GP		-	0.0001 - 1000.0	0.0
ST		+	0.0001 - 1000.0	0.0
VC		-	0.0001 - 1000.0	0.0
JN		+	0.0001 - 1000.0	0.0
MM		-	0.0001 - 1000.0	0.0
		S-WAVE		
VC	N	-	2.0 - 20.0	187.0
VC	E	-	2.0 - 20.0	187.0
VC	V	U	0.0001 - 4.00	0.0

Event 9: 35.9252 -120.4682
Time: 13/08/90 05:36
M_D : 0.71 Depth: 4.79

Station		Polarity	Amplitude	Rotation
		P-WAVE		
ED		+	0.0001 - 1000.0	0.0
JS		+	0.0001 - 1000.0	0.0
GP		-	0.0001 - 1000.0	0.0
ST		+	0.0001 - 1000.0	0.0
VC		+	0.0001 - 1000.0	0.0
		S-WAVE		
VC	N	-	2.0 - 20.0	200.0
VC	E	U	0.0001 - 4.00	200.0
VC	V	U	0.0001 - 1.00	0.0

Event 10: 35.9748 -120.5310
Time: 07/09/90 09:15
M_D : 1.09 Depth: 6.41

Station		Polarity	Amplitude	Rotation
		P-WAVE		
FR		-	0.0001 - 1000.0	0.0
ST		+	0.0001 - 1000.0	0.0
VC		-	0.0001 - 1000.0	0.0
JN		+	0.0001 - 1000.0	0.0
MM		+	0.0001 - 1000.00	0.0
		S-WAVE		
ST	N	U	2.0 - 20.0	120.0
ST	E	-	2.0 - 20.0	120.0
ST	V	U	1.0 - 10.0	0.0
MM	N	U	2.0 - 10.0	138.0
MM	E	-	2.0 - 15.0	138.0
MM	V	U	2.0 - 20.0	0.0

Event 11: 35.9470 -120.4918
Time: 10/11/90 14:37
M_D : 0.52 Depth: 4.65

Station		Polarity	Amplitude	Rotation
		P-WAVE		
VR		-	0.0001 - 1000.0	0.0
GP		-	0.0001 - 1000.0	0.0
ST	N	-	0.0001 - 1000.0	0.0
ST	E	+	0.0001 - 1000.0	0.0
VC		+	0.0001 - 1000.0	0.0
JN		+	0.0001 - 1000.0	0.0
MM		-	0.0001 - 1000.0	0.0
		S-WAVE		
VC	N	-	2.0 - 20.0	200.0
VC	E	+	2.0 - 20.0	200.0
VC	V	U	0.0001 - 4.00	0.0
MM	N	+	2.0 - 20.0	175.0
MM	E	-	2.0 - 15.0	175.0
MM	V	U	0.0001 - 3.00	0.0

+: Ground motion upwards; -: Ground motion downwards; U: Unknown;
O: Opposite.

1

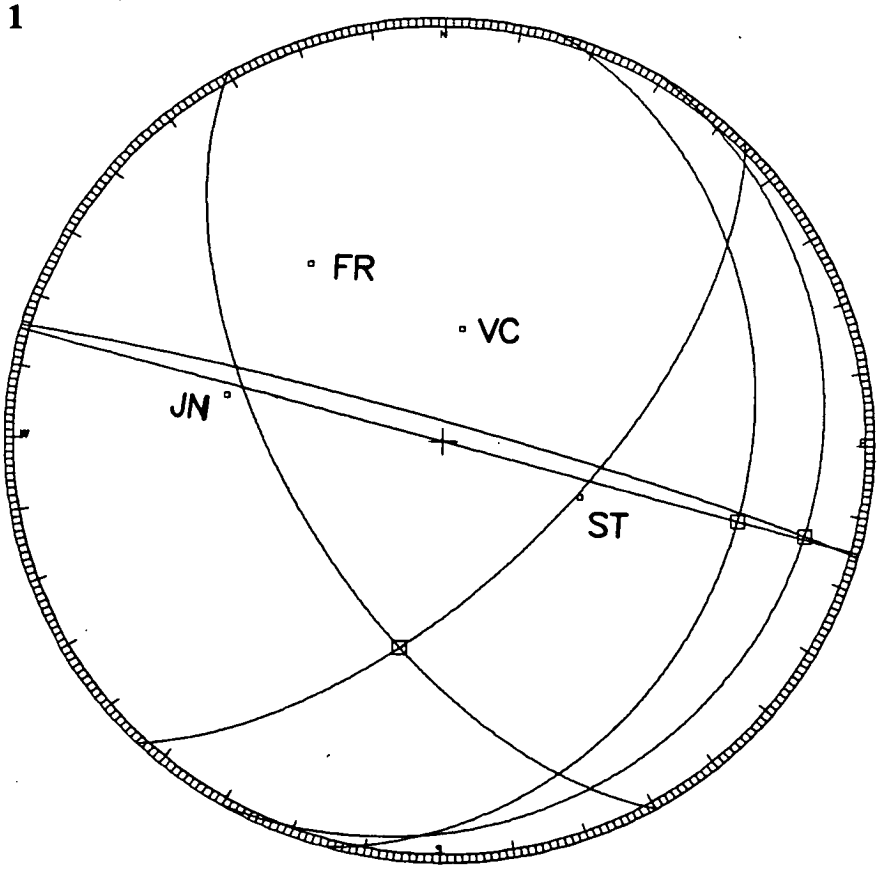

2

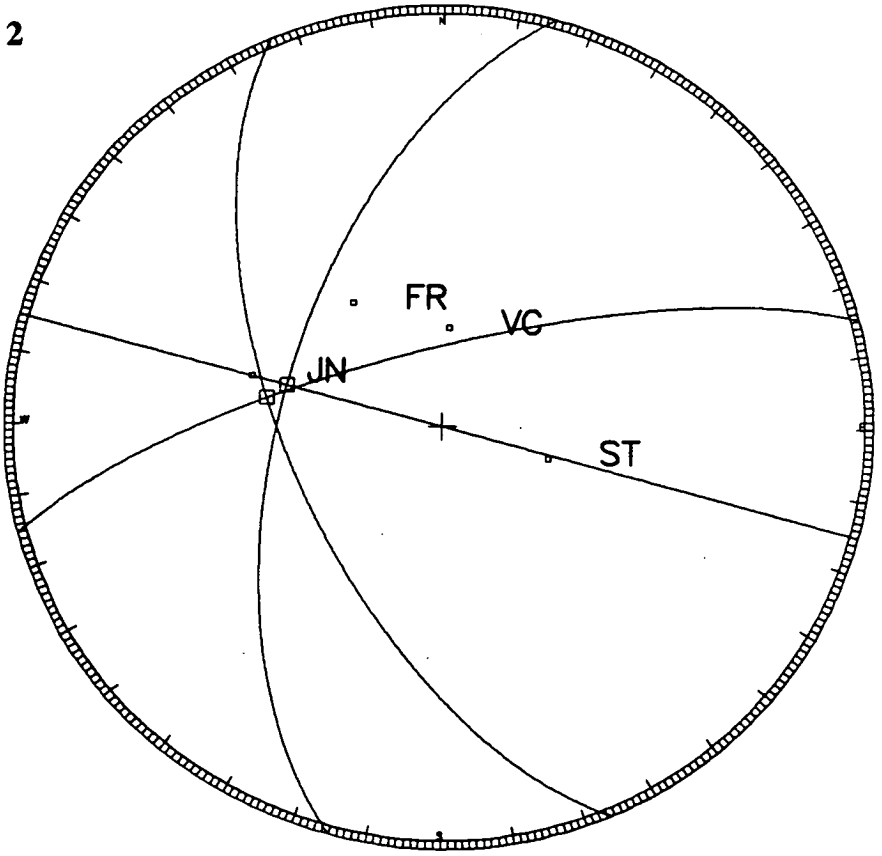

3

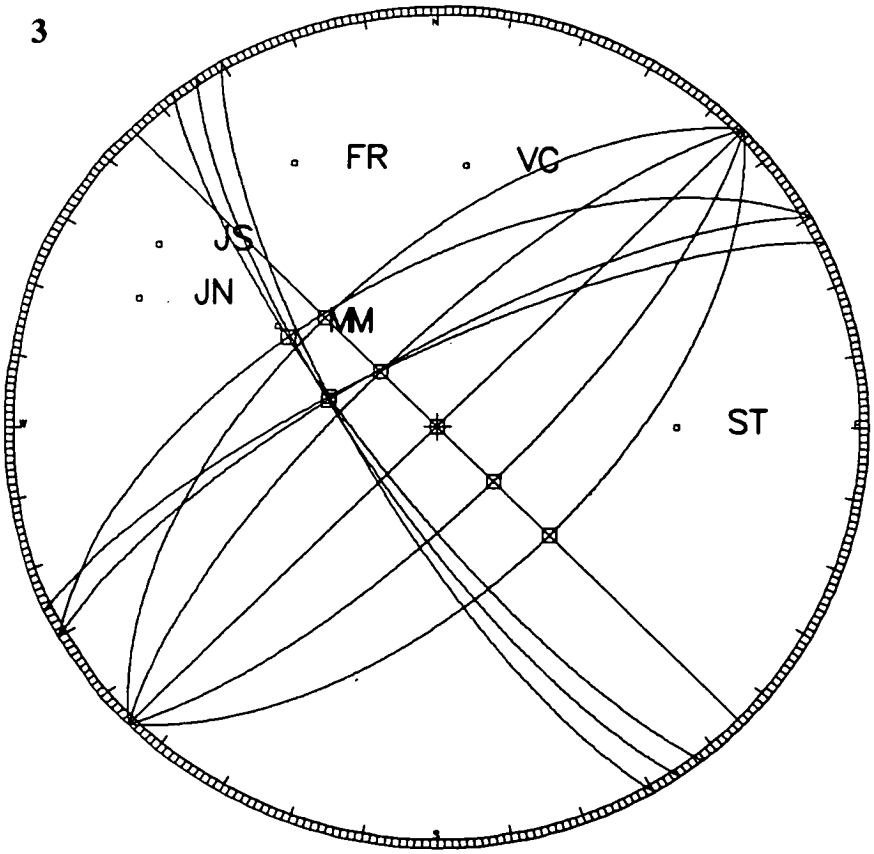

4

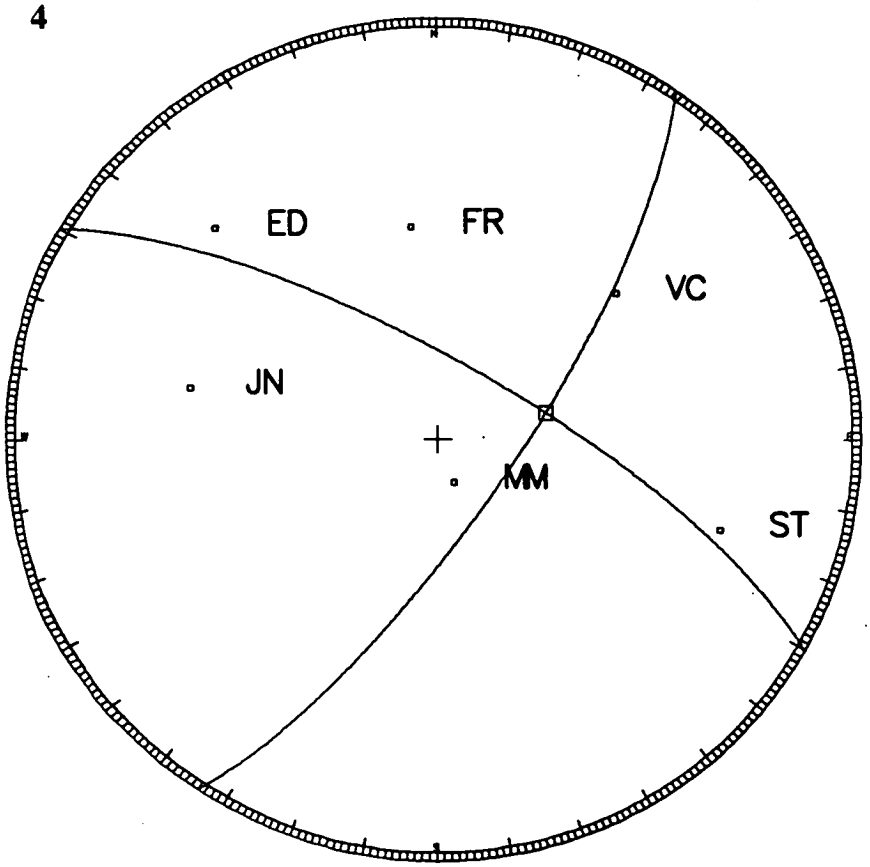

5

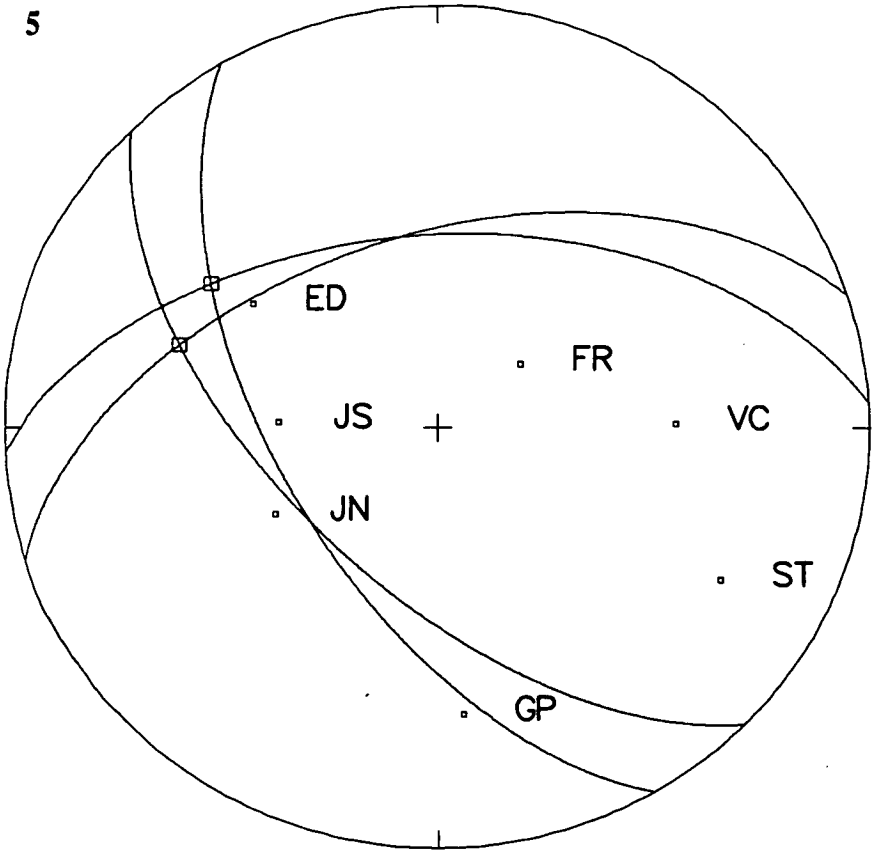

6

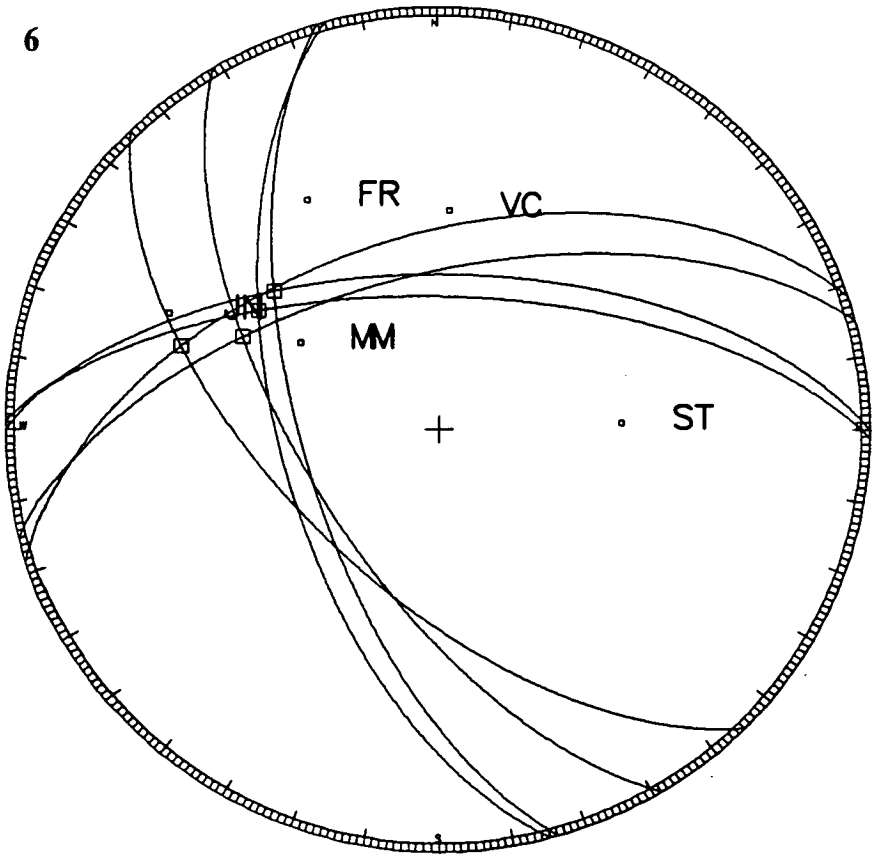

7

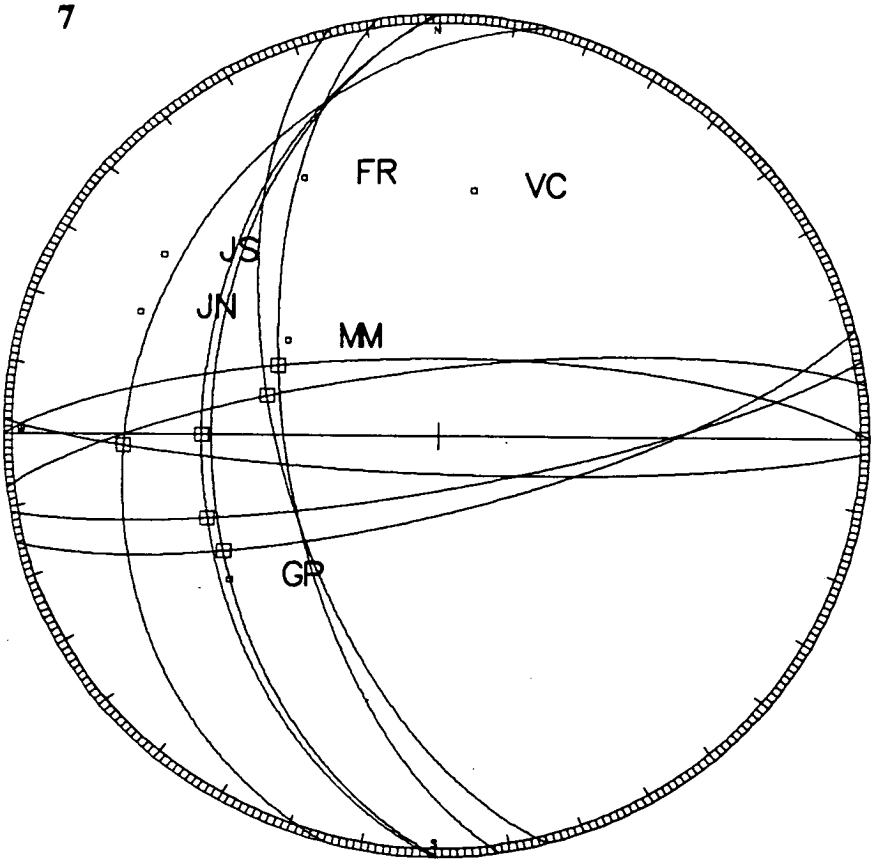

8

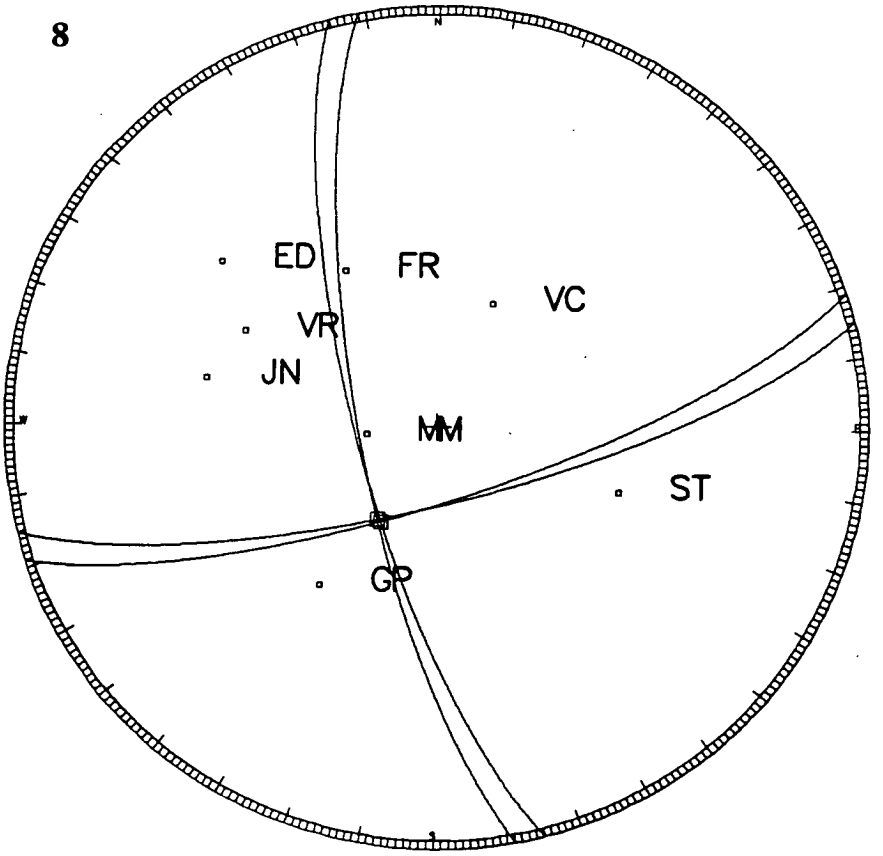

9

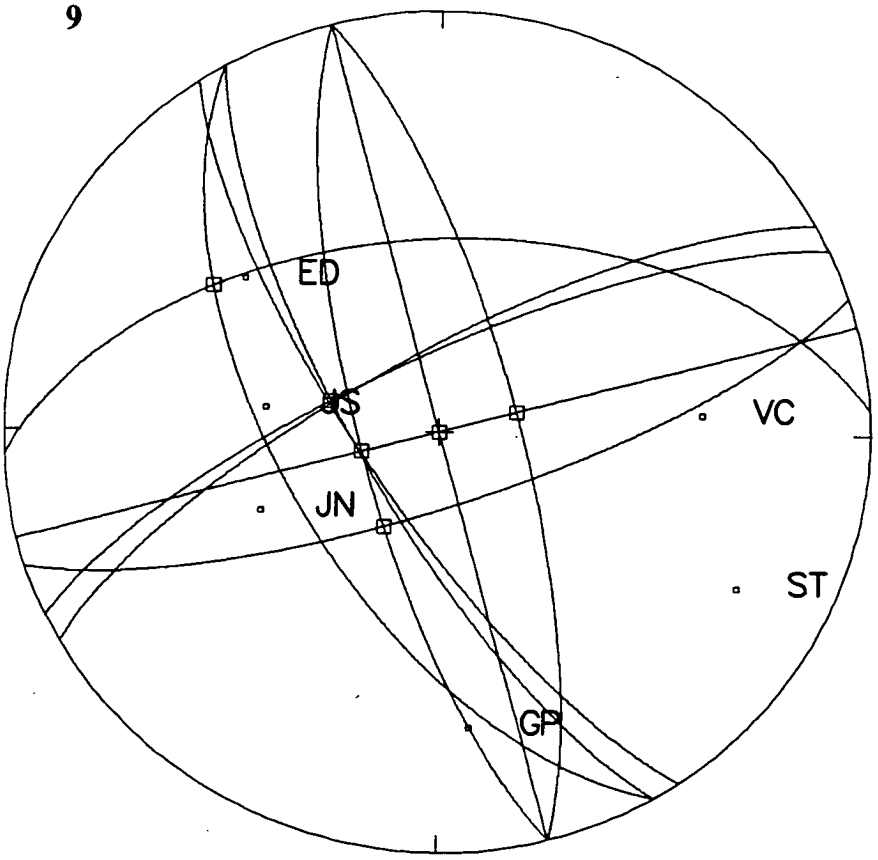

10

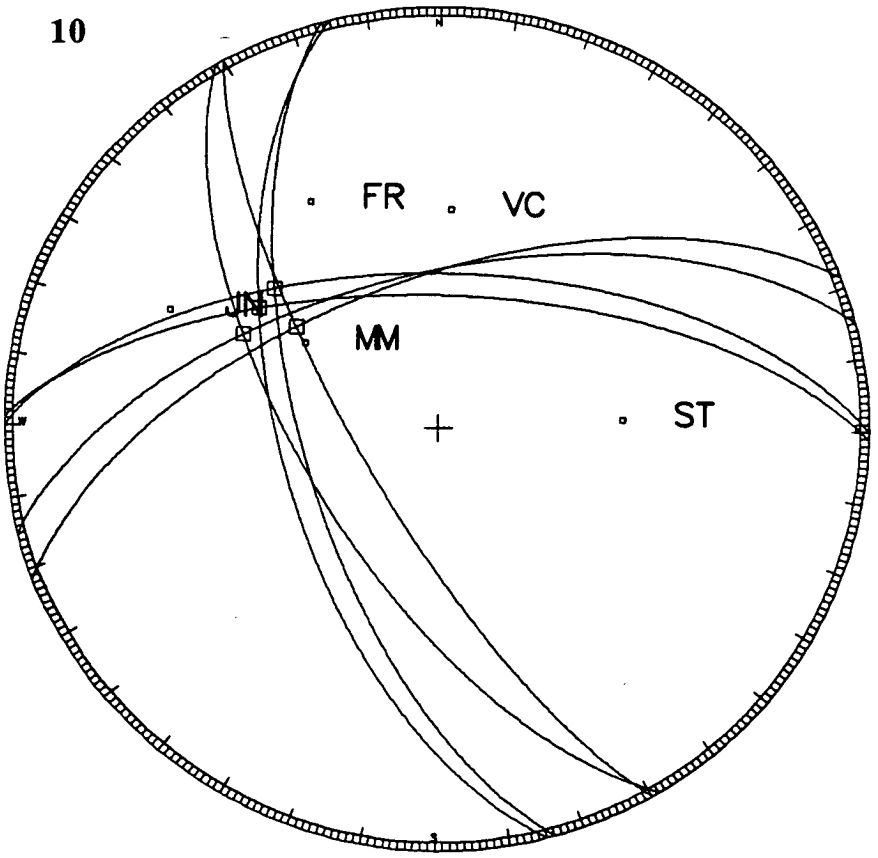

11

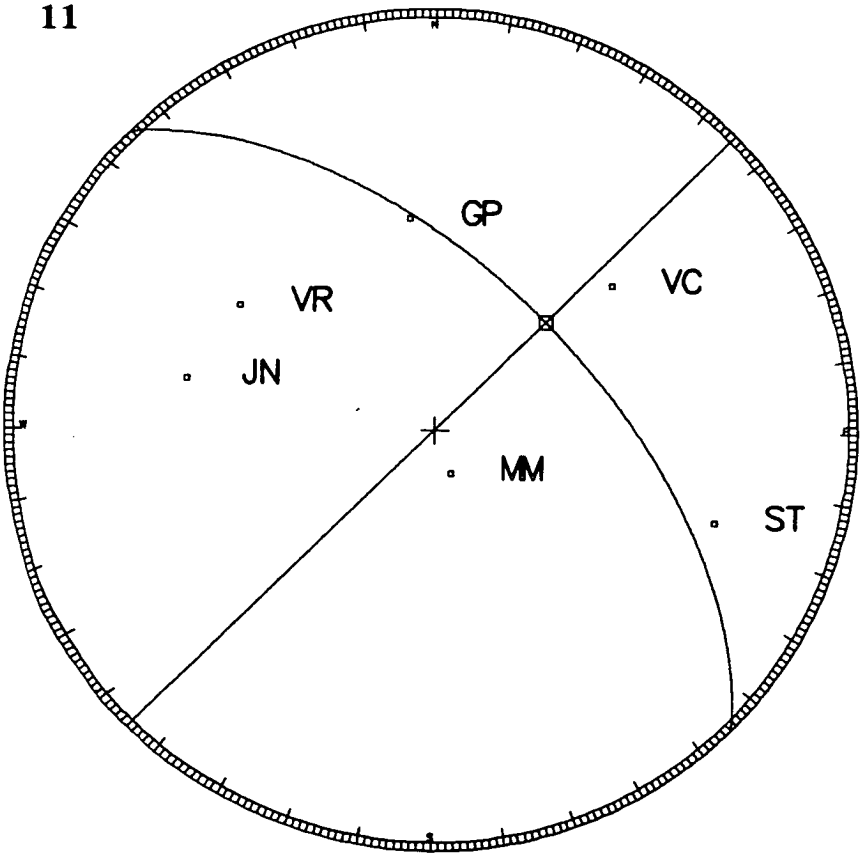

REFERENCES

Abercrombie, R., 1994, Microseismicity on a locked section of the San Andreas fault, recorded at 2.5 km depth in the Cajon Pass borehole, *submitted to J. geophys. Res.*

Abercrombie, R. and Leary, P.C., 1993, Source parameters of small earthquakes recorded at 2.5km depth, Cajon Pass, Southern California, implications for earthquake scaling, *Geophys. Res. Lett.*, **20**, 1511-1514.

Aggarwal, Y.P., Sykes, L.R., Armbruster, J. and Sbar, M.L., 1973, Premonitory changes in seismic velocities and prediction of earthquakes, *Nature*, **241**, 101-104.

Aki, K., 1969, Analysis of the seismic coda of local earthquakes as scattered waves, *J. geophys. Res.*, **74**, 615-631.

Aki, K., 1979, Characterization of barriers on an earthquake fault, *J. geophys. Res.*, **84**, 6140-6148.

Aki, K. and Chouet, B., 1975, Origin of coda waves, Source, Attenuation, and Scattering effects, *J. geophys. Res.*, **80**, 3322-3342.

Aki, K. and Phillips, W.S., 1986, Site amplification of coda waves from local earthquakes in central California, *Bull. seism. Soc. Am.*, **76**, 627-648.

Andersen, T., O'Reilly, S.Y. and Griffin, W.L., 1984, The trapped fluid phase in upper mantle xenoliths from Victoria, Australia: implications for mantle metasomatism, *Contributions to Mineralogy and Petrology*, **88**, 72-85.

Atkinson, B.K., 1979, A fracture mechanics study of subcritical tensile cracking of quartz in wet environments, *Pure appl. Geophys.*, **117**, 1011-1024.

Atkinson, B.K., 1982, Subcritical crack propagation in rocks: theory, experimental results and applications, *J. struct. Geol.* **4**, 41-56.

Atkinson, B.K., 1984, Subcritical crack growth in geological materials, *J. geophys. Res.*, **89**, 4077-4114.

Atkinson, B.K. and Meredith, P.G., 1987, The theory of subcritical crack growth with applications to minerals and rocks, *Fracture Mechanics of Rock*, p111-166.

Aster, R.C. and Shearer, P.M., 1991, High-frequency borehole seismograms recorded in the San Jacinto fault zone, Southern California. part 1, polarization and part 2, Attenuation and site effect, *Bull. seism. Soc. Am.*, **81**, 1057-1100.

Aster, R.C. and Shearer, P.M., 1992, Initial shear-wave particle motions and stress constraints at the Anza Seismic Network, *Geophys. J. Int.*, **108**, 740-748.

Aster, R.C., Shearer, P.M. and Berger, J., 1990, Quantitative measurement of shear wave polarizations at the Anza seismic network, Southern California, Implications for shear wave splitting and earthquake prediction, *J. geophys. Res.*, **95**, 12,449-12,473.

Avé Lallemant, H.G. and Carter, N.L., 1970, Syntectonic recrystallization of olivine and modes of flow in the upper mantle, *Bull. geol. Soc. Am.*, **81**, 2203-2220.

Bamford, D., 1977, P_n velocity anisotropy in a continental upper mantle, *Geophys. J. R. astr. Soc.*, **49**, 29-48.

Baptie, B., Crampin, S. and Liu, E., 1993, Displaying shear-wave splitting in cross-hole surveys for materials with combinations of EDA and PTL anisotropies, *Can. J. Expl. Geophys.*, **29**, 227-235.

Bakun,W.H., 1984, Seismic moments, local magnitude, and coda-duration magnitudes for earthquakes in central California, *Bull. seism. Soc. Am.*, **74**, 439-458.

Bakun, W.H., and McEvilly, T.V., 1984, Recurrence models and Parkfield, California, earthquakes, *J. geophys. Res.*, **89**, 3051-3058.

Bakun, W.H., and Lindh, A.G., 1985, The Parkfield, California, earthquake prediction experiment, *Science*, **229**, 619-623.

Ben-Zion, Y., 1990, The response of two half spaces to point dislocations at the material interface, *Geophys. J. Int.*, **101**, 507-528.

Ben-Zion, Y., and Malin, P., 1991, San Andreas fault zone head waves near Parkfield, California, *Science*, **251**, 1,592-1,594.

Ben-Zion, Y., Katz, S., and Leary, P., 1992, Joint inversion of fault zone head waves and direct P arrivals for crustal structure near major faults, *J. geophys. Res.*, **97**, 1943-1951.

Blakeslee, S. and Malin, P., 1990, A comparison of earthquake coda waves at surface versus subsurface seismometers, *J. geophys. Res.*, **95**, 309-326.

Blakeslee, S. and Malin, P., 1991, High-frequency site effects at two Parkfield downhole and surface stations, *Bull. seism. Soc. Am.*, **81**, 332-345.

Blenkinsop, T.G., 1990, Correlation of paleotectonic fracture and microfracture orientations in cores with seismic anisotropy at Cajon Pass drill hole, Southern California, *J. geophys. Res.*, **95**, 11143-11150.

Bonamassa, O. and Vidale, J.E., 1991, Directional site resonances observed from aftershocks of the 18 October 1989 Loma Prieta earthquake, *Bull. seism. Soc. Am.*, **81**, 1945-1957.

Boore, D.M., 1972, A note on the effect of simple topography on seismic SH-waves, *Bull. seism. Soc. Am.*, **62**, 275-284.

Boore, D.M., Harmsen, S. and Harding, S., 1981, Wave scattering from a step change in surface topography, *Bull. seism. Soc. Am.*, **71**, 117-125.

Booth, D.C., 1982, The anisotropic reflectivity technique, PhD dissertation, University of Edinburgh.

Booth, D.C., and Crampin, S., 1985, Shear-wave polarizations on a curved wavefront at an isotropic free surface, *Geophys. J. R. astr. Soc.*, **83**, 31-45.

Booth, D.C., Crampin, S., Evans, R. and Roberts, G., 1985, Shear-wave polarizations near the North Anatolian Fault-I. Evidence for anisotropy-induced shear-wave splitting, *Geophys. J. R. astr. Soc.*, **83**, 61-73.

Booth, D.C., Crampin, S., Lovell, J.H. and Chiu, Jer-Ming, 1990, Temporal changes in shear wave splitting during an earthquake swarm in Arkansas, *J. geophys. Res.*, **95**, 11,151-11,164.

Borcherdt, R.D., Fletcher, J.B., Jensen, E.G., Maxwell, G.L., VanSchaack, J.R., Warrick, R.E., Cranswick, E., Johnston, M.J.S. and McClearn, R., 1985, A General Earthquake-Observation System (GEOS), *Bull. seism. Soc. Am.*, **75**, 1783-1825.

Bowman, R.J. and Ando, M., 1987, Shear-wave splitting in the upper-mantle wedge above the Tonga subduction zone, *Geophys. J. R. astr. Soc.*, **88,** 25-41.

Brace, W.F., Paulding, B.W. and Scholz. C., 1966, Dilatancy in the fracture of crystalline rocks, *J. geophys. Res.*, **71,** 3939-3953.

Bracewell, R.N., 1965, The fourier transform and its applications, *McGraw-Hill, New York.*

Brodov, L.U., Evstifeye, V.I., Karus, E.V. and Kulichikhina, T.N., 1984, Some results of the experimental study of seismic anisotropy of sedimentary rocks using different types of waves, *Geophys. J. R. astr. Soc.*, **76**, 191-200.

Brodov, L.U., Tikonov, A.A., Chesnokov, E.M., Tertychnyi, V.V. and Zatsepin, S.V., 1991, Estimating physical parameters of cracked-porous oil reservoirs by inverting shear-wave splitting, Geophys. J. Int., **107**, 429-432.

Brown, R.D., Vedder, J.G., Wallace, R.E., Roth, E.F., Yerkes, R.F., Castle, R.O., Waananen, A.O., Page, R.W. and Eaton, J.P., 1967, The Parkfield-Cholame California, earthquakes of June-August 1966-surface geologic effects water-resources aspects, and preliminary seismic data, *U.S. Geol. Surv. Prof. Paper*, **579**, 1-66.

Buchbinder, G.G.R., 1985, Shear-wave splitting and anisotropy in Charlevoix seismic zone, Quebec, *Geophys. Res. Lett.*, **12**, 425-428.

Buchbinder, G.G.R. and Haddon, R.A.W., 1990, Azimuthal anomalies of short period P-wave arrivals from Nahanni aftershocks, N.W.T., Canada and effects of surface topography, *Bull. seism. Soc. Am.*, **80,** 1272-1283.

Budiansky, B. and O'Connell, R.J., 1976, Elastic moduli of a cracked solid, *Int. J. Solid Struct.*, **12**, 81-97.

Burford, R.O., 1988, Retardations in fault creep rates before local moderate earthquakes along the San Andreas Fault system, central California, *Pure appl. Geophys.*, **126,** 499-529.

Bush, I., 1990, Modelling shear-wave anisotropy in the Paris Basin, *PhD dissertation, University of Edinburgh.*

Bush, I. and Crampin, S., 1987, Observations of EDA and PTL anisotropy in shear-wave VSPs, *Expanded Abstracts, 57th Ann.Int. SEG Meeting, New Orleans, 1987*, p 646-649.

Bush, I. and Crampin, S., 1991, Paris Basin VSPs: case history establishing combinations of fine-layer (or lithologic) anisotropy and crack anisotropy from modelling shear wavefields near point singularities, *Geophys. J. Int.*, **107**, 433-447.

Byerlee, J.D., 1978a, Friction of rocks, *Pure appl. Geophys.*, **116,** 615-626.

Byerlee, J.D., 1978b, A review of rock mechanics studies in the United States pertinent to earthquake prediction, *Pure appl. Geophys.*, **116,** 586-602.

Byerlee, J.D., 1990, Friction, overpressure and fault normal compression, *Geophys. Res. Lett.*, **17,** 2109-112.

Chen, T.-C., Booth, D.C. and Crampin, S., 1987, Shear-wave polarizations near the North Anatolian Fault - III. Observations of temporal changes, *Geophys. J. R. astr. Soc.*, **91,** 287-311.

Chouet, B., 1979, Temporal variation in the attenuation of earthquake coda near Stone Canyon, California, *Geophys. Res. Lett.*, **6,** 143-146.

Christensen, N.I. and Salisbury, M.H., 1979, Seismic anisotropy in the oceanic upper mantle: evidence from the Bay of Islands ophiolite complex, *J. geophys. Res.*, **84**, 4601-4610.

Cliet, Ch., Brodov, L., Tikhonov, A., Marin, D. and Michon, D., 1991, Anisotropy survey for reservoir definition, *Geophys. J. Int.*, **107**, 417-427.

Cormier, V.F., 1984, The polarization of S waves in a heterogeneous isotropic Earth model, *J. geophys.* Res., **56,** 20-23.

Crampin, S., 1985, Evidence for aligned cracks in the Earth's crust, *First Break*, **3,** 12-14.

Crampin, S., 1978, Seismic propagation through a cracked solid: polarization as a possible dilatancy diagnostic, *Geophys. J. R. astr. Soc.*, **53**, 467-496.

Crampin, S., 1981, A review of wave motion in anisotropic and cracked elastic-media, *Wave Motion*, **3**, 343-391.

Crampin, S., 1984, Effective elastic-constants for wave propagation in cracked solids, *Geophys. J. R. astr. Soc.*, **76**, 135-145.

Crampin, S., 1986, Anisotropy and transverse isotropy, *Geophys.Prosp.*, **34**, 94-99.

Crampin, S., 1987, Geological and industrial implications of extensive-dilatancy anisotropy, *Nature*, **328,** 491-496.

Crampin, S., 1989, Suggestions for a consistent terminology for seismic anisotropy, *Geophys. Prostect.*, **37**, 753-770.

Crampin, S., 1990, The scattering of shear waves in the crust, *Pure appl. Geophys.*, **132**, 67-91.

Crampin, S., 1991a, Effects of point singularities on shear-wave propagation in sedimentary basins, *Geophys. J. Int.*, **107,** 531-543.

Crampin, S., 1991b, Wave propagation through fluid-filled inclusions of various shapes: interpretation of extensive-dilatancy anisotropy, *Geophys. J. Int.*, **104,** 611-623.

Crampin, S., 1993, A review of the effects of crack geometry on wave propagation through aligned cracks, *Can. J. Expl. Geophys.*, **29,** 3-17.

Crampin, S., 1994, The fracture criticality of crustal rocks, *Geophys. J. Int.*, **118**, 428-438.

Crampin, S. and Atkinson, B.K., 1985, Microcracks in the Earth's Crust, *First Break*, **3,** 16-20.

Crampin, S. and Booth, D.C., 1985, Shear-wave polarizations near the North Anatolian Fault-II. interpretation in terms of crack-induced anisotropy, *Geophys. J. R. astr. Soc.*, **83,** 75-92.

Crampin, S. and Booth, D.C., 1989, Shear-wave splitting showing hydraulic dilatation of pre-existing joints in granite, *Sci. Drilling*, **1,** 21-26.

Crampin, S., Booth, D.C., Evans, R., Peacock, S. and Fletcher, J.B., 1990, Changes in shear wave splitting at Anza near the time of the North Palm Springs earthquake, *J. geophys. Res.*, **95,** 11,197-11,212.

Crampin, S., Booth, D.C., Evans, R., Peacock, S. and Fletcher, J.B., 1991, Comment on "Quantitive measurement of shear wave polarizations at the Anza seismic

network, Southern California, Implications for shear wave splitting and earthquake prediction" by Aster, R.C., Shearer, P.M. and Berger, J., *J. geophys. Res.*, **96,** 6403-6414.

Crampin, S., Booth, D.C., Krasnova, M.A., Chesnokov, E.M., Maximov, A.B., and Tarasov, N.T., 1986, Shear-wave polarizations in the Peter the First Range indicating crack-induced anisotropy in a thrust-fault regime, *Geophys. J. R. astr. Soc.*, **84**, 401-412.

Crampin, S., Chesnokov, Eugenie M. and Hipkin, R.G., 1984a, Seismic anisotropy - the state of the art: II, *Geophys. J. R. astr. Soc.*, **76**, 1-16.

Crampin, S., Evans, R. and Atkinson, B.K., 1984b, Earthquake prediction, a new physical basis, *Geophys. J. R. astr. Soc.*, **76,** 147-156.

Crampin, S., Evans, R., and Üçer, S.B., 1985, Analysis of records of local earthquakes, the Turkish Dilatancy Projects (TDP1 and TDP2), *Geophys. J. R. astr. Soc.*, **83**, 1-16.

Crampin, S., Evans, R., Üçer, S.B., Doyle, M., Davis, J.P., Yegorkina, G.V. and Miller, A., 1980, Observations of dilatancy-induced polarization anomalies and earthquake prediction, *Nature*, **286,** 874-877.

Crampin, S. and King, S.W., 1977, Evidence for anisotropy in the upper mantle beneath Eurasia from the polarization of higher mode seismic surface waves, *Geophys. J. R. astr. Soc.*, **49**, 59-85.

Crampin, S. and Lovell, J.H., 1991, A decade of shear-wave splitting in the Earth's crust, what does it mean? what use can we make of it? and what should we do next? *Geophys. J. Int.*, **107,** 387-407.

Crampin, S., Stephen, R.A. and McGonigle, R., 1982, The polarization of P-waves in anisotropic media, *Geophys. J. R. astr. Soc.*, **68,** 477-485.

Crampin, S. and Yedlin, M., 1981, Shear-wave singularities of wave propagation in anisotropic media, *J. Geophys.*, **49,** 43-46.

Dahlen, F.A., 1972, Elastic velocity anisotropy in the presence of an anisotropic initial stress, *Bull. seism. Soc. Am.*, **62,** 1183-1193.

Daley, T.M. and McEvilly, T.V., 1990, Shear-wave anisotropy in the Parkfield Varian Well VSP, *Bull. seism. Soc. Am.*, **80,** 857-869.

Daley, T.M., McEvilly,T.V. and Majer, E.L., 1988, multiply-polarized shear-wave VSPs from the Cajon Pass drillhole, *Geophy. Res. Lett.*, **15,** 1001-1004.

Dobrovolsky, I.P., Zubkov, S.I. and Miachkin, V.I., 1979, Estimation of the size of earthquake preparation zones, *Pure Appl. Geophys.*, **177**, 1025-1044.

Douma, J., 1988, The effect of the aspect ratio on crack-induced anisotropy, *Geophys. Prosp.*, **36**, 614-632.

Eberhart-Phillips, D. and Michael, A., 1993, Three-dimensional velocity structure, and Fault structure in the Parkfield region, Central California, *J. geophys. Res.*, **98,** 15,737-15,758.

Ehlig, P.L., 1988, Characteristics of basement rocks exposed near the Cajon Pass scientific drill hole, *Geophys. Res. Lett.*, **15,** 949-952.

Eshelby, J.D., 1957, The determination of the elastic field of an ellipsoidal inclusion, and related problems, *Proc.Roy.Soc.London, Ser. A,* **241**, 376-396.

Evans, R., 1984, Effects of the free surface on shear wavetrains, *Geophys. J. R. astr. Soc.*, **76,** 165-172.

Forsyth, D.W., 1975, The early structural evolution and anisotropy of the oceanic upper-mantle, *Geophys. J. R. astr. Soc.*, **43**, 103-162.

Francis, T.J.G., 1969, Generation of seismic anisotropy in the upper mantle along the mid-ocean ridges, *Nature*, **221**, 162-165.

Fuchs, K., 1983, Recently formed elastic anisotropy and petrological models for the continental subcrustal lithosphere in southern Germany, *Phys. Earth Planet. Int.*, **31**, 93-118.

Fyfe, W.S., Price, N.J. and Thompson, A.B., 1978, Fluids in the Earth's crust, *Developments in geochemistry 1, Elsevier, Amsterdam.*

Garbin, H.D. and Knopoff, L., 1973, The compressional modulus of a material permeated by a random distribution of free circular cracks, *Q. appl. Math.*, **3**, 453-464.

Garbin, H.D. and Knopoff, L., 1975a, The shear modulus of a material permeated by a random distribution of free circular cracks, *Q. appl. Math.*, **33**, 296-300.

Garbin, H.D. and Knopoff, L., 1975b, Elastic moduli of a medium with liquid-filled cracks, *Q. appl. Math.*, **33**, 301-303.

Gledhill, K.R., 1990, A shear-wave polarization study in the Wellington region, New Zealand, *Geophy. Res. Lett.*, **17**, 1319-1322.

Gledhill, K.R., 1991, Evidence for shallow and pervasive seismic anisotropy in the Wellington region, New Zealand, *J. geophys. Res.*, **96,** 21,503-21,516.

Gledhill, K.R., 1993a, Shear waves recorded on close-spaced seismographs: I. Shear-wave splitting results, *Can. J. Expl. Geophys.*, **29,** 285-298.

Gledhill, K.R., 1993b, Shear waves recorded on close-spaced seismographs: II The complex anisotropic structure of the Wellington Peninsula, New Zealand, *Can. J. Expl. Geophys.*, **29,** 299-314.

Got Jean-Luc and Fréchet J., 1993, Origins of amplitude variations in seismic doublets: source or attenuation process?, *Geophys. J. Int.*,**114,** 325-340.

Graham, G., and Crampin, S., 1993, Shear-wave splitting from regional earthquakes in Turkey, *Can. J. Expl. Geophys.*, **29,** 371-379.

Graham, G., Crampin, S. and Fernadez, L.M., 1991, Observations of shear-wave polarizations from rockbursts in a South African gold field, an analysis of acceleration and velocity recordings, *Geophys. J. Int.*, **107,** 661-672.

Hashin, Z., 1962, The elastic moduli of heterogeneous materials, *J. appl. Mech.*, **29E,** 143-150.

Healy, J.H. and Zoback, M.D., 1988, Hydraulic fracturing in situ stress measurements to 2.1km depth at Cajon Pass, California, *Geophy. Res. Lett.*, **15,** 1005-1008.

Helbig, K., 1984, Transverse isotropy in exploration seismics, *Geophys. J. R. astr. Soc.*, **76**, 79-88.

Helbig, K., 1993, Foundations of anisotropy for exploration seismic, *Pergamon Press Ltd.*

Hess, H., 1964, Seismic anisotropy of the uppermost mantle under oceans, *Nature*, **203**, 629-631.

Holmes, G.M., Crampin, S. and Young, R.P., 1993, Preliminary analysis of shear-wave splitting in granite at the underground research laboratory, Manitoba, *Can. J. Expl. Geophys.*, **29**, 140-152.

Horne, S. and MacBeth, C., 1994, Inversion for seismic anisotropy using Genetic Algorithms, *Geophys. Prosp.*, **42**, 953-974.

Hudson, J.A., 1980, Overall properties of a cracked solid, *Math. Proc. Camb. Phil. Soc.*, **88**, 371-384.

Hudson, J.A., 1981, Wave speeds and attenuation of elastic waves in material containing cracks, *Geophys. J. R. astr. Soc.*, **64**, 133-150.

Hudson, J.A., 1986, A higher order approximation to the wave propagation constants for a cracked solid, *Geophys. J. R. astr. Soc.*, **87**, 265-274.

Hudson, J.A., 1990, Overall elastic properties of isotropic materials with arbitrary distribution of circular cracks, *Geophys. J. Int.*, **102**, 465-469.

Hudson, J.A., 1991, Crack distributions which account for a given seismic anisotropy, *Geophys. J. Int.*, **104**, 517-521.

Imoto, M., 1991, Changes in the magnitude-frequency b-value prior to large ($M \geq 6.0$) earthquakes in Japan, *Tectonophysics*, **193**, 311-325.

Jin, Anshu and Aki, K., 1989, Spatial and temporal correlation between coda Q^{-1} and seismicity and its physical mechanism, *J. geophys. Res.*, **94**, 14,041-14,059.

Johnson, T.C., Hamilton, E.C. and Berger, W.H., 1977, Physical properties of calcareous sediments: control by dissolution at depth, *Marine Geol.*, **24**, 259-277.

Jones, L.M., 1988, Focal mechanisms and the state of stress on the San Andreas fault in southern California, *J. geophys. Res.*, **93**, 8869-8879.

Joyner, W.B., Warrick, R.E. and Fumal, T.E., 1981, The effect of Quaternary alluvium on strong ground motion in the Coyote Lake, California earthquake of 1979, *Bull. seism. Soc. Am.*, **71**, 1333-1349.

Kaarsberg, E.A., 1968, Elasticity studies of isotropic and anisotropic rock samples, *Trans. Soc. min. Engrs*, **241**, 470-475.

Kaneshima, S., 1990, Origin of crustal anisotropy: Shear wave splitting studies in Japan, *J. geophys. Res.*, **95**, 11,121-11,133.

Kaneshima, S. and Ando, M., 1989, An analysis of split shear waves observed above crustal and uppermost mantle earthquakes beneath Shikoku, Japan: Implications in effective depth extent of seismic anisotropy, *J. geophys. Res.*, **94**, 14,077-14,092.

Kaneshima, S., Ando, M. and Crampin, S., 1987, Shear-wave splitting above small earthquakes in the Kinki district of Japan, *Phys. Earth planet. Inter.*, **45**, 45-58.

Kaneshima, S., Ando, M. and Kimura, S., 1988, Evidence from shear-wave splitting for the restriction of seismic anisotropy to the upper crust, *Nature*, **335**, 627-629.

Kaneshima, S., Ito, H. and Sigihara, M., 1989, Shear wave polarization anisotropy observed above small earthquakes in a rift zone in Japan, *Tectonophysics*, **157**, 281-300.

Kaneshima, S., Maeda, N. and Ando, M., 1990, Evidence for the splitting of shear waves from waveform and focal mechanism analysis, *Phys. Earth planet. Inter.*, **61**, 238-252.

Karageorgi, E., Clymer, R. and McEvilly, T.V., 1992, Seismological studies at Parkfield. II. Search for temporal variations in wave propagation using Vibroseis, *Bull. seism. Soc. Am.*, **82**, 1388-1415.

King, G.C.P., 1983, The accommodation of large fault behaviour, subsurface geology, and three-dimensional velocity models, *Science*, **253**, 651-654.

Korringa, J., 1973, Theory of elastic constants of heterogeneous media, *J. Math. Phys.*, **14**, 509-513.

Kozlovsky, Y., 1984, The world's deepest well, *Sci. Am.*, **12**, 98-104.

Kranz, R.L., 1983, Microcracks in rocks: a review, *Tectonophysics*, **100**, 449-480.

Kuster, G.T. and Toksöz, M.N., 1974, Velocity and attenuation of seismic waves in two-phase media, part I - Theoretical formulations, *Geophysics*, **39**, 587-606.

Leary, P.C., and Ben-Zion, Y., 1992, A 200m wide fault low velocity layer on the San Andreas fault at Parkfield, results from analytic waveform fits to trapped wave groups, *J. geophys. Res.*, **97**, 1943-1951.

Leary, P.C., Li, Y.-G., and Aki, K., 1987, Observation and modelling of fault zone fracture seismic anisotropy - I. P, SV, and SH travel times, *Geophys. J. R. astr. Soc.*, **91**, 461-484.

Lees, J.M., and Malin, P.E., 1990, Tomographic images of P wave velocity variation at Parkfield, California, *J. geophys. Res.*, **95**, 21,793-21,804.

Lerche, I. and Petroy, D., 1986, Multiple scattering of seismic waves in fractured media: Velocity and effective attenuation of the coherent components of *P* waves and *S* waves, *Pure appl. Geophys.*, *124*, 975-1019.

Levin, F.K., 1979, Seismic velocity in transversely isotropic media, *Geophysics*, **43**, 528-537.

Lewis, C., Davis, T.L. and Vuillermoz, C., 1991, Three-dimensional multicomponent imaging of reservoir heterogeneity, Silo Field, Wyoming: *Geophysics*, **56**, 2048-2956.

Li, X.-Y. and Crampin, S., 1991, Complex component analysis of shear-wave splitting: case studies, *Geophys. J. Int*, **107**, 605-614.

Li, X.-Y., Mueller, M.C. and Crampin, S., 1993, Case studies of shear-wave splitting in reflection surveys in South Texas, *Can. J. Expl. Geophys.*, **29**, 189-215.

Li, Y.-G. and Leary, P.C., 1990, Fault zone trapped seismic waves, *Bull. seism. Soc. Am.*, **80**, 1245-1271.

Li, Y.-G., Leary, P.C. and Henyey, T.L., 1988, Stress orientation inferred from shear wave splitting in basement rock at Cajon Pass, *Geophys. Res. Lett*, **15**, 997-1000.

Li, Y.-G., Teng, Ta-Liang, and Aki, K., 1992, Observation and interpretation of fault-zone trapped seismic waves at three different geological and experimental environments in California, Abstract, *Bull. seism. Res. Lett.*, **63**, 76.

Li, Y.-G., Teng, Ta-Liang and Henyey, T.L., 1994, Shear-wave splitting observations in Northern Los Angeles Basin, Southern California, *Bull. seism. Soc. Am.*, **84**, 307-323.

Lindh, A.G., and Boore, D.M., 1981, Control of rupture by fault geometry during the 1966 Parkfield earthquake, *Bull. seism. Soc. Am.*, **71,** 95-116.

Lindh, A.G. and Estrem, J., 1989, May 1989 Parkfield data summary, *United States depertment of the interior geological survey--National Earthquake Hazards reduction program, summaries of technical reports*, **XXIX,** 288.

Lindh, A., Michael, A., Aviles, C. and Hirshorn, B., 1989, Parkfield prediction experiment, *National Earthquake Hazards Reduction Program, Summaries of Technical Reports,* **XXIX,** 284-290.

Liu, E., Crampin, S. and Booth, D.C., 1989, Shear-wave splitting in cross-hole survey, Modelling, *Geophysics*, **54,** 57-65.

Liu, E. and Crampin, S., 1990, Effects of the internal shear wave window, comparison with anisotropy induced splitting, *J. geophys. Res.*, **95,** 11,275-11,281.

Liu, E., Crampin, S. and Queen, J.H., 1991, Fracture detection using crosshole surveys and reverse vertical seismic profiles at the Conoco borehole test Facility, Oklahoma, *Geophys. J. Int.*, **107**, 449-464.

Liu, Y., Booth, D.C., Crampin, S., Evans, R. and Leary, P., 1993, Shear-wave polarizations and possible temporal variations in shear-wave splitting at Parkfield, *Can. J. Expl. Geophys.*, **29,** 380-390.

Louie, J.N., Clayton, R.W. and LeBras, R.J., 1988, Three-dimensional imaging of steeply dipping structure near the San Andreas fault, Parkfield, California, *Geophysics*, **53,** 176-185.

Love, A.E.H., 1944, A treatlise on the mathematical theory of elasticity, *4th ed. Dover, New York.*

Main, I.G., 1988, Prediction of failure times in the Earth for a time-varying stress, *Geophys. J.*, **92**, 455-464.

Main, I.G., Meredith, P.G. and Jones, C., 1989, A reinterpretation of the precursory seismic b-value anomaly from fracture mechanics, *Geophys. J.*, **96,** 131-138.

Main I.G., Meredith, P.G., Sammonds, P.R. and Jones, C., 1990a, Influence of fractal flaw distributions on rock deformation in the brittle field, *From Knipe, R.J. and Rutter, E.H. (eds), 1990, Deformation Mechanisms, Rheology and Tectonics, Geological Society Special Publication No. 54*, p 81-96.

Main, I.G., Peacock, S. and Meredith, P.G., 1990b, Scattering Attenuation and the fractal geometry of fracture systems, *PAGEOPH*, **133**, 283-304.

Malin, P.E., Blakeslee, S.N., Alvarez, M.G., and Martin, A.J., 1989, Microearthquake imaging of the Parkfield asperity, *Science*, **224,** 557-559.

McBride, J.H. and Brown, L.D., 1986, Reanalysis of the COCORP deep seismic reflection profile across the San Andreas fault, Parkfield, California, *Bull. seism. Soc. Am.*, **76,** 1668-1686.

Michelini, A., and McEvilly, T.V., 1991, Seismological studies at Parkfield. I. Simultaneous inversion for velocity structure and hypocenters using cubic B-splines parameterization, *Bull. seism. Soc. Am.*, **81,** 524-552.

Mjachkin, V.I., Brace, W.F., Sobolev, G.A. and Dieterich, J.H., 1975, Two models of earthquake forerunners, *Pure appl. Geophys.*, **113**, 169-181.

Mueller, M.C., 1991, Prediction of lateral variability in fracture intensity using multicomponent shear wave surface seismic as a precursor to horizontal drilling, *Geophys. J. Int.*, **107**, 409-416.

Nadeau, R., Antolik, M., Johnson, P.A., Foxall, W. and McEvilly, T.V., 1994, Seismological studies at Parkfield III: Microearthquake clusters in the study of fault-zone dynamics, *Bull. seism. Soc. Am.*, **84**, 247-263.

Nishizawa, O., 1982, Seismic velocity anisotropy in a medium containing oriented cracks - transversely isotropic case, *J. Phys. Earth.*, **30**, 331-347.

Nikitin, L.V. and Chesnokov, E.M., 1984, Wave propagation in elastic media with stress-induced anisotropy, *Geophys. J. R. astr. Soc.*, **76**, 129-133.

Nishioka, G.K., and Michael, A.J., 1990, A detailed study of the seismicity of the Middle Mountain zone at Parkfield, California, *Bull. seism. Soc. Am.*, **80**, 577-588.

O'Connell, R.J. and Budiansky, B., 1974, Seismic velocities in dry and saturated cracked solids, *J. geophys. Res.*, **79**, 5412-5426.

O'Connell, R.J. and Budiansky, B., 1977, Viscoelastic properties of fluid-saturated solids, *J. geophys. Res.*, **82**, 5719-5735.

Ohtake, M., 1973, Change in the Vp/Vs ratio related with occurrence of some shallow earthquake in Japan, *J. Phys. Earth*, **21**, 173-184.

Ohtsuki, A. and Harumi, K., 1982, Effect of topography and subsurface inhomogeneities on seismic SV-waves, *Earthquake Eng. Struct. Dyn.*, **11**, 441-462.

Peacock, S., 1986, Shear-wave splitting in the Earth's crust, *PhD Dissertation, University of Edinburgh.*

Peacock, S., Crampin, S., Booth, D.C., and Fletcher, J.B., 1988, Shear-wave splitting in the Anza seismic gap, Southern California, Temporal variations as possible precursors, *J. geophys. Res.*, **193**, 3339-3356.

Pearce, R.G., 1977, Fault plane solutions using relative amplitudes of P and pP, *Geophys. J. R. astr. Soc.*, **50**, 381-394.

Pearce, R.G., 1980, Fault plane solutions using relative amplitudes of P and surface reflections: further studies, *Geophys. J. R. astr. Soc.*, **60**, 459-487.

Pearce, R.G. and Rogers, R.M., 1989, Determination of earthquake moment tensors from teleseismic relative amplitude observations, *J. geophys. Res.*, **94**, 775-786.

Pechman, J.C., 1983, The relationship of small earthquakes to strain accumulation along major faults on sout *Ph.D. dissertation, California Institute of Technology, Pasadena, California, p175.*

Peselinick, L. and Nicolas, A., 1978, Seismic anisotropy in an ophiolite peridotite: application to oceanic upper mantle, *J. geophys. Res.*, **83**, 1227-1235.

Phillips, W.S. and Aki. K., 1986, Site amplification of coda waves from local earthquakes in central California, *Bull. seism. Soc. Am.*, **76**, 627-648.

Poley, C.M., Lindh, A.G., Bakun, W.H. and Schulz, S.S., 1987, Temporal changes in microseismicity and creep near Parkfield, California, *Nature*, **327**, 134-137.

Poupinet, G., Ellsworth, W.L. and Fréchet, J., 1984, Monitoring velocity variations in the crust using earthquake doublets: an application to the Calaveras Fault, California, *J. geophys. Res.*, **89**, 5719-5731.

Puzyrev, N.N., Obolentseva, I.R., Trigubov, A.V. and Gorshkalev, S.B., 1984, On the anisotropy of sedimentary rocks from shear-wave analysis, *Geophys. J. R. astr. Soc.*, **76**, 243-252.

Queen, J.H., 1994, Multicomponent VSP measurements at a west Texas waterflood unit: analysis and interpretation, *Abstract, The Sixth International Workshop on Seismic Anisotropy, Trondheim, Norway, July 3-8.*

Rice, J.R., 1992, Fault stress states, Pore pressure distributions and the weakness of the San Andreas fault, in *Fault Mechanics and Transport Properties of Rocks*, eds Evans, B. and Wong Tong-Feng.

Rikitake, T., 1976, Earthquake prediction, Developments in solid earthquake, *Geophyscs*, **9**, Elsevier, Amsterdam.

Roberston, J.D. and Corrigan, D., 1983, Radiation studies on a shear-wave vibrator in near-surface shale, *Geophysics*, **48**, 19-26.

Roecher, S.W. and Ellsworth, W.L., 1978, VELEST Fortran program, *U.S. Geological Survey, Menlo Park, California.*

Rutter, E.H. and Mainprice, D.H., 1978, The effect of water on stress relaxation of faulted and unfaulted sandstone, *Pure appl. Geophys.*, **166,** 634-654.

Sato, H., 1986, Temporal change in attenuation intensity before and after the eastern Yamanashi earthquake of 1983 in central Japan, *J. geophys. Res.*, **91**, 2049-2061.

Saucier, F., Humphreys, E. and Weldon. R., 1992, Stress near geometrically complex strike-slip faults: application to the San Andreas Fault at Cajon Pass, southern California, *J. geophys. Res.*, **97**, 5081-5094.

Savage, J.C., 1993, The Parkfield prediction fallacy, *Bull. seism. Soc. Am.*, **83,** 1-6.

Savage, M.K., Peppin, W.A. and Vetter, U.R., 1990, Shear wave anisotropy and stress direction in and near Long Valley Caldera, California, *J. geophys. Res.*, **95,** 11,165-11,177.

Scholz, C.H., Sykes, L.R. and Aggarwal, Y.P., 1973, Earthquake prediction: a physical basis, *Science*, **181,** 803-810.

Scholz, C.H., 1990, The mechanics of earthquakes and faulting, *Cambridge University Press, Cambridge.*

Semenov, A.W., 1969, Variation in the travel-time of transverse and logitudinal waves before violent earthquake (in Russian), *Izv. Akad, Nauk., SSSR, Fiz. Zemli.*, **4,** 72-77; *245-248 of American Geophys. Union English Edition.*

Shamir, G., Zoback, M.D. and Barton, C.A., 1988, In situ stress orientation near the San Andreas fault, preliminary results to 2.1km depth from the Cajon Pass scientific drillhole, *Geophy. Res. Lett.*, **15,** 989-992.

Shamir, G. and Zoback, M.D., 1992, Stress orientation profile to 3.5 km depth near the San Andreas Fault at Cajon Pass, California, *J. geophys. Res.*, **97**, 5059-5080.

Shearer, P.M. and Orcutt, J.A., 1987, Surface and near-surface effects on seismic waves - theory and borehole seismometer results, *Bull. seism. Soc. Am.*, **77**, 1168-1196.

Shih, X.R. and Meyer, R.P., 1990, Observations of shear wave splitting from natural events, South Moat of Long Valley Caldera, California, June 29 to August 12, 1982, *J. geophys. Res.*, **95,** 11,179-11,195.

Shih, X.R., Meyer, R.P. and Schneider, J.F., 1989, An automated, analytical method to determine shear-wave splitting, *Tectonophysics*, **165,** 271-278.

Shimazaki, K. and Makata, T., 1980, Time-predictable recurrence model for large earthquakes, *Geophys. Res. Lett.*, **7**, 279-282.

Silver, P.G. and Chan, W.W., 1988, Implications for continental structure and evolution from seismic anisotropy, *Nature*, **335**, 34-39.

Silver L.T. and James, E.W., 1988, Geologic setting and lithologic column of the Cajon Pass deep drillhole, *Geophys. Res. Lett.*, **15,** 941-944.

Sims, J.D., 1989, Geologic map of the San Andreas fault in the Parkfield Quadrangle, *Monterey, CA, Misc. Field Studies Map, USGS.*

Simpson, D.W. and Richards, P.G., 1981, Earthquake prediction, *Maurice Ewing Series 4, American Geophysical Union, Washington DC.*

Smith, W.D., 1981, The b-value as an earthquake precursor, *Nature*, **289,** 136-139.

Smith, W.D., 1986, Evidence for precursory changes in the frequency-magnitude b-value, *Geophys. J. R. astr. Soc.*, **86,** 815-838.

Stuart, W.D., 1990, Parkfield slowing down, *Nature*, **345**, 383-384.

Su, F. and Aki, K., 1989, Spatial and temporal variation in coda Q^{-1} associated with the North Palm Springs earthquake of 1986, *Pure appl. Geophys.*, **133**, 23-52.

Vavryčuk Václav, 1993, Crustal anisotropy from local observations of shear-wave splitting in West Bohemia, Czech Republic, *Bull. seism. Soc. Am.*, **83,** 1420-1441.

Walsh, J.B., 1965, The effect of cracks on the compressibility of rock, *J. geophys. Res.*, **70**, 381-389.

Wang, Chi-Yuen and Sun Yan, 1990, Oriented microfractures in Cajon Pass drill cores, stress field near the San Andreas fault, *J. geophys. Res.*, **95,** 11,135-11,142.

Webb, T.H. and Kanamori, H., 1985, Earthquake focal mechanisms in the eastern transverse ranges and San Emigdio mountains, southern California and evidence for a regional decollement, *Bull. seism. Soc. Am.*, **75,** 737-757.

Weldon, R.J. and Sieh, K.E., 1985, Holocene rate of slip and tentative recurrence interval for large earthquakes on the San Andreas Fault, Cajon Pass, southern California, *Bull. Geol. Soc. Am.*, **96,** 793-812.

Weldon, R.J. and Springer, J.E., 1988, Active faulting near the Cajon Pass well, southern California: implications for the stress orientation near the San Andreas fault, *Geophys. Res. Lett.*, **15,** 993-996.

Wesson, R.L., Burford, R.O., and Ellsworth, W.L., 1973, Relationship between seismicity, fault creep and crustal loading along the central San Andreas fault, *Stanford Univ. Pub. Geol. Sci.*, **13,** 303-321.

Whitcomb, J.H., Garmany, J.D. and Anderson, D.L., 1973, Earthquake prediction: variation of seismic velocities before the San Fernado earthquake, *Science*, **180**, 632-635.

White, J.E., 1965, Seismic Waves: Radiation, Transmision, and Attenuation, *McGraw-Hill, New York.*

Wild, P. and Crampin, S., 1991, Effects of azimuthal isotropy and EDA anisotropy in sedimentary basins, *Geophys. J. Int.*, **107**, 513-529.

Winterstein, D.F., 1990, Velocity anisotropy terminology for geophysicists, *Geophysics*, **55**, 1070-1088.

Wu, T.T., 1966, The effect of inclusion shape on the elastic moduli of a two-phase material, *Int. J. Sol. Struct.*, **2**, 1-8.

Wyss, M., 1990, Changes of mean magnitude of Parkfield seismicity: a part of the precursory process? *Geophys. Res. Lett.*, **17**, 2429-2432.

Wyss, M., Bodin, P. and Habermann, R.E., 1990a, Seismic quiescence at Parkfield: an independent indication of an imminent earthquake, *Nature*, **345**, 426-428.

Wyss, M. and Lee, W.H.K., 1973, Time variations of the average earthquake magnitude in central California, *Proceedings of the conference on tectonic problems of the San Andreas Fault system, eds. Kovach and Nur, Stanford University Geol.Sci.*, **13**, 24-42.

Wyss, M., Slater, L. and Burford, R.O., 1990b, Decrease in deformation rate as a possible precursor to the next Parkfield earthquake, *Nature*, **345**, 428-430.

Yao, C. and Xiong, Y.-W., 1993, Shear-wave splitting from local earthquakes modelled by synthetic seismograms, *Can. J. Expl. Geophys.*, **29**, 324-331.

Yardley, G. and Crampin, S., 1993, Shear-wave anisotropy in the Austin Chalk, Texas, from multioffset VSP data: case studies, *Can. J. Expl. Geophys.*, **29**, 163-176.

Zatsepin, Sergey V. and Crampin, S., 1995, A non-linear anisotropic poro-elastic theroy for pre-stressed fluid-saturated rock, *Submitted to Letters to Nature.*

Zhang, Zhi and Schwartz, S.Y., 1994, Seismic anisotropy in the shallow crust of the Loma Prieta segment of the San Andreas fault system, *J. geophys. Res.*, **99**, 9651-9661.

Zoback, M.D. and Healy, J.H., 1992, In situ stress measurements to 3.5 km depth in the Cajon Pass scientific research borehole, *J. geophys. Res.*, **97**, 5039-5058.

Zoback, M.D. and Lachenbruch, A.H., 1992, Introduction to special section on the Cajon Pass Scientific Drilling Project, *J. geophys. Res.*, **97**, 4991-4994.

Zoback, M.D., Silver, L.T., Henyey, T. and Thatcher, W., 1988, The Cajon Pass Scientific drilling experiment, Overview of phase I., *Geophy. Res. Lett.*, **15**, 933-936.

Zoback, M.L. and Zoback, M.D., 1980, State of stress in the conterminous United States, *J. geophys. Res.*, **85**, 6113-6173.

Zoback, M.D. and Zoback, M.L., 1991, Tectonic stress field of North American and relative plate motions, *in Slemmons, D.B, Engdahl, E.R., Zoback, M.D., and Blackwell, D.D.,eds., Neotectonics of North American: Boulder, Colorado, Geological Society of America, Decade Map Volum 1.*

Zoback, M.D., Zoback, M.L., Mount, V.S., Suppe,J., Eaton, J.P., Healy, J.H., Oppenheimer,D., Reasenberg, P., Jones, L., Raleigh, C.B., Wong, I.G., Scotti, O. and Wentworth, C., 1987, New evidence on the state of stress of the San Andreas fault system, *Science*, **238**, 1105-1111.

CANADIAN JOURNAL OF EXPLORATION GEOPHYSICS
VOL. 29, NO. 1 (JUNE 1993), P. 380-390

SHEAR-WAVE POLARIZATIONS AND POSSIBLE TEMPORAL VARIATIONS IN SHEAR-WAVE SPLITTING AT PARKFIELD

YUN LIU[1,2], DAVID C. BOOTH[1], STUART CRAMPIN[1,2], RUSS EVANS[1] AND PETER LEARY[3]

ABSTRACT

Five of the seven stations of the local borehole seismic network on the San Andreas Fault at Parkfield in central California exhibit aligned polarizations of first arriving split shear waves from fault zone earthquakes in an 18-month data set. At stations VC, VR and ED, 1 to 5 km from the fault, the polarizations are consistently normal or subnormal to the fault strike and parallel to the direction of maximum horizontal regional stress. Shear-wave first motion at station JN is 45°from the fault strike but may be influenced by local surface and subsurface topography. Station MM, located within or immediately adjacent to the fault zone, shows first motion polarized parallel to the fault strike. At stations VC and MM, the shear wave train signal-to-noise ratio permits positive identification and timing of the second split shear wave. There is some evidence of temporal variations of the shear-wave time delays in association with a M_L = 4 San Andreas fault earthquake, with the time delays at MM (7ms/km) twice those at VC (4ms/km). The relatively greater shear-wave splitting observed at MM suggests that the fluid-filled fractures within the fault zone are more extensive than in the surrounding crust. The fault-parallel polarization of the leading split shear wave at MM indicates that the stress is highly irregular in the immediate vicinity of the fault or that fault fractures tend to be aligned by fault shearing rather than by the regional principal stress.

INTRODUCTION

Shear-wave splitting is caused by the effective anisotropy of the medium in which the waves propagate. In the Earth's crust, the polarizations of the leading split shear waves typically display parallel alignments approximately orthogonal to the direction of minimum horizontal compressional stress (Crampin and Lovell, 1991). Splitting was first positively identified in the crust above small earthquakes in Turkey by Crampin et al. (1980, 1985) and has been subsequently observed in many parts of the world in a wide variety of rocks in a wide variety of tectonic regimes (reviewed by Crampin, 1987, and Crampin and Lovell, 1991). The splitting has been attributed to propagation through distributions of stress aligned fluid-filled inclusions known as extensive-dilatanc anisotropy or EDA (Crampin and Lovell, 1991). It has bee suggested that since such fluid-filled cracks, microcracks an preferentially oriented pore space are the most compliant el ments of the rock mass, variations in the stress field ma modify the EDA-crack geometry with consequent tempor changes in the orientation and degree of the shear-wave spli ting (Crampin and Lovell, 1991). Variations of time dela between split shear waves are believed to have been observe at or near the time of the M_L = 6 1986 North Palm Spring earthquake (Peacock et al., 1988; Crampin et al., 1990) an an M_L = 3.5 earthquake of the 1982 Enola swarm in Arkansa (Booth et al., 1990). We have analyzed data recorded at th Parkfield network during a period of one and one half yea to document shear-wave polarization alignments and to searc for possible temporal variations in shear-wave splitting.

THE PARKFIELD HRSN NETWORK

It has been suggested that a magnitude M_L = 6 earthquak on the San Andreas fault could occur within the next fe years at a nucleation zone near Middle Mountain (MM Parkfield, California (Bakun and McEvilly, 1984; Bakun an Lindh, 1985). The Parkfield High Resolution Downhol Digital Seismic Network (HRSN), designed to monitor th characteristics of earthquakes before the anticipated even was installed as part of the Parkfield Prediction Experimer (PPE). Both the uphole and downhole sensors of HRSN ar typically three-component 2-Hz Mark Products L22E seis mometers. The downhole seismometers are cemented a depths between 200 m and 300 m. They have a sampling rat of 500 Hz, a low-pass filter at 100 Hz and downhole gains o 60 dB. An accurate 3-D velocity model of the study regio was an early result of the PPE research program (Michelin and McEvilly, 1991) and the details of the Parkfield networ are documented by Blakeslee and Malin (1990).

[1]British Geological Survey, Murchison House, West Mains Road, Edinburgh EH9 3LA
[2]Department of Geology and Geophysics, University of Edinburgh, West Mains Road, Edinburgh EH9 3JW
[3]Department of Geological Science, University of Southern California, Los Angeles, CA 90089 - 0741

We thank Prof. Tom McEvilly for his suggestions and discussion. We also thank Prof. Peter Malin for providing a further data set. This work is supported by th Natural Environment Research Council and is published with the approval of the Director of the British Geological Survey (NERC).

Geology

The geology of the Parkfield area is dominated by the strike-slip plate boundary at the San Andreas Fault (SAF). Figure 1 shows the SAF and associated shallow thrust faults and the station distribution of the Parkfield HRSN network. The Parkfield fault segment is generally understood to be the transition zone between the 170-km-long creeping part of the SAF (average 33 mm/yr, Wesson et al., 1973) to the northwest and the 300-km-long locked portion to the southeast, where the average width of fault gouge in the Parkfield segment varies from 100 to 200 m. Analysis of seismograms recorded at MM in terms of fault zone trapped waves (Li and Leary, 1990; Leary and Ben-Zion, 1992) indicates that the shear-wave velocity of the fault gouge is about 1.1 km/s in the area of the 1966 M_L = 5.9 main shock and is 1.8 km/s in the southeast segment approaching the locked portion of the SAF. There exists a transition zone about 400 m wide with shear-wave velocity of 1.8 km/s on the flank of 1966 main shock area and 2.5 km/s on the northwest and southeast segment of the SAF. The fault is dipping steeply at 86° ±1.1° (Nishioka and Michael, 1990).

The Salinian block on the southwest side of the SAF consists of Gabilan plutonic and metamorphic basement rocks covered by a maximum of 2 km of Tertiary and Quaternary sediments. These deposits generally dip away from the Cholame Hills high, a basement uplift that parallels the SAF system several kilometres to its southwest. Northeast of the SAF, the broadly outcropping basement consists of Franciscan mélange. Overlying this basement to the east are several kilometres of Cretaceous and younger sediments of the Great Valley sequence. In general, Franciscan rocks are moderately to strongly deformed and, in the SAF zone, slivers of various crystalline rocks appear to have been trapped within older branches of the fault (Brown et al., 1967). Some

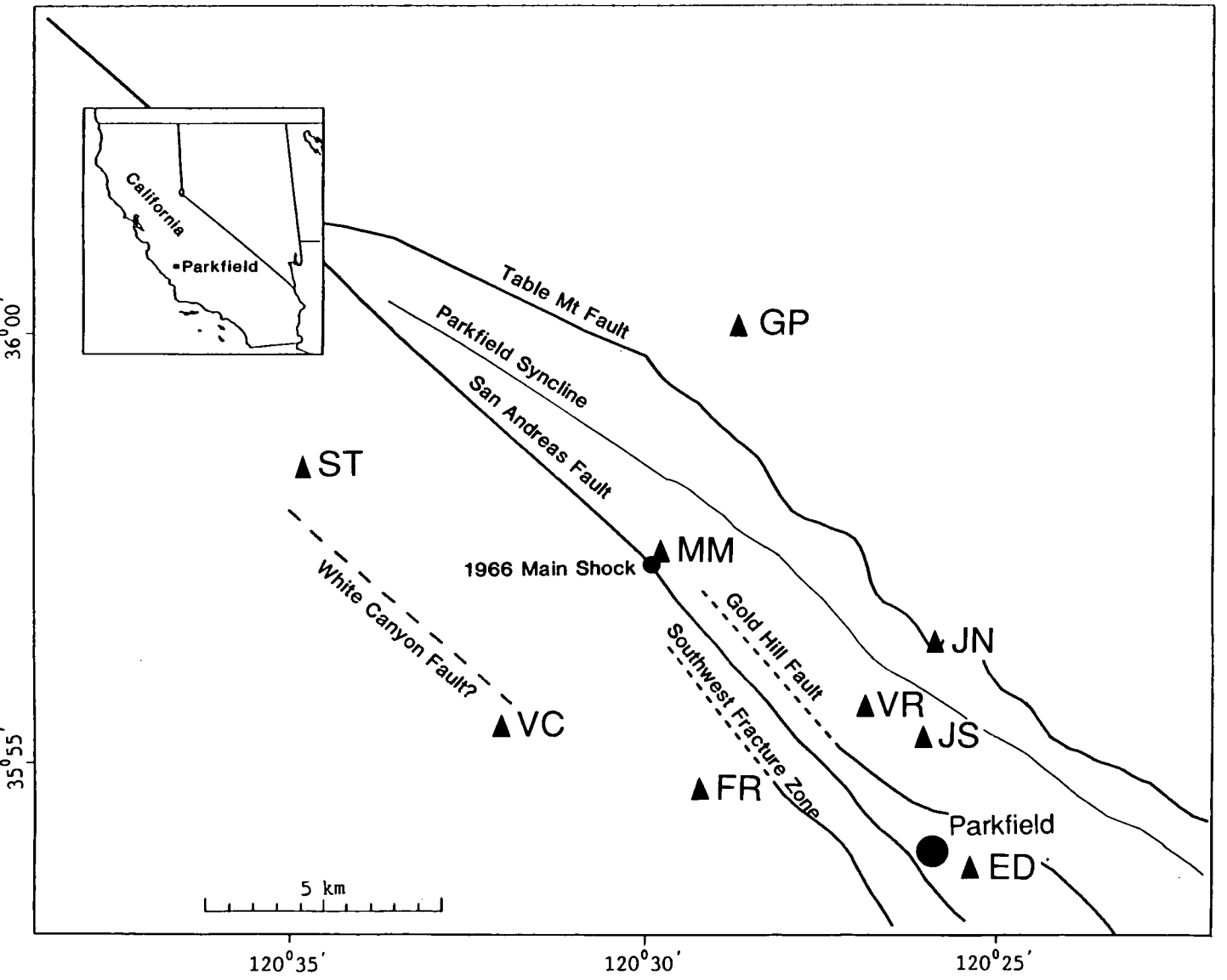

Fig. 1. Map of major faults and station distribution of the Parkfield downhole HRSN network. Triangles denote station locations.

of the numerous thrust faults surrounding the SAF show Holocene movement.

Data Analysis

Data recorded within the shear-wave windows (Evans, 1984; Booth and Crampin, 1985) of nine HRSN stations between January, 1989, and July, 1990, were examined. All earthquakes where shear waves were clearly visible above the *P*-wave coda showed evidence of shear-wave splitting. (The only earthquakes which did not show actual splitting were those where the source excited only one of the anisotropic shear-wave polarizations.) The epicentres of these local events within the shear-wave window of the Parkfield stations are shown in Figure 2. In general, earthquakes recorded by the network occur close to the fault plane with depths between 4 and 15 km and magnitudes between M_L = -0.5 and M_L = 2. An earthquake on 25th May, 1989, with

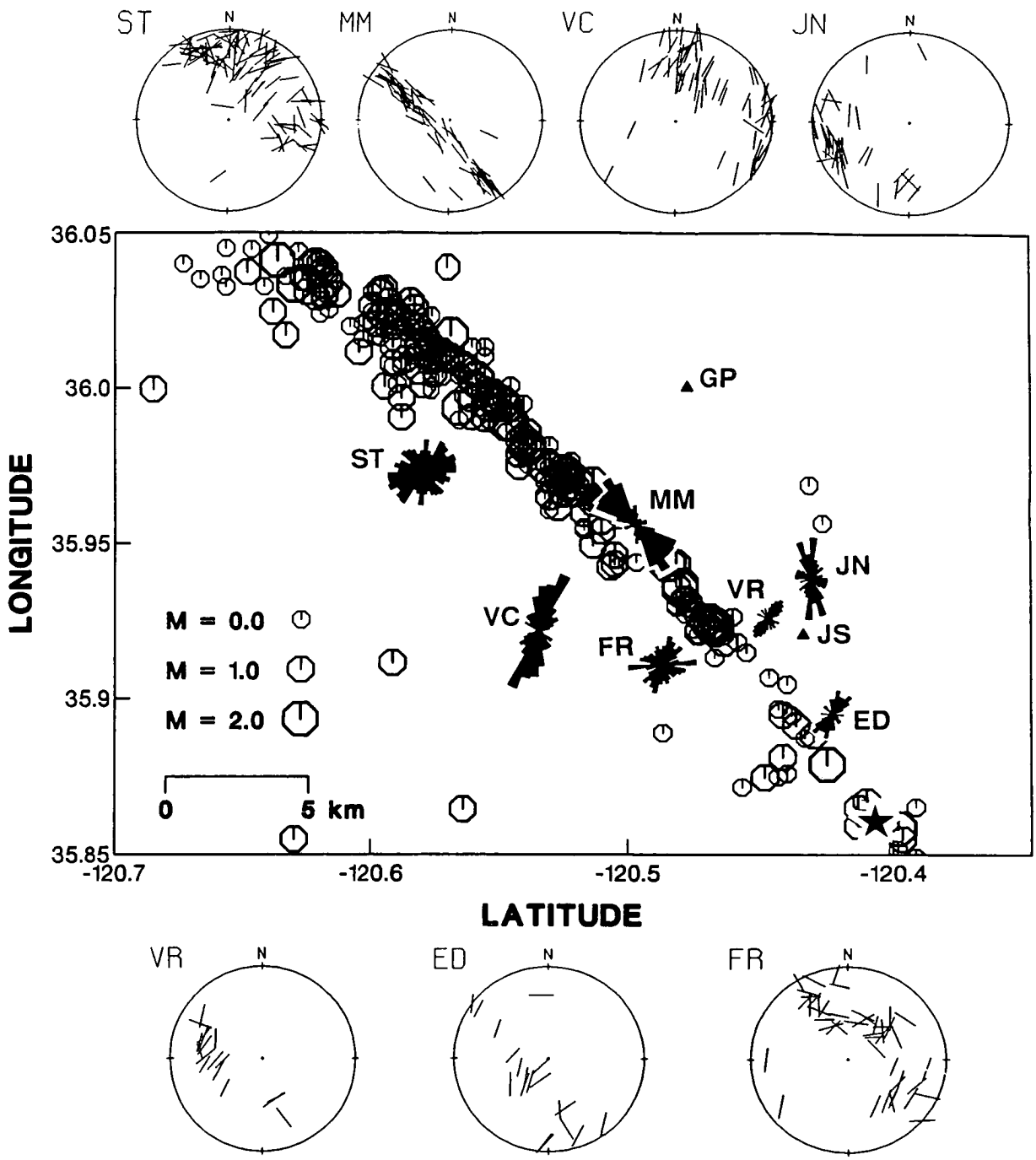

Fig. 2. Equal-area rose diagrams of polarizations of the leading split shear wave and the epicentres of the local events which are used to monitor the shear-wave splitting. The star indicates the M_L = 4 earthquake which occurred on May 25, 1989. Equal-area projections of the lower hemispheres beneath each station, out to angle of incidence of 45°, show polarizations of leading split shear waves. There are no suitable data at stations GP and JS.

magnitude $M_L = 4$ and focal depth of 8.25 km is located near the southeast extremity of the network and is marked with a star in Figure 2. It is about 15 km away from stations MM and VC. This is the largest earthquake which occurred on the 54-km Parkfield segment and its surrounding areas since the recording began, and we seek temporal variations associated with this event.

Representative records exhibiting clear shear-wave splitting are shown in Figure 3 with parameters listed in Table 1. Many seismograms are complicated with a strong *P*-wave coda which interferes with shear-wave arrivals particularly at stations ST and FR. This causes difficulty in identifying the onset of the faster split shear waves and we have not attempted to study the variation of time delays at these stations. Station GP is outside the shear-wave window for most earthquakes and those that are within the window have low-frequency shear waves (less than 10 Hz compared to the dominant frequency at about 20 Hz at other stations) yielding elliptical motion which makes analysis of shear-wave splitting difficult. The recording system at station JS did not function correctly during the period we are examining.

Ben-Zion and Malin (1991) and Ben-Zion et al. (1992) have identifed *P* head waves propagating along the fault plane at stations on the northeast side of the SAF (stations MM, JN, ED and VR). We would expect shear head waves to be observed in similar situations, where they might interfere with the split shear-wave arrivals. The characteristics of shear head waves along the fault plane have been examined with synthetic seismograms and will be the subject of a separate study. We find that shear head waves are probably not important for the study of shear-wave splitting as the amplitude of such shear head waves decays rapidly with the distance from the fault plane and the recorded energy at many of the HRSN stations is small. In any case, their characteristic one-sided waveforms are easily recognizable. We have attempted to eliminate both shear head waves and free surface *S-P* converted waves (the local *SP* phase) (Booth and Crampin, 1985; Crampin, 1990) from the data set in order to reduce the possibility of misidentifying the onset of the faster split shear waves.

Shear-wave polarizations

The distributions of shear-wave polarizations for shear-wave arrivals within the shear-wave window at each station are plotted as equal-area rose diagrams in Figure 2. The polarizations of the faster split shear waves display approximately parallel alignments at stations MM, VC, VR, JN and ED, as is typically observed elsewhere (Crampin and Lovell, 1991). The directions of the polarizations are scattered at stations ST and FR with little evidence of any preferential alignment. The rose diagrams showing polarizations at stations VC, VR and ED are distributed about a N30°E direction which is approximately parallel to the direction of maximum principal stress near the San Andreas Fault in central California (Zoback et al., 1987). The alignment at JN is N5°W and the alignment at MM is about N40°W, approximately parallel to the SAF. [Note that VR shows a large scatter, similar to the scatter seen in the shear-wave VSP observations sampling the uppermost 1400 m of the Varian Well (VR) (Daley and McEvilly, 1990), although the average polarization in Figure 2 is clearly approximately N30°E.]

The reasons for the irregularities in the alignment of such shear-wave polarizations are not fully understood. Certainly, the interaction of shear waves with severe surface topography can in some cases cause parallel polarizations to be systematically rotated by up to 90° (Chen et al., 1987; Graham and Crampin, 1993) and hilltop sites typically display scattered polarizations (Peacock et al., 1988). This sensitivity to topography within 100 m of the recording site is expected as shear waves have severe interactions with the free surface for angles of incidence outside the shear-wave window (Evans, 1984; Booth and Crampin, 1985). Focussing effects and changes in angle of incidence at the free surface due to refraction across near-surface high-impedance hard rock to sediment interfaces may also distort shear-wave arrivals (Crampin, 1990). Several of the HRSN stations (MM, ST, JN and GP) are sited near severe local topography and the subsurface structure beneath many of the stations is complicated.

Time delays between split shear waves

Time delays between the split shear waves are more difficult to estimate than polarizations of the faster split shear wave (Booth and Crampin, 1985; Chen et al., 1987), and scattered polarizations usually indicate other disturbances to the wave train which make it impossible to estimate reliably time delays. Consequently, we confine our analysis to those stations MM, VC, JN and ED, which display approximately parallel polarizations, excluding VR which has no data for the initial 8 months of the period we are examining.

Figure 4 shows the variations of time delay in polar projections of the shear-wave window for stations MM, VC, JN and ED and variations with time of the time delay, shear-wave polarization, and of the focal depths of the earthquakes whose records are analyzed. The time delays have been normalized to a path length of 1 km. The time of the $M_L = 4$ earthquake is indicated by the solid arrows in the time variations.

There is insufficient data to make reliable judgements of variations in time delay before the time of the $M_L = 4$ earthquake, but the stations where there is adequate data, MM and VC, show a (marginal) decrease in the time delay following the $M_L = 4$ earthquake, followed by an irregular increase. Note that the possible significance of this earthquake was not recognized initially and only came to our attention after we had observed the variation of time delays. There is no other larger earthquake recorded in the network during the study period. This behaviour is similar to that seen in previous studies which showed similar decreases in time delay at the time of $M = 6$ (Crampin et al., 1990) and $M = 3.5$ earthquakes (Booth et al., 1990).

The average time delays at station MM on the fault zone are about twice as large as those at station VC 5 km away from the fault zone on the southwest block. A large part of

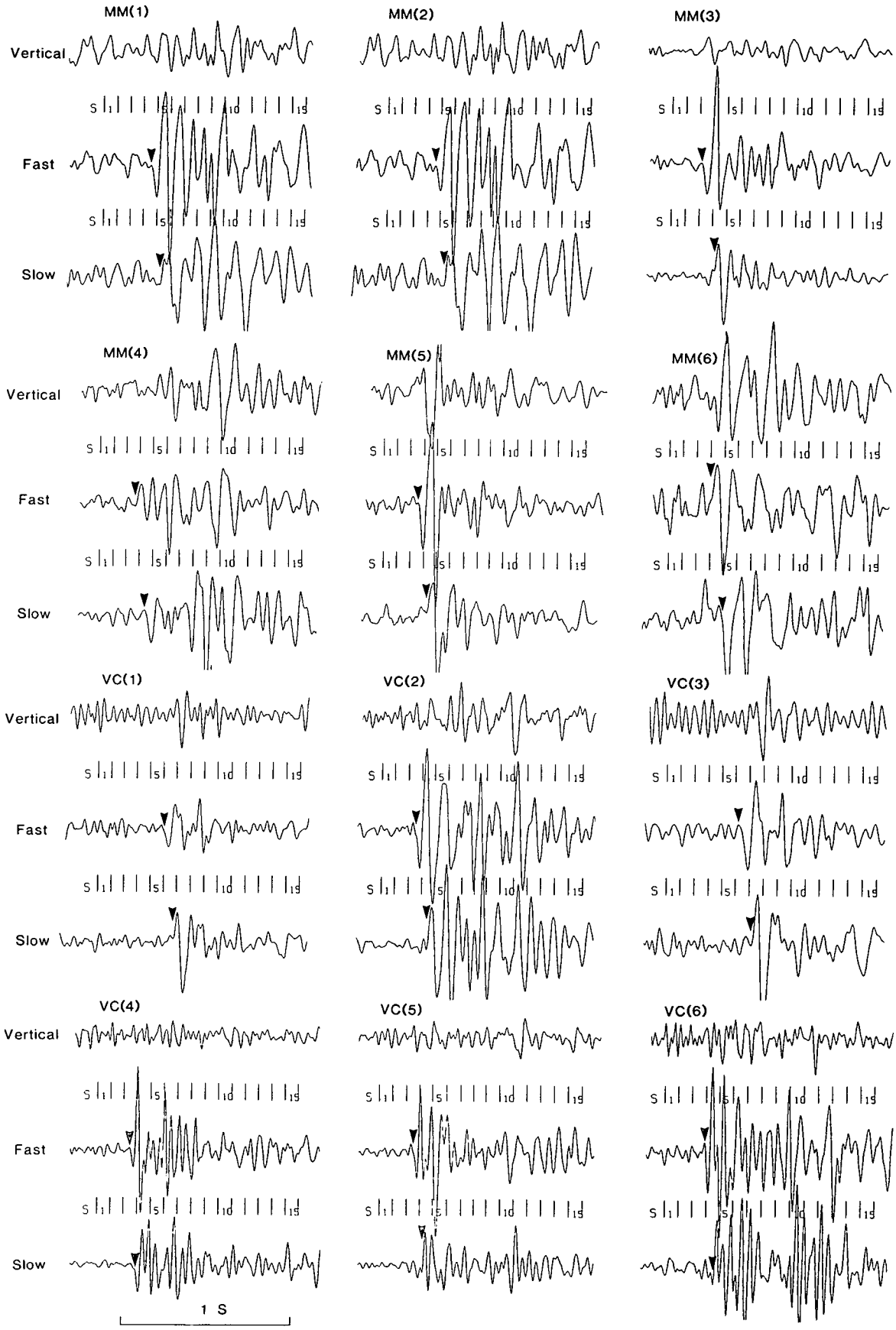

Fig. 3. Representative shear-wave seismograms and corresponding polarization diagrams recorded at stations MM and VC for events listed in Table 1. The horizontal components have been rotated parallel and perpendicular to the polarizations of the faster (F) and slower (S) split shear waves. The rotated seismograms show delayed shear-wave arrivals diagnostic of shear-wave splitting. The polarization diagrams show the horizontal particle motion for the numbered, 0.08-s-long, time windows marked on the seismograms.

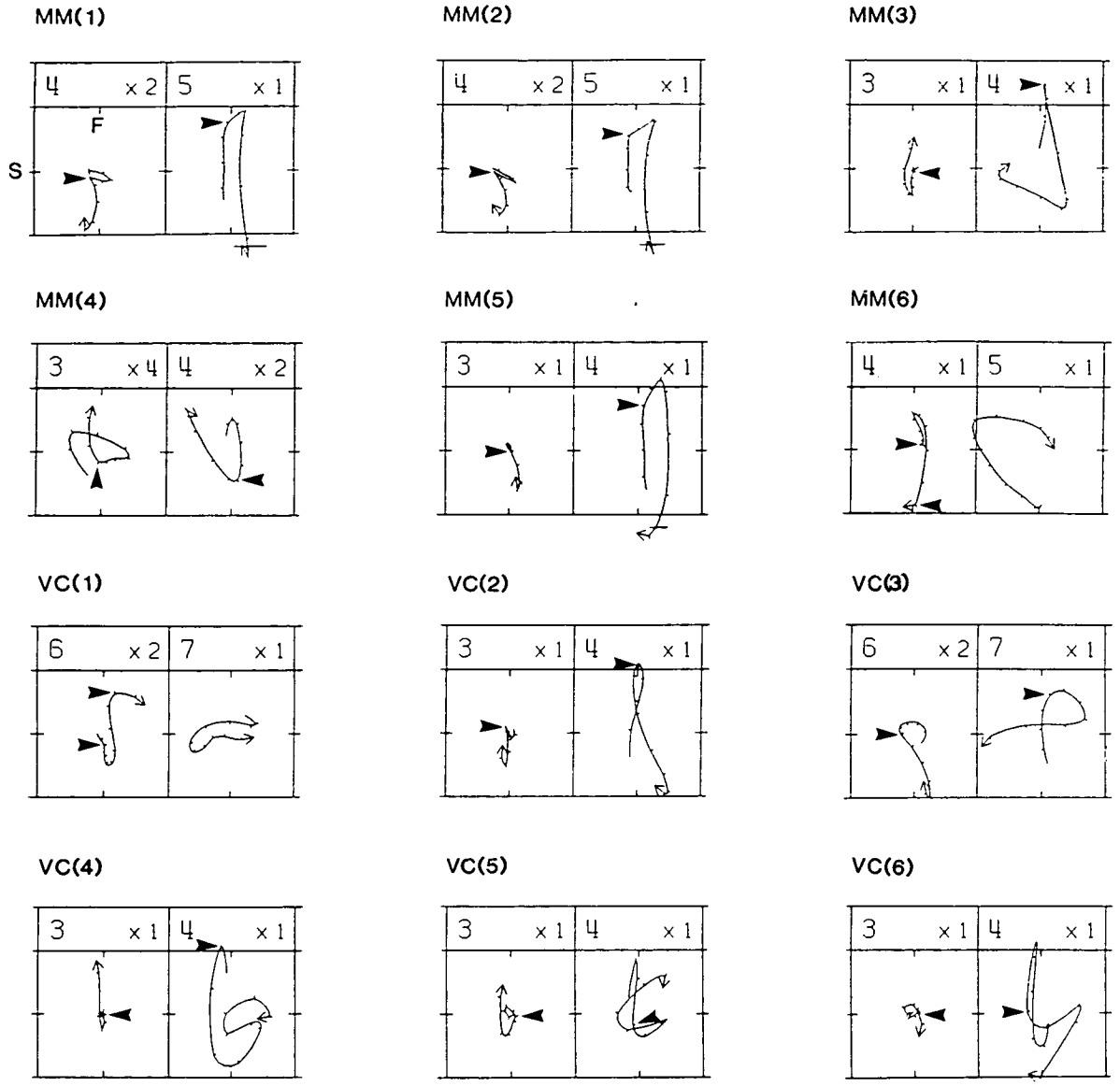

Fig. 3 (Cont'd).

Table 1. Parameters of representative earthquakes shown in Figure 2.

Stn(n)	Date (y.m.d)	Time (h.m)	Latitude (N)	Longitude (W)	Depth (km)	Mag. (M_L)	Spol (N°E)	Sdel (ms/km)
MM(1)	900613	2242	35°55.51'	120°28.30'	5.80	1.05	328	7.9
MM(2)	900305	1632	35°57.47'	120°30.25'	4.47	-0.06	149	12.2
MM(3)	900614	1803	35°59.80'	120°33.65'	8.81	0.22	130	6.4
MM(4)	900505	2356	36°01.55'	120°35.01'	9.51	0.21	317	4.4
MM(5)	900613	2239	35°55.43'	120°28.18'	6.09	1.49	332	8.8
MM(6)	900405	0503	35°58.47'	120°31.53'	4.45	0.14	153	10.4
VC(1)	900511	1120	35°56.18'	120°28.94'	5.21	0.64	357	6.7
VC(2)	900628	0249	35°59.45'	120°35.38'	16.10	0.67	191	5.6
VC(3)	900511	1011	35°56.20'	120°28.89'	5.17	1.12	198	3.3
VC(4)	900702	2043	35°56.61'	120°30.39'	12.76	0.81	9	3.1
VC(5)	900516	1258	35°58.08'	120°31.49'	11.03	0.19	211	2.0
VC(6)	900412	0718	35°57.70'	120°31.65'	11.79	0.80	194	3.9

Stn(n): station name and number corresponds to Figure 3. Spol and Sdel are shear-wave polarizations and time delays, respectively.

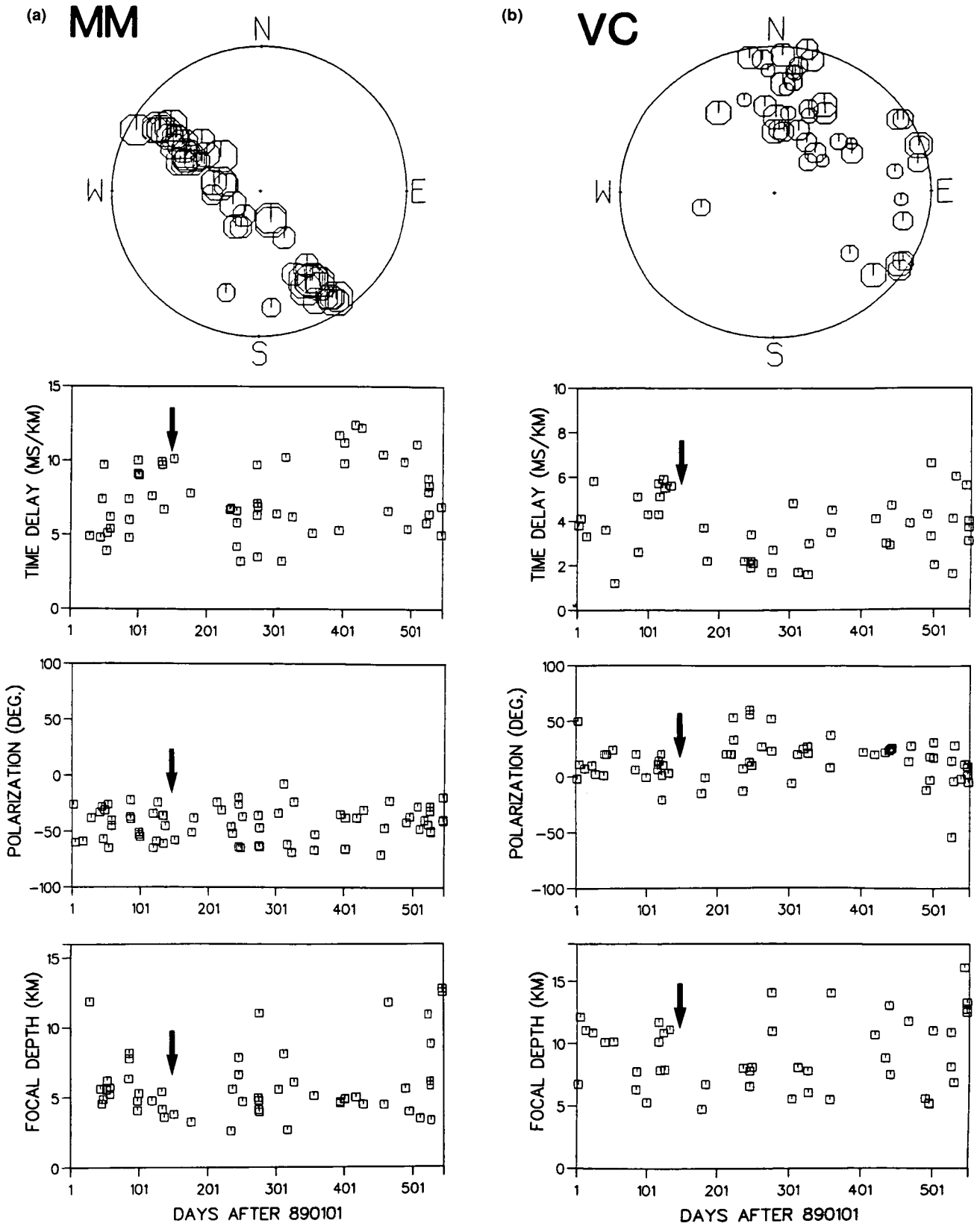

Fig. 4. Variations at stations: **(a)** MM; **(b)** VC; **(c)** JN and **(d)** ED. The diagrams show from the top: equal-area projections (polar maps) out to 45° the time delays; variations of time delays with time from the beginning of the data set; variations of polarizations with time and (bottom) variations focal depth with time. The arrows mark the time of the $M_L = 4$ earthquake.

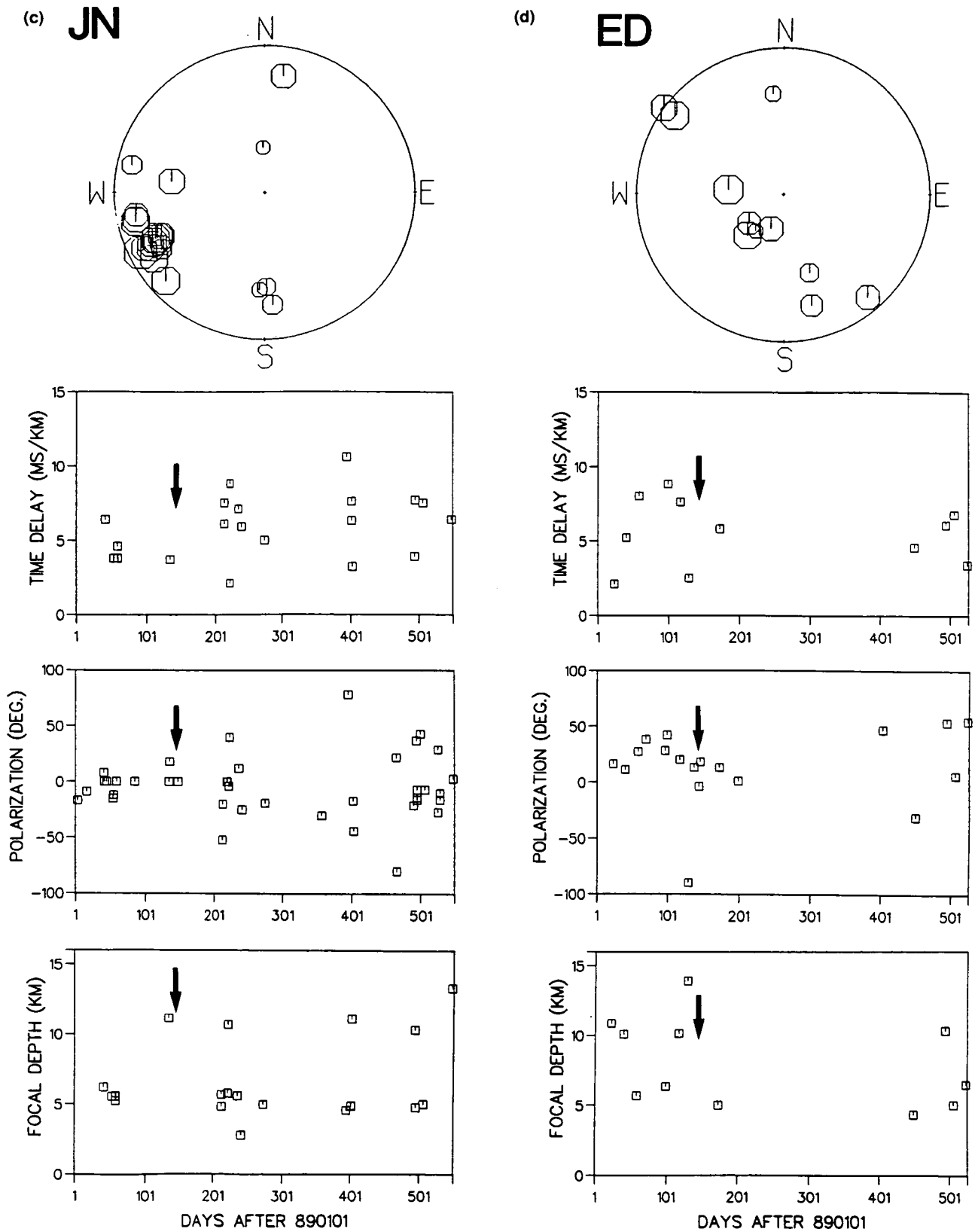
(c)
JN
N
W
E
S
TIME DELAY (MS/KM)
POLARIZATION (DEG.)
FOCAL DEPTH (KM)
DAYS AFTER 890101
(d)
ED
N
W
E
S
TIME DELAY (MS/KM)
POLARIZATION (DEG.)
FOCAL DEPTH (KM)
DAYS AFTER 890101

Fig. 4 (Cont'd).

each raypath to station MM is through the fault zone and the larger time delays are probably due to the greater density of microcracks and fractures trapped in the fault zone. The detailed geometry of these microcracks and fractures would be expected to be modified during any change in the stress field and could cause the possible temporal changes seen in Figure 4.

The corresponding polarizations show a relatively uniform scatter with no marked variation with time. The polarizations at stations MM and VC show a ±25° spread constant in time in a constant direction consistent with the rose diagrams in Figure 2. The polarizations at JN and ED show more scatter, again as expected from Figure 2. Note that the time delays at stations MM and VC are considered to be reliable, but at other stations the shear waves are severely distorted by strong *P* coda waves.

The variation of focal depth with time at stations MM and VC in the bottom diagram of Figure 4 shows a decrease in focal depth for about 100 days after the $M_L = 4$ event, which suggests that the decrease of time delay at the time of the event could be caused by migration of focal depths (note however the small numbers of earthquakes involved: 3 for MM and 7 for VC). Figure 5 shows the variation of the (normalized) time delay with the focal depth of the earthquakes monitored at each station in Figure 4. Stations VC (and ED) show a uniform scatter with no decrease of time delay with depth, as would be required if the anomalies in the temporal variations of time delay were caused by the decrease in focal depth indicated in Figure 4. However, for earthquakes near station MM (and JN), Figure 5 shows that at MM the normalised time delays have a pronounced increase for earthquakes with focal depths above about 7-km depth. This means that a decrease of focal depth, as observed in Figure 4, would tend to increase the time delays, and the temporal decrease is unlikely to be caused by depth migration.

The marked decrease in normalized time delays at MM for focal depths below 7 km suggests that the anisotropy of the fault zone is concentrated above 7 km. This could be explained by fault gouge having more aligned inclusions than the surrounding more intact rocks. The possible depth of the stronger anisotropy is in broad agreement with the results of Malin et al. (1989) and Li et al. (1992) who suggest that the fault gouge may extend from the surface to 10-km depth at the locked portion of the fault zone and about 5-km depth at the creeping portion. This intermediate depth of 7 km might suggest that MM is on a transition zone between creeping and locked sections of the fault.

Discussion and Interpretation

Many studies have demonstrated that the alignment of shear-wave polarizations are not due to the source polarizations (Crampin et al., 1986; Peacock et al., 1988; Gledhill, 1990) and can be attributed to the effective anisotropy of stress-aligned fluid-filled inclusions (Crampin and Lovell, 1991). Shear-wave polarizations appear in most cases to be aligned parallel to the direction of the local maximum

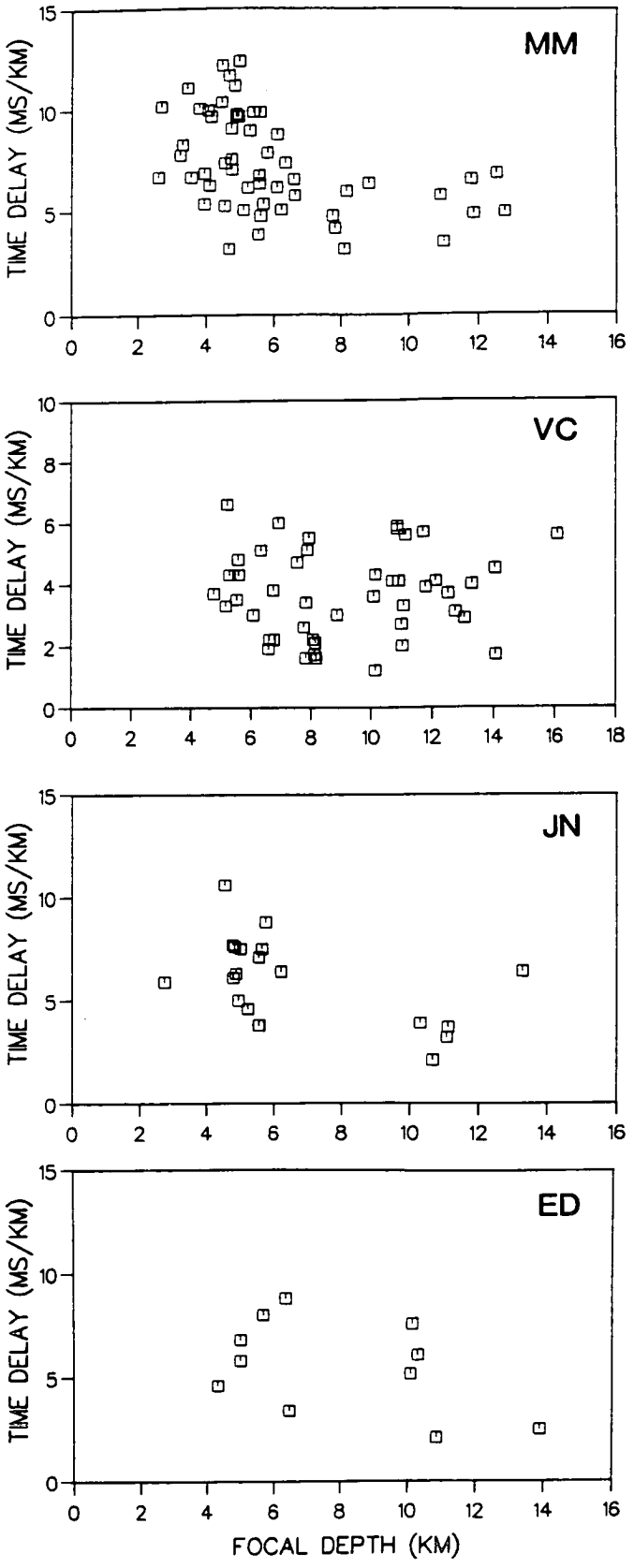

Fig. 5. Variations of (normalized) time delays with focal depth of the earthquakes monitored in Figure 4.

compressional stress or, more strictly, perpendicular to the minimum stress direction which is expected to control the orientations of fluid-filled inclusions in the crust (Crampin and Lovell, 1991). Note that such parallelism constrains the type of anisotropic symmetry to hexagonal symmetry with a subhorizontal axis of symmetry. This strongly suggests a distribution of subparallel vertical EDA cracks as the source of the anisotropy since such structures are the only common source of hexagonal symmetry found in the crust (Crampin, 1993). The polarizations at VC, VR and ED in Figure 2 are approximately perpendicular to the SAF and parallel to the regional stress direction estimated by Zoback et al. (1987) and thus agree with the hypothesis of fluid-filled EDA cracks, in this case, aligned by the regional stress field.

Nearer the fault, the alignment of EDA cracks appears to change. Figure 6 plots the nodal lines of 68 fault plane solutions of earthquakes which were located close to station MM (Nishioka and Michael, 1990). The narrow distribution of inferred stress axes suggests a uniform stress field in the vicinity of the fault. However, the N15°W to N10°E direction of maximum principal stress implied by these mechanisms is not compatible with the N30°E microcrack direction inferred from shear-wave polarizations at VC, VR and ED, which are parallel to the regional principal stress. It is compatible with polarizations at JN but JN is in a region of high topographic relief.

If we accept the hypothesis of shear-wave splitting caused by aligned fluid-filled EDA cracks, the polarizations at MM suggest that the cracks strike parallel to the fault. Studies of shear fracture failure suggest the development of fault parallel fractures (King, 1983), while observations of shear waves specifically associated with fault zones at Izmit, Turkey (Crampin et al., 1985), Oroville, California (Leary et al., 1987) and at seismic station KNW on the San Jacinto Fault, California (Crampin et al., 1990) indicate the same conclusion.

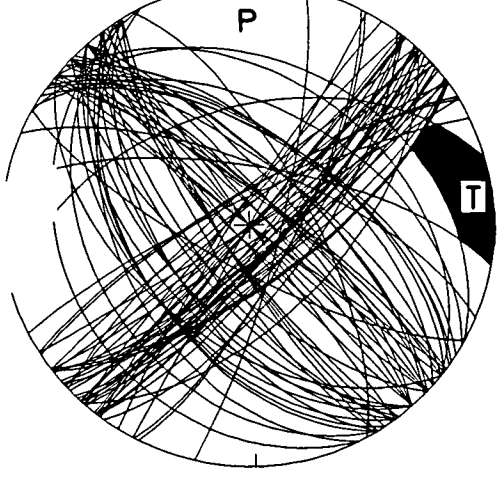

Fig. 6. Superimposed fault plane solutions from the Parkfield area showing common areas of compression (P) and tension (T), in equal-area projections of the upper focal hemisphere (after Nishioka and Michael, 1990).

Station MM is probably on the transition zone of the SAF and it is very close to the 1966 main shock (Figure 1). Ninety-five percent of shear waves from earthquakes recorded within the shear-wave window at this station propagated nearly vertically with an incidence angle of less than 15°, hence the fault internal structure (fault gouge and transition zone), its nearby subparallel folds and various crystalline rocks are presumably the dominant factors in controlling the shear-wave polarizations beneath this station. It is likely that the gouge of the fault zone plays the most significant role in controlling shear-wave anisotropy at this station.

The geological structure at Parkfield is complicated. The fault zone area appears to be heterogeneous in both velocity variation and geological structure (Michelini and McEvilly 1991; Li et al., 1992). This is presumably one of the reasons for the difficulty in picking faster shear-wave onsets. Nevertheless, the results of this study correlate with other independent studies and we believe that the temporal variation o time delays is reliably associated with the $M_L = 4$ event.

Conclusions

The shear-wave polarizations at stations VC, ED and VR are aligned approximately NNE which is approximately parallel to the direction of maximum horizontal regional stress Shear-wave first motion at station JN is 45° from the faul strike but may be influenced by local surface and subsurface topography. Polarizations at station MM are probably controlled by the fault zone internal structure causing an alignment of about N40°W parallel to the fault. The fact that time delays at station MM are about twice as large as those at VC suggests that the fluid-filled microcracks and fractures within the fault zone are more extensive than in the surrounding crust. Possible temporal changes in the time delays betwee split shear waves have been observed at two stations of th Parkfield HRSN network after an $M_L = 4$ earthquake with epi centre about 15 km from the stations. The temporal change suggested in this paper are compatible with similar tempora variations at the time of a larger earthquake observed else where.

References

Bakun, W.H. and Lindh, A.G., 1985, The Parkfield, California, earthqual prediction experiment: Science **229**, 619-623.

_____ and McEvilly, T.V., 1984, Recurrence models and Parkfield, Ca fornia, earthquakes: J. Geophys. Res. **89**, 3051-3058.

Ben-Zion, Y. and Malin, P., 1991, San Andreas fault zone head waves ne Parkfield, California: Science **251**, 1592-1594.

_____, Katz, S. and Leary, P., 1992, Joint inversion of fault zone head wav and direct *P* arrivals for crustal structure near major faults: J. Geophy Res. **97**, 1943-1951.

Blakeslee, S.N. and Malin, P.E., 1990, A comparison of earthquake co waves at surface versus subsurface seismometer: J. Geophys. Res. 9 309-326.

Booth, D.C. and Crampin, S., 1985, Shear-wave polarizations on a curv wavefront at an isotropic free surface: Geophys. J. Roy. Astr. Soc., **83**, 31-4

_____, _____, Lovell, J.H. and Chiu, J.-M., 1990, Temporal changes in shear-wave splitting during an earthquake swarm in Arkansas: J. Geophys. Res. **95**, 11,151-11,164.

Brown, R.D., Jr., Vedder, J.G., Wallace, R.E., Roth, E.F., Yerkes, R.F., Castle, R.O., Waananen, A.O., Page, R.W. and Eaton, J.P., 1967, The Parkfield-Cholame, California earthquakes of June-August 1966 - surface geologic effects, water-resources aspects and preliminary seismic data: U.S. Geol. Surv., Prof. Paper 579, 1-66.

Chen, T.-C., Booth, D.C. and Crampin, S., 1987, Shear-wave polarizations near the North Anatolian Fault - III. Observations of temporal changes: Geophys. J. Roy. Astr. Soc. **91**, 287-311.

Crampin, S., 1987, Geological and industrial implications of extensive-dilatancy anisotropy: Nature **328**, 491-496.

_____, 1990, The scattering of shear waves in the crust: Pure Appl. Geophys. **132**, 67-91.

_____, 1993, Arguments for EDA: Can. J. Expl. Geophys. **29**, 18-30.

_____ and Booth, D.C., 1985, Shear-wave polarizations near the North Anatolian Fault – II. Interpretation in terms of crack-induced anisotropy: Geophys. J. Roy. Astr. Soc. **83**, 75-92.

_____ and Lovell, J.H., 1991, A decade of shear-wave splitting in the Earth's crust: what does it mean? what use can we make of it? and what should we do next?: Geophys. J. Internat. **107**, 387-407.

_____, Booth, D.C., Evans, R., Peacock, S. and Fletcher, J.B., 1990, Changes in shear-wave splitting at Anza near the time of the North Palm Springs earthquake: J. Geophys. Res. **95**, 11,197-11,212.

_____, _____, Krasnova, M.A., Chesnokov, E.M., Maximov, A.B. and Tarasov, N.T., 1986, Shear-wave polarizations in the Peter the First Range indicating crack-induced anisotropy in a thrust-fault regime: Geophys. J. Roy. Astr. Soc. **84**, 401-412.

_____, Evans, R. and Üçer, S.B., 1985, Analysis of records of local earthquakes: the Turkish Dilatancy Projects (TDP1 and TDP2): Geophys, J. Roy. Astr. Soc. **83**, 1-16.

_____, _____, _____, Doyle, M., Davis, J.P., Yegorkina, G.V. and Miller, A., 1980, Observations of dilatancy-induced polarization anomalies and earthquake prediction: Nature **2**, 874-877.

Daley, T.M. and McEvilly, T.V., 1990, Shear-wave anisotropy in the Parkfield Varian Well VSP: Bull. Seis. Soc. Am. **80**, 857-869.

Evans, R., 1984, Effects of the free surface on shear wavetrains: Geophys. J. Roy. Astr. Soc. **76**, 165-172.

Gledhill, K.R., 1990, A shear-wave polarization study in the Wellington region, New Zealand: Geophys. Res. Lett. **17**, 1319-1322.

Graham, G. and Crampin, S., 1993, Shear-wave splitting from regional earthquakes in Turkey: Can. J. Expl. Geophys. **29**, 371-379.

King, G.C.P., 1983, The accommodation of large fault behaviour, subsurface geology, and three-dimensional velocity models: Science **253**, 651-654.

Leary, P.C. and Ben-Zion, Y., 1992, A 200-m-wide fault low-velocity layer on the San Andreas fault at Parkfield: results from analytic waveform fits to trapped wave groups: J. Geophys. Res. **97**, 1943-1951.

_____, Li, Y.-G. and Aki, K., 1987, Observation and modelling of fault zone fracture seismic anisotropy – I. *P*, *SV* and *SH* traveltimes: Geophys. J. Roy. Astr. Soc. **91**, 461-484.

Li, Y.-G. and Leary, P.C., 1990, Fault zone trapped seismic waves: Bull. Seis. Soc. Am. **80**, 1245-1271.

_____, Teng, T.L. and Aki, K., 1992, Observation and interpretation of fault-zone trapped seismic waves at three different geological and experiment environments in California: Seis. Res. Lett. **63**, 76 (Abstr.).

Malin, P.E., Blakeslee, S.N., Alvarez, M.G. and Martin, A.J., 1989, Microearthquake imaging of the Parkfield asperity: Science **224**, 557-559.

Michelini, A. and McEvilly, T.V., 1991, Seismological studies at Parkfield – I. Simultaneous inversion for velocity structure and hypocenters using cubic B-splines parameterization: Bull. Seis. Soc. Am. **81**, 524-552.

Nishioka, G.K. and Michael, A.J., 1990, A detailed study of the seismicity of the Middle Mountain zone at Parkfield, California: Bull. Seis. Soc. Am. **80**, 577-588.

Peacock, S., Crampin, S., Booth, D.C. and Fletcher, J.B., 1988, Shear-wave splitting in the Anza seismic gap, southern California: temporal variations as possible precursors: J. Geophys. Res. **193**, 3339-3356.

Wesson, R.L., Burford, R.O. and Ellsworth, W.L., 1973, Relationship between seismicity, fault creep and crustal loading along the central San Andreas fault: Stanford Univ. Publ. Geol. Sci. **13**, 303-321.

Zoback, M.D. et al., 1987, New evidence on the state of stress of the San Andreas Fault System: Science **238**, 1105-1111.